

DIGITAL ACCESS TO SCHOLARSHIP AT HARVARD
DASH.HARVARD.EDU

HARVARD LIBRARY


Algorithms and Architectures for Quantum Simulation with Neutral-atom Arrays

Citation

Maskara, Nishad. 2025. Algorithms and Architectures for Quantum Simulation with Neutral-atom Arrays. Doctoral Dissertation, Harvard University Graduate School of Arts and Sciences.

Link

https://dash.harvard.edu/handle/1/42726152

Terms of use

This article was downloaded from Harvard University's DASH repository, and is made available under the terms and conditions applicable to Other Posted Material (LAA), as set forth at
https://harvardwiki.atlassian.net/wiki/external/NGY5NDE4ZjgzNTc5NDQzMGIzZWZhMGFlOWI2M2EwYTg

Accessibility

https://accessibility.huit.harvard.edu/digital-accessibility-policy

Share Your Story

The Harvard community has made this article openly available.
Please share how this access benefits you. Submit a story

HARVARD
Kenneth C. Griffin

GRADUATE SCHOOL
OF ARTS AND SCIENCES

THESIS ACCEPTANCE CERTIFICATE

The undersigned, appointed by the

Department of Physics

have examined a dissertation entitled

Algorithms and architectures for quantum simulation with neutral-atom arrays

presented by Nishad Maskara

candidate for the degree of Doctor of Philosophy and hereby
certify that it is worthy of acceptance.

Signature _____

Typed name: Prof. Mikhail Lukin

Signature _____

Typed name: Prof. Subir Sachdev

Signature _____

Typed name: Prof. Anurag Anshu

Date: April 21, 2025

Algorithms and Architectures for Quantum Simulation with Neutral-atom Arrays

a dissertation presented
by
Nishad Maskara
to
The Department of Physics

in partial fulfillment of the requirements
for the degree of
Doctor of Philosophy
in the subject of
Physics

Harvard University
Cambridge, Massachusetts
April 2025

©2025 – Nishad Maskara
all rights reserved.

Thesis advisor: Professor Mikhail D. Lukin Nishad Maskara

Algorithms and Architectures for Quantum Simulation with Neutral-atom Arrays

Abstract

Fast and scalable quantum simulations promise to revolutionize our understanding of complex quantum systems, In this thesis, we primarily aim to develop algorithms and architectures for leveraging programmable quantum devices, to model complex physical phenomena[551]. As quantum computers can natively capture superposition and entanglement, two key attributes which are challenging for classical computers to accurately model, this approach promises significant benefits in the long run[668,691,628]. We focus primarily on neutral-atom arrays, an emerging experimental platform, although many of our results apply more generally as well. The work is structured into three phases, each progressively advancing the complexity and control of considered experimental hardware, and in parallel the importance and applicability of the considered quantum simulations.

In the first phase (Chapters 1–3), we address the challenge of programming and controlling quantum many-body systems through analog techniques. Analog quantum simulation utilizes continuous control parameters to engineer desired quantum states and dynamics. Chapter 1 introduces novel methods for steering entanglement using quantum many-body scars, harnessing special strongly-interacting dynamics to manipulate quantum entanglement robustly. Chapter 2 advances this approach by showing how Floquet engineering can be used to systematically generate interactions, and

how this enables sophisticated control over entanglement and access to novel quantum phases. Chapter 3 integrates these developments into a general framework for programming Hamiltonians into analog quantum simulators with time-reversal capabilities, illustrating the power of programmable analog strategies for simulations of lattice gauge theories.

The second phase (Chapters 4–6) shifts focus to topologically ordered quantum states, known for their exotic long-range entanglement and fundamental significance in condensed matter physics and quantum computation[866,764]. Chapter 4 presents strategies to enhance the experimental detection and verification of topological order using ideas from the renormalization group. The procedure we develop, order parameters dressed by local quantum error correction, significantly improve the practical observability of these delicate quantum phases. In Chapters 5 and 6, we explore novel techniques for realizing topological phases, by exploiting newly developed experimental capabilities, notably atom reconfiguration, to achieve precise digital control. In particular, we show how to engineer chiral Floquet spin liquids - exotic quantum phases exhibiting robust quantum coherence and non-Abelian excitations — as well as simulations of topological fermionic matter[936,746]. These advancements not only illuminate foundational physics but also bridge towards robust quantum error correction schemes.

The final phase (Chapters 7 and 8) expands the techniques developed thus far towards the simulation of increasingly complex physical systems relevant to chemistry and materials science. Chapter 7 discusses a general framework for digital quantum simulation of effective spin models, prevalent in condensed matter physics, introducing crucial techniques for engineering and characterizing these Hamiltonians. Chapter 8 extends these insights by proving that fermionic quantum systems, essential for real-

istic simulations of electronic structures in molecules and materials, can be efficiently encoded into qubits[580,686]. This advance significantly reduces computational complexity and opens pathways for genuine quantum simulations of chemical systems[551,860].

Collectively, these contributions represent substantial progress towards practical quantum simulation with neutral-atom quantum processors, laying critical foundations for future applications in physics, chemistry, and quantum information science[616].

Contents

Title . . . i
Copyright . . . ii
Abstract . . . iii
Table of Contents . . . vi
Citations to previously published work . . . x
Acknowledgments . . . xii

0 Introduction 1
0.1 Developments in neutral atom hardware . . . 3
0.2 Quantum control and scars . . . 5
0.3 Topological phases . . . 6
0.4 Quantum chemistry and materials . . . 7
0.5 Error correction and algorithms . . . 9
0.6 Thesis outline . . . 10

1 Entanglement steering with driven scars 11
1.1 Introduction . . . 11
1.2 Model and phenomenology . . . 13
1.3 Many-body echo in su(2) subspace . . . 16
1.4 Prethermal analysis and effective Hamiltonian . . . 18
1.5 Connections to experiments. . . . 20
1.6 Discussion . . . 21
1.7 Acknowledgments . . . 22

2 Floquet engineering of interactions and entanglement in Rydberg Chains 26
2.1 Introduction . . . 26
2.2 Hamiltonian engineering . . . 28
2.3 Controlled multi-partite entanglement . . . 32
2.4 Luttinger liquid dynamics . . . 35
2.5 Robustness and Implementation in Rydberg arrays . . . 37
2.6 Discussion & Outlook . . . 39
2.7 Acknowledgements . . . 40

3 Programming Hamiltonians in analog simulators 41
3.1 Introduction . . . 41

3.2 Floquet protocol and effective Hamiltonian . . . 45
3.3 Simulating dynamics of a 2D lattice gauge theory . . . 52
3.4 Prospects for experimental realizations . . . 65
3.5 Discussion & Outlook . . . 67

4 Enhancing Detection of Topological Order by Local Error Correction 77
4.1 LED Approach . . . 79
4.2 Numerical Detection of Topological Order with Coherent Perturbations 81
4.3 Effect of Incoherent Errors . . . 83
4.4 Experimental Realization in Rydberg Atom Arrays . . . 86
4.5 Circuit-Based LED and Generic Topological Phases . . . 88
4.6 Discussion . . . 89
4.7 Methods . . . 91

5 Digital engineering of Floquet spin liquids 115
5.1 Floquet spin liquid . . . 118
5.2 Experimental Implementation . . . 123
5.3 Variational Optimization for Near-term Devices . . . 126
5.4 Controlling non-abelian excitations . . . 132
5.5 Fusion and Braiding . . . 137
5.6 Resource estimates and experimental feasibility . . . 140
5.7 Discussion and Outlook . . . 142

6 Probing topological matter and fermion dynamics on a neutral-atom quantum computer 146
6.1 Hardware-efficient digital quantum simulations . . . 148
6.2 Exploring the Kitaev model . . . 150
6.3 Floquet evolution of fermion systems . . . 152

7 Digital simulation for chemistry and materials 163
7.1 Engineering spin Hamiltonians . . . 166
7.2 Dynamical projection with digital Floquet engineering . . . 167
7.3 Hardware-efficient implementation . . . 170
7.4 Spectral information from dynamics . . . 173
7.5 Application to transition metal clusters and magnetic solids . . . 176
7.6 Outlook . . . 177
7.7 Methods . . . 180

8 Qubits can simulate fermions without signficant overhead 211
8.1 Introduction . . . 211
8.2 Dynamical Fermionic Encoding . . . 214

8.3 Constant-overhead structured permutations 216
8.4 Arbitrary Fermionic Permutations 219
8.5 Random graphs and sparse SYK 220
8.6 Quantum simulation with the FFFT 222
8.7 Conclusion 224

References 358

Citations to previously published work

The work in this thesis was completed in collaboration with many people, and is largely drawn from published or soon to be published works. The relevant reference of each chapter is as follows:

Chapter 1 is a lightly edited version of[829]:

> Nishad Maskara, Alexios A Michailidis, Wen Wei Ho, Dolev Bluvstein, Soonwon Choi, Mikhail D Lukin, Maksym Serbyn, "Discrete time-crystalline order enabled by quantum many-body scars: entanglement steering via periodic driving," Phys. Rev. Lett. 127, 090602 (2021) [arXiv:2102.13160 [quant-ph]].

Chapter 2 is a lightly edited version of[779]:

> Nazlı Uğur Köylüoğlu, Nishad Maskara, Johannes Feldmeier, Mikhail D. Lukin, "Floquet engineering of interactions and entanglement in periodically driven Rydberg chains," [arXiv:2408.02741 [quant-ph]].

Chapter 3 is a lightly edited version of[663]:

> Johannes Feldmeier, Nishad Maskara, Nazlı Uğur Köylüoğlu, Mikhail D. Lukin, "Quantum simulation of dynamical gauge theories in periodically driven Rydberg atom arrays," [arXiv:2408.02733 [quant-ph]].

Chapter 4 is a lightly edited version of:

> Iris Cong, Nishad Maskara, Minh C. Tran, Hannes Pichler, Giulia Semeghini, Susanne F. Yelin, Soonwon Choi, Mikhail D. Lukin, "Enhancing Detection of Topological Order by Local Error Correction," Nat Commun 15, 1527 (2024). [arXiv:2209.12428 [quant-ph]].

Chapter 5 is a lightly edited version of:

Marcin Kalinowski, Nishad Maskara, Mikhail D. Lukin, "Non-Abelian Floquet Spin Liquids in a Digital Rydberg Simulator," Phys. Rev. X 13, 031008 (2023). [arXiv:2211.00017 [quant-ph]].

Chapter 6 is a lightly edited version of:

Simon J. Evered, Marcin Kalinowski, Alexandra A. Geim, Tom Manovitz, Dolev Bluvstein, Sophie H. Li, Nishad Maskara, Hengyun Zhou, Sepehr Ebadi, Muqing Xu, Joseph Campo, Madelyn Cain, Stefan Ostermann, Susanne F. Yelin, Subir Sachdev, Markus Greiner, Vladan Vuletić, Mikhail D. Lukin, "Probing topological matter and fermion dynamics on a neutral-atom quantum computer," [arXiv:2501.18554 [quant-ph]].

Chapter 7 is a lightly edited version of:

Nishad Maskara, Stefan Ostermann, James Shee, Marcin Kalinowski, Abigail McClain Gomez, Rodrigo Araiza Bravo, Derek S. Wang, Anna I. Krylov, Norman Y. Yao, Martin Head-Gordon, Mikhail D. Lukin, Susanne F. Yelin, "Programmable Simulations of Molecules and Materials with Reconfigurable Quantum Processors," [arXiv:2312.02265 [quant-ph]].

Chapter 8 is based on an upcomming work with Marcin Kalinowski, Daniel Gonzalez-Cuadra, and Mikhail D. Lukin.

To my parents, for encouraging me to pursue science, and for their constant love and support.

Acknowledgments

The work presented in this thesis is the result of many fun and exciting collaborations which I have been lucky enough to enjoy throughout my PhD. Not enough can be said to adequately acknowledge the many diverse and varied contributions. Nevertheless, I will try and be brief, and start by acknowledging that what I write here is at best a partial set of acknowledgements.

I'd like to start by thanking my PhD advisor and commitee chair, Misha Lukin, for building an amazing research environment where interdisciplinary and risky research is encouraged, and for consistently teaching me the importance of thinking deeply about long-term scientific goals. Also thank you to our administrative team, in particular Sam Dakoulas and Elaine Mangelinkx, for keeping everything running smoothly. I'd also like to thank my commitee members, Subir Sachdev and Anurag Anshu, for being invaluable resources and a great source of support. I'd also like to thank Susanne Yelin, who is in effect an honorary member of my committee, for her outstanding mentorship and leadership during my PhD.

I have also had the privilege of working closely with some amazing graduate student colleagues, without whom none of the content in this thesis would have been pos-

sible. I'd like to especially thank Dolev Bluvstein, Maddie Cain, Iris Cong, Johannes Feldmeier, Daniel Cuadrado Gonzalez, Wen Wei Ho, Marcin Kalinowski, Christian Kokail, Nazli Uğur Köylüoğlu, Daniel Mark, Stefan Ostermann, Rhine Samajdar, Qian Xu, and Harry Zhou for incredibly exciting and close collaborations over the past few years. Also special thanks to the broader theory group in the Lukin group and Harvard, including Gefen Baranes, Pablo Bonilla, Jordan Cotler, Maine Christos, Junkai Dong, Andi Gu, Katherine Van Kirk, Patrick Ledwith, Nathan Leitao, Varun Menon, Simone Notarnicola, Rahul Sahay, Kushal Seethram, Benjamin Schiffer, Andrew Yates and many others.

A large component of my PhD has also been driven by close collaboration with neutral-atom experiments, and I've been lucky to witness the incredibly rapid progress of this platform over the last few years. Many thanks to the senior atom array team from when I joined the group, Sepehr Ebadi, Harry Levine, Alex Keesling, Ahmed Omran, and Guilia Semeghini, for teaching me the foundations, and to the new generation, Dolev Bluvstein, Simon Evered, Sasha Geim, Sophie Li, and Tom Manovitz, for incredible collaborations over the past few years. I'd also like to thank the black diamond team from when I joined, Nate Leitao, Haoyang Gao, Leigh Martin, and Harry Zhou, for our explorations of many-body physics together. Finally, I want to thank Soonwon Choi, Hannes Pichler, and Maksym Serbyn, for being inspirational role models and mentors during various stages of my PhD.

I also had the privilege of spending a summer at Berkeley, where I had the opportu-

nity to join in Martin Head Gordon's group and learn about quantum chemistry from the world's experts. Thank you to both Martin and James Shee for your hospitality during my stay, and for teaching me probably everything I know about chemistry. Also special thanks to Abdul Aldosarry, Leo Cunha, Rebecca Tomann, Josie Hendrix, and the rest of the Head Gordon group. Thank you to Tong Jiang, Joonho Lee, PJ Robinson, for continuing to engage with us on problems related to quantum chemistry at Harvard. Thank you also to Jim Collins, Aarti Krishnan, and Andreas Luttens at the Broad Institute, for teaching us about the magic of biochemistry, and for being amazing and inspirational scientists.

As part of the incredible environment at Harvard, I had the privilege of interacting with an incredible class of senior PhD students and postdocs during my first two years. I learned a lot about how to be a researcher, and how to navigate the PhD, through these interactions. Thanks to Mihir Bhaskar, Tamara Dordovic, Wen Wei Ho, Emil Khabibouline, Leigh Martin, Ralf Riedinger, Emma Rosenfeld, Rhine Samajdar, Tamara Sumarac, Aditya Venkatramani, Dominik Wild, Leo Zhou, Harry Zhou, and many others.

I would also like to thank the DOE CSGF for funding a large portion of my PhD, and to the friends I made during the program reviews and summer practicums. Thanks to Lindsey Eilts and the CSGF admin staff, and to Bryn Barker, Koby Hayashi, Abigail Potashman, Alby Musaelian, Ellis Torrance, Santiago Vargas, for our time together in Berkeley.

I would also like to take this opportunity to thank the many teachers and mentors who had a big impact on me earlier in my life, and who helped set me up for a career in research. Special thanks to my 4th and 5th grade math teacher Mr. Green for teaching us that math can be fun and inspirational, and my high school physics teacher Ms. Todd for seeing my enthusiasm and encouraging me to pursue physics more seriously. And to my piano teacher of nearly a decade, Christina, for teaching me that even when things are challenging, if I practice more I can usually get it right. Also thank you to my chemistry teacher Ms. Shannon, and math teachers Mr. Ashton and Ms. Reichmann, for your positive energy and teaching me the foundations of math and science. I also want to acknowledge and thank my early research mentors: Kathy Lee and Kirill Kovnir from my time at UC Davis; Ross Kerner and Barry Rand from my summer at Princeton; Alex Kubica, Thomas Joychym O'Connor, and John Preskill for introducing me to quantum computing and error correction; Xie Chen, Evert van Nieuwenberg, and Manuel Endres for supervising my undergraduate senior thesis.

Also thanks to my high school and college friends, new friends from grad school, and extended family, for their love and support the past few years. Finally, to my parents, Archana and Arun Maskara, my brother Nihar Maskara, and my partner, Erin Crawley, thank you.

0

Introduction

Quantum systems underlie much of modern physics, chemistry, and materials science, but their intrinsic complexity often places them beyond the reach of classical computational methods. The central challenge arises from the exponential growth of quantum states with system size. For instance, the quantum state of just 50 interacting quantum spins requires roughly $2^{50} \approx 1 \times 10^{15}$, i.e. a million billion, parameters to represent exactly. In the range of 50-100 qubits, this exponential growth causes the state to become so large, that it would require more memory than currently available on even the most powerful supercomputers. In practice, progress on modelling quantum mechanical wavefunctions relies on approximating these states with lower-dimensional descriptions, producing advanced computational techniques such as tensor networks,

quantum Monte Carlo, and density functional theory. Despite this progress however, many important problems remain computationally intractable[954,550].

Quantum simulation offers a fundamentally new approach by harnessing quantum mechanical hardware itself to perform computational tasks[668,628]. The foundational idea, recognizes that quantum systems are inherently suited to emulate other quantum systems directly. In a quantum simulator, the exponential complexity of quantum states becomes a resource rather than a limitation. This strategy could offer capabilities to study quantum phases of matter, simulate quantum chemistry reactions, and explore dynamical phenomena far beyond current classical methods[551,837].

In the past two decades, advances in quantum technologies — such as trapped ions, superconducting circuits, photonics, and neutral-atom arrays — have turned quantum simulation from a theoretical concept into experimental reality[813,855]. These platforms each offer unique strengths and challenges. Neutral-atom arrays have emerged as particularly versatile and scalable platform. In this approach, individual atoms are trapped in optical tweezers formed by tightly focused laser beams, enabling precise spatial control. Further, the well-known level structure of the constituent atoms (Rb-87 is most common) supports reliable internal-state manipulations, and tunable, long-range interactions through highly excited Rydberg states[794,644]. Such flexibility has allowed recent landmark experiments to observe previously inaccessible phenomena, such as quantum many-body scars, and quantum spin liquids, and implementation of error-corrected quantum circuits[557,933,566].

The ability to perform controlled quantum simulations is not only central to understanding fundamental physics but may also hold significant technological potential. For instance, simulations of strongly correlated electron systems can lead to new insights into high-temperature superconductivity, informing the design of novel super-

conductors. Quantum simulations of complex chemical reactions and catalysis might prove valuable in biochemistry and drug discovery by providing accurate predictive capabilities beyond classical approximations. Furthermore, developing the capability to simulate quantum systems accurately is a useful testbed for building large-scale quantum computers, as many algorithmic components and error-correction strategies overlap substantially between simulation and more general quantum computations[963,860].

0.1 Developments in neutral atom hardware

Neutral atoms have emerged as one of the leading platforms for quantum simulation, owing to their exceptional versatility, scalability, and controllability[691,916,794]. The core technology which enables neutral-atom quantum simulation is the optical tweezer array, which employs tightly focused laser beams to trap and hold individual atoms in precisely defined spatial configurations. By controlling the positions of these tweezers through spatial light modulators or acousto-optic deflectors, experiments can construct and manipulate programmable arrays of hundreds to thousands of atoms with programmable spatial connectivity[644,572].

Crucially, neutral atoms offer coherent coupling mechanisms to implement two-qubit interactions essential for quantum simulation. Most prominently, Rydberg excitation—a process where an atom is excited to a highly energetic state—enables strong, controllable, and tunable interactions. Rydberg states have exaggerated properties, such as large electric dipole moments and significant polarizability, leading to dipole-dipole interactions several orders of magnitude stronger than typical ground-state atomic interactions. The hallmark phenomenon known as "Rydberg blockade" arises when a single atom excited to a Rydberg state suppresses excitation of neigh-

boring atoms within a characteristic radius, effectively implementing strong, controllable many-body interactions and gate operations[906,781].

The Rydberg blockade provides an elegant way to engineer quantum interactions with high flexibility. By adjusting laser parameters such as frequency, intensity, and pulse duration, we can effectively program Hamiltonians with tailored interaction profiles and strengths. These tunable interactions have made neutral-atom platforms uniquely suited for studying a broad range of quantum many-body phenomena, including quantum magnetism, quantum critical phenomena, and novel non-equilibrium quantum phases[645,643,572]. Moreover, by periodically modulating these interactions — i.e. Floquet engineering — we can synthesize effective Hamiltonians that cannot be easily realized with static interactions alone[779,826].

A major breakthrough from the past few years is the ability to reconfigure the array while preserving coherence, by simply moving optical tweezers. This has enabled digital quantum control, which unlocks the ability to run discrete, programmable gate sequences akin to those in circuit-based quantum computing[573,659]. Hence, it opens a variety of new opportunities for designing novel protocols including architectures for quantum error correction and techniques for quantum simulation. In Chapters 5–8, we explore how these capabilities can be combined with native Rydberg gates to generate hybrid quantum simulation architectures uniquely suited to addressing challenging quantum simulation tasks such as studying topological phases and simulating quantum chemical systems.

0.2 Quantum control and scars

Analog quantum simulation is a powerful technique where the native interactions of a quantum system are leveraged, with minimal programming, to directly study interesting phenomena in many-body physics. Unlike digital quantum computation—which relies on discrete gates and universal logic circuits—analog simulation operates through continuous-time evolution under a carefully engineered Hamiltonian. This approach capitalizes on the natural quantum dynamics of physical systems, offering access to potentially more complex phenomena, without the overhead of digital programming[691,628].

Neutral-atom quantum devices were initially developed, and still can be used, for analog simulation. In particular, strong interactions are generated through Rydberg blockade, and interactions are tuned by selecting the static position. In this thesis, we further explore how time-modulation of laser intensities and frequencies can more precisely engineer Hamiltonians with tailored properties, accurately modeling quantum systems ranging from spin chains and quantum magnets to lattice gauge theories and quantum fluids[663,870,917].

This starts by studying quantum many-body scars, which are special, non-thermalizing eigenstates arising in otherwise chaotic quantum systems. Quantum scars provide a novel route to coherently control entanglement dynamics, resisting thermalization and decoherence over unexpectedly long timescales[557,937,861,965]. Chapter 1 details how exploiting these scars enables robust, targeted manipulation of quantum states, opening potential avenues for quantum information storage and processing within analog simulators.

We further extend these techniques by Floquet engineering, discussed in Chap-

ter 2. Floquet engineering employs periodic driving to shape effective Hamiltonians and interactions that would be challenging or impossible to achieve with static approaches[826,779,902]. By dynamically modulating system parameters, one can induce artificial gauge fields, stabilize novel quantum phases, and extend coherence times—significantly enriching the capabilities of analog simulation[891,983].

While analog simulators inherently face limitations, in particular sensitivity to experimental errors, they likely have advantages in the near-term, due to their simplicity of implementation and improved efficiency. The hybrid analog-digital approaches developed in Chapters 1-3 of this thesis aim to leverage these strengths while augmenting the engineering capabilities, setting the stage for more sophisticated simulations.

0.3 Topological phases

Topological phases are fundamentally quantum mechanical forms of matter, distinguished not by local order parameters, but by global, non-local patterns of quantum entanglement[764,790]. Unlike conventional phases such as solids or liquids, which are characterized by symmetry breaking and local observables, topological phases are robust to local perturbations and exhibit properties tied to the global structure of the system's wavefunction. These phases often manifest exotic excitations—such as anyons in two dimensions—that obey statistics fundamentally different from their underlying constituents, e.g. bosonic particles can generate emergent low-energy excitations with non-trivial fermionic statics[761,978].

Topological order first emerged in the context of the quantum Hall effect, where certain electron fluids exhibit quantized conductance values insensitive to microscopic

details. Since then, a broad landscape of topological systems has been discovered, including fractional quantum hall states, topological insulators, superconductors, and spin liquids[698]. These systems are not only of deep theoretical interest in condensed matter physics, but are also central to fault-tolerant quantum computation. In particular, their characteristic long-range entanglement and ground-state degeneracy on nontrivial manifolds form the basis of topological quantum error-correcting codes, such as the toric code[759].

Despite their theoretical appeal, topological phases are notoriously difficult to realize and probe experimentally. Their hallmark signatures—topological degeneracies, edge modes, and non-local entanglement—are often subtle and masked by noise or imperfections in real systems[866]. Neutral-atom quantum simulators offer a promising route to address this challenge: their ability to engineer custom geometries, control interactions with high precision, and perform site-resolved measurements enables the creation and diagnosis of topological order in highly tunable settings[933].

This thesis explores both the detection and realization of topological phases using neutral atoms. Chapter 4 introduces techniques based on local error correction to enhance the visibility of topological order in noisy environments. In Chapters 5 and 6, we leverage atom reconfiguration and Floquet engineering to digitally synthesize spin liquid states and topological matter with non-Abelian excitations, paving the way toward the experimental realization of robust topological quantum systems.

0.4 Quantum chemistry and materials

In the long run, one of the most exciting applications of quantum computers lies in the study of quantum chemistry and materials science[837]. The electronic structure

problem—determining the ground and excited states of molecules and solids from first principles—is a cornerstone of these fields, with wide-reaching implications for catalysis, drug design, photovoltaics, and the discovery of novel materials[551]. However, solving the Schrödinger equation for interacting electrons and nuclei is computationally demanding due to the exponential growth of the Hilbert space with system size.

Classical approaches, such as Hartree-Fock, density functional theory (DFT), and coupled-cluster methods, have achieved remarkable success, but they often struggle to describe systems with large quantum fluctuations, including strong spin-correlations, transition states with squeezed or stretched bonds, and excited-state dynamics after photo-excitation[954,825]. These are precisely the regimes where quantum simulators are expected to offer transformative advantages.

Quantum devices can represent electronic wavefunctions and simulate fermionic dynamics natively, offering the potential for exponential speedups in solving quantum chemistry problems[860]. A key challenge, however, is efficiently mapping fermionic degrees of freedom onto qubit-based quantum hardware while preserving their essential antisymmetric properties. Additionally, accurate simulation requires not only algorithmic advances but also hardware capable of representing the complex Hamiltonians found in chemical and material systems.

In this thesis, Chapter 7 introduces quantum algorithms specialized for simulating low-energy spin models relevant to materials, laying the groundwork for more chemically realistic simulations. Chapter 8 then presents a framework for simulating fermions with minimal overhead, showing how structured encodings can efficiently capture fermionic statistics using qubits. These developments are essential for scaling quantum simulation methods toward real-world chemistry and materials applications, where understanding and predicting complex quantum behavior can lead to tangible

technological breakthroughs.

0.5 Error correction and algorithms

Ultimately, scaling quantum simulations to tackle important and classically intractable problems, will inevitably require robust error correction[963]. Quantum systems are inherently fragile, subject to rampant decoherence and gate imperfections. While we have pushed neutral atom hardware to be competitive with other devices, having fidelities over 99.5%, without some form of error mitigation or correction, these errors accumulate and quickly overwhelm the signal in long computations or large-scale simulations. Quantum error correction (QEC) provides a principled framework for detecting and correcting such errors without destroying quantum information.

However, traditional approaches to QEC often leads to large overheads, due in large part to the fact that error correction and algorithms have been designed as independent layers. As quantum hardware matures, a more integrated perspective will become essential: co-designing quantum algorithms and QEC procedures can dramatically reduce overhead and unlock new capabilities.

While not discussed in content of this thesis, we have begun to explore such ideas by developing techniques that leverage algorithmic parallelism to generate lower-overhead quantum gatesets. In the long term, the convergence of algorithmic design, hardware architecture, and QEC strategies will be essential for building scalable quantum simulators that can solve real-world problems with provable quantum advantage

0.6 Thesis outline

The remainder of this thesis is organized into eight chapters, each building on foundational concepts introduced earlier. Chapters 1–3 focus on the development of analog techniques for programming and controlling quantum many-body systems using neutral-atom arrays, including the manipulation of entanglement dynamics via many-body scars and the engineering of effective interactions through Floquet driving. Chapters 4–6 shift toward topologically ordered states, exploring both their detection via local error correction and their synthesis through digital control and atom reconfiguration. Chapters 7 and 8 extend these tools toward simulating complex quantum systems relevant to chemistry and materials, culminating in a powerful set of results that enable efficiently encoding fermionic models and simulating them with qubit-based hardware. Together, these contributions represent a comprehensive advance in the algorithms and architectures required to perform meaningful quantum simulations with neutral-atom platforms. Note that this introduction was written with the help of OpenAI's LLM tools, and served as a small research experience learning how to use new technology. The remaining chapters are all excerpts taken from published or soon-to-be published research papers.

1

Entanglement steering with driven scars

1.1 Introduction

Creating and manipulating entanglement is a fundamental goal of quantum information science, with broad implications in computation, metrology, and beyond. At the same time, not all forms of entanglement are useful. Strongly interacting quantum many-body systems generate large amounts of entanglement under their intrinsic dynamics, in a process known as thermalization[626,751]. However, such dynamics irreversibly scramble quantum information. Controlling entanglement while combating thermalization[519,864,937] in isolated interacting many-body systems[563,680,583] is therefore essential for applications of large-scale entangled states[718,887].

Experimental studies involving programmable quantum simulators based on Rydberg atom arrays[555] have suggested that interacting quantum systems can exhibit a weak breakdown of thermalization, where certain initial conditions exhibit surprising, persistent many-body revivals. This phenomenon comes from quantum many body scars (QMBS)[966,714]– anomalous, non-thermal eigenstates – named in analogy to non-ergodic states in the spectrum of otherwise chaotic single particle Hamiltonians[709]. Intriguingly, in some models with QMBS the system undergoes periodic entanglement and disentanglement cycles[714,613,843,598], providing a potential route to the controlled manipulation of entanglement dynamics. In practice, however, QMBS are fragile[966,613,754,800]; since they rely on a dynamically disconnected subspace of non-thermalizing eigenstates[613,946,937,862,861], additional interactions generically lead to thermalization[800].

Recent experiments[570] demonstrated that periodic driving can dramatically increase the lifetime of scarred oscillations. This observation is surprising, since the driving frequencies used were resonant with the local energy scale, permitting easy energy absorption and rapid heating towards a featureless, infinite-temperature state. Additionally, the experiment observed a robust subharmonic response at half of the driving frequency, suggestive of discrete time-crystalline (DTC) order[755,651].

In this Letter, we propose a theoretical framework for understanding these experimental observations by introducing a mechanism whereby driving stabilizes quantum scarred oscillations, prolonging their lifetime and protecting them against arbitrary perturbations. Specifically, we focus on the PXP model[665,789,555] with kicked driving, an idealized model for the Rydberg atom array experiment[570]. This model exhibits robust subharmonic responses and many-body revivals coming from an effective many-body spin echo. The deviation from a perfect echo introduces a small parameter, al-

lowing us to derive an effective prethermal description of the Floquet dynamics with is stable up until parametrically long times[653].

Namely, we construct an effective Hamiltonian in a rotating frame, hosting an emergent $\mathbb{Z}_2$ symmetry which is spontaneously broken in its gapped ground state manifold. In the laboratory frame, the system oscillates between the two spontaneously broken ground states, resulting in a robust subharmonic response characteristic of DTC[983,653,1007]. However, this subharmonic response is restricted only to Néel-like initial states which have a strong overlap with the ground state of the effective Hamiltonian — a property inherited from QMBS. Our model differs crucially from earlier works on homogenous time crystals in 1D[720,892,863,1010] and mean-field constructions[902], in that the trajectory being stabilized is generated by an interacting Hamiltonian, which produces non-trivial entanglement. Therefore, our construction opens a prospective route towards coherent control of entanglement dynamics.

1.2 Model and phenomenology

We study a periodically kicked model $H(t) = H_{\mathrm{PXP}} + \theta N \sum_{k\in\mathbb{Z}} \delta(t - k\tau)$, which generates the following one-period Floquet unitary,

$$U_F(\theta,\tau) = e^{-i\theta N} e^{-i\tau H_{\mathrm{PXP}}}, \tag{1.1}$$

$$H_{\mathrm{PXP}} = \sum_{i=1}^{L} P_{i-1}\sigma_i^x P_{i+1}, \quad N = \sum_{i=1}^{L} n_i, \tag{1.2}$$

describing evolution with the PXP Hamiltonian H_{PXP}[665,789,555] for time τ, followed by the number operator N applied through rotation angle θ. For simplicity, the model is defined on a 1D chain of L sites with periodic boundaries, although much of the analysis carries over to higher dimensional bipartite lattices. Each site is a two-level

system spanned by a ground ($\circ$) and an excited ($\bullet$) state. Operators $n_i = |\bullet\rangle\langle\bullet|_i$ and $P_i = |\circ\rangle\langle\circ|_i$ are projectors, while $\sigma_i^x = |\circ\rangle\langle\bullet|_i + |\bullet\rangle\langle\circ|_i$ generates Rabi oscillations. In the Hamiltonian, σ_i^x is dressed by projectors on neighboring sites, ensuring that dynamics remain within the blockaded subspace where adjacent sites are never simultaneously excited.

For $\theta = 0$ the Floquet dynamics (1.1) are equivalent to undriven evolution under H_{PXP}. The PXP model is non-integrable and features rapid growth of bipartite entanglement entropy, $S_{\mathrm{ent}}(t) = -\operatorname{tr}\rho\ln\rho$ where ρ is the half-chain density matrix, from the majority of product states. In contrast, quenching from the Néel state $|Z_2\rangle = |\bullet\circ\bullet\circ\ldots\rangle$ leads to coherent oscillations between $|Z_2\rangle$ and its inversion partner $|Z_2'\rangle$, as first seen in[555], with oscillation period $\tau_r \approx 1.51\pi$ that sets an intrinsic resonant timescale. These oscillations, supported on quantum scars[966], are captured by the sublattice imbalance in excitation number, $\mathcal{I} = (2/L)\sum_{i=1}^{L/2}(n_{2i-1} - n_{2i})$, see Fig. 1.1(a), and also occur in higher dimensional bipartite lattices[844,570]. However, dynamics under H_{PXP} generate entanglement, and the coherent many-body oscillations eventually decay.

The addition of strong driving with $\theta \approx \pi$ suppresses thermalization at early times, most clearly seen in the nominal growth of entanglement entropy over multiple cycles, see Fig. 1.1(a). Concomitantly, oscillations of $\mathcal{I}$ synchronize to half the drive frequency, a phenomenon known as subharmonic locking. The origin of this response is related to the existence of a special point at $\theta = \pi$, where driving implements an effective many-body echo; because H_{PXP} anticommutes with the operator $\mathcal{C} = \prod_i \sigma_i^z = e^{-i\pi N}$, then $U_F(\pi,\tau)^2 = \mathcal{C}e^{-i\tau H_{\mathrm{PXP}}}\mathcal{C}e^{-i\tau H_{\mathrm{PXP}}} = e^{i\tau H_{\mathrm{PXP}}}e^{-i\tau H_{\mathrm{PXP}}} = 1$, implying perfect subharmonic revivals across the entire Hilbert space. Furthermore, note that H_{PXP} anticommutes with $\mathcal{C}$, irrespective of the lattice geometry. However, upon deviating from $\theta = \pi$, these revivals rapidly damp out for typical initial states, whose undriven dy-

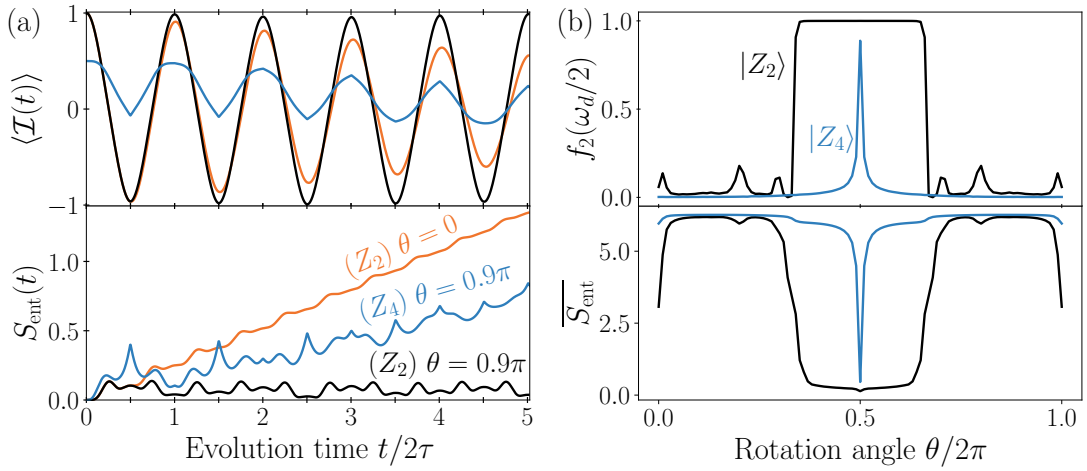


Figure 1.1: (a) The density imbalance $\mathcal{I}$ and bipartite entanglement entropy characterize oscillations between the two Néel ordered states ($|Z_2\rangle$), for undriven (orange) and driven (black) dynamics in an infinite size chain simulated via iTEBD[SOM]. Adding driving with $\tau = 0.993\tau_r/2$ and $\theta = 0.9\pi$ to PXP model arrests the growth of entanglement entropy S_{ent} and prolongs the lifetime. In contrast, driven dynamics from the $|Z_4\rangle = |\bullet\circ\circ\circ\bullet\circ\circ\circ\ldots\rangle$ state, which do not support scar oscillations, thermalize rapidly (blue). (b) Subharmonic weight and average entanglement entropy, computed over 400 cycles ($T = 400\tau$), for an $L = 28$ chain, and $\tau = 0.993\tau_r/2$. Dynamics from the $|Z_2\rangle$ state form a stable plateau around $\theta = \pi$. However from $|Z_4\rangle$, the response disappears for $\theta \neq \pi$.

namics do not exhbit many-body oscillations in $\mathcal{I}$, see Fig. 1.1 and[SOM].

In contrast, long-lived oscillations from the Néel state persist over a wide range of parameters centered at $\theta = \pi$ and $\tau = \tau_r/2$. To quantify the response, we compute the subharmonic weight $f_2(\omega_d/2) \propto |S(\omega_d/2)|^2$, defined as the normalized spectral weight of $\langle \mathcal{I}(t) \rangle$ at half the driving frequency $\omega_d = 2\pi/\tau$, rescaled so $f_2(\omega_d/2) = 1$ for perfect subharmonic response at $\theta = \pi$ from the Néel states, see[SOM]. The plateaus in the subharmonic weight and time-averaged entanglement entropy in Fig. 1.1(b) signal a robust, persistent response at $\omega_d/2$.

1.3 Many-body echo in su(2) subspace

The robust subharmonic response can be qualitatively understood using mean-field-like trajectories on an effective Bloch sphere. We invoke the forward-scattering approximation (FSA), which constructs an $L+1$ dimensional subspace that captures dynamics under H_{PXP} from a Néel initial state, and approximate su(2) algebraic structure[966] of a spin-$L/2$ collective degree of freedom. The S^z operator is defined by the density imbalance, $S^z = \sum_{i=1}^{L/2}(n_{2i-1} - n_{2i})$, so the Néel state $|Z_2\rangle$ ($|Z_2'\rangle$) corresponds to the North (South) pole. The S^x operator is approximately proportional to H_{PXP}, and generates a rotation that exchanges the two Néel states (blue lines in Fig. 1.2). Finally, S^y is calculated using su(2) commutation relations. In contrast, the action of $e^{-i\theta N}$ pulses is more complex, since the operator N does not have a closed form representation in the su(2) subspace. However, it can be approximated as $N \sim (S^z)^2$ in the vicinity of the Néel states $|Z_2\rangle$ and $|Z_2'\rangle$, which accumulate identical phases under $e^{-i\theta N}$, see[SOM] and Fig. 1.2(b). Note that we use the weakly deformed PXP model[613] to generate spin operators, but consider dynamics under H_{PXP}[SOM].

We visualize the many-body dynamics by computing expectation values of the collective spin operators $S^{x,y,z}$. Figure 1.2(a) illustrates that at $\theta = \pi$ the second application of H_{PXP} returns the system to its initial state. Away from $\theta = \pi$, trajectories from $|Z_2\rangle$ are no longer closed, but there exists a nearby closed orbit with period 2τ, see Fig. 1.2(b). States near this periodic orbit, including the Néel state, exhibit stroboscopic precession around the fixed point, explaining subharmonic response. In this picture, the existence of periodic trajectories is qualitatively similar to mean-field descriptions of time crystals[902,612,713]. However, a key difference is that the emergent spin-$L/2$ degree of freedom is not composed of independent spins, evinced by non-trivial

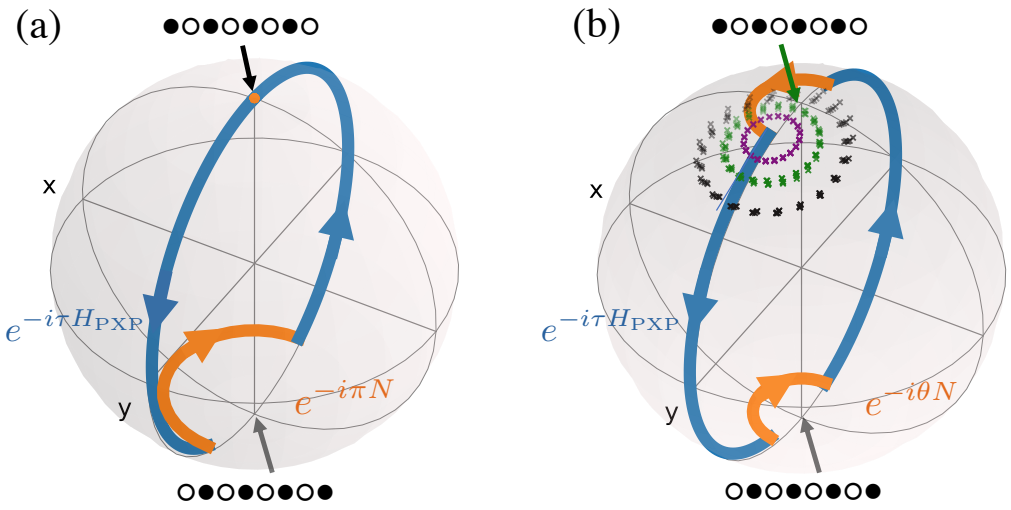


Figure 1.2: Trajectories of driven PXP model for $L=16$, plotted on the Bloch sphere of the collective spin-$L/2$. (a) The dynamics generated by two periods of $U_F(\pi,\tau)$ exhibit a perfect return to the $|Z_2\rangle$ initial state: $e^{-i\tau H_{PXP}}$ with $\tau = 0.45\,\tau_r$ under-rotates the $|Z_2\rangle$ state (blue line), then the application of $e^{-i\pi N}$ (orange line) flips the x,y-projections of the spin so that the second Floquet pulse completes the cycle. (b) The same dynamics but for $\theta = \pi - 0.05$ supports a periodic trajectory near the Néel state. Dynamics initialized near the periodic trajectory precess around it at stroboscopic times forming cycles depicted for 100 driving periods for three initial states (green ring corresponds to $|Z_2\rangle$ initialization).

entanglement oscillations. Furthermore, dynamics outside of collective spin-$L/2$ subspace are ergodic, leading to rapid thermalization from other initial states. As such, this picture does not explain why the spin-$L/2$ subspace is a good approximation, and how driving reduces thermalization, for which we must consider the many-body Floquet unitary.

1.4 Prethermal analysis and effective Hamiltonian

We analyze the many-body dynamics by expanding around the perfect echo point $\theta = \pi$ where the Floquet unitary is denoted $\mathcal{X}_\tau = U_F(\pi, \tau)$. This allows us to write

$$U_F(\theta, \tau) = e^{i\varepsilon N}\mathcal{X}_\tau, \ \ \varepsilon = \pi - \theta, \tag{1.3}$$

where ε is a small parameter quantifying the deviation from the perfect point. Since $\mathcal{X}_\tau^2 = 1$, the dynamics are equivalent to a generalized spin flip, followed by short evolution under N for time t[SOM]. As such, the unitary $U_F(\theta, \tau)$ is written in the canonical time crystal form[651,983]; here, we apply the techniques from Ref.[653,658] to show the Floquet unitary can be approximated by $U_F \approx \mathcal{V} e^{-i\varepsilon H_F}\mathcal{X}_\tau \mathcal{V}^\dagger$, where H_F is an effective Hamiltonian constructed perturbatively in ε, and $\mathcal{V}$ is a perturbative frame transformation[SOM].

As the DTC phenomenology depends on spectral properties of the effective Floquet unitary, we base our analysis on the leading order effective Hamiltonian and Floquet unitary,

$$H_F^{(1)} = -\frac{1}{2}\left(N + \mathcal{X}_\tau N \mathcal{X}_\tau\right), \ \ U_F^{(1)}(\theta, \tau) \equiv e^{-i\varepsilon H_F^{(1)}}\mathcal{X}_\tau. \tag{1.4}$$

The effective Hamiltonian $H_F^{(1)}$ corresponds to the average Hamiltonian in a frame co-rotating with $\mathcal{X}$, and so to leading order ε sets the timescale of dynamics in the rotating frame. Crucially, the expansion of H_F has an emergent $\mathbb{Z}_2$ symmetry $[H_F, \mathcal{X}_\tau] = 0$ at higher orders as well, which ultimately comes from time-periodicity of the drive[SOM,653]; nevertheless, formally the expansion is an asymptotic series, and hence should be truncated at some optimal order to accurately capture dynamics of local observables. The effect of residual terms is rigorously bounded[518,653], guaranteeing accuracy of H_F

up to the prethermal timescale $T_p \gtrsim (\tau/\varepsilon)e^{c_p/\varepsilon}$ for some $c_p > 0$.

The origin of the subharmonic response can be understood by analyzing eigenstates of the transformed Floquet unitary in Eq. (1.4) and their dimensionless quasi-energies ε, defined by $U_F^{(1)} |u\rangle = e^{i\varepsilon} |u\rangle$. For τ near an integer multiple of $\tau_r/2$, the Floquet operator has a pair of eigenstates characterized by strong overlap with $|Z_2\rangle, |Z_2'\rangle$, and featuring nearly degenerate quasi-energies (0-pairing) or quasi-energies separated by π (π-pairing), see Fig. 1.3(a). These observations also imply the eigenstates can be well approximated by the long-range correlated "cat" states $|\pm\rangle = (|Z_2\rangle \pm |Z_2'\rangle)/\sqrt{2}$ as these states carry definite momentum k_0 ($|+\rangle$) and k_π ($|-\rangle$), and underlie spontaneous symmetry breaking (SSB) of the system's translation symmetry. However, the emergent symmetries $\mathcal{X}_\tau$ also play a crucial role, as the π and 0 quasi-energy gaps occur when $\mathcal{X}_\tau$ either exchanges the two Néel states ($\tau = \tau_r/2$) or leaves them invariant ($\tau = 0, \tau_r$). A π quasi-energy gap between the "cat" states $|\pm\rangle$ leads to subharmonic response in dynamics from the $|Z_2\rangle$ or $|Z_2'\rangle$ state, and is characteristic of time-crystalline order[651,983,772,757,891]. At the level of the effective Hamiltonian $H_F^{(1)}$, these $\pi(0)$-paired eigenstates correspond to degenerate ground states in Fig. 1.3(b), separated by a finite gap Δ to excited states, and belonging to different (same) symmetry sectors of $\mathcal{X}_\tau$. Hence $\mathcal{X}_\tau$ symmetry breaking in the ground state is linked to DTC order and the subharmonic oscillations of spatial order[651,983,SOM].

We argue the observed region with DTC order descends from a model with conjectured perfect scars[613,SOM]. Specifically, if we deform the PXP model as described in [613], $\mathcal{X}_\tau$ at $\tau = \tau_r/2$ exactly exchanges the Néel states, and $|\pm\rangle$ become true ground states of $H_F^{(1)}$ with a constant gap $\Delta \geq 1$. The PXP model, as well as driving for τ away from $\tau_r/2$, are weak deformations of this drive. However, these deformations do not preserve the emergent symmetry $\mathcal{X}_\tau$ at the level of $H_F^{(1)}$, and could destroy the

ground state degeneracy. In Ref.[SOM], we argue that since the emergent symmetry changes slowly as we deform the drive, the ground states throughout the π-paired region in Fig. 1.3 may be adiabatically connected to $|\pm\rangle$. Indeed, we confirm the energy splitting in the ground state of $H_F^{(1)}$ decreases exponentially with system size, see Fig. 1.3(b) inset, as expected for SSB.

The above analysis reveals four distinct timescales emergent in the prethermal regime of Eq. (1.4). The shortest timescale $T_s = 2\tau$ is the subharmonic response. The second timescale, determined by the gap Δ in the spectrum of $H_F^{(1)}$, is $T_b \propto \tau(\varepsilon\Delta)^{-1}$ and comes from overlap between the Néel initial state and the lowest lying excited states. Semiclassically, T_b is the precession period from Fig. 1.2(b). Finally, the longest timescale is set by the inverse energy splitting in the ground state manifold of $H_F^{(1)}$, $T_g \propto (\tau/\varepsilon)e^{c_d L}$, characteristic of SSB. All phenomenology is ultimately contingent upon the validity of the prethermal analysis, which holds until $T_p \gtrsim (\tau/\varepsilon)e^{c_p/\varepsilon}$.

1.5 Connections to experiments.

Going beyond the idealized model (1.1), we replace H_{PXP} in Eq. (1.2) by the Rydberg Hamiltonian $H_{\mathrm{Ry}} = (\Omega/2)\sum_i \sigma_i^x - \delta\sum_i n_i + \sum_i (V_1 n_i n_{i+1} + V_2 n_i n_{i+2})$, which includes imperfect Rydberg blockade and next-nearest-neighbor interactions. The PXP Hamiltonian is recovered from H_{Ry} in the limit $V_1 \to \infty$, $V_2 = 0$, and the resonant time $\tau_r \propto 1/\Omega$ is rescaled. Here, we consider a 1D chain with $V_2 = V_1/2^6$, $V_1 = 10\,\Omega$, and choose $\delta = V_2$ to cancel the static background from the next-nearest-neighbor interactions[570].

Figure 1.4 illustrates the timescales T_s, T_b, and T_g from stroboscopic dynamics of the revival fidelity $F_n = |\langle Z_2|U_F(\theta,\tau)^n|Z_2\rangle|^2$ generated by the kicked Hamiltonian

$H(t) = H_{\mathrm{Ry}} + \theta N \sum_k \delta(t - k\tau)$. Over tens of driving cycles, we observe a robust subharmonic response, and an emergent beating timescale T_b. Over hundreds of driving cycles, we observe slow oscillations between even periods F_{2n} and odd periods F_{2n+1}, with timescale T_g. Specifically, in the rotating frame, the two ground states of H_F, $\approx |\pm\rangle$, form an effective two-level system with energy splitting $\Delta E = E_+ - E_-$. The initial state can be expanded as $|Z_2\rangle \equiv (|+\rangle + |-\rangle)/\sqrt{2}$, and after a time $T_g = \pi/(2\Delta E)$, it evolves into a superposition $(|+\rangle + i|-\rangle)/\sqrt{2}$ equivalent to $(|Z_2\rangle - i|Z_2'\rangle)/\sqrt{2}$ modulo global phase, which is a macroscopic superposition corresponding to the so-called Greenberger-Horne-Zeilinger (GHZ) state. Dynamics in the lab frame are related by $\mathcal{X}_\tau$ kicks, which exchange the Néel states every period. Finally, the prethermal time, when all fidelities may become exponentially small in L, is not visible for the system sizes or times simulated.

1.6 Discussion

These considerations demonstrate that entanglement dynamics associated with quantum many-body scars can be stabilized and steered in the periodically kicked PXP model, resulting in an evolution strongly reminiscent of prethermal DTC order. Our construction relies on the effective many-body π-pulse realized through quantum scars, which connect the two Néel states via an entangled trajectory, and a driving pulse that reverses the direction of time. Similar to prethermal time crystals, the emergent order features a robust, long-lived subharmonic response and spatiotemporal order for a range of parameters. However, in our model these signatures are present only for eigenstates which are perturbatively close to the Néel initial state, and require sufficiently high fidelity state preparation to be observed[892]. Nevertheless, we

demonstrate that the signatures of DTC physics survive in an experimentally relevant model, thus providing a possible explanation for recent experimental observations in[570]. Moreover, we theoretically predict new emergent timescales that could be observed in future experiments and the possibility of preparing GHZ states[871] in driven quench dynamics.

The phenomenon described here drastically enhances the stability of non-ergodic dynamics thus opening a large number of exciting directions. Specifically, by extending this construction to the more complicated trajectories in the PXP model[843] or to quantum scars in other models[586,598,852,937,861], control over more complex entanglement dynamics could be implemented. From a practical perspective, there remains a number of questions related to experiments in Rydberg arrays[570]. In particular, it is desirable to understand the dynamics in two-dimensional lattices[844], including the situations where two sublattices have different numbers of nearest neighbours. In higher dimensions, there exists an intriguing possibility of realizing a true prethermal time crystal, with a finite temperature phase transition in H_F. It is also desirable to build a theory for higher order subharmonic responses observed in experiments[570], and obtain analytical understanding for continuously driven models. Finally, it is important to understand if one can implement full control over the many-body dynamics within the effective spin-$L/2$ subspace[788], which could be utilized for applications such as robust quantum information storage and quantum metrology.

1.7 Acknowledgments

We thank Dmitry Abanin, Ehud Altman, Iris Cong, Sepehr Ebadi, Alex Keesling, Harry Levine, Ahmed Omran, Hannes Pichler, Rhine Samajdar, Guilia Semeghini,

Tout Wang, Norman Yao, and Harry Zhou for stimulating discussions. We acknowledge support from the Center for Ultracold Atoms, the National Science Foundation, the Vannevar Bush Faculty Fellowship, the U.S. Department of Energy, the Army Research Office MURI, and the DARPA ONISQ program (M.L., N.M, W.W.H., D.B.); the European Research Council (ERC) under the European Union's Horizon 2020 Research and Innovation Programme Grant Agreement No. 850899 (A.M. and M.S.); the Department of Energy Computational Science Graduate Fellowship under Award Number(s) DE-SC0021110 (N.M.); the Moore Foundation EPiQS initiative grant no. GBMF4306, the National University of Singapore (NUS) Development Grant AY2019/2020 and the Stanford Institute for Theoretical Physics (W.W.H.); the NSF Graduate Research Fellowship Program (grant DGE1745303) and The Fannie and John Hertz Foundation (D.B.); and the Miller Institute for Basic Research in Science (S.C.).

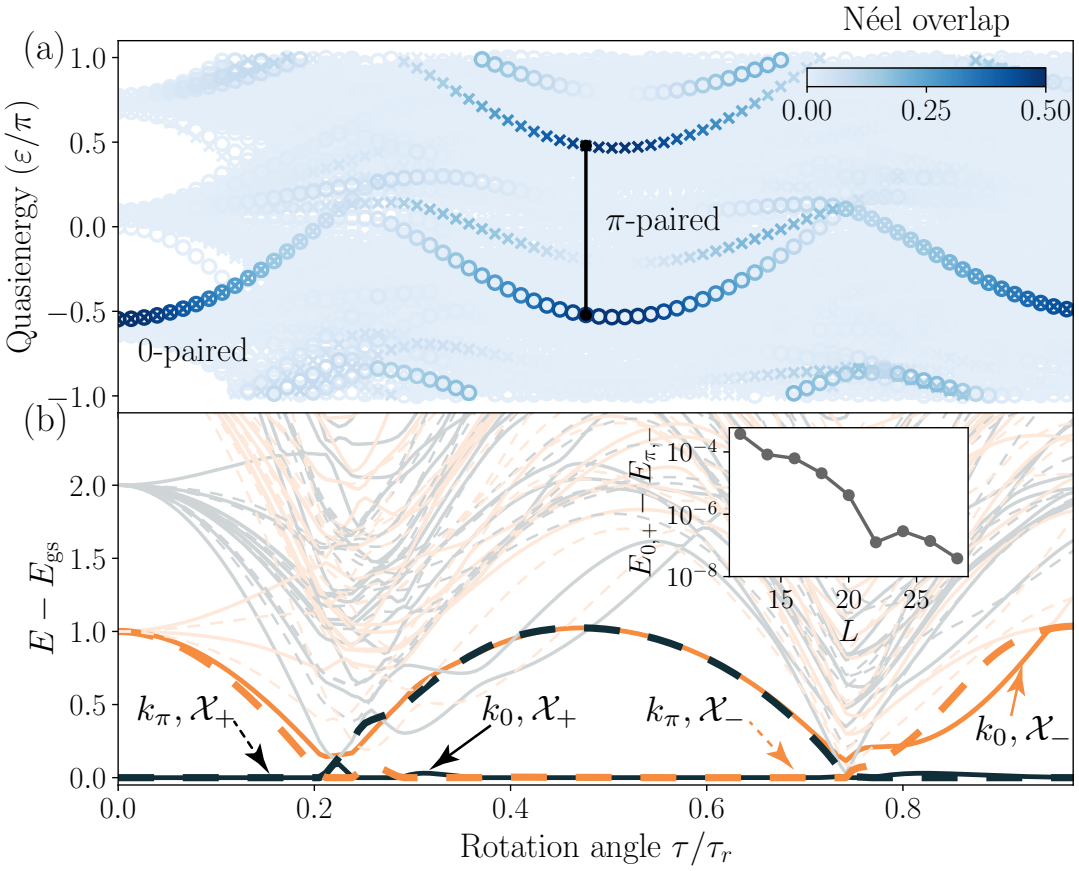


Figure 1.3: (a) Eigenspectrum of $U_F^{(1)}$ plotted for various rotation angles τ, $L=16$, and $\varepsilon=1$, with color intensity reflecting overlap with Néel state. Near $\tau/\tau_r \approx 1/2$, the states with largest overlap exhibit π-pairing, indicating subharmonic response. However, near $\tau/\tau_r \approx 0$, 1, they exhibit 0-pairing. (b) Low-energy spectrum of $H_F^{(1)}$ reveals two-fold degeneracy between ground states from $k=0$ and π momentum sectors (denoted as $k_{0,\pi}$) with $\mathcal{X}_\tau$ eigenvalues $\pm 1 (\mathcal{X}_\pm)$ in the region that corresponds to π-pairing in (a). The splitting of the ground state manifold vanishes exponentially with system size within the paired regions, with the inset showing finite size scaling at $\tau/\tau_r = 1/2$.

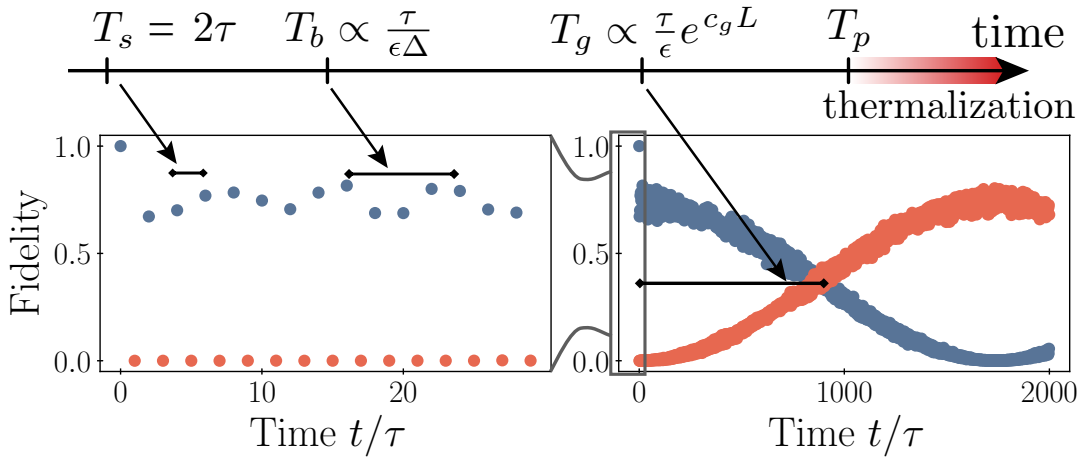


Figure 1.4: Dynamics of revival fidelity under the periodically kicked Rydberg Hamiltonian, and emergent prethermal timescales. Stroboscopic dynamics of fidelity for $\theta = 1.1\pi$, and $\tau = 0.993\tau_r/2$ reveal the subharmonic timescale T_s, the beating timescale T_b, and Rabi oscillations in the groundspace, with characteristic timescale T_g. Even (odd) multiples of τ_d are colored blue (red). Data is for the $L = 14$ chain.

2

Floquet engineering of interactions and entanglement in Rydberg Chains

2.1 Introduction

Programmable quantum simulators provide unique insights into complex many-body systems. They can be used for explorations of strongly correlated quantum phases of matter[836,646,934,599,667], non-equilibrium quantum dynamics[783,923,751,1015,557,573,578,712,824], many-body entanglement[675,731,751,872,585,743], and quantum metrology[915,882,618,578,650,712]. Neutral atom arrays are a promising approach to realizing programmable quantum simulators[557,583,781,857], where tunable atom trapping geometry along with strong in-

teractions resulting in Rydberg blockade allow one to generate a variety of strongly correlated spin models. Coherent laser excitation into Rydberg states generates dynamics within the accessible Hilbert space, similar to that provided by a global transverse field in the Ising model. These constrained dynamics result in new physical phenomena such as quantum many-body scars[557,967,573], which evade thermalization starting from certain product initial states. At the same time, extending the toolbox of Rydberg quantum simulation in the blockade regime to dynamical generators beyond simple transversal fields is an open challenge. This is important, for instance, for realizing spin liquids[934,971,975,959] and lattice gauge theories[953,909,911,592,715], for steering the dynamics of many-body states via counterdiabatic terms[632,931,807], for realizing new types of quantum optimization algorithms[888,588,868], and for recent efforts to generate metrologically useful entanglement in systems with quantum many-body scars[636,638].

Motivated by these considerations, in this Letter we introduce a technique for Floquet engineering[685,826,649,526,851,744,670,840,679,920] that employs time-dependent control to realize effective Rydberg-blockaded models with versatile interactions. While Floquet engineering is widely utilized for interacting spin systems[990,992,609,1017,1018,678], conventional techniques rely on local Pauli frame transformations that generally violate the blockade constraint, or are limited to few-body gates in digital approaches employing optimal control techniques[831]. Our approach, illustrated in Fig. 5.1 (b), leverages driven, periodic many-body trajectories originally discovered in the context of stabilizing quantum many-body scars[573,829,723]. The complex micromotion of these trajectories serves as a resource for programmable Hamiltonian engineering, since perturbations applied during the periodic drive act at stroboscopic times via an effective Hamiltonian generated by time-evolved operators[829]. The resulting class

of time-evolved operators forms a basis for the realization of novel interactions with tunable coefficients, which are not accessible in the static native Hamiltonian. Using this approach, we show how blockade-consistent spin exchange interactions can be engineered, enabling the investigation of gapless phases with emergent particle number conservation[977]. Moreover, in this new regime, we demonstrate the dynamic generation of structured multi-partite entanglement from Néel ($\mathbb{Z}_2$) product initial states and explain this effect in terms of the dynamics of domain walls.

2.2 Hamiltonian engineering

The key idea of this work can be understood by considering the driven PXP model illustrated in Fig. 5.1 (a), which describes a one-dimensional atom chain with periodic boundary conditions, driven into the Rydberg state with fixed Rabi frequency Ω under idealized nearest-neighbor Rydberg blockade, with time-dependent global detuning $\Delta(t)$:

$$H(t) = \frac{\Omega}{2} H_{\mathrm{PXP}} - \Delta(t) N, \tag{2.1}$$

$$H_{\mathrm{PXP}} = \sum_i P_{i-1} \sigma_i^x P_{i+1}, \quad N = \sum_i n_i. \tag{2.2}$$

Here the operators $P_i = \frac{1+\sigma_i^z}{2} = |\circ\rangle_i\langle\circ|_i$ and $n_i = \frac{1-\sigma_i^z}{2} = |\bullet\rangle_i\langle\bullet|_i$ project site i onto ground ($\circ$) and Rydberg ($\bullet$) states respectively, while $\sigma_i^x = |\circ\rangle_i\langle\bullet|_i + |\bullet\rangle_i\langle\circ|_i$ generates Rabi oscillations. Our objective is to realize off-diagonal number conserving processes beyond single spin flips, utilizing the intrinsic controls Ω and $\Delta(t)$. In a conventional (static) approach ($\Delta(t) = \Delta$) to this problem, one typically relies on large detuning $\Delta \gg \Omega$, where multi-body spin flips emerge perturbatively in powers of $(\Omega/\Delta)^n$. The relative

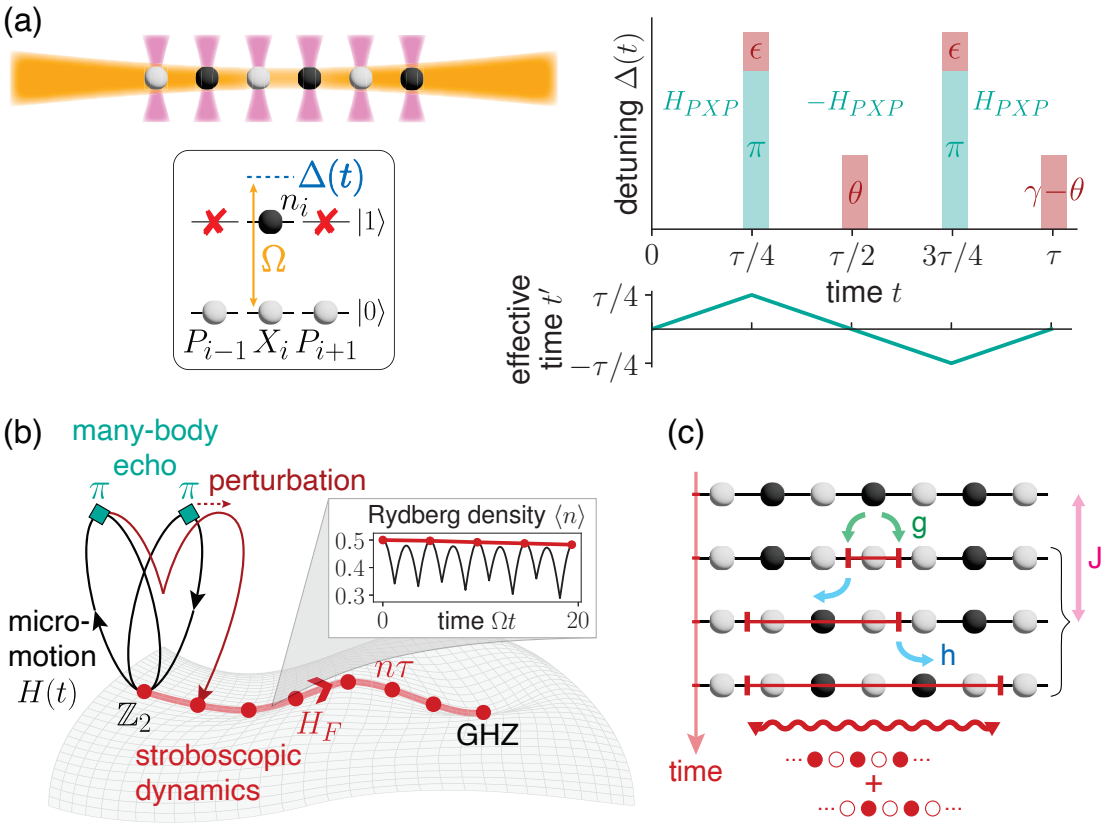


Figure 2.1: Hamiltonian engineering. (a) We consider the driven PXP model as an approximate description of Rydberg atoms in optical tweezers, with Rabi frequency Ω and τ-periodic time-dependent global detuning $\Delta(t)$. Our protocol consists of π-pulses that realize a many-body echo (green) and deliberately placed perturbations (red). The echo realizes evolution under H_{PXP} for effective time $-\frac{\tau}{4} \leq t' \leq \frac{\tau}{4}$, returning to $t' = 0$ at stroboscopic times. (b) The resulting dynamics perturbs around the periodic trajectories of the many-body echo, illustrated as micromotion in the full blockade-constrained Hilbert space. At stroboscopic times $n\tau$, an effective Floquet Hamiltonian H_F generates evolution within a constant energy submanifold. In our main application, the stroboscopic dynamics evolves a Néel ($\mathbb{Z}_2$) initial state towards a highly entangled GHZ-like state. Inset: Micromotion (black) and stroboscopic dynamics (red) of the Rydberg density $\langle n \rangle$ on an $L = 16$ periodic chain. Despite large oscillations within Floquet cycles, the stroboscopic evolution approximately conserves $\langle n \rangle$. (c) Our approach realizes effective models H_F with tunable control over the dynamics of domain wall excitations on top of the Néel order. This includes a chemical potential J, blockade-consistent spin exchange interactions h that act as two-site hopping for domain walls, as well as creation/annihilation terms g of domain wall pairs. The regime of small g provides a mechanism for generating long-range multi-partite entanglement via growing superpositions of alternate $\mathbb{Z}_2$ orders.

strengths of such processes are generally weak and cannot be tuned independently.

Our dynamic protocol circumvents this restriction by modulating laser detuning $\Delta(t)$ and leveraging a many-body spin echo. Specifically, since H_{PXP} anti-commutes with the operator $\prod_i \sigma_i^z = e^{i\pi N}$, π-pulses of the global detuning effectively reverse its sign[967,829]: $e^{i\pi N} H_{\mathrm{PXP}} e^{i\pi N} = -H_{\mathrm{PXP}}$. This property enables a dynamical decoupling in the strongly interacting PXP model by means of a simple pulse sequence ($n \in \mathbb{N}$),

$$\Delta_0(t) = \pi \sum_n \delta\big(t - \frac{\tau}{4} - n\frac{\tau}{2}\big). \tag{2.3}$$

Within each Floquet period τ, the system evolves forward under H_{PXP} for $\tau/4$, backward for $\tau/2$, and forward again for $\tau/4$. At a given time $t \leq \tau$, the system has thus undergone an effective evolution by H_{PXP} for a time $t' = t'(t) = ||t - \tau/4| - \tau/2| - \tau/4$, where $t' \in [-\frac{\tau}{4}, \frac{\tau}{4}]$, as shown in Fig. 5.1 (a) (see Supplemental Material[sup], Sec. I A). As $t'(\tau) = 0$, the system exhibits periodic revivals at stroboscopic times $n\tau$.

To generate a nontrivial effective evolution, we utilize complex micromotion along the periodic trajectory, as illustrated in Fig. 5.1 (b). Specifically, we introduce global detuning perturbations consisting of τ-periodic discrete pulses around the echo protocol of Eq. (2.3), $\Delta(t) = \Delta_0(t) + \tilde{\Delta}(t)$ with $\tilde{\Delta}(t) = \sum_{j,n} \tilde{\Delta}_j \, \delta\left(t - t_j - n\tau\right)$. At stroboscopic times, these perturbations translate into evolution under a static, local effective Floquet Hamiltonian H_F, which holds up to an exponentially long prethermal timescale $T_p \gtrsim (\tau/|\tilde{\Delta}|) e^{c_p/|\tilde{\Delta}|}$, where $|\tilde{\Delta}| = \sum_j |\tilde{\Delta}_j|$ and $c_p > 0$[521,516]. In the interaction picture with respect to the perfect echo evolution for $\tilde{\Delta} = 0$, we obtain the leading contributions to H_F through a Floquet-Magnus expansion[654,829] (see[sup], Secs. I B-I C), result-

ing in $H_F = \sum_{n=0}^{\infty} H_F^{(n)}$, with

$$H_F^{(0)} = -\sum_j \frac{\tilde{\Delta}_j}{\tau} \tilde{N}(t'_j),\ H_F^{(1)} = \sum_{j>\ell} \frac{\tilde{\Delta}_j \tilde{\Delta}_\ell}{2i\tau} \left[\tilde{N}(t'_j), \tilde{N}(t'_\ell)\right]. \tag{2.4}$$

We note that $H_F^{(n)}$ are constructed from Rydberg number operators conjugated by evolution under H_{PXP} for the effective times $t'_j = t'(t_j)$ of the echo protocol,

$$\tilde{N}(t') \equiv e^{it' \frac{\Omega}{2} H_{\mathrm{PXP}}} N e^{-it' \frac{\Omega}{2} H_{\mathrm{PXP}}}.$$

Consequently, operator spreading under the micromotion generated by H_{PXP} induces interactions in the form of n-nested commutators $(t')^n [H_{\mathrm{PXP}}, ..., [H_{\mathrm{PXP}}, N]...]$ in $\tilde{N}(t')$ and thus H_F.

Coefficients of these terms in H_F are controlled by the locations t_j and weights $\tilde{\Delta}_j$ of the pulses. Pulses with $t'_j = 0$ couple to the bare Rydberg number operator N. Further, symmetric weights of pulses at $\pm t'_j$ ensures that all terms containing an odd number of commutators vanish in $H_F^{(0)}$, which thus conserves Rydberg number parity. Hence, for small t'_j the leading non-trivial contribution to $H_F^{(0)}$ appears at order $(t'_j)^2$, which contains nearest-neighbor pair flips. Single spin flips appear only in $H_F^{(1)}$. Based on this intuition, we introduce the following detuning perturbations, parameterized in terms of the (dimensionless) variables $\gamma, \theta, \varepsilon$, see Fig. 5.1 (a),

$$\begin{aligned} \tilde{\Delta}(t) =& (\gamma - \theta) \sum_n \delta(t - n\tau) + \theta \sum_n \delta\big(t - \frac{\tau}{2} - n\tau\big) \\ &+ \varepsilon \sum_n \delta\big(t - \frac{\tau}{4} - n\tau\big) + \varepsilon \sum_n \delta\big(t - \frac{3\tau}{4} - n\tau\big). \end{aligned} \tag{2.5}$$

Here, the first two pulses both occur at effective time $t' = 0$, while the latter occur

at $t' = \pm\frac{\tau}{4}$. Inserting into Eq. (2.4) and expanding $\tilde{N}(\tau/4)$ perturbatively for short periods $\frac{\Omega\tau}{4} \ll 1$, we obtain an approximate closed-form expression for the effective Hamiltonian,

$$\begin{aligned} H_F &\approx -J\,N - h\,H_{\mathrm{PXYP}} + g\,H_{\mathrm{PXP}} + \frac{h}{4}\,H_{ZIZ}, \\ J &= \frac{(\gamma+2\varepsilon)}{\tau} - \frac{3\varepsilon\Omega^2\tau}{32},\ h = -\frac{\varepsilon\Omega^2\tau}{32},\ g = -\frac{\varepsilon(\theta+\varepsilon)\Omega}{8}. \end{aligned} \tag{2.6}$$

Here, we have kept all terms to quadratic order in $\Omega\tau, \varepsilon, \gamma, \theta$ (see details in[sup], Sec. I C); $H_{\mathrm{PXYP}} \equiv \frac{1}{2}\sum_i P_{i-1}\left(\sigma_i^x\sigma_{i+1}^x + \sigma_i^y\sigma_{i+1}^y\right)P_{i+2}$ is a blockaded nearest-neighbor spin-exchange interaction and $H_{ZIZ} \equiv \sum_i \sigma_i^z\sigma_{i+2}^z$. Our Floquet protocol provides flexible relative tunability of the coefficients J, h, g by controlling the period $\Omega\tau$ and parameters $\varepsilon, \gamma, \theta$. Thus, our construction extends the capabilities of the Rydberg quantum simulator to blockade models with independent control over quasiparticle number conservation, motion, and creation/annihilation processes (for comparison with static approach see[sup], Sec. I D). In particular, this enables access to exchange-dominated regimes $h \gtrsim g$, which we explore in the following.

2.3 Controlled multi-partite entanglement

We consider dynamics starting from a Néel state, $|\Psi(t=0)\rangle = |\mathbb{Z}_2\rangle$. Excitations on top of this state can be viewed as domain walls, created in pairs by H_{PXP}, see Fig. 5.1 (c); J sets a chemical potential and H_{PXYP} generates (two-site) hopping of domain walls. We fix the parameters of the Floquet drive to $\frac{\Omega\tau}{2\pi} = 0.77$ (close to the scar period of the bare PXP model[?]), and $\varepsilon = -0.45, \gamma = 1.0, \theta = 0.15$. This translates to an effective model of Eq. (2.6) with $J \approx 0.225, h \approx 0.068, g \approx -0.017$, where the rate of domain wall hopping is stronger than of creation/annihilation. As shown in Fig. 5.1 (b),

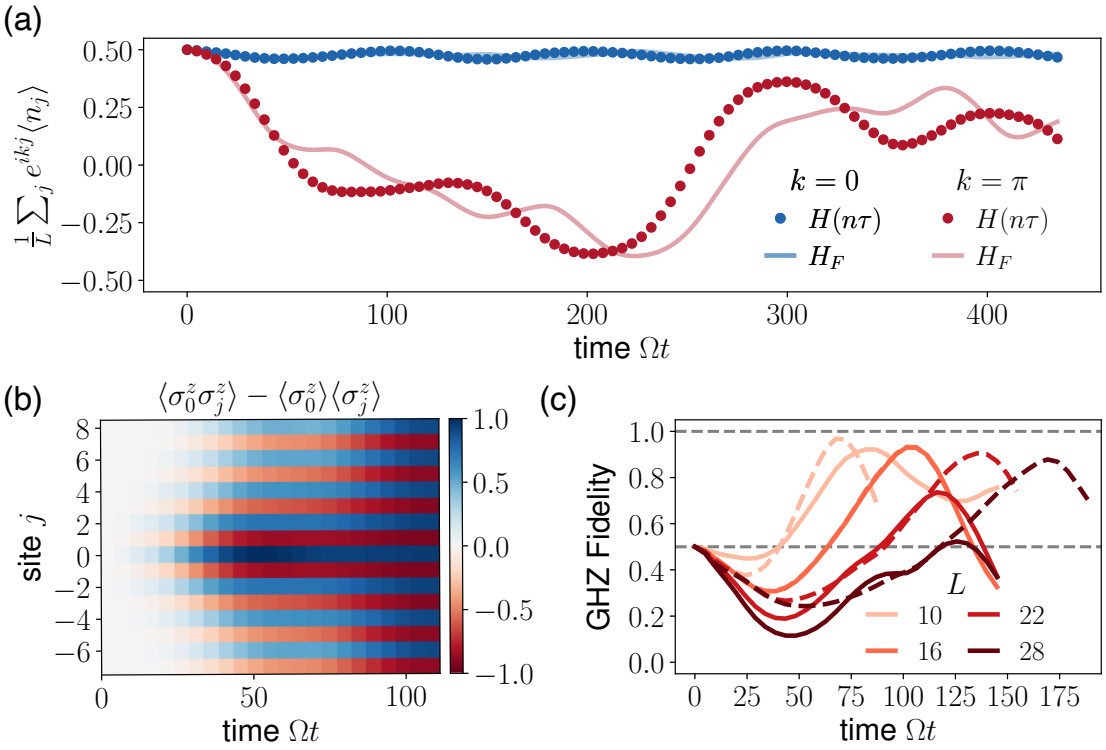


Figure 2.2: Entanglement dynamics. (a) Stroboscopic evolution of an $L = 16$ periodic chain under a drive with period $\frac{\Omega\tau}{2\pi} = 0.77$ and perturbations set to $\varepsilon = -0.45$, $\gamma = 1.0$, $\theta = 0.15$. Starting from a Néel initial state, the Rydberg number density (blue) remains high, while the $\mathbb{Z}_2$ order (red) washes out, in qualitative agreement with evolution under the effective Hamiltonian Eq. (2.6). (b) Dynamics under the drive $H(n\tau)$ generates spreading, connected σ^z-correlations with antiferromagnetic (AFM) spatial profile. (c) The driven dynamics realizes an AFM GHZ state for $L = 16$ once the connected σ^z-correlations peak near unity at all distances. For fixed drive parameters, as system size increases, the peak in GHZ fidelity shifts approximately linearly with L, with decreasing height (solid). However, drive parameters can be tuned for each system size to maintain large GHZ fidelity (dashed, see text and [sup], Sec. III B).

the average Rydberg density $\langle n(t)\rangle$ varies rapidly during micromotion, but evolves only slowly at stroboscopic times. Even though the parameters perturbing the echo are sizeable, the effective Hamiltonian Eq. (2.6) nonetheless provides a good description of the stroboscopic evolution as demonstrated in Fig. 5.2 (a). We confirm in[sup], Sec. IV B that quantitative discrepancies are dominated by higher order terms in the effective Hamiltonian rather than heating. Interestingly, while the density of Rydberg excitations remains high, the staggered magnetization $\sum_j (-1)^j \langle \sigma_j^z(t)\rangle$ washes out. As this happens, the system develops growing connected correlations $\langle \sigma_i^z(t)\sigma_j^z(t)\rangle - \langle \sigma_i^z(t)\rangle \langle \sigma_j^z(t)\rangle$; Fig. 5.2 (b). Once these fluctuations reach the system size (here: $L = 16$), the state develops large overlap with an antiferromagnetic GHZ state, defined as $|\mathrm{GHZ}\rangle = \frac{1}{\sqrt{2}}\left(|\mathbb{Z}_2\rangle + e^{i\varphi}|\mathbb{Z}_2'\rangle\right)$, which we quantify via the fidelity $\max_{\varphi} |\langle \mathrm{GHZ}|\Psi(t)\rangle|^2$ [856,872], see Fig. 5.2 (c). At maximum fidelity, we find $\varphi = \pm\frac{\pi}{2}$ (see[sup], Sec. III B).

This generation of multipartite entanglement can be understood based on the effective model Eq. (2.6), as sketched in Fig. 5.1 (c): gH_{PXP} slowly creates a superposition of the initial $\mathbb{Z}_2$ state with states containing a pair of domain walls, which move rapidly via the strong hH_{PXYP} interaction. The coherently propagating pair carries a growing string of the alternate $\mathbb{Z}_2'$ order, thus generating local patches of antiferromagnetic GHZ-like correlations. On a periodic chain, the pair may re-annihilate at the antipodal point to form the state $|\mathrm{GHZ}\rangle$. However, in large systems, we expect that after a time $t^* \sim 1/g$, interactions among the growing number of domain walls effectively limit the achievable multipartite entanglement to some finite length scale l^*, leading to a decreasing overlap with $|\mathrm{GHZ}\rangle$ for increasing L in Fig. 5.2 (c). To determine this length scale l^*, we note that under hH_{PXYP}, individual domain walls form a band of quasiparticles with dispersion $\varepsilon_k = -2h\cos(k)$, see Fig. 5.3 (a). The initial state $|\mathbb{Z}_2\rangle$ couples to pairs $|k;-k\rangle$ of domain walls with opposite momenta $\pm k$. As the

velocity of these domain walls is $v^* \sim h$, within the time $t^* \sim 1/g$ they will spread for a length $l^* = v^* t^* \sim h/g$, setting the achievable scale of multipartite entanglement.

We verify this relation in thermodynamically large systems via the Quantum Fisher Information (QFI) density, which quantifies the metrological potential of the pure state $|\Psi(t)\rangle$, evolving under H_F, with respect to a staggered z-field: $F_Q/L \equiv \frac{1}{L}\mathrm{Var}\left(\sum_j (-1)^j \sigma_j^z\right)^2_{|\Psi(t)\rangle}$. In particular, a QFI density $F_Q/L > m$ rigorously guarantees at least $(m+1)$-body entanglement[725,964]. In Fig. 5.3 (b), iTEBD simulations of an infinite chain for varying values of g and h demonstrate that the QFI obeys the predicted scalings for the formation time t^* and maximum size l^* of the multipartite entangled regions. As a consequence, we note that scaling $g \sim 1/L$ in finite systems implies $l^* \sim L$, and a GHZ state may form within linear time $t^* \sim L$. We verify this numerically in Fig. 5.2 (c); for a detailed analysis of the parameters that yield high fidelity GHZ states, see[sup], Sec. III B.

2.4 Luttinger liquid dynamics

Due to the small value of g, the entanglement features observed in the previous section may be understood as a dynamical probe of the low energy properties of the constrained model Eq. (2.6) with $U(1)$ symmetry at $g = 0$. In particular, $H_F|_{g=0}$ is known to be integrable[529]. Its ground state phase diagram, which we calculate from Bethe ansatz integral equations (see[sup], Sec. II A), is shown in Fig. 5.3 (c). For $J/h \in (-3, 6)$, the system is in a Luttinger liquid phase[977] with gapless domain wall excitations. Outside this regime, the ground state transitions into a gapped paramagnetic ($J/h < -3$) or $\mathbb{Z}_2$ ($J/h > 6$) phase.

We thus see that the protocol of the previous section corresponds to a quantum

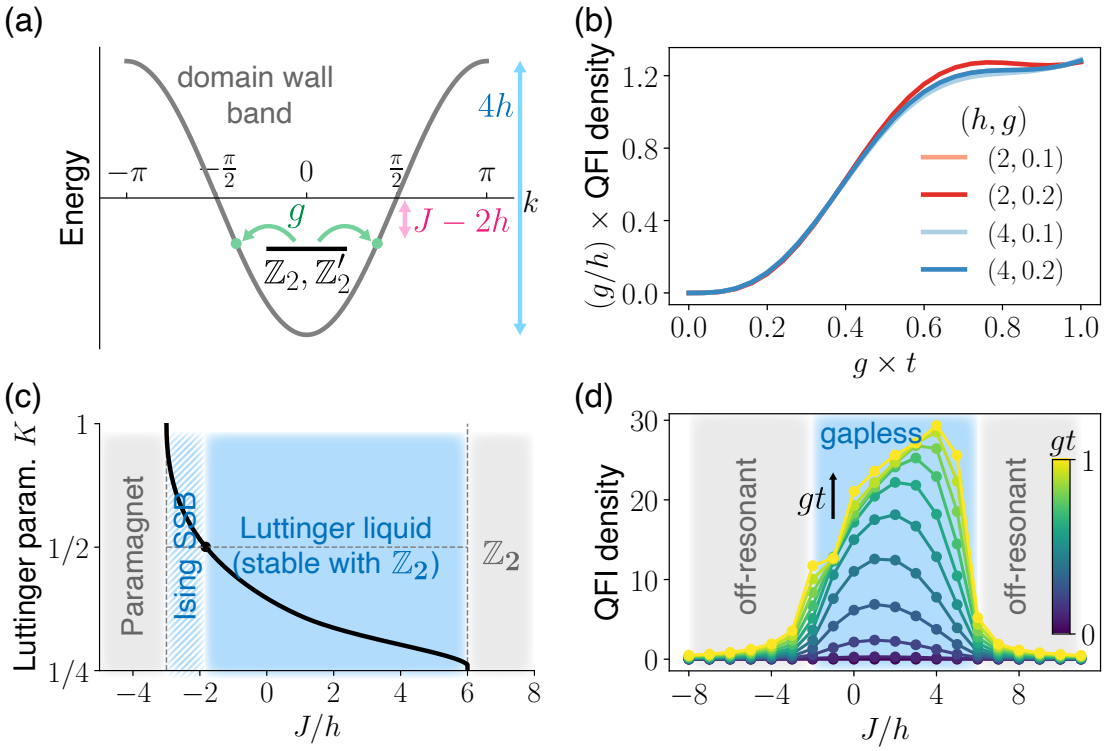


Figure 2.3: Blockaded spin-exchange and approximate $U(1)$ symmetry. (a) The effective Hamiltonian of Eq. (2.6) for $g/h \lesssim 1$ weakly couples the Néel states to pairs of domain walls with momenta $\pm k$ and quasiparticle dispersion $\varepsilon_k = -2h\cos k$. Depending on the energy offset between Néel states and the dispersive band, this coupling can be on- or off-resonant. (b) Dynamics under H_F for small g generates a maximum QFI density (see text) of order $\sim h/g$ within a time $t^* \sim 1/g$. This is seen through a scaling collapse for the dynamics of an infinite size chain simulated via iTEBD for different values of h, g at fixed $J = 2h$. (c) Phase diagram of H_F at the integrable point $g = 0$, with gapped paramagnetic and $\mathbb{Z}_2$ phases, as well as a Luttinger liquid that is stable for $K < 1/2$ (in the presence of $\mathbb{Z}_2$ number parity), and unstable for $K > 1/2$ (towards a gapped Ising SSB state[977,666]). The Luttinger parameter K (black curve) is obtained from the Bethe ansatz solution. (d) iTEBD simulation of the QFI density as a function of time t from a $\mathbb{Z}_2$ initial state for weakly broken integrability at fixed small g. The QFI functions as a dynamical probe of the transition between $\mathbb{Z}_2$ phase and Luttinger liquid in c), and grows at a rate tied to the domain wall dispersion.

quench of the $\mathbb{Z}_2$ state into the Luttinger liquid phase. In particular, for small g, $|\mathbb{Z}_2\rangle$ couples resonantly to domain wall pairs $|k,-k\rangle$ mediating the entanglement dynamics when $J-2h+2\varepsilon_k=\mathcal{O}(g)$, with matrix element $\langle k,-k|gH_{PXP}|\mathbb{Z}_2\rangle \sim 2g\sin(k)$ proportional to the group velocity (see Fig. 5.3 (a) and derivation in[sup], Sec. II B). For J/h outside the Luttinger liquid phase, domain walls can only be created virtually, suppressing the growth of the QFI. As a consequence, dynamics of multipartite entanglement quantified by the QFI density[993] could serve as a dynamical order parameter for the transition from the gapped $\mathbb{Z}_2$ phase to the gapless Luttinger liquid, with its early time growth reflecting the domain wall group velocity. We confirm this prediction numerically by computing the dynamics of the QFI under H_F of Eq. (2.6) using iTEBD for different values of J/h, see Fig. 5.3 (d). The growth of the QFI accurately captures the phase boundary at $J/h=6$ and shows an enhanced rate towards the center of the Luttinger liquid phase. We also verify these features in a direct simulation of the Floquet protocol for finite systems in[sup], Sec. III A.

2.5 Robustness and Implementation in Rydberg arrays

Successfully realizing and controlling H_F in Eq. (2.6) relies on the expansions in small perturbations $\varepsilon,\gamma,\theta$ and drive period $\Omega\tau$, which also tune the rate of dynamics. Thus, an optimal choice of drive parameters must consider the trade-off between a high-accuracy target Hamiltonian and the realistic constraint of observing significant dynamics within finite coherence time of an experimental device, an interplay we explore in[sup], Sec. IV A. In addition, in experiment, Rydberg atoms interact via van der Waals interactions $V_{\mathrm{vdW}}=\Omega\sum_{ij}\left(\frac{R_b}{|i-j|}\right)^6 n_i n_j$, with blockade radius R_b. To demonstrate that our approach applies qualitatively, we construct a pure spin exchange model

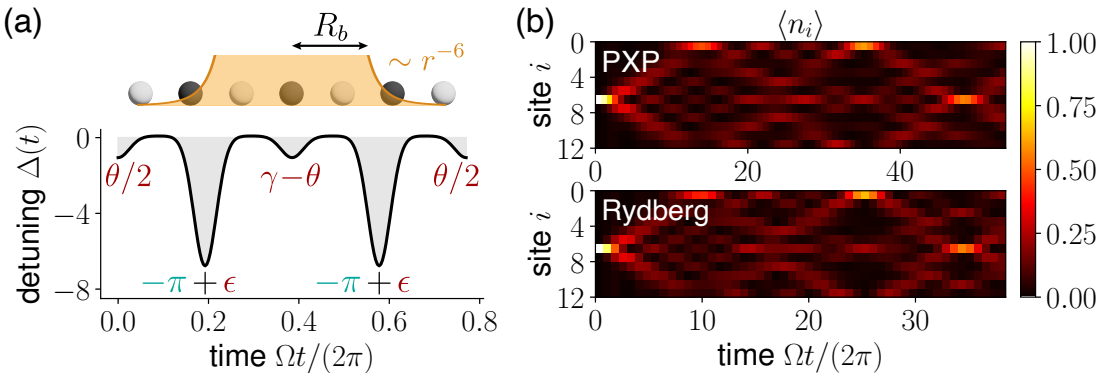


Figure 2.4: Experimental applicability. (a) In experiment, Rydberg atoms at distance $r = |i-j|$ interact via V_{vdW} with strength $\Omega(R_b/r)^6$; here, blockade radius $R_b = 1.5$. In implementing the Floquet drive in (b), we use realistic Gaussian pulses with width $w = 0.046\tau$, ensuring each pulse integrates to the desired detuning (we apply $-\pi$-pulses to avoid blockade violations). A small constant detuning $\delta_{\text{MF}}/\Omega = 0.09$ is added to mitigate the long range tail of V_{vdW}[573]. (b) We benchmark Floquet evolution of the full Rydberg Hamiltonian under finite-width pulses, as described in (a), against the idealized PXP model driven by infinitely sharp pulses. We apply a drive $\varepsilon = -\gamma/2 = -\theta = 0.45$ that generates an effective Hamiltonian with $h = \frac{J}{3} = -\frac{\varepsilon\Omega^2\tau}{32}$, $g = 0$ to engineer a single-particle quantum walk on an $L = 12$ periodic chain. The dynamics of local Rydberg occupations $\langle n_i \rangle$ are consistent with this target; the effective hopping is slightly stronger in the Rydberg model.

$(-2\varepsilon = \gamma = 2\theta \Rightarrow J = 3h \neq 0, g = 0)$ and numerically evaluate the quantum walk of a single Rydberg excitation resulting from Floquet evolution including V_{vdW} at $R_b = 1.5$. We further add a small constant detuning to mitigate the long range tail of V_{vdW}[573] and use Gaussian pulse profiles suitable for realistic control hardware with limited rate of detuning modulation; Fig. 5.4 (a). Comparison with the corresponding PXP result in Fig. 5.4 (b) shows very good qualitative agreement over an extended duration. Quantitatively, the effective hopping is even stronger in the experimentally relevant scenario, likely due to residual contributions from finite pulse width and long range tails. A detailed analysis of these effects is left for future work.

2.6 Discussion & Outlook

We have introduced a Floquet protocol for Rydberg atoms that exploits periodic trajectories of quantum states and enables versatile Hamiltonian engineering with independent control over various interactions, achieved uniquely through our dynamic approach. As an application, we realized models with emergent particle number conservation and dominant blockade-consistent exchange interactions in one dimension, exploring previously inaccessible gapless Luttinger liquid phases. In particular, we found that combining Rydberg blockade and gapless domain wall excitations leads to the generation of long-range, multi-partite entanglement upon evolving $\mathbb{Z}_2$ product states. Our scheme opens the door to investigating interacting Luttinger liquids on near-term quantum simulators. In particular, it could be promising to explore the utility of our Floquet protocol as a novel tool for preparing such low energy states.

Although our discussion focuses on one-dimensional systems, generalization to other geometries is natural. For instance, models akin to Eq. (2.6) are relevant to Rydberg spin liquids in two dimensions[975,959], as well as to achieving quantum speedup in combinatorial optimization by enabling delocalization in the adiabatic algorithm[588]. Moreover, going beyond short evolution times of the operator $\tilde{N}(t')$ provides access to even higher-body spin interactions, an approach we employ in Ref.[663] to study the dynamics of two-dimensional lattice gauge theories. We further emphasize that our Floquet scheme uses only simple global controls, but may be extended by incorporating site-resolved detuning fields[824], which could allow exploration of spatially inhomogeneous or chiral interactions[870]. It would also be interesting to study the connection of our protocol with time-dependent methods for state preparation, such as counter-diabatic driving[633,594,914] and trajectory optimization[807]. Finally, we note

that our Floquet protocol can be extended to other quantum simulation platforms, contingent on time-dependent control to engineer non-trivial periodic trajectories, as is available in dipolar interacting systems[990,992,609,1017,678], trapped ions[677,681], neutral atoms[804,619], or superconducting devices[564,841,579].

2.7 Acknowledgements

We thank Gefen Baranes, Dolev Bluvstein, Pablo Bonilla, Madelyn Cain, Simon Evered, Alexandra Geim, Andi Gu, Marcin Kalinowski, Nathaniel Leitao, Sophie Li, Tom Manovitz, Varun Menon, Simone Notarnicola, Hannes Pichler, Maksym Serbyn, and Peter Zoller for stimulating discussions. Matrix product state simulations were performed using the TeNPy package[707]. We acknowledge financial support from the US Department of Energy (DOE Gauge-Gravity, grant number DE-SC0021013, and DOE Quantum Systems Accelerator, grant number DE-AC02-05CH11231), the National Science Foundation (grant number PHY-2012023), the Center for Ultracold Atoms (an NSF Physics Frontiers Center), the DARPA ONISQ program (grant number W911NF2010021), the DARPA IMPAQT program (grant number HR0011-23-3-0030), and the Army Research Office MURI (grant number W911NF2010082). N.U.K. acknowledges support from The AWS Generation Q Fund at the Harvard Quantum Initiative. N.M. acknowledges support by the Department of Energy Computational Science Graduate Fellowship under award number DE-SC0021110. J.F. acknowledges support from the Harvard Quantum Initiative Postdoctoral Fellowship in Science and Engineering.

3

Programming Hamiltonians in analog simulators

3.1 Introduction

A central challenge in the field of quantum simulations is the programmable realization of a wide range of many-body systems on current devices. Within any given approach, the primary control tools for engineering specific quantum many-body Hamiltonians are typically provided by geometric configuration and time-dependent classical control of external fields. Neutral atoms in optical tweezers constitute a promising platform for programmable quantum simulations with an exceptional de-

gree of geometric flexibility[556,584,780,857]. In combination with Rydberg blockade interactions, highly constrained Hilbert spaces can be realized as emergent low energy subspaces. These can in turn give rise to exotic phases of matter including spin liquid states[556,647,935], novel out-of-equilibrium phenomena such as quantum many-body scars[556,571,967], and can be used to encode classical optimization problems[643,889] or local gauge constraints[684,953,592,972,911,715,1014]. The latter open the door to probing the nonequilibrium dynamics of lattice gauge theories (LGTs) beyond one dimension, an important quantum simulation goal with relevance to high energy physics and emergent phenomena in condensed matter[996,629,1025,545,527].

However, a remaining key challenge for realizing these models is the generation of interesting dynamics while simultaneously preserving the local constraints. In particular, energetic conditions that stabilize a desired subspace may also lead to strong suppression of subspace-preserving evolution, which typically arises through high-order, multi-body perturbative processes. Consequently, the limited tunability of perturbation theory poses an inherent difficulty to simulating different regimes of dynamical gauge field theories. A specific manifestation of this challenge is the implementation of magnetic plaquette terms with analog quantum simulators[624], corresponding to multi-body interactions in the electric field representation. While many advances in the quantum simulation of LGTs have been achieved across a variety of platforms in recent years[556,827,767,989,847,929,846,1006,674], a direct, large-scale implementation of such interactions remains difficult.

In this work, we show that combining Rydberg blockade and periodic driving allows for the realization of dynamical gauge field theories based on tunable multi-body interactions. The central idea is related to the observation of Ref.[571] that periodic driving can act as a many-body echo and tuning knob for stabilizing the dy-

namics of the so-called quantum many-body scars in the 'PXP' models associated with the Rydberg blockade. These observations indicate the possibility that Floquet-engineering[685,826,649,526,851,744,670,840,679,920] can provide a potent tool for controlling many-body dynamics in systems with Rydberg blockade[830,723,808]. Building on these insights, we develop a method involving the use of a Floquet perturbation theory around closed periodic trajectories generated by a many-body echo. Within this framework, initial states periodically revive under continued forward- and backward-evolution generated by a blockade-consistent PXP model. The effect of deviations from an exact many-body echo are described by an effective Hamiltonian[830] with multi-body interactions, which can be engineered from local operators dressed by interacting time evolution, see Fig. 5.1. Making use of operator spreading within a finite time window, multi-body interactions are generated and can be controlled via the choice of a global detuning profile. Small operator evolution times allow for a perturbative expansion of the resulting Hamiltonian, an approach which we use in Ref.[779] to implement novel, blockade-consistent spin exchange interactions.

In this work, we develop and leverage a numerical optimization technique that enables an extension of this Floquet engineering protocol to intermediate time scales. Crucially, this scheme takes into account the role of the detuning profile as a perturbation around the echo evolution, which we balance with the practical requirement of a substantial prefactor for the effective Hamiltonian. We find that interactions involving a moderate number of spins are generated non-perturbatively, enabling a hardware efficient realization of many-body systems in previously inaccessible regimes.

We subsequently apply our approach to the implementation of a two-dimensional $U(1)$ lattice gauge theory containing dynamical gauge and matter degrees of freedom. The local gauge constraints are realized through nearest-neighbor blockade on

a Kagome lattice, and we use our Floquet protocol to engineer the strengths of both gauge and matter interactions in this setup. Since gauge dynamics are the most challenging, we further present two optimized schemes for engineering the six-body terms required to generate gauge field dynamics. In particular, we are able to access the most interesting strong coupling regime in which gauge and matter field dynamics are of comparable strength and we numerically explore their dynamical interplay. We conclude by discussing the realization of our PXP-based approach in arrays of Rydberg atoms with long range van-der-Waals interactions and realistic constraints on the available pulse profiles. We show how these practical challenges can be addressed and outline promising directions for future work.

Finally, before proceeding with the remainder of this work, we want to emphasize that related pulse control techniques are widely used for decoupling interactions in NMR and for Hamiltonian engineering e.g. in dipolar-interacting spin ensembles[990,992,609,1017,678]. In these settings, the effective Hamiltonian is obtained by averaging over site-local basis rotations. Here, we instead average over rotations generated by an interacting evolution, which enables control of larger weight operators. In addition, the stroboscopic implementation of a finite time step using an optimized detuning profile is reminiscent of pulse control techniques for applying two- or multi-qubit gates in digital neutral atom quantum circuits[794,735,877,660,815,746,832]. Indeed, our protocol is a way of generalizing this approach to the many-body limit, while avoiding direct optimization of an exponentially large many-body unitary by restricting to finite evolution times.

3.2 Floquet protocol and effective Hamiltonian

To illustrate the key idea we consider a time-dependent PXP model on an arbitrary lattice geometry,

$$\hat{H}(t) = \frac{\Omega}{2} \sum_i \hat{P}\hat{\sigma}_i^x \hat{P} - \Delta(t) \sum_i \hat{n}_i, \tag{3.1}$$

where $n_i \in \{0,1\}$ labels the occupation number at site i, Ω is the Rabi frequency and $\Delta(t)$ a time-dependent detuning coupling to the global occupation number $\hat{N} = \sum_i \hat{n}_i$. The operator $\hat{P}$ projects onto the space of configurations without nearest neighbor sites simultaneously occupying the $n_i = 1$ state; explicitly, $\hat{P} = \prod_{\langle i,j \rangle}(1 - \hat{n}_i \hat{n}_j)$, where the product runs over nearest neighbor sites $\langle i,j \rangle$ of the lattice. Eq. (3.1) is commonly used as an approximation for the dynamics of Rydberg atoms subject to strong van der Waals interactions that decay rapidly as $V_{ij} = \Omega(R_b/r_{ij})^6$: Two atoms at a distance r_{ij} smaller than the blockade radius R_b are effectively forbidden to both occupy the Rydberg state, thus satisfying the constraint enforced by the projector $\hat{P}$.

3.2.1 Many-body echo and effective Hamiltonian

The starting point for our construction is the ability to generate a closed periodic trajectory through time-dependent control of the detuning operator. Specifically, we can reverse the sign of the off-diagonal (PXP) part of Eq. (3.1),

$$\hat{H}_0 = \frac{\Omega}{2} \sum_i \hat{P}\hat{\sigma}_i^x \hat{P}, \tag{3.2}$$

by applying a global detuning pulse operator $e^{i\pi\hat{N}} = \prod_i \hat{\sigma}_i^z$, such that $e^{-i\pi\hat{N}} \hat{H}_0 \, e^{i\pi\hat{N}} = -\hat{H}_0$. This pulse thus generates a many-body echo and repeated application at regular spacing τ leads to periodic revivals with period 2τ. We denote the time-dependent

Hamiltonian corresponding to this many-body echo protocol as

$$\hat{H}_e(t) = \hat{H}_0 - \pi\hat{N}\sum_{m\in\mathbb{N}} \delta(t - m\tau). \tag{3.3}$$

The unitary evolution operator $\hat{U}_e(t) = \hat{\mathcal{T}} \exp\{-i\int_0^t dt' \hat{H}_e(t)\}$ then indeed reduces to the identity at multiples of 2τ:

$$\hat{U}_e(2\tau) = e^{-i\pi\hat{N}} e^{-i\hat{H}_0\tau} e^{-i\pi\hat{N}} e^{-i\hat{H}_0\tau} = \hat{1}, \tag{3.4}$$

where we assume the pulses to be applied infinitesimally prior to the times $m\tau$. We emphasize the special role of the blockade in this construction: The model Eq. (3.2) is a strongly interacting, non-integrable system, yet can be dynamically decoupled using a simple π-pulse sequence, as would more commonly be used for non-interacting disorder fields.

The stroboscopic time evolution at multiples of 2τ is described by an effective Hamiltonian, $\hat{U}_e(2\tau m) = e^{-i2\tau m\hat{\mathcal{H}}}$. Since Eq. (3.3) generates a perfect many-body echo, $\hat{\mathcal{H}} = 0$ is trivial. However, by adding perturbations to Eq. (3.3), we can controllably generate a variety of terms in the effective Hamiltonian. In order to show this, we consider a modified detuning profile,

$$\Delta(t) = \pi\sum_{m\in\mathbb{N}} \delta(t - m\tau) + \Delta_p(t), \tag{3.5}$$

where $\Delta_p(t+2\tau) = \Delta_p(t)$ denotes a 2τ-periodic deviation from the pure echo. Moreover, we restrict to profiles $\Delta_p(t) = \Delta_p(2\tau - t)$ symmetric around $t = \tau$, as contributions to Δ_p antisymmetric around τ can always be absorbed into a redefinition of the echo evo-

lution $\hat{U}_e(t)$. Following Refs.[655,830], we move to an interaction picture with respect to the time evolution $\hat{U}_e(t)$ and perform a high-frequency expansion[826]. Then, to leading order in the perturbation $\Delta_p(t)$, the effective Hamiltonian governing the stroboscopic time evolution is given by

$$\hat{\mathcal{H}}[\Delta_p] = -\int_0^\tau \frac{dt}{\tau} \Delta_p(t) \hat{N}_0(t). \tag{3.6}$$

Here, $\hat{N}_0(t) = e^{i\hat{H}_0 t} \hat{N} e^{-i\hat{H}_0 t}$ is the global number operator time-evolved under $\hat{H}_0$. Using results from the theory of prethermalization[523,778,858,517,522], in particular Ref.[655], $\hat{\mathcal{H}}$ is guaranteed to be the leading order expression for an approximate, static Hamiltonian description of the time evolution on a prethermal time scale $t_* \gtrsim \exp\{C/(\sqrt{\tau}\|\Delta_p\|)\}$, with $\|\Delta_p\| \equiv \left(\int_0^\tau dt\, |\Delta_p(t)|^2\right)^{1/2}$ the two-norm of Δ_p over one period of the drive and a constant $C > 0$. Beyond this time scale the system is expected to eventually thermalize to infinite temperature. Here, our goal is to control the dynamics for times smaller than t_* via its dominant contribution of Eq. (3.6).

3.2.2 Optimizing the detuning profile

The effective Hamiltonian $\hat{\mathcal{H}}$ in Eq. (3.6) is a linear combination of the time-evolved number operators $\hat{N}_0(t)$. Under this evolution, the operator weight of $\hat{N}_0(t)$ grows, producing multi-body interactions in $\hat{\mathcal{H}}$. In the following, we develop a formalism for controlling such terms through selection of suitable detuning profiles $\Delta_p(t)$. Specifically, our goal is to optimize the choice of $\Delta_p(t)$ such that $\hat{\mathcal{H}}$ is as close as possible to a desired target Hamiltonian $\hat{T}$. Their distance can be quantified most directly by the standard (Frobenius) two-norm $\|\hat{T} - \hat{\mathcal{H}}[\Delta_p]\|$, taking into account all matrix elements between states in Hilbert space. However, in practice, we often optimize $\hat{\mathcal{H}}$ only with

respect to a subset S of all such matrix elements. Accordingly, the above two-norm will be restricted to matrix elements in S,. For example, we may be interested in optimizing matrix elements of $\hat{\mathcal{H}}$ between low-energy states of a Hamiltonian we attempt to engineer. Further, reducing the number of matrix elements renders the optimization of $\hat{\mathcal{H}}[\Delta_p]$ more tractable.

Then, we optimize the detuning profile by minimizing the cost function

$$C_{\lambda,\tau}(\hat{T}) \equiv \left\| \hat{T} - \hat{\mathcal{H}}[\Delta_p] \right\|^2 + \lambda \left\| \Delta_p \right\|^2. \tag{3.7}$$

This cost function has two hyperparameters, the Floquet period τ and a regularization parameter λ. The purpose of regularization is to ensure the norm of the perturbation remains small, while simultaneously attempting to achieve the best approximation to the target Hamiltonian $\hat{T}$ *. In particular, large values of $\|\Delta_p\|$ would introduce higher order contributions to the effective Hamiltonian, and – crucially – eventually lead to a breakdown of the prethermal regime of the Floquet system. Ultimately, we will vary τ and λ in order to achieve the best performance possible.

To perform the optimization, we transform it into a linear-regression task. First, we discretize the problem via small equidistant time steps $t_{i=1,...,M}$, with $t_1 = 0$, $t_M = \tau$. Accordingly, we define the vector $\Delta_{\boldsymbol{p}} = \big(\Delta_p(t_1), ..., \Delta_p(t_M)\big)^T \in \mathbb{R}^M$ for the discretized detuning profile. In addition, we adopt the notation $\boldsymbol{N}_0(t) \in \mathbb{C}^{|S|}$ for the relevant subset of matrix elements, written as a column vector of dimension $|S|$. Then, we can define an $|S| \times M$ matrix $\underline{N_0} = \big(\boldsymbol{N}_0(t_1), ..., \boldsymbol{N}_0(t_M)\big)$ that acts as a linear map from a

*We define the energies in Eq. (3.7) to be given in units of the Rabi frequency Ω.

detuning profile $\Delta_{\boldsymbol{p}}$ to an effective Hamiltonian,

$$\boldsymbol{\mathcal{H}}[\Delta_p] = -\frac{dt}{\tau}\,\underline{N_0}\cdot\Delta_{\boldsymbol{p}}. \tag{3.8}$$

Within this discretization, the solution of the least squares minimization problem defined by Eq. (3.7) can be given in closed form[908]. It reads

$$\tilde{\Delta}_p = \tilde{\Delta}_p(\lambda,\tau,\boldsymbol{T}) = -\left(\frac{dt}{\tau}\underline{N_0}^\dagger\underline{N_0} + \tau\lambda\,1\right)^{-1}\underline{N_0}^\dagger\cdot\boldsymbol{T}, \tag{3.9}$$

and is linear in the target matrix elements $\boldsymbol{T}$. With the discretized, time-evolved number operators in $\underline{N_0}$ as input, Eq. (3.9) returns a detuning profile that optimizes the matrix elements of the effective Hamiltonian subject to a finite cost for large detuning perturbations. As the number of discretized steps $M \to \infty$ ($dt \to 0$) increases, the optimized profile $\tilde{\Delta}_p$ converges to a continuous function $\tilde{\Delta}_p(t)$. This property follows from the continuity of the time-evolved operator $\hat{N}_0(t)$. We note that we may in principle also consider discrete contributions to $\Delta_p(t)$ in Eq. (3.6). However, for the remainder of this work, we restrict our use of this possibility to sharp detuning pulses of weight Δ_0/Ω at multiples of the period 2τ, which gives rise to a detuning contribution $-\frac{\Delta_0}{2\tau\Omega}\hat{N}$ to $\hat{\mathcal{H}}$. To first order, the detuning in the effective Hamiltonian $\hat{\mathcal{H}}$ is thus freely adjustable.

In Sec. 3.3 we apply this optimization protocol to several examples by evaluating $\hat{N}_0(t) = \sum_i \hat{n}_i(t)$ numerically for small systems. Importantly however, due to the locality of the operators $\hat{n}_i(t \leq \tau)$, the presence of Lieb-Robinson bounds ensures that our approach generalizes to large systems and eventually converges in the thermodynamic limit.

3.2.3 Effect of Regularization

In order to gain intuition about the optimization procedure, it is helpful to consider the singular value decomposition (SVD) of the operator matrix $\underline{N_0} = WDV^\dagger$. The matrix W is an $|S| \times |S|$ unitary matrix, whose columns form an orthonormal basis for the subspace of engineerable Hamiltonians in Eq. (3.8). In contrast, the matrix V is an $M \times M$ real unitary matrix, whose columns form an orthonormal basis of detuning profiles. Each detuning profile $\Delta_j(t_i) = V_{ij}$ realizes the effective Hamiltonian $(\boldsymbol{\mathcal{H}}_j)_l = W_{lj}$ when applied. The proportionality constant is given by the singular values D_j, encoded by the diagonal matrix D. As such, the singular value associated with each profile/Hamiltonian pair tells us about the efficiency of realizing the corresponding interaction. Typically, we find that large singular values arise from smoothly varying profiles, which thus correspond to 'easy-to-engineer' interactions. In constrast, small singular values arise from rapidly oscillatory contributions and thus represent interactions that are more challenging to capture.

Including the parameter λ in Eq. (3.9) then amounts to an effective cutoff on the profiles that contribute to the optimization procedure. When $D_j \ll \lambda$, the contribution of Δ_j to the optimized solution $\tilde{\Delta}_p$ is suppressed. This is physically intuitive: Profiles Δ_j with small D_j generate contributions to $\hat{\mathcal{H}}$ with small efficiency, i.e., small prefactor $\sim D_j$. To make such contributions sizeable, i.e., observable on accessible timescales, one must scale up Δ_j, contrary to its role as a perturbation. This highlights a limitation inherent to our approach: Only target operators $\hat{T}$ contained in the span of profiles with large singular values can be engineered with both high fidelity and appreciable prefactor. For target operators outside this span, our regularization can be thought of as biasing the effective Hamiltonian towards the closest efficiently engineer-

able approximation.

It remains to choose the period τ and the parameter λ that both enter the cost function Eq. (3.7). When the target matrix elements $\hat{T}$ include multi-body interactions, small evolution times τ are not sufficient to generate such terms at appreciable weight in $\hat{N}_0(t)$ for $t \leq \tau$. On the other hand, for very long times τ the operator $\hat{N}_0(t)$ is expected to scramble across an exponential number of Pauli strings, thus strongly reducing the weight available in particular terms of interest. Similarly, we can formalize our intuition on the role of λ presented above: For small λ, the optimized $\hat{\mathcal{H}}$ is increasingly aligned with the target direction $\hat{T}$. This results in a large value of the quantity

$$Q_{\measuredangle}(\lambda, \tau) \equiv \frac{(\hat{T}, \hat{\mathcal{H}}[\tilde{\Delta}_p])}{\|\hat{T}\| \, \|\hat{\mathcal{H}}[\tilde{\Delta}_p]\|} \leq 1, \tag{3.10}$$

where $(\cdot, \cdot)$ denotes the operator inner product (with respect to the matrix elements S). However, small λ also leads to large detuning perturbations, and so the contribution of the desired target $\hat{T}$ to $\hat{\mathcal{H}}$ per amount of perturbation $\|\tilde{\Delta}_p\|$ is small, as quantified by

$$Q_{\Delta}(\lambda, \tau) \equiv \frac{(\hat{T}, \hat{\mathcal{H}}[\tilde{\Delta}_p])}{\|\hat{T}\| \, \|\tilde{\Delta}_p\|}. \tag{3.11}$$

Hence, there is a tradeoff in the choice of λ, and indeed $\partial_\lambda Q_{\measuredangle}(\lambda, \tau) \leq 0$ and $\partial_\lambda Q_{\Delta}(\lambda, \tau) \geq 0$ hold. Therefore, $Q_{\measuredangle}$ and Q_{Δ} quantify the accuracy and efficiency of a given protocol respectively, and give insight into the tradeoff between supressing unwanted terms and achieving fast dynamics on early time scales. In practice, we may then examine the quantities of Eqs. (3.10,3.11) for a range of values for λ and τ to find suitable choices.

3.3 Simulating dynamics of a 2D lattice gauge theory

We now consider the application of our Hamiltonian engineering scheme for the analog simulation of lattice gauge theories. Due to the presence of local gauge constraints, dynamics in lattice gauge theories requires the presence of multi-body interactions beyond two-body terms. In analog schemes, such interactions can be generated in perturbation theory of a small parameter[624]. However, if the required perturbative order is high, their tunability relative to lower-order terms in the Hamiltonian will be limited, and their simulation on experimentally accessible time scales might be challenging. In the following, we present a concrete example in which our Floquet-approach can overcome these limitations.

3.3.1 Kagome lattice PXP model and $U(1)$ gauge theory

We consider a PXP model of spins on the sites of the Kagome lattice, see Fig. 3.2 (a). Due to the blockade, each elementary triangle can host at most one site occupying the $n_i = 1$ state. The subspace of states with exactly one occupied site on each triangle is exponentially large and equivalent to the close-packed dimer coverings of a honeycomb lattice. The close-packing constraint is equivalent to the condition

$$\hat{G}^{(\text{dimer})}_{\triangle/\triangledown} = 1 - \sum_{i \in \triangle/\triangledown} \hat{n}_i = 0 \tag{3.12}$$

for each triangle of the Kagome geometry. Dimer models on bipartite lattices that preserve these close-packing constraints map onto pure $U(1)$ gauge theories[854]. Under this equivalence, the occupation numbers $n_i = 0, 1$ map onto a spin-1/2-valued local electric field $E_i = \pm 1/2$; thus giving rise to quantum link models[716,873,597]. Accord-

ingly, the constraints Eq. (3.12) correspond to local Gauss laws, with $\hat{G}_{\triangle/\triangledown}$ generating $U(1)$ gauge transformations.

Flipping a single qubit in a close-packed state creates a pair of up- and downward pointing vacant triangles, see Fig. 3.2 (a). In the language of gauge theory, these correspond to positively and negatively charged matter excitations, respectively. Introducing a local occupation number $\hat{\rho}_{\triangle/\triangledown} \in \{0,1\}$ for vacant triangles, the Gauss laws in the presence of charged matter become

$$\hat{G}_{\triangle/\triangledown} = 1 - \hat{\rho}_{\triangle/\triangledown} - \sum_{i \in \triangle/\triangledown} \hat{n}_i = 0. \tag{3.13}$$

In the physical setup on the Kagome lattice, the $\hat{\rho}_{\triangle/\triangledown}$ are not independent degrees of freedom, but entirely determined by the electric fields $\hat{n}_i$. Per nearest-neighbor blockade, the Gauss laws Eq. (3.13) are thus valid by construction. In this approach of "integrating out the Gauss laws", gauge invariance need not be enforced explicitly. However, to construct a sensible gauge theory, we generally demand that the charged matter excitations have a finite energy gap. In particular, often it is interesting to consider the limit in which the number $\sum_{\triangle} \hat{\rho}_{\triangle} + \sum_{\triangledown} \hat{\rho}_{\triangledown}$ of matter excitations, and thus also $\hat{N}$, is conserved.

One can directly realize this condition in the PXP model at large static detuning, $\Delta(t) = \Delta \gg \Omega$. A Schrieffer-Wolff transformation in the small parameter Ω/Δ leads to an effective Hamiltonian[972]

$$\begin{aligned} \hat{H}_{\text{static}} = &- \Delta \hat{N} - \frac{\Omega^2}{4\Delta} \sum_{|\Lambda|=2} \hat{P} \hat{\sigma}^y_{\Lambda_1} \hat{\sigma}^y_{\Lambda_2} \hat{P} \\ &- \frac{3}{32} \frac{\Omega^6}{\Delta^5} \sum_{|\Lambda|=6} \hat{P} \left(\prod_{i=1}^{6} \hat{\sigma}^y_{\Lambda_i} \right) \hat{P} + \ldots, \end{aligned} \tag{3.14}$$

where each term is given to leading order. Note that Eq. (3.14) is a perturbative description valid in a rotated basis given by the Schrieffer-Wolff transformation. In the original basis of $n_i = 0, 1$ spin states, the conservation of $\hat{N}$ holds only approximately and deteriorates as the ratio Ω/Δ increases. The second term in Eq. (3.14) sums over all strings of spin flips along connected paths Λ of length $|\Lambda| = 2$ on the Kagome lattice. This process corresponds to a nearest neighbor hopping of charged matter excitations, see Fig. 3.2 (b). The third term in Eq. (3.14) constitutes a six-body plaquette resonance as depicted in Fig. 3.2 (b). This term is the analogue of a magnetic term $\sim B^2$ in the language of gauge theory and generates pure gauge field dynamics in the close-packed dimer model without vacancies.

The lattice gauge theory Eq. (3.14) features dynamical matter and gauge field degrees of freedom but features several significant limitations. Specifically, magnetic plaquette terms occur at sixth order in Ω/Δ. Thus, the pure gauge dynamics is weak and possibly challenging to observe on moderate time scales. Increasing the ratio Ω/Δ enhances such terms, but is detrimental to the approximate conservation of $\hat{N}$ and leads to a high density of virtual charge excitations. Moreover, the dynamics of charged matter excitations occurs already at second order in Ω/Δ and naturally dominates the six-body plaquette terms. This limits tunability and precludes access to an interesting strong coupling regime where gauge and matter field dynamics occur on comparable timescales. One approach to overcome such limitations in analog setups is to encode gauge and matter degrees of freedom separately in the hardware. Given sufficient local control, such a 'bottom-up' approach to lattice gauge theories affords more tunability, see e.g.[544,956,1024,547], or [715,700] for recent proposals. At the same time, gauge invariance needs to be enforced explicitly, for example via large energy penalties[699]. We emphasize that there also exists a large body of work using digital

approaches[545,676]. In what follows we present an alternative hardware efficient route towards realization of these ideas.

3.3.2 Floquet protocol: Time-evolved operators

We now apply the Floquet framework introduced previously to the Kagome lattice PXP model. Concretely, we work with a system of $L \times L = 3 \times 3$ unit cells containing $3L^2$ sites and periodic boundary conditions, shown in Fig. 3.2 (c). The occupation number basis states are denoted as

$$|n\rangle = |n_1, ..., n_{3L^2}\rangle\,, \tag{3.15}$$

and $N_n \equiv \sum_{i=1}^{3L^2} n_i$ is a short hand label for the number of excited spins in $|n\rangle$. Before targeting a specific Hamiltonian engineering goal, we develop a more general intuition on the capabilities of our approach in this setting. For this purpose, we inspect the properties of the time evolved operator $\hat{N}_0(t)$, the central ingredient in our construction. Specifically, we are interested in the overlap of $\hat{N}_0(t)$ with the most relevant, off-diagonal processes of the gauge theory framework depicted in Fig. 3.2 (b). They correspond to hopping of charge excitations and six-body plaquette terms as present also in Eq. (3.14), as well as single- and three-body spin flip terms that create/annihilate pairs of charge excitations. These processes can be captured via the off-diagonal operators

$$\hat{O}_\gamma \equiv \sum_{|\Lambda|=\gamma} \hat{P}\left(\prod_{i=1}^{\gamma} \hat{\sigma}^y_{\Lambda_i}\right)\hat{P}. \tag{3.16}$$

In order to evaluate the contribution of these operators to $\hat{N}_0(t)$ numerically, we restrict to the translationally invariant zero momentum sector, spanned by the states

$$|n_k\rangle = \frac{1}{\mathcal{N}} \sum_{x,y} e^{ik_x x + ik_y y} \hat{T}_{x,y} |n\rangle , \tag{3.17}$$

for $k = 0$. Here, $\hat{T}_{x,y}$ denotes the translation operator by x, y unit cells and $\mathcal{N}$ is a normalization constant. Accordingly, the set of matrix elements between all $k = 0$ basis states is given by

$$S = \{(|n_{k=0}\rangle , |n'_{k=0}\rangle)\}. \tag{3.18}$$

Within this set of matrix elements, we subsequently compute the overlap

$$\frac{1}{\mathcal{N}_\gamma} \left(\hat{N}_0(t), \hat{O}_\gamma\right), \tag{3.19}$$

with the normalization constant $\mathcal{N}_\gamma = \left\|\hat{O}_\gamma\right\|^2$.

The result of Eq. (3.19) for the 3×3 Kagome system is depicted in Fig. 3.2 (c). At very early times $\Omega t \ll 1$, the overlaps grow as $(\hat{N}_0(t), \hat{O}_\gamma) \sim t^\gamma$ as expected from a small time expansion of $\hat{N}_0(t)$. Beyond perturbative times, the overlaps display oscillatory behavior, with a period of oscillation that increases with the weight γ of the corresponding operator. Thus, intuitively, evolution to later times is required for $\hat{N}_0(t)$ to acquire appreciable overlap with larger weight operators. At the same time, the maxima of the overlap decrease for increasing γ. This agrees with the intuition that $\hat{N}_0(t)$ starts to scramble across many different operators at late times $\Omega t \gg 1$, such that overlaps with particular operators of interest become smaller. As a consequence, overlap with operators of very large weight is necessarily small at all times. We further include the contribution of the single-body operator $\hat{N}$ to $\hat{N}_0(t)$ in Fig. 3.2 (c).

The key observation of Fig. 3.2 (c) is that between very short Floquet periods $\Omega\tau \ll 1$, where multi-body contributions to $\hat{N}_0(t)$ for $t \leq \tau$ are perturbatively suppressed by their operator weight γ, and long periods $\Omega\tau \gg 1$, where $\hat{N}_0(t \lesssim \tau)$ is scrambled, there exists a non-perturbative regime $\Omega\tau = \mathcal{O}(1)$ of intermediate Floquet periods that allow for flexible Hamiltonian engineering via Eq. (3.6). In particular, the structure of $\hat{N}_0(t)$ at intermediate times allows us to find detuning profiles $\Delta_p(t)$ such that contributions of operators with intermediate weights $\gamma \lesssim \mathcal{O}(\Omega\tau)$ to the effective Hamiltonian can be tuned relative to each other. We emphasize that the qualitative structure of $\hat{N}_0(t)$ at finite times visible in Fig. 3.2 (c) generalizes to other lattice geometries and system sizes. In the following, we investigate two specific protocols for engineering gauge field dynamics on the Kagome lattice.

3.3.3 Floquet protocol for six-body terms

In our first example, we directly engineer the required six-body plaquette terms $\hat{O}_{\gamma=6}$, following the scheme developed in Sec 3.2. A close-packed dimer model is realized in the sector of maximum Rydberg excitation number $N = L^2$, which our effective Hamiltonian should preserve. For this purpose, on top of the continuous detuning $\Delta_p(t)$ derived below, we add a discrete detuning perturbation of strength Δ_0/Ω at multiples of $t = 2\tau$. This gives rise to a detuning field $-\frac{\Delta_0}{2\tau\Omega}\hat{N}$ in the effective Hamiltonian that stabilizes global Rydberg number. For concreteness, we fix $\Delta_0/\Omega = 0.7$ in the following.

We then use the optimized continuous part $\Delta_p(t)$ of the detuning profile to construct the six-body plaquette terms. We are mainly interested in the sector of maximum Rydberg occupation number $N = L^2$, and thus restrict our optimization to matrix elements within this sector, as well as matrix elements between this sector and states with occupation number $N = L^2 - 1$. Moreover, we again work in the transla-

tionally invariant sector of zero momentum states. Thus, we define the set of relevant matrix elements to optimize over as

$$S = \left\{ \left(|n_{k=0}\rangle , |n'_{k=0}\rangle \right) : N_n + N_{n'} \geq 2L^2 - 1 \right\}. \tag{3.20}$$

Our target operator within this set of matrix elements is given by

$$\hat{T} = g\, \hat{O}_{\gamma=6}, \tag{3.21}$$

with prefactor g. Here, we fix a small $g/\Omega = 0.012$ to keep deviations from number conservation small. Taking Eq. (3.20) and Eq. (3.21) together, our approach targets six-body processes within the $N = L^2$ sector while simultaneously minimizing all matrix elements connecting it to the sector with $N = L^2 - 1$. An illustration of the matrix elements S and the desired target operator is given in Fig. 3.3 (a).

We now determine $\Delta_p(t)$ by minimizing the cost function $C_{\lambda,\tau}(\hat{T})$ of Eq. (3.7). To choose the period τ as well as the detuning cost parameter λ, we perform this optimization for multiple values of λ, τ and plot the quantities $Q_{\measuredangle}(\lambda, \tau)$ and $Q_{\Delta}(\lambda, \tau)$ defined in Eqs. (3.10,3.11) in Fig. 3.3 (b). They quantify the alignment of the resulting effective Hamiltonian with the target direction along $\hat{T}$ and the strength of the effective Hamiltonian along the target direction per amount of detuning perturbation, respectively. Based on the result of Fig. 3.3 (b), we select $\Omega\tau = 6.0$ and $\lambda = 0.1$, where both $Q_{\measuredangle}(\lambda, \tau)$ and $Q_{\Delta}(\lambda, \tau)$ are large. The detuning profile $\Delta_p(t)$ resulting from the optimization at these parameter values is shown in Fig. 3.3 (c).

With $\Delta_p(t)$ fixed, we consider time evolution under the full, time-dependent Hamiltonian $\hat{H}(t)$ and compare it with the dynamics resulting from our expression for the

effective Hamiltonian $\hat{\mathcal{H}}$. Here, we consider $\hat{\mathcal{H}}$ as calculated from Eq. (3.6) acting on the full $k = 0$ Hilbert space. Fig. 3.3 (d) shows the dynamics of the density $n(t) \equiv \langle \hat{N} \rangle / (3L^2) \leq 1/3$ of excited spins starting from a close-packed dimer initial state. The dynamics under $\hat{H}(t)$ leads the system far away from the initial Rydberg number sector, but comes back to it at multiples of the stroboscopic time $2\tau\Omega = 12$, in agreement with dynamics under the static effective Hamiltonian $\hat{\mathcal{H}}$. The driven system thus approximately conserves the manifold of dimer states at stroboscopic times. To verify that non-trivial dynamics occurs within this manifold, we define the number of next-nearest neighbor excited spins,

$$\hat{V} = \sum_{\langle\langle i,j \rangle\rangle} \hat{n}_i \hat{n}_j, \tag{3.22}$$

and consider the time evolution of its variance,

$$\langle (\Delta \hat{V}(t))^2 \rangle = \langle \hat{V}^2(t) \rangle - \langle \hat{V}(t) \rangle^2 . \tag{3.23}$$

Starting from the translationally invariant version of the dimer initial state $|\psi_1\rangle$, $\langle (\Delta \hat{V}(0))^2 \rangle = 0$. As the state turns into a superposition of dimer states with different values of $\hat{V}$, $\langle (\Delta \hat{V}(t))^2 \rangle$ starts to increase on the time scale at which effective plaquette terms occur. Fig. 3.3 (e) demonstrates oscillating dynamics of $\langle (\Delta \hat{V}(t))^2 \rangle$, with good agreement between the driven time evolution and dynamics under $\hat{\mathcal{H}}$. Simultaneously, the excitation number density remains very high, $n(t) \gtrsim 0.33$, demonstrating that the increasing variance $\langle (\Delta \hat{V}(t))^2 \rangle$ is indeed due to the formation of superpositions in the subspace of dimer states. Moreover, we consider dynamics for the initial state $|\psi_2\rangle$ containing a pair of charged matter excitations. Again, we find a high quality of approximate number conservation and excellent agreement between driven evolution and the dynamics

of $\hat{\mathcal{H}}$. Non-trivial dynamics of $\langle(\Delta\hat{V}(t))^2\rangle$ occurs on timescales similar to the dimer initial state.

Although our approach suppresses terms in $\hat{\mathcal{H}}$ that do not commute with $\hat{N}$, they generally remain non-zero. To verify that dynamics of $\hat{\mathcal{H}}$ in the fully-packed manifold is indeed dominated by six-body interactions, we consider a modified version of the effective Hamiltonian (in the $k = 0$ sector):

$$\hat{\mathcal{H}}(\nu) \equiv \nu\hat{\mathcal{H}} + \frac{1-\nu}{\|\hat{N}\|^2}\left(\hat{N}, \hat{\mathcal{H}}\right)\hat{N}. \tag{3.24}$$

$\hat{\mathcal{H}}(\nu)$ rescales the part of $\hat{\mathcal{H}}$ orthogonal to $\hat{N}$ by a factor ν. To analyze the effect of this rescaling on the dynamics of $\langle(\Delta\hat{V}(t))^2\rangle$, starting from $|\psi_1\rangle$, we consider the frequency $\omega_{\max} \equiv \max_{\omega\neq 0}\left|\mathcal{F}[\langle(\Delta\hat{V}(t))^2\rangle](\omega)\right|$ at which the Fourier transform $\mathcal{F}[\langle(\Delta\hat{V}(t))^2\rangle](\omega)$ of the time-evolved variance is maximal. For dominant six-body terms, we expect a linear relation $\omega_{\max} \sim \nu$ upon rescaling, and our numerics are consistent with this expectation as shown in Fig. 3.5 (b). This further becomes manifest in a linear scaling collapse of the early time dynamics of $\langle(\Delta\hat{V}(t))^2\rangle$, Fig. 3.5 (c). At the same time, the long-time average $\overline{n(t)}$ of the density remains near its maximum value, see Fig. 3.5 (a). By contrast, applying an analogous rescaling to a PXP model at static detuning results in a sixth-order relation $\omega_{\max} \sim \nu^6$ and leads to a rapidly changing average density $\overline{n(t)}$, see Fig. 3.5 (a,b).

Overall, the protocol of this section induces dynamics dominated by six-body plaquette terms at a very high quality of number conservation. In the following, we attempt to further enhance the strength of effective six-body dynamics to enable evolution on even faster time scales.

3.3.4 Floquet protocol for three-body terms

In this section, we follow a different route towards effective plaquette terms: Instead of generating six-body interactions directly, we engineer an effective Hamiltonian in which the pure gauge field dynamics is predominantly generated via second-order perturbative processes from three-body terms. As in the previous example, we employ a discrete pulse at multiples of the period 2τ to generate a discrete contribution $-\frac{\Delta_0}{2\tau\Omega}\hat{N}$ to the effective Hamiltonian, fixing $\Delta_0/\Omega = 1.0$ in the following.

For the optimization of the continuous part of the detuning profile, we take into account all matrix elements between $k = 0$ states with either $N = L^2$ or $N = L^2 - 1$, i.e.,

$$S = \left\{ \left(|n_{k=0}\rangle , |n'_{k=0}\rangle \right) : N_n, N_{n'} \geq L^2 - 1 \right\}. \tag{3.25}$$

We now define our target operator within this set of matrix elements as

$$\hat{T} = -\Delta\hat{N} + g_3\,\hat{O}_{\gamma=3} + g_2\,\hat{O}_{\gamma=2}, \tag{3.26}$$

where we set $\Delta/\Omega = 0.22$, $g_3/\Omega = -g_2/\Omega = 0.055$. Hence, $\hat{T}$ gives an additional contribution to the detuning and balances the two- and three-body terms corresponding to the processes shown in Fig. 3.2 (b). Crucially, $\hat{T}$ does not contain single-body spin flip terms. We illustrate the matrix elements and target operator entering our optimization scheme in Fig. 3.4 (a). Next, we perform the optimization and evaluate the quantities $Q_{\measuredangle}(\lambda, \tau)$, $Q_{\Delta}(\lambda, \tau)$ for multiple values of λ, τ in Fig. 3.4 (b). Both are found to be large for $\Omega\tau = 2.0$, $\lambda = 1.5$. The optimized detuning profile corresponding to these parameter values is shown in Fig. 3.4 (c). The chosen Floquet period is significantly shorter compared to the previous section, a consequence of optimizing for oper-

ators with smaller weight. Moreover, Fig. 3.4 (b) shows that $\hat{\mathcal{H}}$ is well-aligned with the target direction along $\hat{T}$, $Q_{\measuredangle}(\lambda = 1.5, \Omega\tau = 2.0) \approx 0.9$.

With $\Delta_p(t)$ fixed, we show the dynamics from the state $|\psi_1\rangle$ under $\hat{H}(t)$ in Fig. 3.4 (d). At stroboscopic times, the approximate conservation law is less pronounced compared to the previous section, but $n(t) \gtrsim 0.31$ remains very high, consistent with evolution under $\hat{\mathcal{H}}$. This observation extends to the variance $(\Delta V(t))^2$ of Eq. (3.23), which exhibits oscillations, and thus non-trivial gauge field dynamics, already on the times $\Omega t \leq 20$ shown in Fig. 3.4 (e). Dynamics from the state $|\psi_2\rangle$ with a pair of charged matter excitations occurs on similar time scales.

As in the previous section, we want to verify that the gauge field dynamics of $\hat{\mathcal{H}}$ is indeed dominated by low-order perturbative processes. For this purpose, we consider the rescaling of all terms orthogonal to $\hat{N}$ as in Eq. (3.24). Accordingly, for strong second-order processes, we see the dominant oscillation frequency $\omega_{\max}$ of the variance $(\Delta V(t))^2$ scale approximately as $\omega_{\max} \sim \nu^2$, Fig. 3.5 (b). This relation becomes manifest in the early time dynamics of $(\Delta V(t))^2$ upon rescaling the time axis with the factor ν^2. We further see in Fig. 3.5 (a) that the long time average $\overline{n(t)}$ varies more strongly with ν compared to the six-body case of the previous section, but remains well above the static PXP case despite orders-of-magnitude more efficient gauge field dynamics.

Finally, we point out the general tradeoff between accuracy and efficiency of implementing the targeted dynamics in Fig. 3.5: As the strength ν in Eq. (3.24) becomes stronger, terms that were not optimized for are scaled up as well. Thus, while dynamics becomes faster, Fig. 3.5 (b), its accuracy decreases as shown for example in the decreasing quality of number conservation in the six-body protocol, Fig. 3.5 (a), which was initially optimized for ideal number conservation. In addition, there may be processes besides those specifically targeted that contribute to the gauge field dynamics,

such as third order processes. We leave as an interesting open question whether an even better tradeoff between accuracy and efficiency for realizing pure gauge field dynamics can be constructed by specifically targeting such processes as well.

3.3.5 Interplay of gauge and matter dynamics

We next investigate the physical consequences of the strong plaquette interactions generated via our Floquet approach. In particular, we are interested in the interplay between dynamical gauge and matter degrees of freedom in this strong coupling regime. For this purpose, we first examine the local relaxation dynamics starting from the non-translationally invariant versions (in contrast to the previous sections) of occupation number initial states $|\psi\rangle$. To quantify their relaxation, we consider the autocorrelation function

$$C_\psi(t) \equiv \frac{1}{N_\psi} \sum_i \left[\langle \psi | \hat{n}_i(t) | \psi \rangle - \langle \hat{n}_i \rangle_{N_\psi} \right] \langle \hat{n}_i \rangle_\psi . \tag{3.27}$$

Here, $\langle \hat{n}_i \rangle_\psi = \langle \psi | \hat{n}_i | \psi \rangle$, and $\langle \hat{n}_i \rangle_{N_\psi}$ denotes the average of $\hat{n}_i$ over the ensemble of all product states $|n\rangle$ with total occupation number $N_n = N_\psi$ equal to the initial state. In a thermalizing system at high temperature but with number conservation, we expect $C_\psi(t \to \infty) = 0$ at long times. We show $C_\psi(t)$ starting from $|\psi_1\rangle$ and $|\psi_2\rangle$ containing no charge excitations and a pair of charges, respectively, in Fig. 3.6 (a-c). Crucially, we observe that while a static approach leads to a large separation of timescales in the decay of $C_{\psi_1}(t)$ and $C_{\psi_2}(t)$ (Fig. 3.6 (a)), both initial states relax on comparable times in the Floquet protocols introduced in Sec. 3.3.3 and Sec. 3.3.4 (Fig. 3.6 (b-c)). The more oscillatory character of $C_{\psi_1}(t)$ compared to $C_{\psi_2}(t)$ is likely due to the smaller Hilbert space of fully packed dimer states, and thus a finite size effect. We further

show that computational basis snapshot measurements provide a qualitative view into the mechanism by which gauge field dynamics is generated in each protocol[663].

For initial states containing matter excitations, the balance between gauge and matter field couplings results in a dynamical competition that can be diagnosed by the local plaquette operators

$$\hat{X}_p \equiv \hat{\sigma}^x_{p_1}\hat{\sigma}^y_{p_2}\hat{\sigma}^y_{p_3}\hat{\sigma}^y_{p_4}\hat{\sigma}^y_{p_5}\hat{\sigma}^y_{p_6}. \tag{3.28}$$

We note that $\hat{X}_p$ is different from the operators $\hat{O}_{\gamma=6}$ appearing in the effective Hamiltonian. In particular, the presence of $\hat{O}_\gamma$ in $\hat{\mathcal{H}}$ will generate a large expectation value of $\hat{X}_p$ for plaquettes initially in a flippable product state configuration. By evaluating the strongest plaquette resonance in the system, $\max_p |\langle \hat{X}_p \rangle (t)|$, we show in Fig. 3.6 (a-c) (right panels) that this is indeed the case in the dynamics from the fully packed dimer initial state $|\psi_1\rangle$. However, starting from the state $|\psi_2\rangle$ with matter excitations, no such plaquette resonances build up for quenches under a static detuning, Fig. 3.6 (a). This is due to charge hopping dynamics dominating the weak pure gauge interactions. In contrast, starting from $|\psi_2\rangle$ in our Floquet protocols, Fig. 3.6 (b,c) demonstrate that significant plaquette resonances still appear at early times before eventual relaxation to a homogenous state. This picture is further substantiated by the real-space resolved dynamics of the local densities $\hat{n}_i$ and plaquette resonances $\hat{X}_p$ displayed in Fig. 3.6 (d-f). In the static setting, Fig. 3.6 (d), $|\psi_1(t)\rangle$ exhibits a strong memory of the initial state $|\psi_1\rangle$ at times where $|\psi_2(t)\rangle$ quickly relaxes to a homogenous distribution of $\langle \hat{n}_i \rangle$. $|\psi_2(t)\rangle$ does not feature significant plaquette resonances $\langle \hat{X}_p \rangle$ at any location in the system. In the Floquet approach, Fig. 3.6 (e,f), $|\psi_1(t)\rangle$ develops strong resonances for plaquettes initially in a flippable configuration and reaches a ho-

mogenous distribution of $\langle \hat{n}_i \rangle$ at similar times as $|\psi_2(t)\rangle$, see in particular Fig. 3.6 (f). $|\psi_2(t)\rangle$ still develops significant resonances $\langle \hat{X}_p \rangle$ at plaquettes initally in a flippable configuration, demonstrating the competition between gauge and matter dynamics.

3.4 Prospects for experimental realizations

The scheme developed in our work relies on relatively simple control provided by a global detuning field, which is readily available in state-of-the-art Rydberg quantum simulators. In addition, we have identified promising protocols, such as the three-body scheme investigated in Sec. 3.3.4, which display non-trivial gauge field dynamics already at times of a few decades in units of $1/\Omega$. Assuming a Rabi frequency of $\Omega = 2\pi \times 3.0\text{MHz}$ and a coherence time of $\tau_c = 1\mu\text{s}$, these interactions, as well as their interplay with dynamical matter degrees of freedom, are accessible with present-day hardware. Moreover, as pointed out in Secs. 3.2.3,3.3.4, our approach exhibits a tradeoff between supressing unwanted terms and generating fast dynamics, such that the targeted processes may be enhanced to even earlier times by partially relaxing the high quality of Rydberg number conservation. A more detailed analysis of the effects of noise and other experimental imperfections on our Floquet protocol, in particular for potential heating, is left for future work.

In addition, while we consider a nearest-neighbor blockaded PXP-setup throughout most of this work, a significant aspect of realistic hardware is the presence of long-range tails in the van-der-Waals interactions of the Rydberg Hamiltonian $\hat{H}_{\text{Ryd}}$,

$$\begin{aligned} \hat{H}_{\text{Ryd}}(t) &= \frac{\Omega}{2} \sum_i \hat{\sigma}_i^x - \Delta(t)\hat{N} + \hat{V}_{\text{vdW}} \\ \hat{V}_{\text{vdW}} &= \sum_{i,j} V_{ij}\, \hat{n}_i \hat{n}_j = \sum_{i,j} \Omega \left(\frac{R_b}{r_{ij}} \right)^6 \hat{n}_i \hat{n}_j, \end{aligned} \tag{3.29}$$

where R_b denotes the blockade radius. When contributions to V_{vdW} from sites i,j with $r_{ij} > R_b$ are sufficiently small, such long-range terms can be incoporated as additional interactions (conjugated by PXP-evolution) in our formulation of the effective Hamiltonian. They can furthermore be partially counteracted with a constant mean field shift of the global detuning[571]. However, while contributions from long-range tails may be reduced by lowering the blockade radius R_b, this also leads to a decrease of the energy penalty for nearest-neighbor blockade violations, which constitute another source of perturbation to our scheme. Thus, upon tuning R_b, there is a tradeoff in the severity of long-range tails and blockade violations, and both must be considered jointly in a realistic treatment of our approach for experimental setups. We further emphasize that these perturbations depend on the geometry of the setup and we generally expect them to be smaller in one dimension and on two-dimensional lattices with a small ratio of nearest- to next-nearest-neighbor distances[571]. This suggests that the hexagonal lattice and the Kagome geometry considered in this work are good candidates for two-dimensional realizations.

Finally, although we previously considered infinitely sharp detuning pulses, we should use finite-width pulses in experimental settings. Small deviations from the idealized delta-shape can again be straightforwardly incorporated as contributions to the effective Hamiltonian in our approach, and will depend both on the location and precise shape of the pulses. A realistic pulse duration for experimental realizations ranges around $\tau_{\mathrm{pulse}} = 20\mathrm{ns}$. With the above Rabi frequency, $\Omega\tau_{\mathrm{pulse}} \approx 0.4$, and the pulse width does account for a sizeable fraction of the Floquet period $2\Omega\tau = 4.0$ chosen in our three-body protocol. This suggests that the broadened pulses will contribute substantially to the resulting effective Hamiltonian. However, strong contributions from broadened pulses do not per se run counter to our approach: For pulses at even

multiples $2m\tau$ of the pulse period τ, deviations from a delta-shape primarily induce contributions to the effective Hamiltonian from $\hat{N}_0(t)$ within a pulse-width of time zero. Per Fig. 3.2 (c), $\hat{N}_0(0 < t < \tau_{\text{pulse}}/2)$ is dominated by the number operator $\hat{N}$, leading to an effective detuning contribution that is desirable in our approach, as it enforces Rydberg number conservation. Moreover, for the three-body protocol with $\Omega\tau = 2.0$, broadened pulses at odd multiples $(2m+1)\tau$ of τ yield contributions of the operators $\hat{N}_0(\tau - \tau_{\text{pulse}}/2 < t < \tau)$ to $\hat{\mathcal{H}}$. Fig. 3.2 (c) shows that such terms are associated with sizeable three- and two-body interactions but only small single spin-flip contributions; they can thus be used to realize the strong three-body dynamics targeted in Sec. 3.3.4. Therefore, we may partially view these experimental demands as additional restrictions on the echo-perturbing detuning profiles $\Delta_p(t)$ that can be implemented in practice. Integrating these experimental restrictions into our optimization procedure is an important avenue for future work. In addition, we note that a finite pulse duration may further be helpful to prevent an abundance of blockade violations, as sharp pulses contain high-frequency components that may resonantly couple to blockade-violating states. A more detailed analysis that combines our approach with $\hat{H}_{\text{Ryd}}$ of Eq. (3.29) beyond the approximation of a blockaded Hilbert space and with the full set of experimental constraints on the time-dependent detuning $\Delta(t)$ is left for future work.

3.5 Discussion & Outlook

We have introduced and analyzed a new method for realizing dynamical gauge theories with strong multi-body interactions in periodically driven systems with nearest-neighbor Rydberg blockade. The key ingredient is a many-body echo realized upon

applying a simple global detuning pulse. The micromotion between pulses is then used a resource for operator spreading, which contributes tunable multi-body interactions to an effective Hamiltonian. The latter can be steered towards a given target upon selecting suitable perturbations around the ideal echo point. Using this approach, we constructed effective Hamiltonians of a two-dimensional $U(1)$ lattice gauge theory and demonstrated access to previously unexplored regimes. In particular, this allows us to combine a high quality of particle number conservation with strong six-body magnetic plaquette terms on par with two-body particle hopping processes, a constellation that is otherwise challenging to realize in analog simulation.

Our approach builds on a number of key concepts in the field of quantum many-body dynamics, such as Floquet engineering, operator spreading, or prethermalization, and exhibits connections to quantum many-body scars and discrete time crystals[830,756,652,1008]. On the one hand, it yields new insights on the dynamics of periodically driven many-body systems far from equilibrium. On the other, it combines these concepts to create a new quantum simulation tool that extends the capabilities of systems with Rydberg blockade interactions and enables experimental applications.

Our results can be extended along several promising directions. In particular, the many-body echo considered here is only one of (infinitely) many possible approaches. We recall that Eq. (3.6) considers only profiles $\Delta_p(t)$ symmetric around $t = \tau$. Contributions to $\Delta_p(t)$ that are antisymmetric around τ may be absorbed into a new echo evolution $\hat{U}'_e(t)$, leading to differently time-evolved operators in $\hat{\mathcal{H}}$ upon introducing perturbations. In addition, the timing of π-pulses as in Fig. 5.1 (b) may be shifted, giving rise to effective models $\hat{\mathcal{H}} \sim \int_{-\tau_-}^{\tau_+} dt\, \Delta_p(t)\hat{N}_0(t)$ with $\hat{N}_0(t)$ evaluated at negative times. Moreover, larger system sizes and longer evolution times may be analyzed by combining our approach with tensor network methods[980,922,874,708] to compute

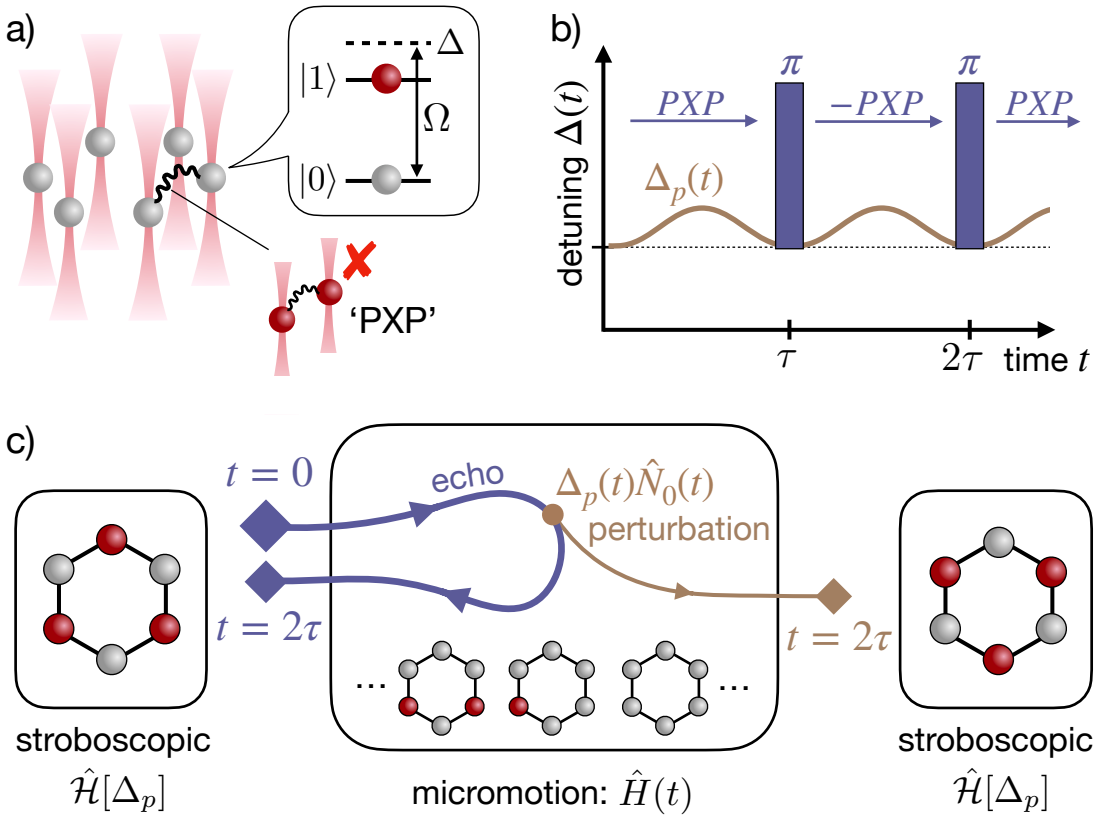
the time-evolved local operators $\hat{n}_i(t)$, for example as matrix product operators. Furthermore, we note that our scheme applies equally to systems with Rydberg blockade beyond nearest neighbors and systems with site-dependent detuning fields[824], which allows for the simulation of lattice gauge theories beyond the example studied in this work.

While we focused on nonequilibrium dynamics of the resulting effective Hamiltonian for high-energy initial states, future work may address ground state properties or exotic low-energy dynamics of models that can arise in our Floquet protocol[782,664]. In particular, it would be interesting to determine the presence of ground state phases that are stabilized by multi-body ring-exchange terms, such as plaquette valence bond solids[853] or even topological spin liquid phases[849,972,935,770]. A related question concerns the preparation of low energy states of the effective Hamiltonian, potentially by exploring connections to counterdiabatic driving schemes[559,932,615]. In addition, our protocol unlocks the simulation of blockaded systems with conserved Rydberg number more generally. In Ref.[779] we show that this allows for probing gapless phases of matter and the construction of Hamiltonians that generate multi-partite entanglement starting from simple product initial states.

Finally, we note that our method involving the perturbation around periodically reviving many-body trajectories can be applied to other experimental systems beyond Rydberg atom arrays. Time-periodic many-body dynamics is commonly employed in dipolar-interacting quantum systems[990,992,609,1017,678], and can be implemented, for instance, in neutral atoms in optical lattices and cavities[804,619], in trapped ions[677,681], or digitally in superconducting devices[564,841,579]. Furthermore, state-dependent periodic revivals occur in systems with quantum-many body scars[556,571]. Devising Hamiltonian engineering protocols for such systems, analogous to the present work, is a

promising direction for future work.

We thank Dolev Bluvstein, Sepehr Ebadi, Simon Evered, Alexandra Geim, Sophie Li, Marcin Kalinowski, Tom Manovitz, Roger Melko, Simone Notarnicola, Hannes Pichler, Maksym Serbyn, Norman Yao, and Peter Zoller for insightful discussions. We acknowledge financial support from the US Department of Energy (DOE Gauge-Gravity, grant number DE-SC0021013, and DOE Quantum Systems Accelerator, grant number DE-AC02-05CH11231), the National Science Foundation (grant number PHY-2012023), the Center for Ultracold Atoms (an NSF Physics Frontiers Center), the DARPA ONISQ program (grant number W911NF2010021), the DARPA IMPAQT program (grant number HR0011-23-3-0030), and the Army Research Office MURI (grant number W911NF2010082). J.F. acknowledges support from the Harvard Quantum Initiative Postdoctoral Fellowship in Science and Engineering. N.M. acknowledges support by the Department of Energy Computational Science Graduate Fellowship under award number DE-SC0021110. N.U.K. acknowledges support from The AWS Generation Q Fund at the Harvard Quantum Initiative.



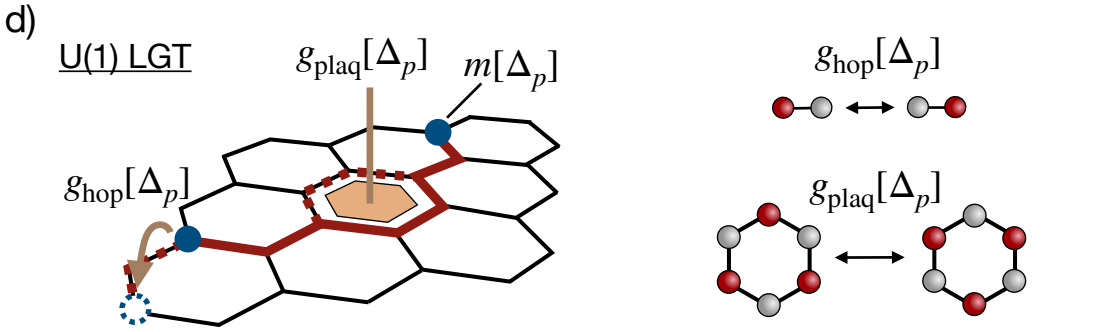


Figure 3.1: Hamiltonian engineering and gauge theories. a) We consider PXP models as an approximate description of Rydberg atoms in optical tweezers. b) Due to blockade, simple global detuning π-pulses reverse the direction of time evolution, leading to an effective many-body echo. c) Introducing detuning perturbations $\Delta_p(t)$ around this echo realizes an effective Hamiltonian that consists of the time-evolved Rydberg number operators $\hat{N}_0(t)$. The spreading of this operator leads to multi-body interactions in the effective Hamiltonian. Intuitively, for an optimized choice of $\Delta_p(t)$, part of the wave function 'scatters' into a desired final state, realizing a coherent interaction term. d) Our approach can be applied to study lattice gauge theories, where multi-body plaquette terms are required to realize dynamical gauge fields. We achieve increased flexibility in tuning the relative strength of various interactions, enabling access to regimes previously difficult to realize.

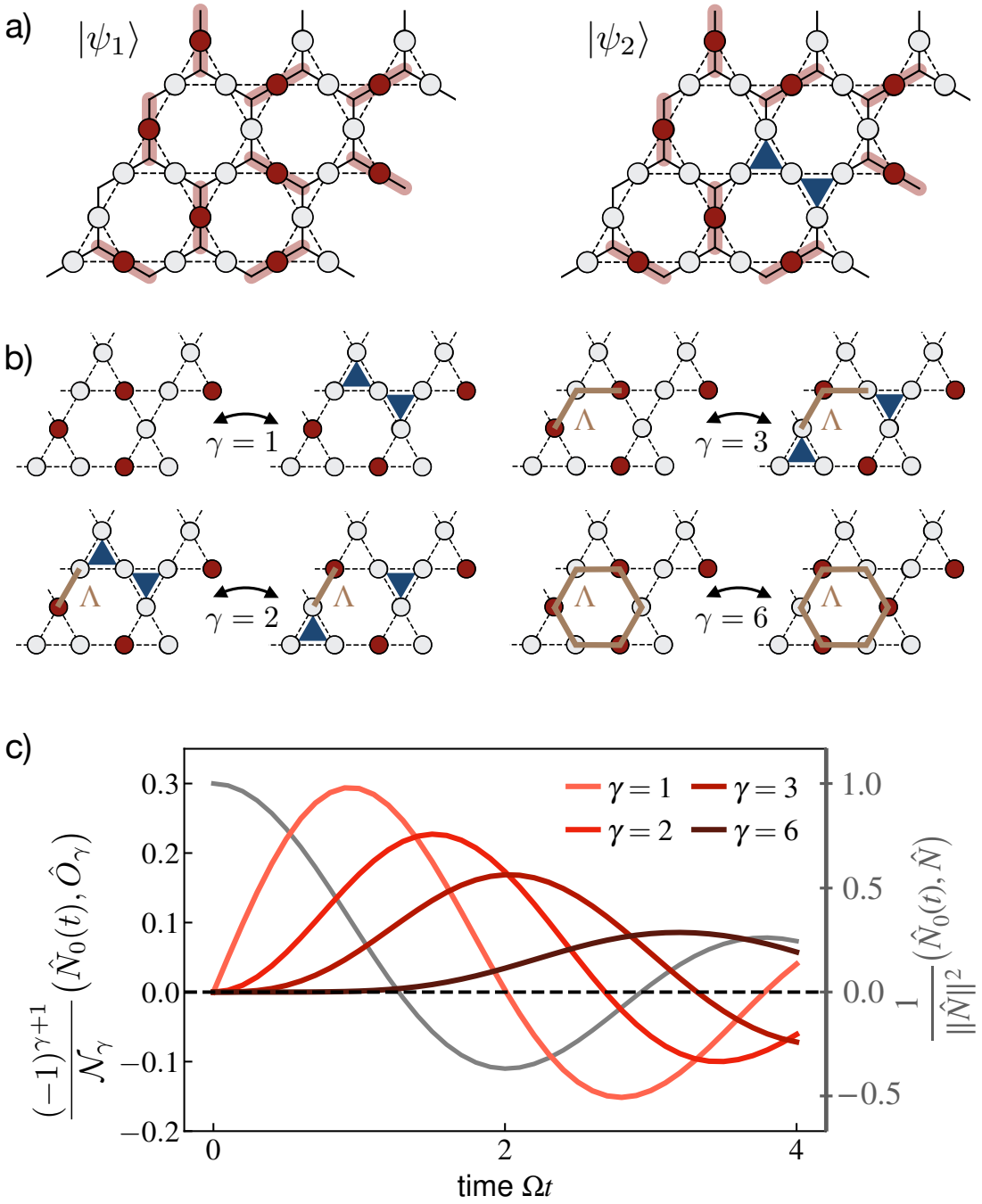


Figure 3.2: Kagome lattice PXP model. a) We numerically study a PXP model on a Kagome lattice of 3×3 unit cells. Each elementary triangle hosts at most one excited spin (full circles) due to nearest neighbor blockade. Left: States with maximum number of excited spins map to close-packed dimer states on the honeycomb lattice, yielding a $U(1)$ gauge theory. Shown is a specific example $|\psi_1\rangle$. Right: Triangles without excited spins are created in pairs and correspond to charged matter excitations under this $U(1)$ gauge field. The depicted state $|\psi_2\rangle$ contains a pair of charges. b) Dynamical processes of increasing (off-diagonal) operator weight γ. $\gamma = 2$ corresponds to hopping of charges, $\gamma = 6$ to plaquette terms that generate pure gauge field dynamics; $\gamma = 1$ and $\gamma = 3$ create/annihilate pairs of charges. c) Overlap of the time evolved operator $\hat{N}_0(t)$ with the off-diagonal operators illustrated in b). For intermediate times, $\hat{N}_0(t)$ develops significant overlap with off-diagonal processes beyond single spin flips.

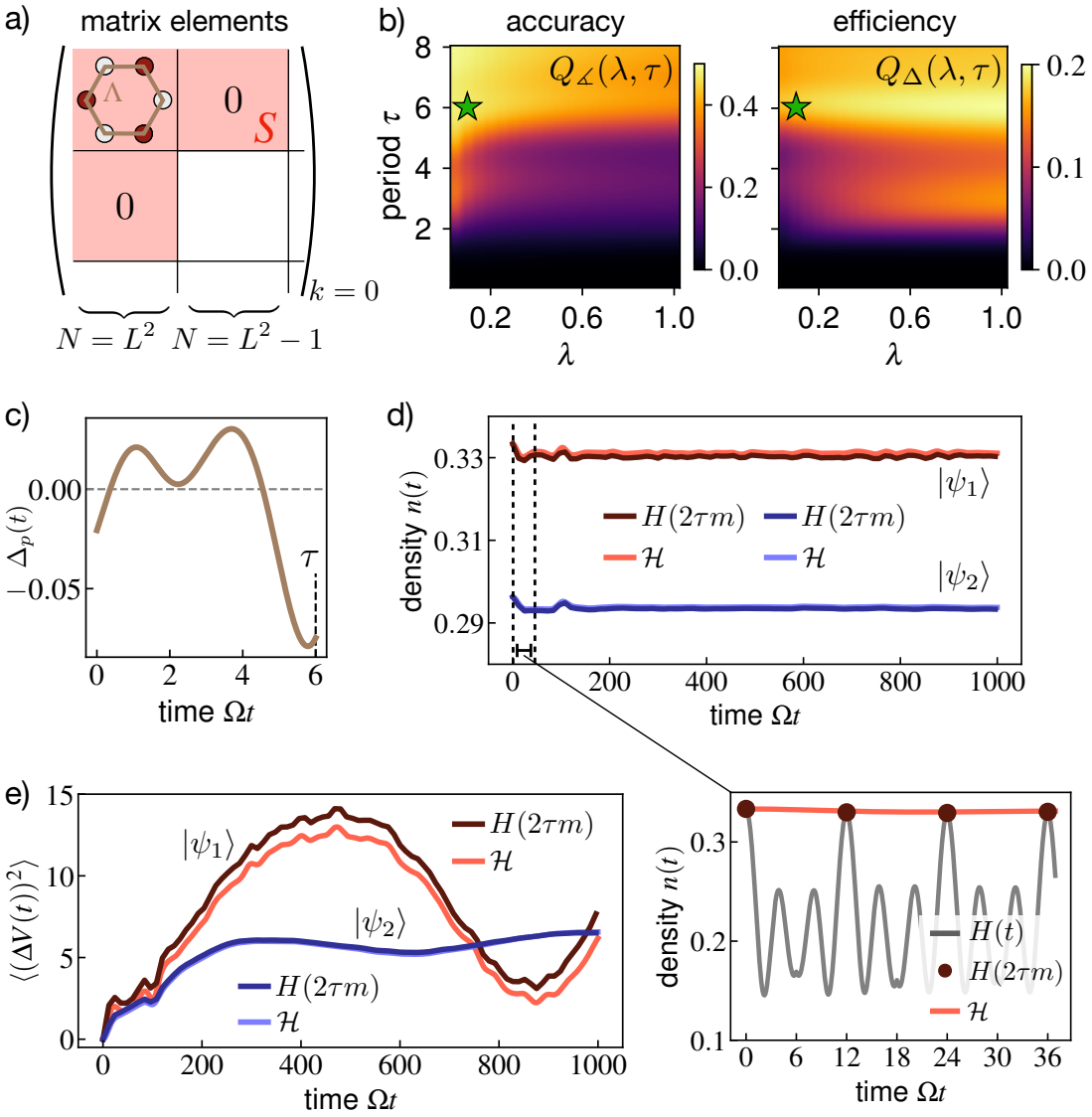


Figure 3.3: Engineering six-body terms. a) We optimize the effective Hamiltonian in the $k = 0$ momentum sector with respect to the matrix elements S of Eq. (3.20). Within the subspace of dimer states with $N = L^2$ excited spins, we optimize towards six-body plaquette terms while minimizing all number-changing matrix elements. b) The optimization is carried out for different values of the Floquet period τ and the detuning cost λ. We fix values (marked with a green star) where both the alignment with the target matrix elements $Q_\measuredangle(\lambda, \tau)$, as well as the target strength per amount of detuning $Q_\Delta(\lambda, \tau)$ for the corresponding effective Hamiltonian are large. c) The resulting, optimized detuning profile for $\Omega\tau = 6, \lambda = 0.1$. d) Time evolution of the Rydberg number density $n(t)$, starting from $|\psi_1\rangle$ (red) and $|\psi_2\rangle$ (blue), see Fig. 3.2 (a). Under $\Delta_p(t)$ of c) and discrete pulses described in the main text, number conservation is strongly broken in the micromotion (see inset), but highly accurate at multiples of the stroboscopic time $2\Omega\tau = 12$, in agreement with dynamics under the effective Hamiltonian $\hat{\mathcal{H}}$. e) Dynamics of the variance $(\Delta V(t))^2$ of next-nearest-neighbor excitations, Eq. (3.23). Oscillations in $(\Delta V(t))^2$ for $|\psi_1\rangle$ (red) mark the onset of plaquette dynamics, while $|\psi_2\rangle$ (blue) includes the dynamics of charged matter excitations.

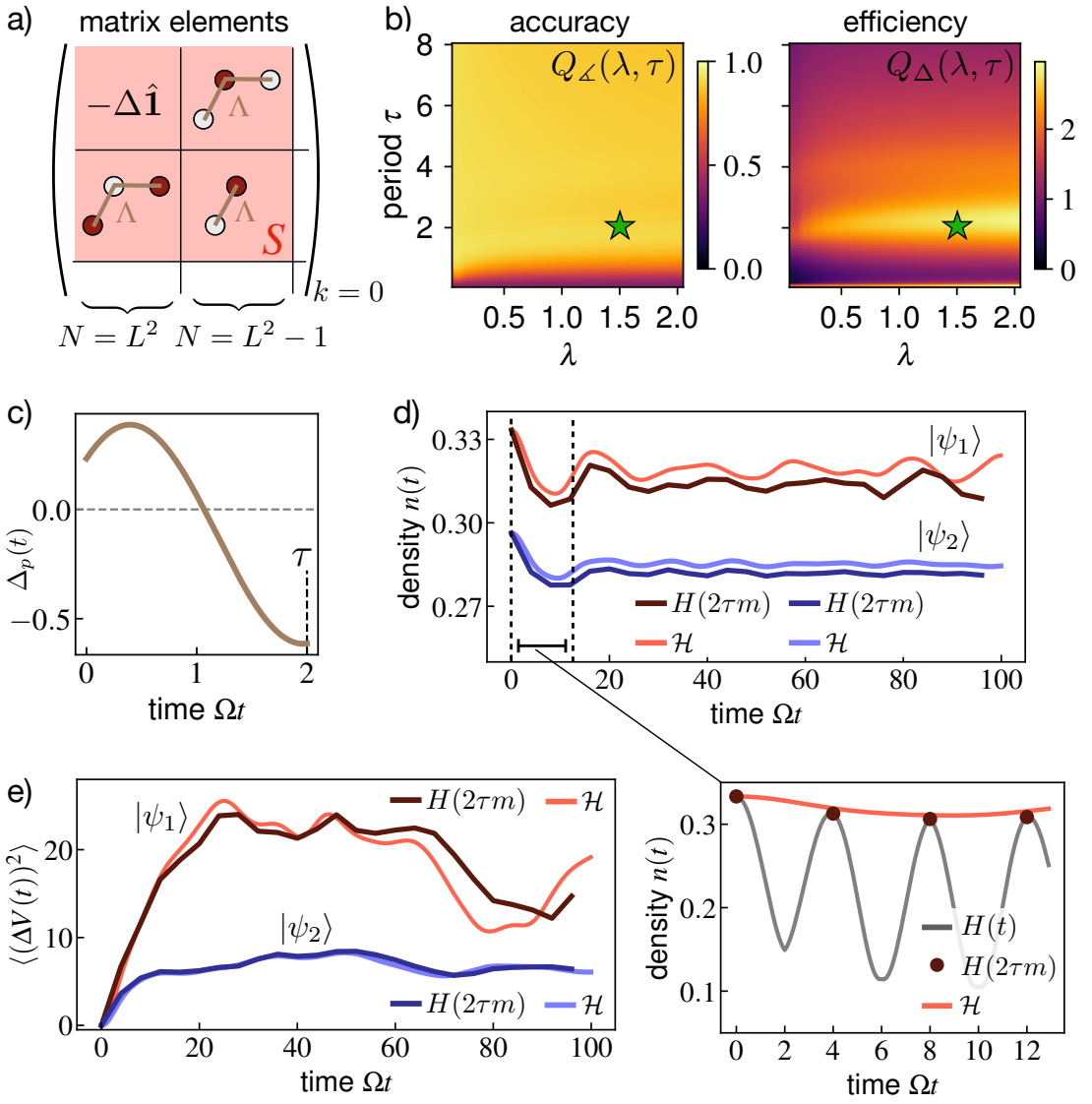


Figure 3.4: Engineering three-body terms. a) Optimization of $\hat{\mathcal{H}}$ in the $k = 0$ momentum sector with respect to the matrix elements S of Eq. (3.25). Within the subspace of states with $N = L^2$ or $N = L^2 - 1$ excited spins, we optimize towards three-body number-changing terms, two-body hopping processes for charged matter excitations, and a detuning contribution. b) Optimization across different values of period τ and detuning cost λ. We fix values marked with a green star, where both $Q_\measuredangle(\lambda,\tau)$ and $Q_\Delta(\lambda,\tau)$ (see Eqs. (3.10,3.11)) are large. Due to optimization for lower-weight terms compared to Fig. 3.3, smaller periods τ are sufficient. c) Optimized detuning profile for $\Omega\tau = 2, \lambda = 1.5$. d) Time evolution of the density $n(t)$ starting from $|\psi_1\rangle$ and $|\psi_2\rangle$ (see Fig. 3.2 (a)). Stroboscopic number conservation remains robust, and agreement with effective Hamiltonian dynamics remains accurate at early times. Inset: Micromotion of the density in between stroboscopic times. e) The variance $(\Delta V(t))^2$ shows non-trivial dynamics for both $|\psi_1\rangle$ (red) and $|\psi_2\rangle$ (blue) already on intermediate timescales, indicating the presence of strong effective six-body dynamics induced by three-body interactions.

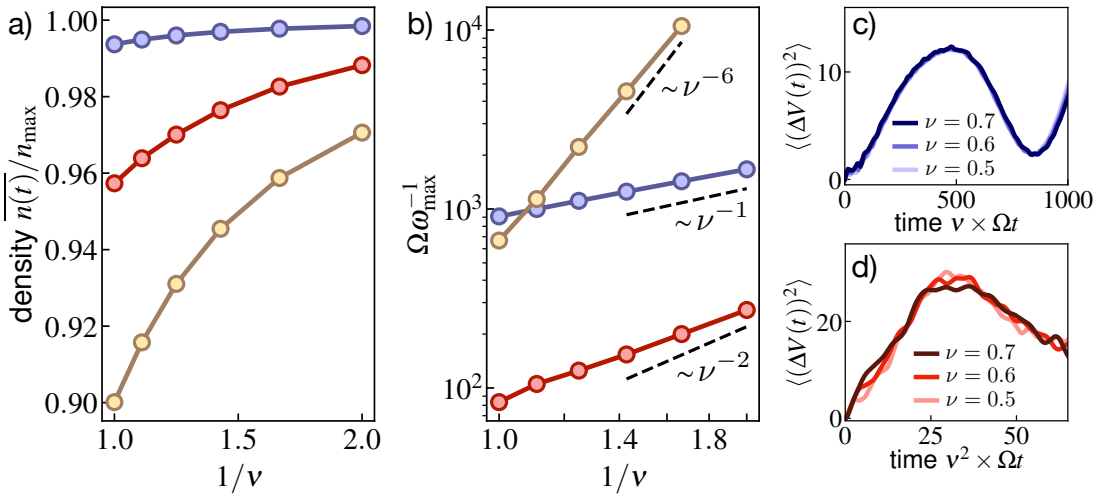


Figure 3.5: Effective Hamiltonian dynamics. Dynamics of dimer state $|\psi_1\rangle$ under $\hat{\mathcal{H}}(\nu)$ of Eq. (3.24), which rescales the all terms in $\hat{\mathcal{H}}$ orthogonal to $\hat{N}$ by a factor ν. a) Long-time average $\overline{n(t)}$ of the density as a function of ν for the six-body protocol outlined in Sec. 3.3.3 (blue), the three-body protocol of Sec. 3.3.4 (red), and a static PXP model at $\Delta/\Omega = 2.0$ (yellow). b) Dominant frequency $\omega_{\max}$ in the dynamics of the variance $(\Delta V(t))^2$. The observed scalings $\omega_{\max} \sim \nu, \nu^2, \nu^6$ are consistent with dominant six-body, three-body and single-body terms, respectively. c)+d) Scaling collapse of early time dynamics of $(\Delta V(t))^2$ for six- and three-body protocols.

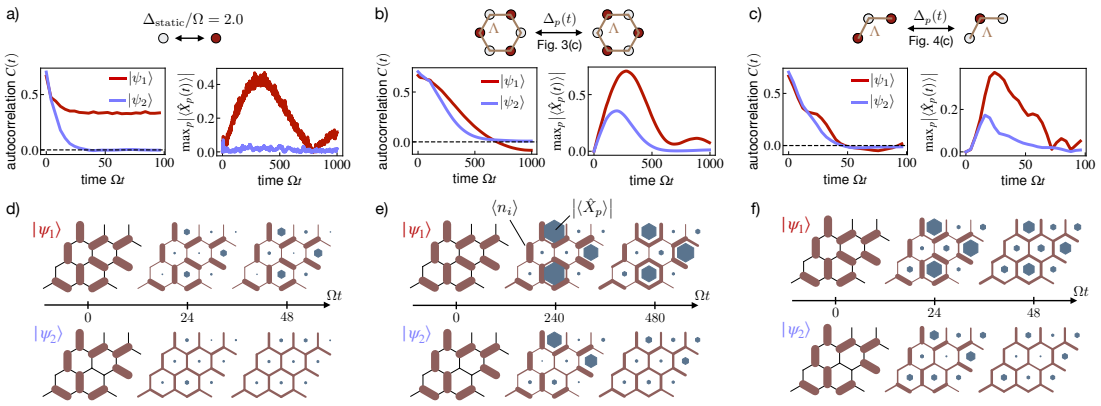


Figure 3.6: Local quantum dynamics. a)-c) (left panels) We characterize the time evolution of local observables for a constant static detuning $\Delta_{\text{static}}/\Omega = 2.0$ and the Floquet protocols of Sec. 3.3.3 and Sec. 3.3.4. In the static setting a), the autocorrelation $C(t)$ (see Eq. (3.27)) of local densities exhibits a large separation of timescales between the fully packed dimer initial state $|\psi_1\rangle$ and the initial state $|\psi_2\rangle$ containing a pair of charge excitations. In contrast, the autocorrelation function of both initial states decays on similar timescales in our Floquet protocols b)+c), indicating comparable coupling strengths of pure gauge and matter dynamics. a)-c) (right panels) Time evolution of the strongest plaquette resonance $\max_p |\langle \hat{X} \rangle_p|$ in the system (see Eq. (3.28)). For the dimer initial state $|\psi_1\rangle$, signifcant resonances eventually develop in all protocols. For $|\psi_2\rangle$, the resonances are lost due to dominant matter hopping processes in the static case a), but persist in the strongly coupled Floquet schemes of b) and c). d)-f) Site-resolved dynamics of densities and plaquette expectation values in the protocols of a)-c), respectively. The thickness of the bonds indicates the local Rydberg density $\langle \hat{n}_i \rangle$, the area of the blue hexagons the local plaquette resonance expectation value $|\langle \hat{X}_p \rangle|$. In the static protocol d), the local densities show a strong memory of the dimer initial state $|\psi_1\rangle$, while the state $|\psi_2\rangle$ rapidly becomes homogeneous due to dominant matter dynamics. In contrast, in the Floquet approaches e) and f), both states become homogeneous on roughly similar time scales and develop plaquette resonances even in the presence of matter excitations. The protocol shown in f) achieves this on relatively short time scales.

4

Enhancing Detection of Topological Order by Local Error Correction

Topological ordering is an exotic phenomenon which can occur when quantum fluctuations and local constraints stabilize a state with long-range entanglement[995]. With their non-local correlations, topologically-ordered states feature many remarkable properties and can be used for protecting quantum information non-locally[995,866,963]. Yet, because these states appear to be liquid-like at short length-scales[903], they cannot be identified or characterized using any local order parameters. Instead, the canonical approach to discern topological order is to measure operators supported on large

closed loops, the Wilson loops[705,998,995,693]. However, such operators are challenging to identify or measure: while they have simple forms in certain fixed-point models, this is generally not the case for states realized experimentally in the presence of noise or other perturbations. In these cases, the expectation values of the simple or 'bare' Wilson loop operators described above decay exponentially with the loop's perimeter, which hinders the experimental certification of topological order.

To address these challenges, several methods have been developed to construct 'fattened' Wilson loops which do not decay with loop size. These include a systematic method utilizing quasi-adiabatic connections to the fixed-point models[705], as well as variational and tensor-network-based approaches[582,727,642,733]. Nevertheless, these methods are challenging to apply in realistic experiments, especially in the presence of incoherent noise (e.g., spontaneous emission). Other signatures, such as topological entanglement entropy[764,790] are likewise difficult to measure in large systems.

Motivated by these considerations, we introduce a powerful framework, locally error-corrected decoration (LED), for studying and characterizing topologically-ordered states. By leveraging the error-correcting properties of topological phases, LED provides a systematic method to construct and efficiently measure 'decorated' Wilson loop operators, a variant of the fattened loop operators. This enables the identification and characterization of topological order at large length-scales in the presence of both coherent perturbations and incoherent noise, which are particularly challenging or impossible using conventional methods.

In its most general form, LED corresponds to a class of hierarchically-structured quantum circuits which resemble the classification of quantum phases using RG flow[924,603]. Yet, for a wide range of experiments where the prepared state is known to approximate a fixed-point state with zero correlation length (see Supplementary Informa-

tion), there is an efficient 'snapshot-based' realization of LED using only classical post-processing of experimental measurements in a few fixed bases. In this work, we primarily focus on snapshot-based LED due to current experimental limitations and the hardness of simulating 2D quantum circuits.

4.1 LED Approach

The key idea of LED can be understood by considering Kitaev's toric code model, a canonical example of topological order. Specifically, we consider qubits localized on the edges of a square lattice. The ideal, fixed-point Hamiltonian is defined as[759]:

$$H_{\mathrm{TC}} = -J\sum_{v} A_v - J\sum_{p} B_p \tag{4.1}$$

where $A_v = \prod_{i\in \mathrm{adj}(v)} X_i$, $B_p = \prod_{i\in \mathrm{adj}(p)} Z_i$, and $\mathrm{adj}(v)$ (resp., $\mathrm{adj}(p)$) denote the set of edges touching a given vertex v (plaquette p) of the lattice. The ground state space, given by the simultaneous $+1$ eigenspace of all stabilizer operators $\{A_v, B_p\}$, forms a quantum error-correcting code: all local operators either act trivially on ground states or couple them to excited states[759]. By measuring stabilizers, one can detect the presence of excitations and apply a recovery procedure to return the system back to this ground state space.

In this model, contractible Wilson loops can be constructed by multiplying stabilizers, so their expectation values in any ground state of H_{TC} are $+1$, independent of loop size. However, in realistic situations, the prepared state differs from the fixed-point state by local fluctuations such as coherent perturbations and incoherent errors (Figure 8.1a). This causes bare Wilson loops to decay exponentially with the number

of locations where a fluctuation can intersect the loop (i.e., its perimeter).

The snapshot-based LED approach begins with a measurement of all qubits in the same (Pauli-Z or Pauli-X) basis. For each measurement snapshot, one can calculate the stabilizer and Wilson loop values. Local fluctuations appear as stabilizer violations, which are identified with anyonic excitations[759] (Figure 8.1b). A local decoder partially removes such fluctuations by flipping measured qubits using only nearby stabilizer values. The simplest such local decoder can remove single-qubit errors, by flipping a qubit if and only if both adjacent vertices (resp., plaquettes) are occupied by an m (e-anyon). However, it cannot remove higher-weight errors, which flip two or more adjacent qubits. Subsequently, the lattice is coarse-grained, which can also be done efficiently on measurement snapshots (see methods). Together, the anyon-pairing and coarse-graining steps are repeated for n layers. Crucially, the weight of uncorrected errors is reduced in each layer, so that all local errors eventually become single-qubit errors which the decoder can correct; this mimics a real-space RG flow towards the fluctuation-free fixed-point state (see Methods). Finally, a bare Wilson loop is measured on the final, corrected and coarse-grained state (Figure 8.1b).

This bare operator measured on the final state is equivalent to a decorated Wilson loop operator measured on the original state (Figure 8.1). Moreover, it is determined solely by the fixed-point state and is independent of the specific fluctuations in the system; this crucially differentiates LED from prior approaches to construct fattened loop operators[705,582,727]. Notice that all steps in snapshot-based LED can be performed in post-processing (see Methods), making it uniquely suited for integration into experimental measurement procedures. More general LED operators can be constructed through the quantum circuit formulation; one example is presented in the Supplementary Information.

The hierarchical LED procedure is also inspired by the quantum convolutional neural network (QCNN) approach to phase classification, and the decorated Wilson loop operators resemble the multiscale string order parameters studied in Ref.[620]. However, in this context, the LED framework is more general: one can construct LED Wilson operators of diameter L with any desired correction distance $d \ll L$ (Figure 8.2a) by choosing any local decoder which pairs anyons up to distance d (see Methods). The construction of Figure 8.1b with alternating local-decoding and coarse-graining layers is a particularly efficient way to construct local decoders and LED loops with longer-range (e.g., $d, L \propto 2^n$).

We emphasize that the locality of our procedure ensures that only topologically-ordered states can flow to the fixed-point state. Thus, LED gives rise to a sufficient condition or witness for topological order. This distinguishes LED from general decoders, which do not typically respect locality and hence cannot be used to certify topological order.

4.2 Numerical Detection of Topological Order with Coherent Perturbations

To demonstrate the applicability of LED for coherent local perturbations to H_{TC}, we consider a family of states

$$|\psi(g_X, g_Z)\rangle = \frac{1}{\mathcal{N}} e^{g_X \sum_i X_i + g_Z \sum_i Z_i} |\psi_{\mathrm{TC}}\rangle , \tag{4.2}$$

generated by imaginary-time evolution of a toric code ground state $|\psi_{\mathrm{TC}}\rangle$[602,695,1021]. As each operator Z_i (resp., X_i) creates a pair of m anyons (e anyons), $|\psi(g_X, g_Z)\rangle$ contains virtual anyon fluctuations on top of $|\psi_{\mathrm{TC}}\rangle$. In the special case where $g_X = 0$, topological order is known to survive for perturbations $g_Z \leq g_c = 0.220343$, beyond

which the m-anyons condense, driving a second-order phase transition into the Z-paramagnet state[591]. More generally, $|\psi(g_X \neq 0, g_Z \neq 0)\rangle$ is also topologically-ordered for small g_X and g_Z, but the transitions to paramagnetic phases can occur at points which differ from g_c.

In testing LED, we numerically simulate projective measurements of $|\psi(g_X, g_Z)\rangle$ and use them as input "experimental snapshots" in Figure 8.1b (see Methods). Figure 8.2b shows the value of the LED order parameter for a trivial and a topological state with $g_Z = 0.14$, when n is varied (and $d, L \propto 2^n$). Clearly, the order parameter stays at 0 for the trivial state, but increases from a small, finite value to one for the topological state as n is increased. Similar behavior is also observed throughout a one-dimensional parameter space in Figures 8.2c and 8.2d, whenever the correction distance d is increased, while keeping $d \ll L$ to prevent overcorrection (see Methods). Importantly, amplification occurs only if the input state is topological, and the order parameter approaches 0 for all trivial states.

Another important set of observables for characterizing topological order are X and Z open string operators, which detect the transition from the topological phase to the trivial, paramagnet phase. Because LED Wilson Z-loop operators (resp., X-loop operators) are linear combinations of Z (X) closed loops supported on an annulus, they anti-commute with conjugate X (Z) open strings connecting the interior and exterior of the annulus. As such, the expectation value of any long, open string must flow to zero in the topological phase, whereas closed-loop LED operators flow to unity with increasing d. The topological-to-trivial phase transition occurs when certain long, open X or Z strings acquire non-zero expectation value, due to the condensation of m or e anyons, respectively. Indeed, deep in the paramagnetic phase the state $\lim_{g_x \to \infty} |(g_x, g_z)\rangle$ is polarized along the X direction, and X open strings become

unity. However, for generic trivial states, open strings also decay exponentially with length, due to local fluctuations of the opposite type; nevertheless, LED can still amplify their expectation values by removing the effect of local fluctuations. This behavior is demonstrated in our simulations: in Figure 8.2e,f, open string expectation values stay at 0 in the topological phase, but are amplified and saturate to a non-zero value in the trivial (paramagnetic) phase. Because LED amplifies the contrast between trivial states and a large class of topological states, the topological order can be detected using with lower sample complexity—that is, by using substantially fewer experimental repetitions[620,694] (see Supplementary Information).

Let us note that the boundary dividing the states whose LED operators approach zero and one does not necessarily correspond to the topological phase boundary: in general, it depends on the choice of decoder and coarse-graining length-scale. For instance, this is observed in Figure 8.2g, where closed loops are nearly one after $n = 3$ layers for a large region within, but not fully encompassing, the topological phase. Hence, LED is not always a necessary condition for topological order.

4.3 Effect of Incoherent Errors

We next demonstrate the application of LED in the presence of incoherent local noise such as spontaneous emission or dephasing, which commonly occur in experiments. Because local decoders can recover topologically encoded information in the presence of small, local error channels[634,764] it is reasonable to ask whether mixed states prepared in these systems exhibit topological ordering.

To study such examples, we introduce incoherent bit- and phase-flip errors by independently flipping, with probability p_{flip}, each measured qubit in a snapshot of

$|\psi(g_X, g_Z)\rangle$. Here, we associate topological order with states that can be transformed into a ground state of H_{TC} via local operations. Our analysis then suggests that the resulting mixed-state phase space contains a $\mathbb{Z}_2$-topological phase, a Z-paramagnet, an X-paramagnet, and a disordered phase with large incoherent error rates. However, it is especially difficult to distinguish the topological and disordered phases using measurements of bare operators alone: in both phases, open strings remain close to zero, while bare Wilson loops decay exponentially with perimeter as $e^{-\alpha L}$, where the exponent α interpolates smoothly between the phases (Figure 8.3a,b). This is in contrast to the paramagnet phases, where closed loops exhibit similar behavior, but certain open strings decay with the same exponent α as the closed loops[673].

Upon studying the behavior of LED operators, one finds that the mixed-state phase space exhibits two qualitatively different regimes (Figure 8.3b). LED reduces α to 0 with increasing d in the 'correctable' regime, while α grows in the 'uncorrectable' regime. Further, correctable states with small p_{flip} are connected to topologically-ordered pure states, suggesting these mixed states are topologically-ordered as well. Indeed, we show that correctability implies the input state cannot be prepared from a product state using only local operations. In particular, if LED Wilson loops are amplified to above $1-\varepsilon$ under depth d correction, this certifies topological order up to length-scale $O(\mathscr{L}-d)$ where $\mathscr{L} \sim 1/\sqrt{\varepsilon}$. Furthermore, we argue (see Methods) that, under plausible conditions, this implies the entanglement negativity of the input state contains a topological term; this connects the LED characterization of mixed state topological order to other studies [884,717,786].

The ability of LED to distinguish between the topological and disordered phases can be understood by analogy to quantum error correction. Conceptually, since any given LED loop operator is supported on an annulus, we can consider this opera-

tor as being embedded in a surface code on this annulus with open boundary conditions, which supports a logical qubit. Then, an LED Z-loop operator corresponds to a logical-Z operator for this qubit, while an X-string connecting the interior of the annulus to the exterior corresponds to a logical-X operator (see Figure 8.2a). In this framework, the decay rate α of Wilson loops corresponds to a local logical error rate per unit length, and in the correctable phase, LED-based decoding succeeds with high probability as long as the code distance d is sufficiently large (Figure 8.3c). However, in the uncorrectable phase, such as when p_{flip} is above the error correction threshold or when long, open strings condense in a paramagnetic phase, decoding cannot correctly pair anyons, resulting in a high rate of logical errors[634].

The above results are deeply rooted in the stability of topological order against local perturbations. In contrast, any finite temperature destroys long-range topological order as it leads to freely propagating thermal anyons. In Figure 8.3d, we consider the toric code model at finite temperature, with local incoherent errors, and find that the LED loop operators indeed approach zero upon increasing n. Interestingly, their expectation values flow non-monotonically, being amplified at small n before eventually turning to 0. This occurs because of a competition between two effects: thermal anyons are uncorrectable, so their density accumulates under RG flow; however, local fluctuations are corrected at early layers, which initially amplifies LED loop expectation values. Because loops at different n probe correlations at different length-scales, the turning point in these curves can be used to identify the characteristic length-scale of separation between thermal anyons, or equivalently, the system's temperature.

4.4 Experimental Realization in Rydberg Atom Arrays

We now use LED to characterize and provide new insights into the $\mathbb{Z}_2$-topologically-ordered states recently realized on a 219-qubit programmable quantum simulator[933]. In the experiment, qubits are encoded in ground states and $n = 70$ Rydberg states of neutral ^{87}Rb atoms and placed in an array on the links of a kagome lattice (Figure 8.4). This model maps onto a dimer model, where each Rydberg atom can be viewed as a dimer covering the two adjacent vertices of the kagome lattice[973]: the Rydberg blockade interaction between nearby atoms enforces a "dimer constraint" by preventing, with high probability, any vertex from being covered by more than one dimer[906].

This dimer model is predicted to support a $\mathbb{Z}_2$-topologically-ordered state of the resonating valence bond (RVB) type, involving the equally-weighted superposition of all dimer coverings[973,850,894]. In this model, Z-stabilizers are given by (-1) times the product of single-qubit Z-operators on the edges touching a vertex, X-stabilizers are given by the product of off-diagonal operators supported on the triangles bordering a hexagon (see Methods), and the RVB state forms a fixed-point state. An e (resp., m) anyon arises when a Z (X) stabilizer is violated[910,960,976]. Here, the (-1) factor for Z-stabilizers ensures stabilizer expectation values of $+1$, because each vertex is touched by exactly one dimer.

In the experiment, a topologically-ordered state is prepared by quasi-adiabatically adjusting the detuning Δ and Rabi frequency Ω of a global laser drive[933]. The onset of topological order is observed by studying the expectation values of Wilson loops and open strings[673,581,689,973,933]. A state consistent with $\mathbb{Z}_2$ topological order emerges when using a quasi-adiabatic sweep from initial $\Delta/\Omega < 0$ to a final value of Δ/Ω in

the range $3.3 \lesssim \Delta/\Omega \lesssim 4.5$. In practice, several factors make quantitative characterization of such states difficult, as they cause the prepared state to differ from the ideal fixed-point state for the dimer model. In particular, the finite sweep speed and experimental imperfections (e.g., off-resonant scattering, laser phase noise, spontaneous emission events) can modify the experimentally created state. Moreover, the Rydberg interaction Hamiltonian is only an approximation of the parent Hamiltonian of the fixed-point state: for example, the $1/r^6$ interaction between Rydberg atoms gives rise to long-range tails in the interaction Hamiltonian. These long-range tails also destabilize the spin-liquid ground state, which could cause a first-order phase transition between regions (II) and (IV) in Figure 8.4. Nonetheless, a spin-liquid state can be prepared by using finite ramp speeds, as was done in the experiments[682,605,973]. These factors correspond to both coherent and incoherent perturbations, similar to those considered in our toric code simulations. As a result, while topological order can be discerned at modest length-scales, the expectation values of large, bare Wilson loop observables have nearly vanishing signal for almost all final values of Δ/Ω (Figure 8.4b,e).

To circumvent these imperfections, we measure LED loops on the experimentally prepared states. Due to the limited experimental system size, it is not possible to consider loops which strictly satisfy the limit where $\xi \ll d \ll L$, resulting in relatively small expectation values for the LED loop operators. Nonetheless, we clearly observe a range of values of Δ/Ω where both Z- and X-loops are amplified, which corresponds to the spin-liquid interval identified in Ref.[933] (blue shaded region in Figure 8.4). In particular, some of the largest loops within the system acquire non-zero expectation values in this parameter regime. To further confirm our findings in this intermediate system size setting, we also examine the behavior of open Z- and X-strings under

LED, and we find that there are four regimes (I-IV). Regimes I, II, and III correspond to the Z-paramagnet, X-paramagnet, and spin-liquid regime, in agreement with the prior interpretation of experimental results[933]. We emphasize that our analysis of Regime III goes beyond that of[933], showing non-trivial coherence in closed loops at significantly longer length-scales. Furthermore, LED provides novel insights into the nature of Regime IV: because LED does not amplify open or closed string expectation values, our analysis appears to be consistent with a decoherence-dominated disordered phase (see also Supplementary Information). Such a phase is analogous to the disordered part of the mixed-state phase diagram (see Figure 8.3c), which has a high density of dephasing (Z) errors, in contrast to the valence-bond solid (VBS) phase predicted for the ground state[973].

4.5 Circuit-Based LED and Generic Topological Phases

While our current LED analysis uses classical post-processing of Z- and X-basis experimental snapshots, the most generic LED formulation involves a quantum circuit model following the QCNN framework of Ref.[620]. Here, the entropy associated with both incoherent and coherent fluctuations are systematically removed by introducing ancillary degrees of freedom and applying local unitary transformations, ultimately leaving a purified state supported on fewer degrees of freedom. Notably, this enables the application of LED to a large class of non-abelian topological orders known as string-net models[759,791]. The anyon content of these models is characterized by a modular tensor category (MTC) $\mathcal{C} = \mathcal{Z}(\mathcal{A})$, where $\mathcal{Z}$ denotes the Drinfeld center[988,543] of a unitary fusion category $\mathcal{A}$[759]. Here, the possible topological charges (i.e., anyon types) are given by the simple objects $\alpha_0, \alpha_1, ..., \alpha_{N-1}$ of $\mathcal{C}$. It is conjectured

that any MTC is uniquely determined by modular S and T matrices which capture its anyon braiding statistics:

$$s_{ij} = \frac{1}{\mathcal{D}} \quad \alpha_i \quad \alpha_j \tag{4.3}$$

$$t_{ij} = \frac{\delta_{ij}}{d_i} \quad \alpha_i \tag{4.4}$$

where d_i is the quantum dimension of α_i and $\mathcal{D} = \sqrt{\sum_i d_i^2}$. For example, a key signature of the toric code MTC $\mathcal{C} = \mathfrak{D}(\mathbb{Z}_2)$ is the -1 twist product between e and m anyon loops ($s_{em} = -1$).

Direct measurements of s_{ij} and t_{ij} involve braiding anyons along large loops, and hence are affected by coherent perturbations and incoherent errors. The inability to extract their precise values prevents accurate identification of the topological phase. To circumvent this, we use a hierarchical LED circuit which systematically detects and identifies errors (anyons) at each site by using ancillary qubits, removes them by inputting the fusion rules of $\mathcal{C}$ into a maximum-likelihood decoder, and applies an entanglement renormalization circuit to coarse-grain the system[769]. After multiple layers, the S and T matrices can be measured with much higher accuracy and efficiency (Figure 6.5). We note that circuit-based LED is required for the detection and removal of non-abelian anyons. More details on circuit-based LED and generic topological phases can be found in Methods and Supplementary Information.

4.6 Discussion

These results demonstrate that LED constitutes an exceptionally promising approach to enhance the detection and characterization of topological order. Several generaliza-

tions and future avenues can be considered. For example, the variational methods of QCNN circuits can enable adaptive measurement procedures, which can recognize a much larger portion of the topological phase. This opens the door towards achieving a necessary and sufficient criterion for topological order using LED, which cannot be done using any fixed linear observable[722]. Moreover, our results indicate that LED is applicable to generic topological orders in higher dimensions, which is challenging to analyze using any currently known techniques. LED can also potentially serve as an order parameter for efficiently characterizing glassy gauge models[987], through a mapping shown in Methods. Additionally, while our present work analyzes a spin-liquid state prepared using a Rydberg-atom quantum simulator, LED is also directly applicable to other platforms such as superconducting qubits[912] or trapped ions[951].

Another promising direction is to further study whether the "correctability" of states in our mixed-state phase diagram can be used to characterize topological order in mixed states more generally[786,733,734,546,703]. In particular, it could be intriguing to further explore the dependence of the correctable regime on the choice of local error correction and/or coarse-graining procedure. Finally, while our approach can be directly applied to any string-net topological order, it could be interesting to consider more general topological phases, fracton phases or gauge theories with continuous gauge groups[974,976]. Such methods can then become indispensable parts of quantum simulation toolboxes for understanding exotic states of entangled quantum matter.

4.7 Methods

4.7.1 Numerical Simulations for the Toric Code

In this section, we explain how the numerical simulations underlying Figures 8.2 and 8.3 are performed. We begin by constructing a projected entangled pair state (PEPS) representation of the exact toric code ground state[925]. This construction utilizes a parity tensor P defined as

$$P_{ijkl} = \begin{cases} 1 & \text{if } i+j+k+l = 0 \mod 2 \\ 0 & \text{otherwise} \end{cases} \tag{4.5}$$

where each index $i,j,k,l \in \{0,1\}$ (i.e., the tensor P has bond dimension two). Because the toric code is defined with qubits on the links of a square lattice, our PEPS representation of the state has one PEPS tensor with two physical indices per unit cell. Letting p,q be the physical indices and $ijkl$ be the virtual indices, the toric code PEPS tensor A is then given by $A^{pq}_{ijkl} = \delta^p_i \delta^q_j P_{ijkl}$. Our perturbed states $|\psi(g_X,g_Z)\rangle$ are constructed from the toric code state by applying imaginary time evolution to each site $L(g_X,g_Z) = e^{g_X X + g_Z Z}$:

$$A(g_X,g_Z)^{pq}_{ijkl} = \sum_{p',q'} L(g_X,g_Z)^p_{p'} L(g_X,g_Z)^q_{q'} A^{p'q'}_{ijkl}\,. \tag{4.6}$$

Notice that this operation does not change the PEPS bond dimension, thereby allowing for efficient simulation.

Our goal is to simulate projective Z-basis measurements to serve as the "experimental snapshot" input in Figure 8.1b. The key ingredient which enables efficient sam-

pling is an algorithm for efficiently computing marginal and conditional probabilities, which can be implemented as follows: We first label every unit cell by its coordinate (x, y). There are four possible measurement outcomes at each unit cell, and we compute the probability $P(\sigma_{(1,1)} = ab)$ that measurement of the first site $(x, y) = (1, 1)$ yields the outcome $ab = 00, 01, 10$, or 11. Next, we select a sample ab_{11} based on this probability distribution, compute the conditional probability distribution on the second site, $P(\sigma_{(2,1)} = ab|\sigma_{(1,1)} = ab_{11})$, and sample the second measurement outcome ab_{21}. The process then repeats, with each subsequent distribution being conditioned on all prior measurements.

Computing the probabilities requires contracting a 2D tensor network (Figure 4.6), which is in general $\#P$-hard[926]. In practice, however, the states we encounter have finite correlation length, and the computation becomes remarkably efficient throughout much of the phase diagram[614]. In particular, we work on a strip of finite height L_x and infinite length L_y, and introduce boundary matrix product states (MPS) to efficiently capture the effect of the environment—that is, the sites different from the one currently being sampled[865]. Because singular-value decomposition truncation is used at each step to prevent the bond dimension of the boundary MPS from growing exponentially[981], the method is approximate; however, we only discard singular values $< 10^{-8}$, so truncation errors are insignificant. Details of the boundary conditions and contraction ordering are discussed in the Supplementary Information.

In our simulations, we choose $L_x = 300$ unit cells and sample 1000 columns, giving us access to very large snapshots with 600,000 qubits. To minimize boundary effects, we compute observables supported on sites at least 30 unit cells away from the boundaries. Near the phase boundaries, the bond dimension (entanglement) of the boundary MPS becomes large due to the large correlation length, which increases the com-

putational demands for sampling (gray data points in Figure 8.2g). We numerically confirm this phase boundary with an independent calculation (see Supplementary Information).

4.7.2 Details on Error-Correction and Coarse-Graining Procedures

Here, we explain the details of the LED decoding and coarse-graining procedures and demonstrate how bare Wilson loops become decorated under the LED protocol. Without loss of generality, we consider Z-basis measurements, from which we can calculate plaquette stabilizers B_u. Here, each plaquette is labelled by the 2D coordinate of its unit cell $u = (x, y)$. Since there are two qubits per unit cell, each qubit carries a coordinate and a link label v or h, depending on whether its corresponding edge in the square lattice is vertical or horizontal, respectively. Finally, the projective measurement outcomes are denoted by $\sigma \in \{+1, -1\}$ (see Figure 4.7).

To illustrate local error correction, we consider the "pairing decoder," which flips a qubit if and only if its two neighboring plaquettes are simultaneously occupied. Importantly, to preserve locality, we first compute all stabilizer values and then flip qubits based on these values. The decision of whether to flip any qubit then depends only on its value, and the values of the six adjacent qubits with which it shares a plaquette. Equivalently, this error correction procedure corresponds to an operator transformation

$$\sigma_{u+\hat{x},v} \to \sigma_{u+\hat{x},v} \left(1 + B_u + B_{u+\hat{x}} - B_u B_{u+\hat{x}}\right)/2 \tag{4.7}$$

$$\sigma_{u+\hat{y},h} \to \sigma_{u+\hat{y},v} \left(1 + B_u + B_{u+\hat{y}} - B_u B_{u+\hat{y}}\right)/2 \tag{4.8}$$

To ensure all local errors are removed after a finite number of LED steps, we also pair

anyons which occupy two plaquettes separated by a diagonal, such as B_u and $B_{u+\hat{x}+\hat{y}}$. The locality of the decoder ensures that the support of any local operator only grows by a finite amount with each step. Subsequently, the coarse-graining procedure replaces each $b \times b$ block of plaquettes with a single plaquette whose value is the product of b^2 plaquettes; microscopically, this can be done by defining new qubits as a product of b corresponding qubits in the original lattice. The combination of a local pairing step and a coarse-graining step forms a layer of real-space RG; with each additional layer, one can correct errors of higher and higher weight.

The bare Wilson loops measured in the final state are equivalent to decorated loop operators acting on the original state. These decorated operators can be efficiently computed from projective measurement data, since their eigenstates are product states in the Z and X bases, respectively. Furthermore, in the operator transformation picture, any loop or string of length L maps onto a linear combination of exponentially many ($2^{O(L)}$) loops or strings, respectively. Thus, while the operator transformation picture is helpful for conceptual reasons, it is computationally much easier to use the original picture of error-correction and coarse-graining.

A few remarks are in order. First, one important property of LED is that it preserves commutation relations: consider two anti-commuting X and Z strings which intersect at a single point, far from the strings' endpoints. Upon applying LED, the resulting decorated strings still anti-commute. This is because the correction is computed only using stabilizers, so it decorates Z-operators by a linear combination of closed Z-loops, and similarly for X. Moreover, other local decoding algorithms, such as cellular automata and RG decoders, can also be used to generate different LED operators[641]. In the following section, we describe a flexible, "patch-based" local decoder for the toric code, which allows LED to classify a wider range of states as topological.

4.7.3 Patch-Based Decoder

The patch-based decoder with variable correction distance d is based on a local minimum-weight perfect matching (MWPM) procedure. In the first decoding step, a local MWPM decoder is convolved with all l by l square regions of the toric code, where $l \sim d$; for each region, MWPM takes as input the location of the enclosed anyons. Because both e and m anyons can freely move into and out of the region, this is analogous to decoding a surface code with open boundaries. Therefore, MWPM pairs any given anyon either with another anyon or with the boundary.

The second step aggregates MWPM pairings. Since the square regions can overlap, a pair may appear more than once. As such, after choosing a natural indexing of the plaquettes, we create a list of all MWPM pairings between two plaquettes (p, q) with $p < q$; pairings with the boundary are not included (Figure 4.8). For each plaquette p containing an anyon, the patch-based decoder then performs the pairing (p, q) which occurs most often. This procedure naturally favors pairings that flip fewer qubits, because shorter-range pairings can be included in more local patches.

A critical property of this decoder is that it preserves locality. In the first step, MWPM only uses information from local l by l patches, while the distance between partner plaquettes in the second step is always less than l. Aggregation can thus be performed using only the results from a small number of overlapping local patches.

4.7.4 Decoder Details for the Ruby Lattice Spin Liquid

We now explain the decoding procedure for a dimer model where qubits lie on the vertices of the ruby lattice, or equivalently, on the links of a kagome lattice. This dimer model supports a $\mathbb{Z}_2$ spin-liquid phase, whose fixed-point is a resonating valence-bond

(RVB) state[973]. This state is in the same universality class as the toric code, as it supports e and m anyons with similar string operators.

We first describe the decoding procedure for e anyons, which correspond to vertices with an even number of adjacent dimers. (We note that this is an odd Z_2 spin liquid, and the trivial empty state corresponds to maximal occupation of e anyon states.) In the first correction step, we apply the pairing decoder between adjacent vertices. We then coarse-grain the kagome lattice to a triangular lattice by grouping vertices within each upward-pointing triangle. This transforms vertex stabilizers in the kagome lattice to vertex stabilizers in the triangular lattice (Figure 4.9a). The pairing decoder is then applied between adjacent triangles in the second correction step. In the main text, we study the flow from uncorrected loops to vertex-paired and triangle-paired loops, which are denoted as as layers 0, 1, and 2, respectively.

We next consider the m anyons, which are associated with hexagonal plaquettes. A rotation is first performed within each triangle, such that the string operators associated with m anyons become diagonal in the measurement basis. This allows us to map each configuration onto a triangular lattice, whose vertices are located at the center of each hexagon in the kagome lattice; this mapping transforms X-stabilizers of the dimer model into vertex Z-stabilizers in the triangular lattice (Figure 4.9b). Due to the small experimental system size, we can only perform one layer of correction, and we use the pairing decoder on the triangular lattice. We note that open strings on the triangular lattice map onto open strings on the ruby lattice, although the resultant strings are slightly different from the ones measured in[973,933].

4.7.5 Quantum Circuit Formulation of LED

As discussed in the main text, the most general formulation of LED uses a hierarchical quantum circuit like the QCNN circuit introduced in Ref.[620]. The structure of such a circuit is illustrated in Supplementary Figure S11 in a one-dimensional example for simplicity of illustration, but can be easily generalized to the two-dimensional cases considered in LED.

In this framework, stabilizer measurements are performed at each layer using quantum circuits to preserve the coherence of qubits in the system, in the same fashion as for surface-code quantum computation[672]. When the lattice is coarse-grained as in Figures 8.1, 4.7, a fraction of the system's qubits are measured, and local operations are applied to each remaining qubit based on nearby stabilizer measurement values, to correct for local errors. One example circuit construction of LED stabilizer measurement, decoding, and coarse-graining for recognizing the toric code phase is presented in the Supplementary Information. For more general string-net models, ancillas can be used to detect the presence of anyons, and the decoding steps perform anyon transport and fusion via procedures described in Ref.[1020]; meanwhile, the coarse-graining circuit is constructed as the inverse circuit of a multiscale entanglement renormalization ansatz (MERA) representation of the fixed-point state (Figure 6.5)[769]. Additionally, a layer of variational unitary operations is placed in front of each anyon-detection step.

These variational unitaries can be tuned to optimize the LED order parameter values, especially in the presence of (quasi-)local rotations of qubits on top of a known fixed-point state. For example, if every qubit in a perfectly-prepared toric code state underwent a Haar-random, single-qubit operation, both the bare and snapshot-based

LED Wilson loop operators will be exponentially small. However, the layer of variational unitaries in front of the first local decoding step enables one to un-do these single-qubit operations and again achieve a high LED signal. In particular, one uses here an adaptive procedure, whereby a hybrid quantum-classical feedback loop is used to tune each unitary to optimize LED loop values. More generally, variational unitaries in front of subsequent local decoding steps l allow us to compensate for local operations acting on multiple qubits of the system. This is a major step towards achieving a necessary and sufficient criterion for topological order, which is not possible using a single, fixed observable such as a bare Wilson loop operator[722]. Moreover, due to the special hierarchical structure of QCNN and LED circuits, the optimization of the variational unitaries can be done efficiently without encountering the so-called "barren plateau" challenges of variational quantum circuits[838,886].

Finally, one other advantage of circuit-based LED is that it enables the simultaneous measurement of loop operators in multiple bases in each experimental repetition. This allows us to capture anyonic braiding statistics, which is critical to the application of LED to non-abelian phases. In particular, the final measurement of s_{ij} (Figure 6.5d) can be performed by initializing an ancilla qubit in the state $|+\rangle = \frac{1}{\sqrt{2}}(|0\rangle + |1\rangle)$, and applying a controlled operation which, conditioned on the ancilla being in $|1\rangle$, creates anyon pairs $\alpha_i, \overline{\alpha_i}$ and $\alpha_j, \overline{\alpha_j}$, braids $\overline{\alpha_i}$ around α_j, and fuses the pairs $\alpha_i, \overline{\alpha_i}$ and $\alpha_j, \overline{\alpha_j}$. s_{ij} is then measured in two steps: First, the magnitude $|s_{ij}|^2$ is equal to the probability of $\alpha_j, \overline{\alpha_j}$ fusing to vacuum when the ancilla is in $|1\rangle$; this probability can be obtained by measuring local energy densities (e.g., by performing stabilizer measurements). Then, when $|s_{ij}|^2 > 0$, we post-select on both $\alpha_i, \overline{\alpha_i}$ and $\alpha_j, \overline{\alpha_j}$ fusing to

vacuum and measure the ancilla's final state

$$|S_{ij}\rangle \propto |0\rangle + s_{ij}|1\rangle \tag{4.9}$$

in an appropriate basis to obtain the phase of s_{ij}.

For topological phases described by abelian quantum double models[759], the quantum circuit and snapshot-based versions of LED can be combined by measuring all qubits in a fixed basis after some chosen depth d, and performing snapshot-based LED using the resulting stabilizer measurement values (see Supplementary Information). The choice of d is then determined by a tradeoff between the quantum circuit depth/fidelity and the generality of local rotations which can be compensated for.

4.7.6 Topological Order Witness

Here, we show that LED provides a topological order witness—that is, it does not misclassify any trivial product state as topological. For simplicity, we study the case of $\mathbb{Z}_2$ topological order on a surface with trivial topology, where the fixed-point state is the unique ground state $|\psi_{\mathrm{TC}}\rangle$ of H_{TC}. We begin by considering the ideal case where LED operators go to one.

Theorem 1. Let ρ be an arbitrary input state defined on a surface with trivial topology. Then, after performing LED with correction distance d, assume the resultant state ρ_f has, as a subsystem, qubits living on the links of a square lattice, as in the toric code. Then, if the stabilizer expectation values $\left\langle \frac{1+A_v}{2} \right\rangle = \left\langle \frac{1+B_p}{2} \right\rangle = 1$ at every vertex v and plaquette p of the subsystem, then, the input state ρ is topologically-ordered, in the sense that it is connected to an output state of the form $\rho_f = |\psi_{\mathrm{TC}}\rangle\langle\psi_{\mathrm{TC}}| \otimes \alpha_{\mathrm{anc}}$ by generalized local unitary (gLU) transformation of depth $O(d)$.

The key to the proof is a unitary implementation of LED by introducing product state ancillas and performing local unitary gates to perform stabilizer measurement and correction (see Supplementary Information for details). These operations, which cannot change the long-range entanglement structure of the state, are known as gLU transformations[602], and preserve phase boundaries. Thus, if we further assume the output ancillas α_{anc} are in a trivial state, Theorem 1 guarantees the input state is in the toric code phase. However, we do not certify this condition holds, which is in general more difficult: measurements in multiple bases are needed to uniquely determine α_{anc}. Instead, LED certifies that the toric code state can be distilled from the input state by gLU transformations. Because long-range entanglement cannot be created from a trivial state by gLU transformations[602], Theorem 1 implies that LED operators flowing to unity forms a sufficient condition for topological order, or equivalently, a topological order witness (see also Ref.[693]).

While the above argument works well in theory, any practical system cannot measure LED observables equal to one with infinite precision. Indeed, even infinitesimal local perturbations to the toric code ground state, such as $e^{-i\varepsilon H}|\psi_{\text{TC}}\rangle$ for arbitrarily small ε and some local Hamiltonian H, can create error strings larger than the correction length d. This causes LED loop expectation values to decay exponentially, even in the topological phase. To show that LED still provides a topological order witness in the presence of local perturbations, finite measurement errors, and finite system size, we show the following Theorem:

Theorem 2. Consider an arbitrary input state ρ and LED with correction distance d, as in Theorem 1. Suppose the corresponding subsystem of ρ_f has stabilizer expectation values $\left\langle \frac{1+A_v}{2} \right\rangle > 1-\varepsilon$, $\left\langle \frac{1+B_p}{2} \right\rangle > 1-\varepsilon$ at every vertex v and plaquette p. Then, the input state ρ exhibits topological ordering at least up to a length-scale $O(\mathscr{L}-d)$;

that is, no purification of ρ can be prepared using a local quantum circuit of depth less than $O(\mathscr{L} - d)$, where $\mathscr{L} \sim 1/\sqrt{\varepsilon}$.

Our proof of Theorem 2 hinges on the following two Lemmas, proved in the supplement.

Lemma 3. Given an output state ρ_f satisfying the conditions of Theorem 2, and a simply connected $(\mathscr{L} - 2) \times (\mathscr{L} - 2)$ square region R on the system part, the reduced density matrix $\rho_d = \mathrm{tr}_{R^c}[\rho_f]$ is indistinguishable from the toric code reduced density matrix $\sigma_{\mathrm{TC}} = \mathrm{tr}_{R^c}[|\psi_{\mathrm{TC}}\rangle \langle\psi_{\mathrm{TC}}|]$ defined on the same region, up to the bound $||\rho_d - \sigma_{\mathrm{TC}}|| \leq \max\left(\sqrt{\varepsilon}, 2\mathscr{L}^2\varepsilon\right)$

Lemma 4. Consider an input state ρ and an LED procedure satisfying the conditions of Theorem 2. Then the final state ρ_f after LED cannot be prepared using a local quantum circuit with depth less than $O(\mathscr{L}) \sim O(1/\sqrt{\varepsilon})$.

Upon combining the result of Lemma 4 with the fact that our LED procedure corresponds to a local quantum circuit with depth $O(d)$, we find that the original input state $|\psi\rangle$ cannot be prepared using a quantum circuit of depth smaller than $O(\mathscr{L} - d)$—which is precisely the statement of Theorem 2. So, if we measure loops of length $L \gg d$ to be $1 - \varepsilon$, this shows that LED provides a topological order witness up to length-scales of $O(L/\sqrt{\varepsilon})$.

We now discuss how these theoretical results are reflected in our numerical simulations. First, when fluctuations are local, the probability of having an error string of length ℓ decays exponentially with ℓ, and the exponent is determined by the characteristic length-scale ξ of fluctuations. In these systems, we expect the error rate after an optimal LED procedure with correction distance d to be given by $\varepsilon(d) \propto e^{-d/\xi}$,

so correction distance $d = \Omega(\xi \log \mathscr{L})$ is sufficient to certify topological order up to length-scale $\mathscr{L}$. Second, when LED uses the hierarchical, anyon-pairing decoder, the anyon density is observed to decrease faster than exponentially in the number n of LED steps (Figure 4.10). In this case, both the measured stabilizer size and the correction distance d grow exponentially with n, which implies that the certification length-scale $\mathscr{L}$ grows at least exponentially with n as well. Third, our argument does not certify topological order to any length-scale when $L < d$; this is because the support of such an LED operator no longer has an interior, potentially giving rise to signal even in the trivial phase. Indeed, this is reflected in our numerics as well (Supplementary Information, Figure S12).

4.7.7 Connection to Topological Entanglement Negativity

The entanglement negativity of a mixed state ρ_S is defined as $S_N(\rho) = \log ||\rho||_1 = \log(\sum \lambda_i)$, where λ_i are the eigenvalues of ρ. Prior works have shown, via a combination of analytical arguments and numerical results, that in a topological phase, S_N obeys an area-law with a constant correction, i.e. $S_N = \alpha L - \gamma$. Further, recent results have also shown that the topological term γ vanishes at finite-temperature[812], or for high incoherent error rates[662]. Thus, the negativity appears to capture important features of mixed state topological order.

The unitary circuit construction of LED also enables us to connect a positive classification under LED, to the topological entanglement negativity of the input state. In particular, theorem 1 implies that states classified as topological are connected to an output state $\rho_f = |\psi_{\mathrm{TC}}\rangle \langle \psi_{\mathrm{TC}}| \otimes \alpha_{\mathrm{anc}}$ via local unitary circuits. If we further assume the ancillas contain no long-range order (see SM for rigorous definition), then since $|\psi_{\mathrm{TC}}\rangle$ is topologically ordered, the output state indeed has a topological correction in the

entanglement negativity. It is further believed that γ is a topological invariant, i.e. it should remain invariant under local unitary circuits. As such, this should be sufficient to certify the input state ρ_S has topological order.

We show this in the SM, for the special case where the LED circuit is composed of Clifford gates, by extending the stabilizer formalism introduced in Ref.[812]. Interestingly, there, the topological correction to S_N comes from the presence of decorated Wilson loops operators with non-trivial twist product in the input state ρ_S (see also proof of Lemma 4). Thus we conjecture a connection to topological entanglement negativity holds for LED Wilson loops more generally.

Data and Code Availability Statement. The data that support the plots within this paper and other findings of this study are available at https://osf.io/k8up2/. We note that more extensive data from the Rydberg-atom spin liquid experiment of Ref.[933] are available at https://dataverse.harvard.edu/dataset.xhtml?persistentId=doi:10.7910/DVN/BDCTRX.

Acknowledgments. We thank E. Altman, Y. Bao, D. Bluvstein, Z.-P. Cian, S. Ebadi, G. Giudici, M. Hafezi, H.-Y. Huang, A. Kitaev, H. Levine, J. Preskill, S. Sachdev, R. Sahay, N. Tantivasadakarn, R. Verresen, A. Vishwanath, T. T. Wang, and X.-G. Wen for insightful discussions, and we especially thank D. Aasen and Z. Wang for providing helpful information and conversations on applying LED to non-abelian topological phases. This work was supported by the US Department of Energy [DE-SC0021013 and DOE Quantum Systems Accelerator Center (contract no. 7568717)], the Defense Advanced Research Projects Agency (grant no. W911NF2010021), the National Science Foundation, the Department of Defense Multidisciplinary University Research Initiative (ARO MURI, grant no. W911NF2010082), and the Harvard-MIT Center

for Ultracold Atoms. I.C. acknowledges support from the Alfred Spector and Rhonda Kost Fellowship of the Hertz Foundation, the Paul and Daisy Soros Fellowship, and the Department of Defense through the National Defense Science and Engineering Graduate Fellowship Program. N.M. acknowledges support from the Department of Energy Computational Science Graduate Fellowship under Award Number DE-SC0021110. H.P. acknowledges support from the ERC Starting grant no. 101041435 and the Erwin Schrödinger Center for Quantum Science and Technology.

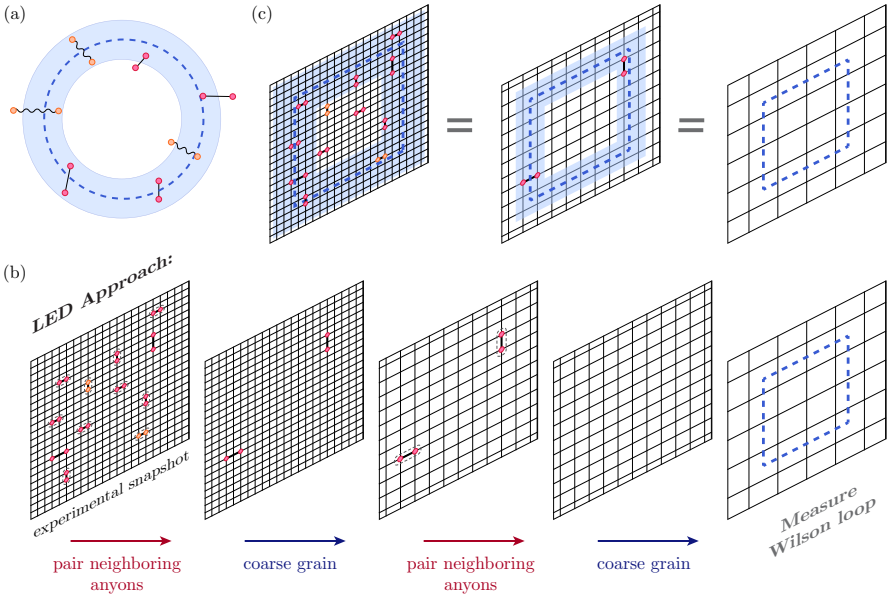


Figure 4.1: Detecting topological phases via snapshot-based LED. (a) In the absence of perturbations, a topologically-ordered state with zero correlation length such as Kitaev's toric code state[759] is characterized by +1 expectation values of 'bare' Wilson loop operators, which are typically tensor products of single-site operators (dotted blue loop). In realistic systems, however, coherent perturbations give rise to virtual anyon pairs (red dots/straight lines), and incoherent errors introduce physical anyon pairs (orange dots/wavy lines); this causes the expectation value of bare Wilson operators to decay exponentially with the loop's perimeter. To account for these local fluctuations, one can measure 'fattened' Wilson operators supported on an annulus (blue); the LED loops constitute one realization of this. (b) LED method to measure decorated Wilson loop observables for $\mathbb{Z}_2$ topological order in a system where qubits live on the links of a square lattice, and stabilizers are associated with vertices. Given an experimental snapshot of all qubits in the Z or X basis, one can obtain values for all stabilizer operators in that basis, thereby identifying the locations of all e or m anyons, respectively. In the first step, neighboring anyons are paired using a local decoder (dashed pairings), and each pair is removed by flipping the value(s) of qubit(s) lying on a path of minimal length connecting the two anyons; subsequently, the lattice is coarse-grained so that only a fraction of the original qubits remain. These two steps are iterated n times (here, $n = 2$), after which a bare Wilson loop is evaluated on the final, coarse-grained state. (c) The final, bare Wilson loop operator evaluated on the final state is equivalent to decorated Wilson loop operators evaluated at earlier iterations (see Methods).

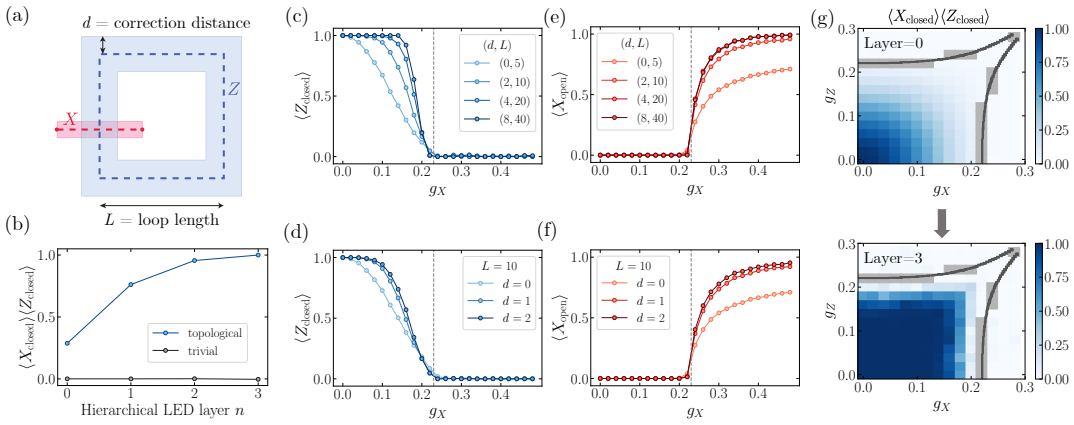


Figure 4.2: Numerical demonstration with coherently perturbed toric code states. (a) In a general construction of our LED Wilson loop operator, we use a local decoder which pairs anyons within a region of radius d (blue annulus). Conjugate LED open string operators (red stripe) anti-commute with Wilson loops, and hence must vanish in the topological phase. (b) Order parameter $\langle X_{\text{loop}}\rangle\langle Z_{\text{loop}}\rangle$ for a trivial state ($g_Z = 0.0, g_X = 0.26$) and a topological state ($g_Z = 0.12, g_X = 0.12$), upon varying n, using a distance-four patch decoder and coarse-graining blocksize two respectively (see Methods). (c) Output at different n along the $g_Z = 0.14$ line of the phase diagram. Gray dotted line is conjectured phase transition region. (d) Expectation values of generic LED Wilson loops with the same diameter L, using the pairing decoder ($d = 1$) and distance-four patch decoder ($d = 2$) without coarse-graining. (e,f) Corresponding expectation values of bare and decorated open string operators. (g) Order parameter values constructed from bare Wilson loops ($n = 0$) and LED Wilson loops ($n = 3$), using the same LED procedure as (c,e), across varying values of (g_X, g_Z). Dark gray regions are numerical estimates for the phase boundary between topological and trivial (Methods). Light gray regions correspond to locations where sampling is expensive due to large correlation length.

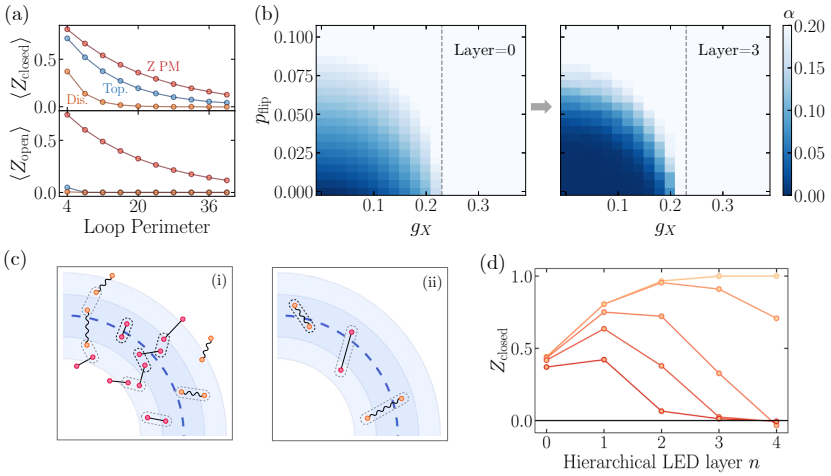


Figure 4.3: Application to mixed states. (a) Without error correction, generic points in the topological and trivial, disordered phase ($g_Z = 0.12, g_X = 0.18, p_{\text{flip}} = 0.0$ and $g_Z = 0.06$, $g_X = 0.0$, $p_{\text{flip}} = 0.11$ resp. shown in the plot) appear very similar qualitatively, as closed loops decay exponentially with loop perimeter in both cases, while open strings remain close to zero (see Methods). In contrast, in the trivial, paramagnet phase ($g_Z = 0.32, g_X = 0.2, p_{\text{flip}} = 0$), open strings decay with the same perimeter-law as closed loops. (b) $g_Z = 0.14$ slice of mixed state phase diagram, containing topological, disordered, and X-paramagnetic phases. These phases are associated with fixed-point states $g_x = g_z = p_{\text{flip}} = 0$, $g_z \to \infty$, $g_x \to \infty$, and $p_{\text{flip}} \to 0.5$, respectively. The flow of the closed-loop decay exponent α under LED provides a sharp divider between two kinds of perimeter-law decay, observed in different regimes of the mixed-state phase diagram. (c) In the uncorrectable regime (i), the local decoder of LED pairs anyons incorrectly, resulting in perimeter-law decay with large α in disordered and paramagnetic phases. Moreover, the probability of such an incorrect pairing can increase with the number n of LED iterations. Here, the black pairings are made by LED at or before one specific value of n, and gray pairings are made upon performing one additional LED iteration. In the correctable (topological) regime (ii), increasing n can reduce α to zero, as fluctuations of higher characteristic length ξ can be reliably corrected using only local information. In the conceptual framework where an LED operator is embedded in a surface code on an annulus (see Figure 8.2a), incorrect pairings corresponds to logical errors (e.g. X_L). (d) Expectation values of LED loop observables upon increasing n ($d, L \propto 2^n$), in thermal states of varying temperatures (between 0 and 0.35, with darker colors indicating higher temperatures) and $p_{\text{flip}} = 0.02$.

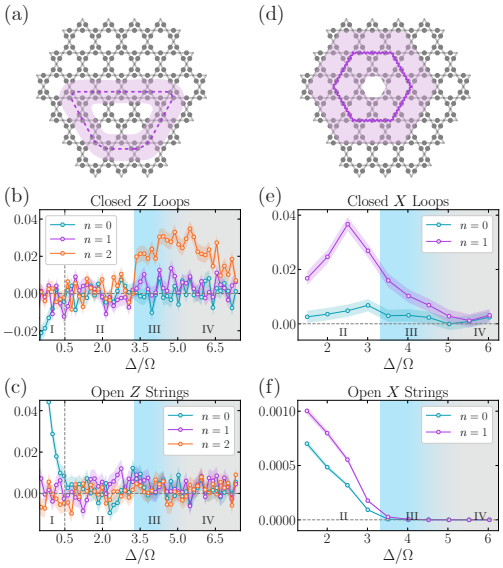


Figure 4.4: Enhancing experimental detection of $\mathbb{Z}_2$ spin liquid. (a,d) In the experiment[933], 219 qubits are placed on the links of a kagome lattice. Upon applying LED, the Z and X closed-loop observables are amplified for certain ranges of Δ/Ω. The shaded purple regions show the support of large, decorated Wilson loops after one layer of correction with $n = 1$. (b,e) Expectation value of Wilson loops depicted in (a,c) for different correction layers n. Plotted error bars (shaded regions) show expected variation (one standard error) of the mean. The regime in which both types of loops are amplified corresponds nicely to the spin-liquid regime identified in Ref.[933] (shaded blue region). (c,f) The behavior of expectation values of open Z- and X-strings under LED further confirms our findings, as both types of open strings stay at 0 in the spin-liquid regime. Here, the measured open strings are half of the Wilson loops. By considering the behavior of all types of loops and strings—closed and open, Z and X—we find that there are four regimes (I-IV), corresponding to four phases: (I) Z-paramagnet, (II) X-paramagnet, (III) topological spin liquid (blue), and (IV) a phase which is consistent with strong decoherence effects (gray). In our analysis, the progression from Regime (III) to (IV) appears to be smooth.

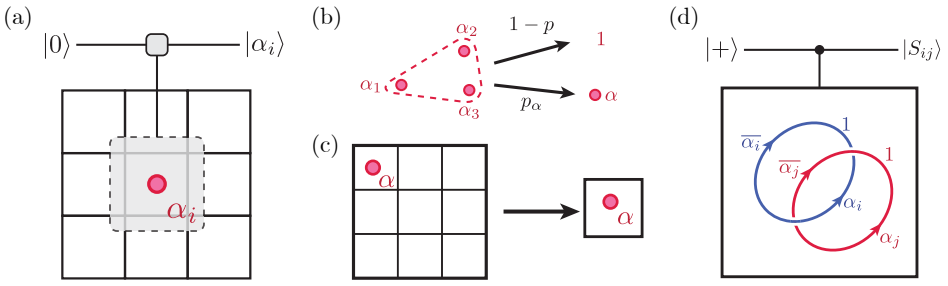


Figure 4.5: LED for generic string-net models. (a) An ancilla qudit is used to measure the topological charge within each local region $\mathcal{R}$: we initialize the ancilla in $|0\rangle$, apply a local unitary $U = \sum_{i,j=0}^{N-1} |(i+j) \bmod N\rangle\langle j|_{\text{anc}} \otimes P_i$, where P_i projects $\mathcal{R}$ onto the subspace with topological charge α_i, and finally measure the ancilla's state. (b) Local error correction is performed by inputting the fusion rules of $\mathcal{C}$ into a maximum-likelihood patch-based decoder. Given any $l \times l$ patch, one identifies possible groupings of anyons (including groupings to the boundary) that can remove all nontrivial topological charges within the patch. The decoder performs the grouping of highest probability by fusing anyons or dragging them to the boundary of the patch[1020]. If $\mathcal{C}$ is non-abelian, the vacuum topological charge may only be attained probabilistically with probability $1 - \sum_\alpha p_\alpha$, or a nontrivial topological charge α remains with some probability p_α. (c) The system is then coarse-grained by applying a quantum circuit corresponding to a multiscale entanglement renormalization ansatz (MERA) representation of the fixed-point state[769]. (d) At the final layer, S- and T-matrix elements can be measured by introducing an ancilla qubit in the $|+\rangle$ state and applying controlled-anyon-braiding operations. More details on implementing Steps (c) and (d) can be found in Methods.

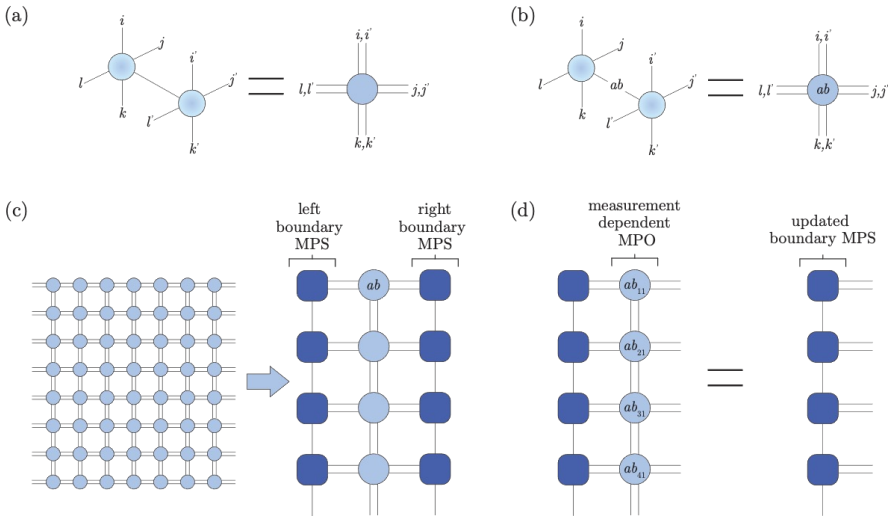


Figure 4.6: PEPS sampling algorithm. Expectation values are computed with respect to both $|\psi\rangle$ (back) and $\langle\psi|$ (front). (a) Tracing, or averaging over measurement outcomes can be done by contracting the physical indices, and is needed to compute marginal probabilities. (b) To compute the probability of a particular Z basis measurement, the physical index is assigned a particular value ab. (c) We can efficiently contract a 2D PEPS tensor network on an infinite strip of finite height, by using a left and right boundary MPS (only top four rows shown). The probability distribution for projective measurements on a particular site, e.g. $xy = 11$, can then be computed efficiently. (d) Once an entire column has been sampled, the measurement-dependent MPO can applied to the boundary MPS. Although performing this contraction exactly causes the bond-dimension to grow rapidly, away from phase boundaries, finite bond dimension is sufficient for accurate simulation. See Supplementary Information for more details.

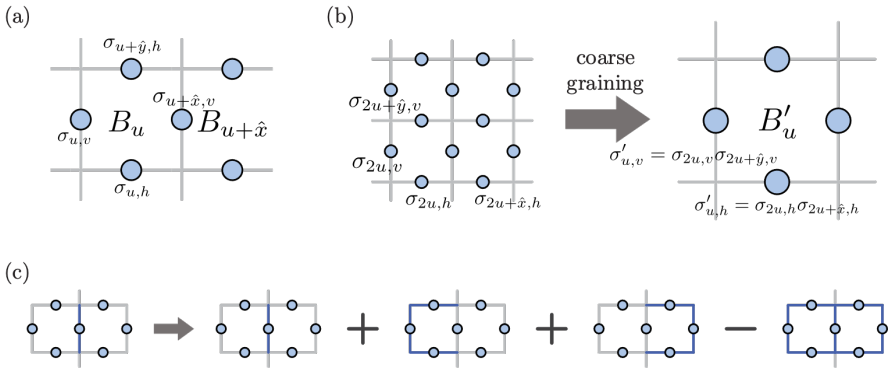


Figure 4.7: LED coarse-graining and operator transformation. (a) In the toric code model, qubits are located on the links of a square lattice, and the stabilizer associated with any plaquette is given by a product of four single-qubit Pauli-Z operators. (b) Coarse-graining maps a $b \times b$ block of plaquettes to a single plaquette whose value is the product of the b^2 plaquettes (here $b = 2$). Microscopically, coarse-grained qubits σ' are products of b lower-level qubits σ. Coarse-grained stabilizers B'_u are therefore equivalent to a product of $b \times b$ stabilizers at the lower level. (c) Pairing correction flips a qubit conditioned on the state of its two neighboring stabilizers. This is equivalent to an operator transformation where the qubit is decorated by products of closed loops.

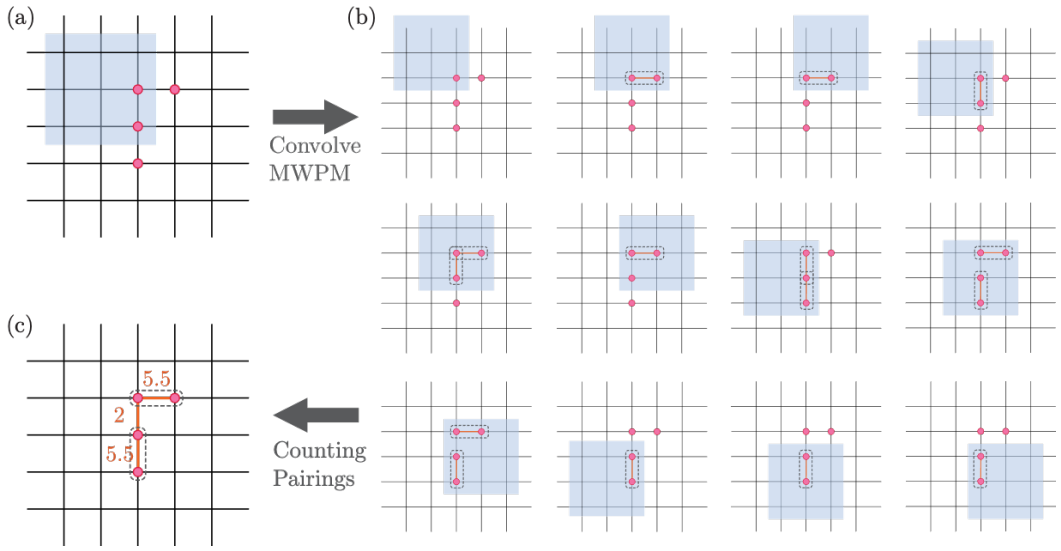


Figure 4.8: MWPM-based patch decoder. (a) Example of an error chain which creates four e-anyons. (b) The decoding algorithm performs correction using only local information by splitting the large system into smaller overlapping regions, within each of which the MWPM algorithm is used to find the lowest-weight pairing of anyons. These local regions have open boundaries, hence MWPM can also pair anyons to the boundaries if this is of lower weight. In practice, a slight boundary bias is added to break ties in favor of boundary pairing. (c) The final step requires locally combining the pairing outputs to determine the final pairing. In particular, we count the number of times each site p is paired to sites $q > p$. In the diagram, two equal-weight pairings contribute 0.5 each, though we randomly break the tie in practice. Then, the algorithm pairs p with the q that appears most often. In this example diagram, we connect two pairs which have weight$= 5.5$, and do not form the weight$= 2$ pairing. We see in the simple four-anyon case depicted above, the procedure correctly recovers the pairing with windows of size $l = 3$. In general, this patch-based decoder can correct errors up to distance $d = \lfloor l/2 \rfloor$; moreover, the distance by which it spreads information and the thickness of any associated LED operators are both proportional to l.

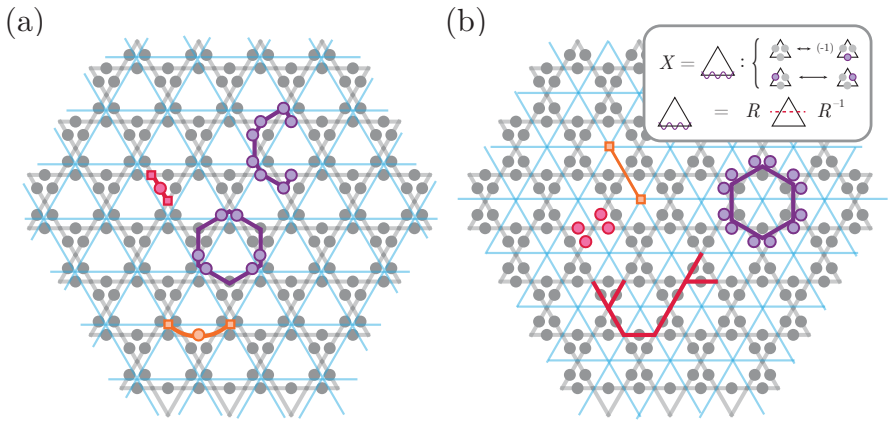


Figure 4.9: Decoding for the ruby lattice spin liquid realized in Ref.[933]. (a) For Z-loops, two layers of LED can be performed. In both layers, we use the pairing decoder, which flips a qubit (e.g., red or orange circle) if and only if both neighboring stabilizers (e.g., red or orange squares) are equal to -1. Stabilizers in the first layer (e.g., red squares) are given by $(-1)\prod_{i\in v} Z_i$ for each vertex v of the kagome lattice. The coarse-graining procedure after the first decoding step maps three stabilizers to a single stabilizer (e.g., orange square) in the coarse-grained lattice (blue lines), whose value is determined by the product of the qubits along a loop enclosing a triangle (e.g., purple closed loop). The open strings considered in the main text start and end at hexagons (e.g., purple open string). (b) To measure X-loops, a basis rotation is first performed within each triangle of the kagome lattice, so that the X-string operators become diagonal in the measurement basis (inset and Refs.[933,973]). Each configuration is then mapped to a triangular lattice (blue lines), where each edge of the triangular lattice is determined by the product of four qubits in the original lattice (e.g., red circles); moreover, the X stabilizers of the dimer model become vertex stabilizers in the triangular lattice (e.g., purple hexagons). As before, the pairing decoder flips qubits (orange edges) conditioned on the values of stabilizers (e.g., orange squares). Open strings on the triangular lattice also map to open strings in the kagome lattice (e.g., red string), although the resulting strings are slightly different from the ones measured in Refs.[933,973].

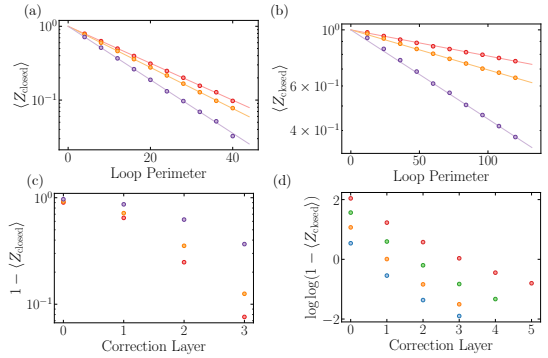


Figure 4.10: Perimeter-law decay of Wilson loops is clearly visible at various points in the topological phase—(orange) $g_Z = 0, g_X = 0.18, p_{\text{flip}} = 0$, (red) $g_Z = 0.18, g_X = 0.18, p_{\text{flip}} = 0$, (purple) $g_Z = 0.10, g_X = 0.18, p_{\text{flip}} = 0.03$. This is observed for both (a) uncorrected loops and (b) $d = 6$ corrected loops under two layers of $d = 3$ MWPM patch decoding. (c) LED Wilson loops appear to approach one faster than exponential in n. (d) In a model with only incoherent errors ($p_{\text{flip}} = 0.02$ (blue), 0.03 (orange), 0.04 (green), 0.05 (red)), we can study the effect of even more layers, where we see hints that the decay is doubly-exponential in n, or exponential in $d \sim 2^n$.

5

Digital engineering of Floquet spin liquids

Techniques for quantum simulation of topological quantum matter and lattice gauge theories are now being actively explored. Since many of these systems are difficult to treat analytically or to simulate on classical computers, often even fundamental concepts are not well understood. Of particular interest are topological phases[536], whose long-range entanglement generates a host of interesting properties, such as emergent gauge fields[997,904], quantum error correcting codes[760], and excitations with non-trivial statistics[867]. Recent developments in superconducting qubit technology[913]

and neutral atom arrays[648,568,917] have provided exciting signatures of $\mathbb{Z}_2$ topological order[936,913], the simplest realization of an abelian topological order. An outstanding challenge is developing methods which would enable these platforms to explore and control non-abelian topological order. In such systems, the exchange of quasiparticles can result in non-abelian unitary operations acting on a degenerate set of ground states, which encode protected quantum information (logical qubits). This property makes the non-abelian anyons not only a fascinating condensed-matter phenomenon but also a building block of topological quantum computation (TQC)[760,867], since the logical subspace is robust against local errors and protected by a gap to the rest of the spectrum. While there has been a long-lasting effort to realize this kind of topological order in solid-state systems[957] and several theoretical proposals have been put forward to probe it with synthetic systems, such as cold atoms[639,806,952] and polar molecules[845,823], the direct observation of its exceptional properties has thus far eluded experimental realization.

In this work, we introduce an approach to creating and controlling non-abelian topological matter based on periodic modulation. Specifically, we show how the gapped non-abelian phase of the Kitaev honeycomb model can be effectively realized as a Floquet spin liquid, generated by time evolution under a repeating sequence of two-body Ising Hamiltonians[577]. In particular, while the time-averaged Hamiltonian corresponds to the gapless phase in Kitaev's model, the first-order correction breaks time-reversal symmetry and induces a finite energy gap, which is crucial for stabilizing the non-abelian excitations.

We demonstrate that such a Floquet spin liquid can be implemented in a hardware-efficient way using programmable arrays of neutral atoms. This approach combines coherent qubit transport with parallel two-qubit controlled phase gates and global

single-qubit rotations to realize the Floquet spin liquid in a digital fashion. Using these efficient primitives, we develop a Hamiltonian simulation toolkit to prepare, control, and measure topological matter. By combining physical insights and variational optimization, we first demonstrate how to reliably perform time evolution and prepare ground states of the honeycomb model in the non-abelian phase. Subsequently, we show that this toolbox can be used to study the defining properties of the chiral non-abelian theory at different levels of experimental complexity: The chiral nature of the edge modes can be probed by performing a simple quench of the boundary conditions while a minimal additional overhead allows us to create and adiabatically transport the non-abelian Majorana particles characteristic of the Kitaev B phase.

These Majorana zero modes are fractionalized fermions and when brought together can fuse to either an occupied or unoccupied fermion mode. We show how the tools developed here can be used to implement braiding and fusion experiments, probing their non-abelian nature. In particular, the degenerate subspace formed by multiple Majoranas can be manipulated by exchanging particles which is the basis for topological quantum computing. We furthermore design a dynamical protocol to readout the local fermion content—a necessary component for characterizing the fusion and braiding rules of the anyonic theory. By introducing a local magnetic field, we couple the fermion to a system with $\mathbb{Z}_2$ vortices, which correspond to simple qubit observables. Then, we leverage an emergent two-level system analogy to design a composite pulse sequence which improves the fidelity of the particle-to-vortex mapping.

We note that the Majorana modes can also be created in the abelian toric code phase, either at the intersection of e and m boundaries, or in the bulk at the endpoints of 1D lattice defects[576,787]. Recent experiments[534] explored gate-based manipulation of such states without energetic protection provided by the spectral gap.

In contrast, the Floquet spin-liquid phase and the non-abelian anyons explored in this work are analogous, respectively, to $p + ip$ superconductors and the corresponding Majorana modes pinned to vortex excitations. The anyons discussed in this work are pinned to pseudo-vortices, which reside at the ends of flipped-bond strings.

Our method can also be adapted to implement generalizations of the Kitaev honeycomb model with long-range and many-body interaction, or external fields. These systems are subjects of extensive theoretical and experimental studies[957], and cannot be simulated efficiently on a classical device, making them prime candidates for quantum simulation. Finally, the tools developed here for the implementations of generalized Kitaev models can also be used to study integrability-breaking quenches and to potentially simulate lattice gauge theories in (1+1)D with substantially shorter circuit depths compared to existing methods.

5.1 Floquet spin liquid

First, we describe the dynamical mechanism for creating the gapped non-abelian phase in a periodically driven system. Consider a two-dimensional honeycomb lattice with three types of interactions in the three different directions [Fig. 5.1(a)]. Their respective Hamiltonians are,

$$H_X = -J_X \sum_{\langle i,j\rangle_X} X_i X_j, \tag{5.1a}$$

$$H_Y = -J_Y \sum_{\langle i,j\rangle_Y} Y_i Y_j, \tag{5.1b}$$

$$H_Z = -J_Z \sum_{\langle i,j\rangle_Z} Z_i Z_j, \tag{5.1c}$$

where $\langle i,j\rangle_{X/Y/Z}$ denotes the appropriate set of links. Each of these two-body interactions can occur naturally in a magnetic system, but due to their extreme spatial anisotropy it is difficult to realize the three of them, $H_0 = H_X + H_Y + H_Z$, at the same time.

In a digital simulation, however, it is possible to periodically apply the interactions (5.1a)-(5.1c) one at a time. Then, over one driving period, the unitary evolution is described by

$$U(\tau) = e^{-iH_X\tau}e^{-iH_Y\tau}e^{-iH_Z\tau} = e^{-iH_F[\tau]\tau}, \tag{5.2}$$

where τ is the trotter step. If the frequency of the drive is high enough (τ is small), this evolution can be captured by an effective Hamiltonian $H_F[\tau]$ is approximated by the Magnus expansion[819]. For Eq. (5.2), the first two terms are

$$\begin{aligned} H_F[\tau] = &\underbrace{H_X + H_Y + H_Z}_{H_0} - \frac{i}{2}\tau[H_X, H_Y] \\ &- \frac{i}{2}\tau[H_X, H_Z] - \frac{i}{2}\tau[H_Y, H_Z] + O(\tau^2). \end{aligned} \tag{5.3}$$

This kind of Floquet Hamiltonian engineering by time averaging has been used in the past to construct prethermal phases including time crystals[656,818,1009,611], and lattice gauge theories[1026,930]. In these approaches, the terms other than H_0 are typically detrimental to the desired evolution and must be suppressed. In contrast, we find that the first-order terms $O(\tau)$, explicitly written in Eq. (5.3), are crucial for an efficient realization of the desired non-abelian phase, as discussed below.

The leading-order term,

$$H_0 = H_X + H_Y + H_Z, \tag{5.4}$$

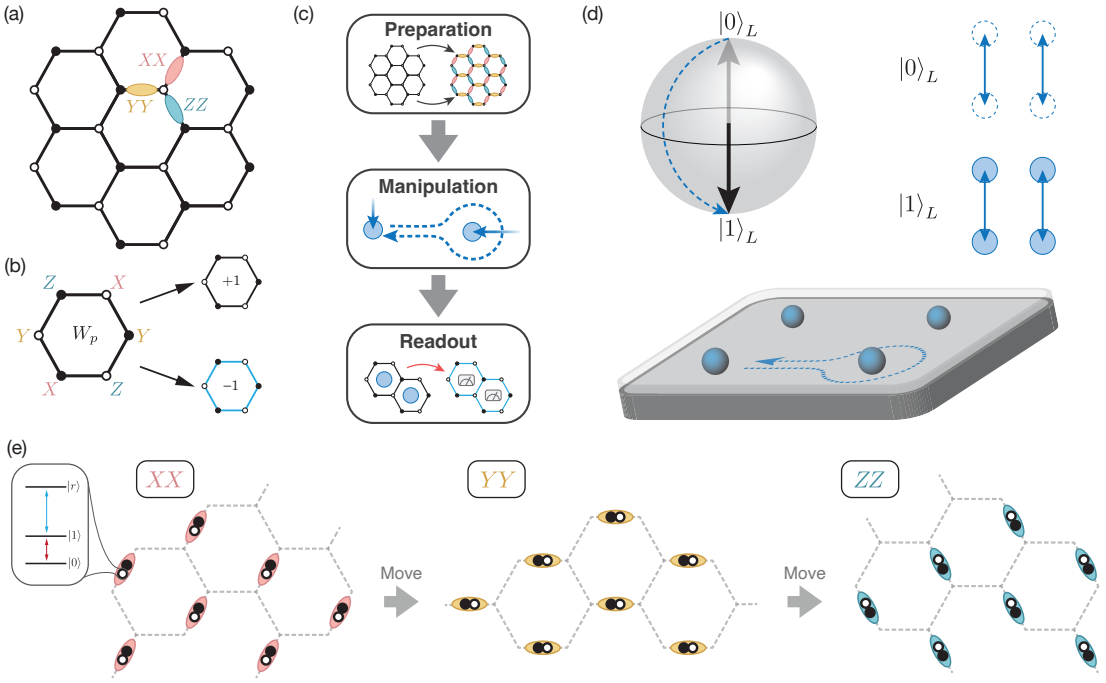


Figure 5.1: Kitaev honeycomb model on a digital Rydberg simulator. (a) The three types of spin-spin interactions H_X, H_Y, and H_Z applied along the three directions of the honeycomb lattice together form the highly anisotropic Kitaev honeycomb model described by the Hamiltonian H_0 in Eq. (5.4). After breaking the time-reversal symmetry, this model hosts a gapped non-abelian phase. (b) The plaquette operators $W_p = Y_1Z_2X_3Y_4Z_5X_6 = \pm 1$ commute with all the link operators H_X, H_Y, H_Z and form an extensive set of conserved quantities. We associate the presence of a $\mathbb{Z}_2$ vortex at the plaquette p if $W_p = -1$. The ground state has no vortices, i.e., $W_p = +1$ for all p. (c) In this work we develop the toolbox for the three capabilities necessary to fully probe a non-abelian system on a digital simulator: state preparation, manipulation, and readout. (d) Four Majorana zero modes encode a topological qubit, as they span a two dimensional Hilbert space (for the case shown here) that is separated by the gap from the rest of the spectrum. The logical states $|0\rangle_L, |1\rangle_L$ correspond to the unoccupied and occupied zero mode, respectively. Measurement in the logical Z_L or X_L basis is performed by fusing the majoranas in an appropriate configuration, and measuring the presence of a fermion particle. Moving the Majorana particles around each other performs non-trivial unitary operations in the logical subspace—a manifestation of their non-abelian nature. (e) The spin degrees of freedom are encoded in the magnetically insensitive hyperfine states $\{|0\rangle, |1\rangle\}$ of ^{87}Rb atoms and a highly excited Rydberg state $|r\rangle$ is used to perform two-qubit entangling gates. We utilize reconfigurable Rydberg arrays to implement the Floquet Hamiltonian of the Kitaev spin liquid in a parallel fashion. This approach is simple, scalable, and all of its components have already been demonstrated in recent experiments[568].

realizes the Kitaev honeycomb model[762], which describes a highly anisotropic spin system on a honeycomb lattice [Fig. 5.1(a)]. This model features several gapped abelian topological phases when $|J_\alpha| > |J_\beta|, |J_\gamma|$, and a gapless non-abelian phase where the linear dispersion is protected by the time-reversal symmetry. That symmetry needs to be broken in order to introduce a gap in the spectrum, which is necessary for a finite correlation length of the excitations thus making them localizeable. The first-order dynamical correction to the effective Hamiltonian,

$$H_1 = -\frac{i\tau}{2}([H_X, H_Y] + [H_X, H_Z] + [H_Y, H_Z]), \tag{5.5}$$

which consists of three-body operators of the form $X_i Y_j Z_k$, breaks the time-reversal symmetry since the signs depend on the particular ordering of applied Hamiltonians in (5.2); here, H_X, H_Y, H_Z. Because the gapped phase disappears in the static, high frequency limit $\tau \to 0$, the effective Hamiltonian realizes an intrinsically dynamical Floquet spin liquid. In the latter part of this work, we develop more sophisticated sequences to further suppress higher-order terms in Eq. (5.3), enabling coherent control of the particles, while at the same time, controlling the relative signs and magnitudes of the desired three-body terms H_1. We discuss this procedure, and a more specialized approach for the state preparation, in Sec. 5.3. Similar dynamical constructions have been used to propose Floquet SPT phases[898] and the realization of chiral edge phenomena[893].

The Kitaev Hamiltonian $H_0 + H_1$ has an extensive number of conserved quantities given by plaquette operators [Fig. 5.1(b)],

$$W_p = Y_1 Z_2 X_3 Y_4 Z_5 X_6, \tag{5.6}$$

for each plaquette $p \in \{1...\mathcal{M}\}$ where $\mathcal{M} = N/2$ is the total number of plaquettes and N is the number of spins in the system. The collection of values $\mathcal{W} = \{W_p = \pm 1 \,|\, p \in 1...\mathcal{M}\}$ defines a symmetry sector and it can be shown that the ground state lies in the sector where $W_p = +1$ for all p[799]. We associate the presence of a $\mathbb{Z}_2$ vortex on the plaquette p if $W_p = -1$ and call the collection $\mathcal{W}$ a "vortex sector"; in this language the ground state is vortex-free. Even though the number of symmetries is extensive, the vortex configuration does not specify the wavefunction exactly and each sector has a Hilbert space of dimension $2^{N/2}$.

Before proceeding we note that in many previous proposals, including the original work of Kitaev[762], the time-reversal symmetry was broken in a perturbative fashion—either by applying an external magnetic field[762] or introducing ancillary gadgets to mediate interactions[1002]. A key advantage of our dynamical scheme is that the time-reversal symmetry is broken without creating vortices: Each driving term in (5.2) separately commutes with the plaquette operators, $[H_{Z,X,Y}, W_p] = 0$, so the effective Hamiltonian commutes as well $[H_F[\tau], W_p] = 0$, irrespective of τ. Additionally, each of the Hamiltonians $H_{X,Y,Z}$ can be written as a free fermion Hamiltonian[762], which means the heating due to trotterized time evolution is significantly suppressed and does not grow indefinitely[784,690]; see Appendix ?? for more details. This makes our Floquet spin liquid especially attractive for experimental implementation, where trotter heating can be a limiting factor. The implementation can also be made hardware efficient, especially on reconfigurable Rydberg atom arrays, where dynamically toggling between $H_{X,Y,Z}$ is a natural operation[568].

5.2 Experimental Implementation

Recently, Rydberg atom arrays have been used to implement analog simulation of quantum spin systems with Ising[648,917] and XXZ[921] Hamiltonians, using programmable, fixed atom geometry. Most recently, a new architecture introduced coherent and parallel transport of atoms allowing for dynamically re-configurable connectivity[568]. In this approach, qubits are encoded in two magnetically insensitive hyperfine (HF) states $|0\rangle$,$|1\rangle$ while excitation to the Rydberg state $|r\rangle$ is used for performing entangling gates [Fig. 5.1(e)]. This encoding provides long coherence times, enabling the execution of tens of thousands of parallel moves. Even for hundreds of qubits, the quantum gates can be performed by illuminating the atoms with a global laser beam which provides a native parallelism of quantum operations with little to no cross-talk[795,661], thanks to the rapidly decaying van der Waals interactions. Therefore, reconfigurable Rydberg atom arrays are easily scalable and especially well suited for performing parallel quantum circuits where during each step, or gate layer, each qubit participates in at most one gate.

Here we describe how the Floquet unitary (5.2) can be implemented in this experimental platform in a hardware-efficient manner. Since the honeycomb lattice is bipartite, every link connects the odd (●) and even (○) sublattices; see Fig. 5.1(a). Therefore, the evolution under each of the two-body Hamiltonians H_X,H_Y,H_Z can be implemented within a single gate layer using a global pulse that simultaneously acts on all qubits. This pulse performs the two-body gate $\mathcal{G}_2(\theta) = e^{i\theta ZZ}$, which is equivalent to a controlled phase gate up to local Z rotations. First, the atoms are all transported in parallel and brought together along the XX links [see Fig. 5.1(e)], and a Raman pulse performs a global single-qubit gate that changes the basis from Z to X in the HF man-

ifold. Then, the entangling gate operation $\mathcal{G}_2$ is applied to all pairs in parallel, which effectively performs $e^{-iH_X\tau}$. The atoms are then transported again to the next link configuration and the procedure is repeated, with an appropriate basis change in-between, requiring at all times only a single family of entangling gates (controlled phase gates). The dynamical change of connectivity in a system of 10s-100s of qubits available in Rydberg atom arrays is central to the realization of our Floquet protocol. Moreover, such programmability allows us to implement periodic boundary conditions without significant overhead, which removes gappless edge modes that obstruct ground state preparation under open boundary conditions.

The characteristic coherence time of such a digital simulation depends on the error rates of the constituent components. In particular, since the global single-qubit gates within the HF manifold and the transport of atoms have negligible effect on the coherence of stored qubits[942,792,568], the errors will be dominated by the two-qubit operations. Most recently, control-Z Rydberg gates with fidelities beyond 99.5% have been demonstrated[661], and are expected to go above 99.9% in the near future. Moreover, the control-Z gate is a special case of the $\mathcal{G}_2$ gate ($\theta = \pi/4$) and similar gates with smaller angles are faster and therefore expected to work at even higher fidelities.

While the implementation in reconfigurable Rydberg tweezer arrays is particularly efficient, the scheme described in the this work can be realized in other quantum simulation platforms. For example, trapped-ion quantum charge-coupled devices[890,728] support dynamical connectivity while superconducting-qubit devices allow for selective application of two-body gates[913], both of which can be used to realize the Floquet cycle as described here.

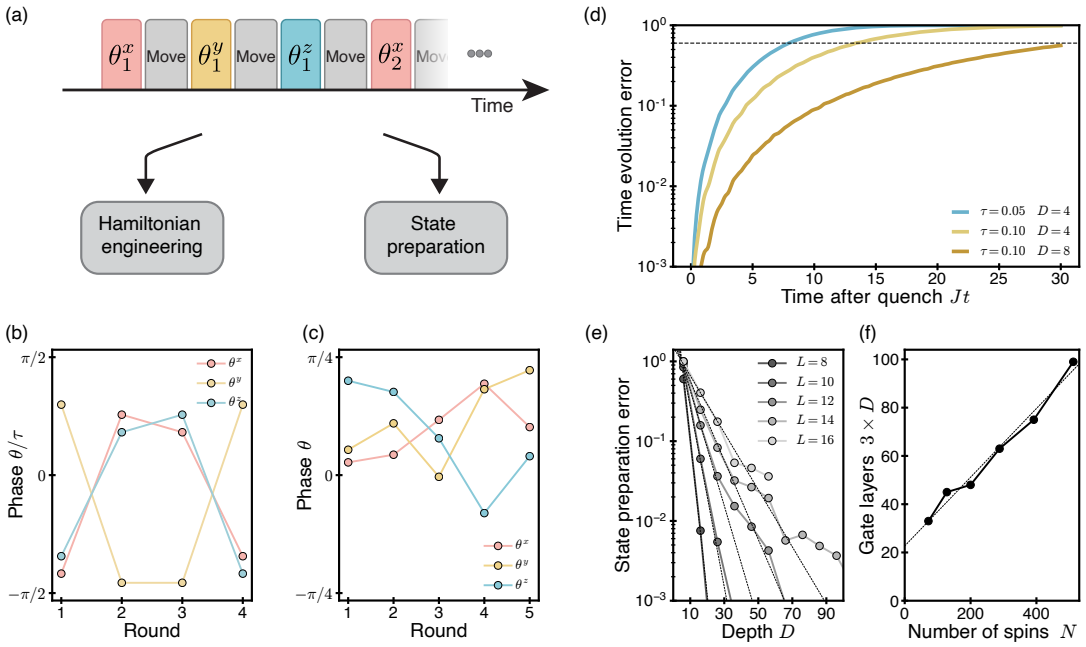


Figure 5.2: Variational circuits for Hamiltonian engineering and state preparation. (a) The circuit ansatz from Eq. (5.7) suffices for efficient approximation of the target Hamiltonian as well as finding specialized circuits for state preparation. The variational circuit yields pulse sequences that result in Floquet Hamiltonians where both the strength and signs of couplings can be controlled. Preparing a certain output state is less demanding then reconstructing a many-body operator; thus, with the same variational ansatz, we can prepare the non-abelian ground state more efficiently than performing adiabatic evolution both in terms of the gate count and resulting fidelities. (b-c) Phases obtained through variational optimization on a relatively small 30-qubit system realizing effective Hamiltonian evolution and variational state preparation, respectively. (d) For engineered Floquet Hamiltonians, longer pulse sequences can systematically improve the approximation to the target Hamiltonian H. (e) Performance of the variational state preparation on an $L \times L$ lattice. Error in the final state as a function of the circuit depth D for several system sizes. The error decreases exponentially with D as $1-\mathcal{F} \propto \exp(-AL^{-\alpha}(D-D_0))$ for low depths; we estimate $\alpha \approx 2.43$, $A \approx 73$, and $D_0 = 5$. (f) The number of two-qubit gate layers necessary to achieve the many-body state fidelity of 90% for a system of $N = 2L^2$ spins.

5.3 Variational Optimization for Near-term Devices

In this section, we describe a procedure to systematically construct high-fidelity pulse sequences for resource efficient Hamiltonian simulation and state preparation through variational optimzation, guided by physical insights and experimental simplicity.

As described in Eq. (5.3), the symmetry-breaking three-body terms appear in the first order of the Magnus expansion in the Floquet unitary (5.2). Thus, the repeated application of this unitary, with an appropriate value of τ, should already resemble the time evolution under H to a certain degree. We can further improve the fidelity if we promote the individual phases to variational variables which we then optimize. Concretely, the circuit ansatz of depth D consists of D blocks based on the Floquet unitary in Eq. (5.2),

$$U_D(\{\theta\}) = \prod_{i=1}^{D} U_b(\vec{\theta}_i), \tag{5.7}$$

where $\{\theta\}$ enumerates the set of all variational parameters. The ith block, $U_b(\vec{\theta}_i)$, is

$$U_b(\vec{\theta}_i) = e^{i\theta_i^x XX} e^{i\theta_i^y YY} e^{i\theta_i^z ZZ}, \tag{5.8}$$

where XX, YY, ZZ denote the respective two-qubit gates applied to all appropriate links in parallel—this corresponds to Eq. (5.2) with the couplings promoted to variational variables. Thus, a circuit ansatz of depth D consists of $3D$ two-qubit gate layers interleaved with global single-qubit rotations.

Within a fixed vortex sector, the Floquet dynamics are exactly solvable and the individual terms correspond to quadratic, free-fermion operators; see Ref.[762] and Appendix ??. This enables efficient analytical/numerical treatment of the circuit in Eq. (5.7) including calculation of gradients $\partial_{\vec{\theta}} U_D$. In particular, we can simulate a sys-

tem of N sites by working with matrices of size $N \times N$. Then, we are free to optimize the phases $\{\theta\}$, and hence the pulse sequence, using our choice of a numerical optimization method. The cost function Q to be minimized would depend on the specific application. Moreover, the translational invariance of the system enables us to analytically evaluate low-order terms in the Magnus expansion. In the next section, we use it to build intuition underlying good solutions to the variational problem.

5.3.1 Effective Hamiltonian

First, we focus on constructing effective Floquet Hamiltonians using the variational ansatz above. Specifically, we minimize the cost function

$$Q_H = \left\| U_D(\{\theta\}) - e^{-iH\tau} \right\|_F^2$$

using gradient descent starting from a randomized symmetric configuration of phases, as described below. The norm we use is the squared Frobenius norm $\|A\|_F^2 = \mathrm{tr}\{AA^\dagger\}$, which is amenable to simple gradient calculation; see Appendix ?? for details.

An example pulse for $\tau = 0.05$ and $D = 4$ is presented in Fig. 5.2(b). Here, the general structure can be understood as the optimizer fixing the correct signs and magnitudes of the target three-body terms. The intuition that such a symmetric configuration of phases is enough for this purpose can be inferred from a simpler $D = 2$ case where we parameterize all phases with two variables φ, δ, $U_2 = e^{i(\varphi-\delta)H_X} e^{i\varphi H_Y} e^{i(\varphi+\delta)H_Z} e^{i(\varphi+\delta)H_X} e^{i\varphi H_Y} e^{i(\varphi-\delta)H_Z}$.

The first two orders of the Magnus expansion are $H_F^{(0)} = 2\varphi H_0$ and

$$\begin{aligned} -iH_F^{(1)} &= \varphi(\varphi - \delta)[H_X, H_Y] \\ &\quad + (\varphi^2 - 2\varphi\,\delta - \delta^2)[H_X, H_Z] \\ &\quad + \varphi(\varphi - \delta)[H_Y, H_Z]. \end{aligned}$$

In particular, by choosing δ appropriately, we can make the $[H_X, H_Z]$ coefficient negative while keeping $[H_Y, H_Z]$ and $[H_X, H_Y]$ positive. Demanding the two have opposite signs and equal magnitude—which guarantees uniform couplings when combined with the signs from commutators—we get the condition

$$0 = 2\varphi^2 - 3\varphi\delta - \delta^2 \qquad \Rightarrow \qquad \delta = (-3 \pm \sqrt{17})\varphi/2,$$

which we can straightforwardly solve. This simple example shows that we can freely tune the strength and signs of the three-body terms arising in $H_F^{(1)}$.

Unfortunately, reducing the contribution of higher-order terms $H_F^{(n>1)}$ while preserving the first two is a formidable challenge and we empirically find that the variational landscape has many local minima and plateaus making the optimization result strongly dependent on a good initial seed. However, it is much easier to find good $H_F[\tau]$ for small τ and thus the following recursive procedure turns out to be successful: After obtaining a good approximation to $H_F[\tau]$ at depth D, we apply the $e^{-iH_F[\tau]\tau}$ unitary twice and use it as an initial guess for a depth-$2D$ approximation to $H_F[2\tau]$. This corresponds to evolving the system for time 2τ and asking the optimizer to correct the combined discrepancies, which intuitively should be perturbatively small in τ and thus amenable to gradient-based methods.

The results are presented in Fig. 5.2(d) where the many-body evolution is simulated with various effective Hamiltonians and the failure rate of this process is measured via the many-body state overlap as $1-\left|\langle e^{iH_F[\tau]t}e^{-iHt}\rangle\right|^2$. As expected, the $H_F[\tau=0.1]$ evolution (yellow) at $D=4$ outperforms the $D=4$ simulation with $H_F[\tau=0.05]$ (blue) by a factor of 2 in the time it takes to reach a certain threshold (dashed line); intuitively, this is consistent with the $\tau=0.05$ circuit requiring twice the number of gates for the same physical time Jt. However, the $D=8$ Hamiltonian $H_F[\tau=0.1]$ (brown) obtained by the above-mentioned recursive construction allows for 6 times longer time evolution while requiring the same number of total applied gates as the $\tau=0.05$ case. While the improvement is not surprising, we found that already at circuit depth $D=8$ it is difficult to find reasonable solutions without guided initial state and thus this iterative procedure is essential for finding good Hamiltonians at larger τ, allowing for long evolution time. The general task of finding optimal pulse sequences is an interesting optimization problem and could be a fertile ground for quantum signal processing[828] and machine learning methods, which have been used in the past to successfully engineer robust pulse sequences for nuclear magnetic resonance (NMR)[883].

5.3.2 Variational state preparation

In principle, an efficient Floquet Hamiltonian enables both the energetically protected operations on the non-abelian excitations and adiabatic state preparation. However, each Hamiltonian evolution step requires several gate layers, which limits the total available evolution time. We find that the state preparation step can be significantly improved, compared to the adiabatic state preparation, by employing the same variational methods used to develop efficient Floquet Hamiltonians. Intuitively, it is easier to transform a given initial vector to the final one (state preparation) compared

to approximating many-body evolution on the full Hilbert space (effective Hamiltonian construction). Again, we use the same circuit ansatz from Eq. (5.7) but instead of minimizing a Frobenius norm of the Hamiltonian evolution we choose to use the many-body state overlap as the cost function for the optimizer,

$$\mathcal{Q}_{\mathrm{VSP}} = -\left|\langle \psi_{\mathrm{fin}} | U_D(\{\theta\}) | \psi_{\mathrm{ini}} \rangle\right|^2,$$

where ψ_{ini} and ψ_{fin} are the initial and target states, respectively. This cost function and its gradient can also be evaluated efficiently using the free-fermion picture; see Appendix ?? for details.

In Fig. 5.2(e), we present the performance of variational state preparation (VSP) for ψ_{ini} and ψ_{fin} being the vortex-free ground states of H_Z and H, respectively. The ground state of H_Z is obtained by projecting a product state ψ_0 into the no-vortex symmetry sector, which can be done in a single step by performing projective measurements of W_p operators or, alternatively, by passively cooling the state using conditional gate operations which progressively remove vortices; we describe these procedures in Appendix ??. The task accomplished by the VSP corresponds to the transition from the toric code (the abelian phase) to the non-abelian chiral phase. We find that the error in the preparation of the target state decreases as $\exp(-DL^{-\alpha})$ in the low-depth regime, where $L = \sqrt{N/2}$ and we numerically estimate $\alpha \approx 2.43$. Remarkably, even though the circuit depth scales with the system size—as required since crossing a phase transition involves building up long-range order—the depth necessary for state preparation is accessible in Rydberg atom arrays even for hundreds of spins. We note that a similar state preparation scheme, although not employing the Floquet stabilization of the non-abelian phase nor experimental co-design, has been

explored in Ref.[561].

The many-body fidelity is convenient for optimizing the performance of the VSP but it is not very useful for experimentally assessing the quality of the final state and its robustness to errors. For this purpose, we additionally benchmark the state preparation under a control noise model. We simulate a VSP circuit, which prepares a logical state encoded in the ground state, with the optimal phases modified by errors sampled from a uniform distribution. We then read out the logical state with our dynamical quench protocol (discussed later) and the outcome allows us to quantify the quality of the prepared state in an experimentally feasible way. We find that even imperfect state preparation results in a high probability of correct measurement outcome, up to large phase fluctuations of $\delta\theta \approx 0.06$. This suggests that our state preparation procedure is, to a certain extent, robust against these types of errors; the details of this benchmark can be found in Appendix ??.

We also point out a subtlety related to the different ground-state degeneracy of the abelian and non-abelian phases: The dimension of the ground-state manifold in the toric code phase is 4, while for the non-abelian phase it is 3. This means that one of the ground states is not adiabatically connected to the non-abelian theory and becomes an excited state. By choosing an appropriate initial product state $|\psi_0\rangle = |0\rangle^N$, we ensure that the system is orthogonal to this undesired state. We discuss this important point in more detail in Appendix ??.

Finally, we note that Hamiltonian learning methods[768,880] could be used to confirm the preparation of the non-abelian phase without the need for sophisticated control of the excitations. Similarly, variational state preparation combined with effective Hamiltonian evolution suffice to probe the chiral nature of the edge modes. However, performing basic TQC operations, such as braiding and fusion measurements, not

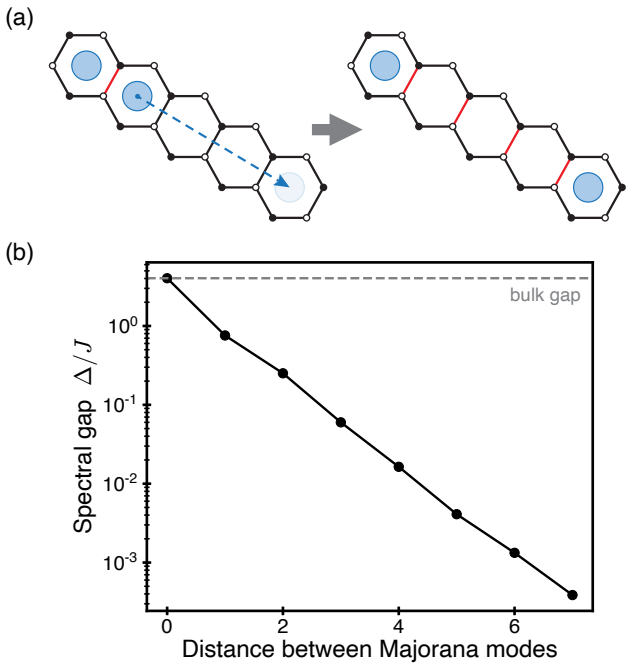


Figure 5.3: Majorana zero modes. Movement of non-abelian modes can apply non-trivial unitary operations to the logical subspace. (a) Two modes localized on adjacent plaquettes are created when the sign of a single bond coupling is adiabatically flipped (red). The flipping of subsequent bonds in a ladder-like pattern allows for their transport. (b) As the modes are moved away from each other, their energy decreases exponentially fast with the separation distance, eventually resulting in the Majorana zero modes. The degenerate logical subspace encodes the protected qubit: The empty mode corresponds to $|0\rangle_L$ and the occupied one to $|1\rangle_L$. See also Fig. 5.1(d).

only verifies the non-abelian nature of the particles but also paves the way to more complex computing tasks. In the rest of this work we focus on describing steps necessary to achieve these goals.

5.4 Controlling non-abelian excitations

One of the remarkable properties of the Kitaev honeycomb model is the presence of excitations that exhibit non-abelian statistics, specifically of the Ising anyon type[867]. Unlike the abelian anyons present in the toric code model[760], operations on the non-

abelian σ particles result in unitary matrices—not only a global phase—acting on the logical qubit subspace. In this section, we present the steps necessary to create, manipulate, and read out the non-abelian σ particles, which hold Majorana zero modes. For the rest of this work, we will use the terms "Majorana zero mode" and "σ particle" interchangeably.

5.4.1 Creating and moving zero modes

To create Majorana zero modes, first the sign of a single bond can be flipped adiabatically, which affects the J coupling and the overlapping three-body terms in the extended Hamiltonian H, without changing the vortex sector $\mathcal{W}$[1002]. This modifies the spectrum, turning one of the excited fermion eigenstates states into a low-energy bound state localized around the flipped bond. As a chain of adjacent bonds are adiabatically flipped, the energy of the original fermion state decreases exponentially with distance, rapidly approaching a zero energy mode that can be occupied at no cost. This forms a nearly-degenerate two-dimensional ground space. Furthermore, local measurements can no longer determine whether the originally excited state is occupied or unoccupied; hence these states form topologically protected "logical states" ($|0\rangle_L$ and $|1\rangle_L$) which we identify with sectors 1 and ψ respectively.

Taken together, this degenerate subspace can also be interpreted as two Majorana zero modes, supported on plaquettes connected by the flipped bond [Fig. 5.3]. Since the global fermion parity is conserved, the simplest non-trival system consists of four Majorana modes, which span a two-dimensional logical subspace. For a given pairing, these two states correspond to no fermions (11) or two fermions present ($\psi\psi$) [Fig. 5.1(d)]. This two-level system can be manipulated by transporting Majorana modes. This can be done in a topologically and energetically protected way by adia-

batically flipping the signs of appropriate bonds using the effective Hamiltonian evolution.

Our Floquet approach to stabilizing the excitations has the crucial advantage that a local modification of phases in the variational ansatz (5.7) automatically modifies, to leading order, the emergent three-body terms in an appropriate manner. The variational circuit is straightforwardly extended to include such local modifications, and can be optimized at every step if necessary. Experimentally, local phases can be realized either with local Rydberg laser control or by separating local terms into separate gate layers.

5.4.2 Localized fermion readout

The key step necessary to complete the particle fusion is the readout of the localized fermion state (either 1 or ψ). In our case, these fermions are formed from two adjacent Majoranas, $\psi = (c_1 + ic_2)/2$, brought together to perform fusion, as in the final step of Fig. 5.5(a). In other words, we want to check whether the two Majorana modes are paired or not. In our figures we indicate such pairing checks with solid blue arrows. The key insight is that the magnetic field in the Z direction, applied to the bond shared by the adjacent Majorana particles, couples the ψ particle to an empty state with two vortices [Fig. 5.4(a)]; i.e, it destroys a fermion and flips adjacent plaquettes. This state, without a localized fermion, is the ground state in the two-vortex sector. Because the initial state couples strongly to another eigenstate, the two effectively form a detuned two-level system (TLS) with the detuning Δ on the order of the bulk gap; see Appendix ?? for the details of this TLS model. Alternatively, if the fermionic mode is initially empty, we create a localized fermion mode in addition to the two vortices. However, in the two-vortex sector, there is no localized-fermion state

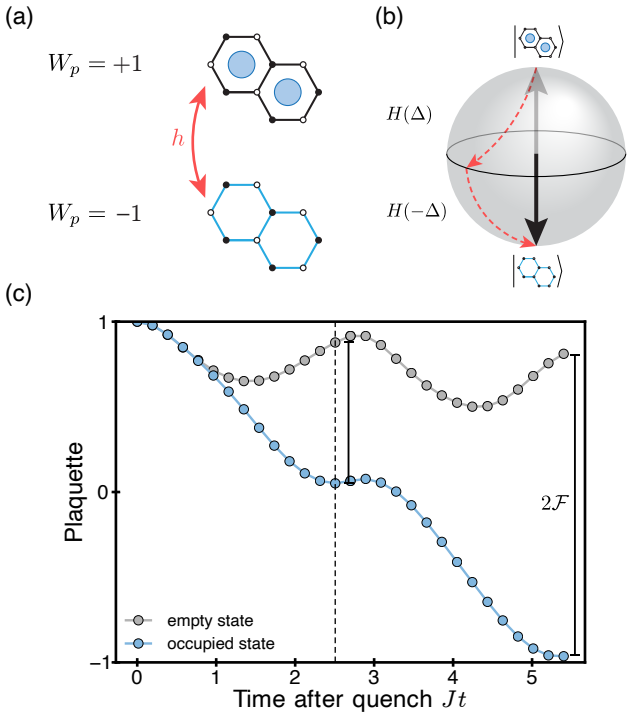


Figure 5.4: Readout of the localized fermion. (a) Magnetic field h creates/annihilates the localized fermion mode and flips the neighboring plaquettes. This allows for mapping the presence of a local excitation to a spin observable. (b) The effective two-level system is conveniently represented on a Bloch sphere. We use a two-part pulse consisting of the Rabi drive under the Hamiltonian $H(\Delta)$ and the second equally long evolution under $H(-\Delta)$ with an opposite sign of the detuning. (c) The plaquette expectation value for the two states of interest under evolution with the two-stage pulse sequence. The opposite detuning is achieved by utilizing the digital nature of the simulation and applying $-H$ instead of H. The use of the composite pulse increases the contrast from $\mathcal{F} = 0.43$ (first pulse, dashed line) to $\mathcal{F} = 0.89$ (both pulses).

and the momentum eigenstates form a band with quadratic dispersion. Hence, the empty state is weakly coupled to a detuned continuum, and the response to the local magnetic field quench is different than for the occupied state discussed above.

This discrepancy in the response allows us to differentiate between the two states in an experiment: We utilize the strong coupling to map the ψ particle to the two $\mathbb{Z}_2$ vortices whose presence is read-out by measuring the adjacent plaquette operator W_p—a simple spin observable. This realizes a measurement within the TQC frame-

work. It is also similar in spirit to phase measurements in AMO systems. We emphasize that our protocol does not depend on any fine-tuned parameters and can be calibrated independently in a small-scale experiment.

In Fig. 5.4(c), we show the time evolution of the relevant plaquette expectation value $\langle W_p \rangle$ after the quench. As expected, we observe a much stronger response during the quench from the occupied fermionic mode compared to the empty one. The figure of merit for the readout is the difference between the two cases

$$\mathcal{F} = \left| \langle W_p \rangle_{\text{emp.}} - \langle W_p \rangle_{\text{occ.}} \right| /2, \tag{5.9}$$

and, ideally, we could map the empty state to $\langle W_p \rangle_{\text{emp.}} = +1$ and the occupied state to $\langle W_p \rangle_{\text{occ.}} = -1$. That would allow us to distinguish them with perfect fidelity $\mathcal{F} = 1$. Unfortunately, the system undergoes detuned oscillations in the TLS, never achieving the maximal contrast. However, we can leverage the two-level analogy, and the flexibility of digital simulation, to devise robust composite drives that increase the fidelity dramatically. Such pulses have long been used in the NMR community. We find that a simple two-stage composite drive already increases $\mathcal{F}$ substantially. It consists of the time evolution until the first local minimum and the subsequent evolution for the same time albeit with a negative detuning [Fig. 5.4(b)]. We achieve the negative detuning by keeping the local magnetic field fixed while driving with $-H$, an easy task in our digital approach. In Fig. 5.4(c), the first pulse lasts until the dashed line and the use of the composite pulse improves the fidelity from $\mathcal{F} = 0.43$ to $\mathcal{F} = 0.89$.

Including effective magnetic fields in the model prevents the exact solution and makes the analysis of the system much more difficult. However, we can obtain an approximate solution using the fermionic Gaussian state (FGS) ansatz[773,944]—this

choice is well motivated here since eigenstates in well-defined vortex sectors are exactly Gaussian. Hence, we expect this variational ansatz to interpolate well between them. We find that the FGS predictions are in good agreement with the exact results for small system sizes and short to intermediate times; see Appendices ?? and ?? for details.

In the effective Hamiltonian, we include the magnetic field by performing a single-qubit Z-phase gate $e^{i\theta Z}$ at the appropriate site; since the field is local, this first-order treatment is enough to approximate the full Hamiltonian evolution. Finally, because the readout procedure depends only on local quenches, it can be calibrated in a relatively small 30-qubit experiment where the degree of control over the state is much larger, and subsequently used in the full-scale simulation. We describe such a protocol in detail in Appendix ?? and supplement it with exact spin-picture simulations. We note that going beyond quench dynamics, and optimizing the performance of this readout scheme with a variational procedure, is an interesting direction for future work.

With these tools, allowing for the preparation, movement, and readout of the excitations, it should now be possible to perform the two basic experiments characterizing an anyonic theory: Fusion and braiding. We describe them briefly in the following section.

5.5 Fusion and Braiding

First, we consider a procedure to confirm the non-abelian fusion rule,

$$\sigma \times \sigma \to 1 + \psi, \tag{5.10}$$

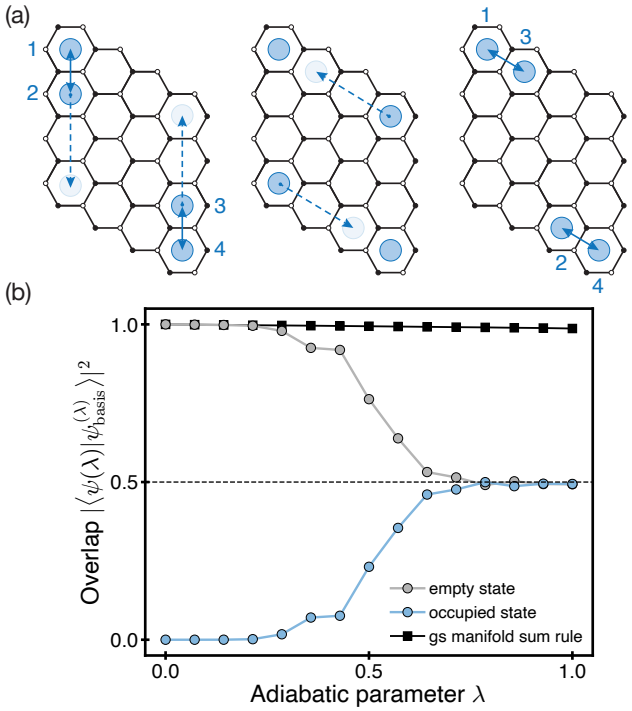


Figure 5.5: Fusion of non-abelian anyons. (a) Two pairs of Majorana modes (1,2 and 3,4) are created in the logical $|0\rangle_L$ state (empty zero mode) and subsequently moved and brought together in a different configuration. During each step the modes are moved a single site by adiabatically flipping the sign of the subsequent bond. (b) Many-body overlap with instantaneous logical basis states along the adiabatic path. The λ=0, 0.5, and 1.0 correspond to initial, intermediate, and final state of the fusion experiment depicted in (a). This adiabatic process corresponds to a change of logical basis or, equivalently, applying a Hadamard gate. The simulation was performed on an $L \times L$ lattice with L=20 with an idealized, target Hamiltonian. In practice, this will be realized using Floquet circuits (see Fig. 5.2). The modes are initially placed on neighboring plaquettes and the two pairs are separated by $L/2 - 2$, which results in the total of $2(L/2 - 2 - 1) = 14$ steps necessary to complete the fusion. For braiding at a characteristic distance $\lfloor \frac{L}{3} \rfloor$, the required number of steps is $9\lfloor \frac{L}{3} \rfloor - 23$.

corresponding to the recombination of two σ particles. Unlike the toric code case, where combining two particles always gives a deterministic result, here fusing σ particles can, under certain circumstances, produce either a vacuum state or a ψ fermion, with equal probabilities. This behavior is a hallmark of a non-abelian theory[867].

We initialize the logical $|0\rangle_L$ state by preparing two pairs of unoccupied Majorana modes (labeled 1-2 and 3-4) using the adiabatic protocol described in the previous part. Next, we move modes 2 and 3 in such a way that they recombine in the opposite pairing [Fig. 5.5(a)]; i.e., 1-3 and 2-4. In the language of TQC, this operation corresponds to the measurement in an orthogonal basis, e.g., $\{|+\rangle_L, |-\rangle_L\}$, and thus we expect both results to appear with equal probability. Physically, along the adiabatic path, the states become exponentially degenerate (zero modes) and thus the transition from one configuration to another is maximally diabatic, resulting in equal superposition of the final states $|11\rangle + |\psi\psi\rangle$. The evolution of the state can be traced by monitoring the state's decomposition in terms of the instantaneous logical basis [Fig. 5.5(b)]. Finally, we check for the presence of the ψ fermion with our dynamical quench protocol. In experiment, measuring equal weights of the vacuum and ψ states, combined with the high correlation between the two pairs, would confirm the non-abelian fusion rule (5.10).

Fusion rules do not specify an anyonic theory completely. On top of it, we need to identify the braiding properties of excitations; i.e., the transformations of the degenerate state manifold upon moving anyons around each other. As we have discussed in the case of fusion, swapping the modes 2 and 3 results in the application of a $\pi/2$ rotation on a Bloch sphere, or equivalently a change of basis. Now, performing this operation twice (in a way that results in mode 2 looping around mode 3) corresponds

to applying the $\pi/2$ rotation twice—resulting in a π-pulse that encodes the

$$U_{\text{braid}} = \begin{pmatrix} 0 & 1 \\ 1 & 0 \end{pmatrix} \tag{5.11}$$

operation in the logical manifold up to global phases. The initial configuration is the same as the fusion experiment, but now mode 2 is looped around mode 3 and the logical state is measured in the original basis; i.e., 1-2 and 3-4. At the end, we end up in the starting configuration, but a non-trivial braid has been completed between the Majorana particles.

After completing the braiding operation, we should end up in a flipped state: $|0\rangle_L \to |1\rangle_L$, which can be verified by performing the readout and measuring the state $|1\rangle_L$ with probability close to unity. This concludes the characterization of the non-abelian properties of the excitations in the system.

5.6 Resource estimates and experimental feasibility

Next, we discuss resources necessary to implement our proposal in quantum hardware. In Rydberg atom arrays, two-qubit gate fidelities are the dominant source of error, compared to extremely efficient single-qubit gates and atom transport[942,792,568], and thus we focus on the number of two-qubit gate layers necessary. We summarize our findings in Table. 5.1, where we assume a time step $J\tau = 0.25$ for the time evolution and the readout procedure; this value is large enough to enable efficient implementation while still ensuring good performance of fusion and braiding operations. We emphasize that even larger trotter angles do not necessarily lead to the breakdown of the topological phase due to the free-fermion nature of the honeycomb model, see Ap-

pendix ?? for details. The resource estimates for these circuits are quite favorable for

Table 5.1: Gate-layer estimate for the proposal. The number of required two-qubit gate layers varies between the different steps of the proposal. Several ingredients, such as state preparation, can be realized in current experimental platforms. The estimate is performed for a system size with $N = 2L^2$ qubits and the time evolution implemented with depth-D circuit.

Stage	Number of gate layers	Source
Initial projection	6	App. ??
State preparation	$22 + 0.3L^2$	Fig. 5.2(f)
Time evolution (1 step)	$3D$	Eq. (5.7)
Topological readout	$60D$	Fig. 5.4
Total (edge dynamics)	$28 + 0.3L^2 + 30D$	App. ??
Total (fusion)	$28 + 0.3L^2 + 12D(L-1)$	Fig. 5.5
Total (braiding)	$28 + 0.3L^2 + 12D(9\lfloor\frac{L}{3}\rfloor - 18)$	Fig. 5.5

near-term experimental exploration of the non-abelian phase. For example, preparation of the non-abelian phase in a 72-qubit system would consume only 33 two-qubit gate layers. This remarkable efficiency is a direct result of the hardware-efficient encoding, utilizing simple Floquet sequences of parallel two-qubit gates and global single-qubit rotations to generate the higher-order terms that stabilize the non-abelian phase.

Finally, we estimate the achievable many-body fidelity in near-term devices with faulty two-qubit gates. There are two competing processes: Longer sequences can ideally achieve higher state preparation fidelity, but accumulate more errors due to noisy entangling operations. To estimate the optimal circuit depth D_*, for a given two-qubit gate fidelity f, we use the heuristic scaling presented in Fig. 5.2(e) and assume an exponential decay of the many-body fidelity with the circuit volume,

$$\mathcal{F}(D,f) \sim (1 - e^{-A(D-D_0)L^{-\alpha}}) f^{6L^2 D}, \tag{5.12}$$

which allows us to calculate the optimal depth $D_*(f)$ and the corresponding maximal many-body overlap $\mathcal{F}_*$. In Fig. 5.6, we plot D_* and $\mathcal{F}_*$ as a function of the system size N and the gate fidelity $f = 1 - 10^p$. Since current state-of-the-art devices can readily reach $f > 0.995$ and are projected to achieve $f > 0.999$ in the near-term, our estimate shows that significant many-body overlap with the topological ground state can be achieved in large systems of approximately a hundred qubits. In practice, the many-body fidelity is the most stringent measure and generically decays exponentially with system size. As such, signatures of the non-abelian topological phase should remain visible at larger system sizes as well.

5.7 Discussion and Outlook

The results presented in this work indicate that non-abelian Floquet spin liquids can be dynamically created through applications of periodic pulse sequences in a hardware-efficient manner. In particular, we developed a dynamical protocol where the desired gapped Hamiltonian is obtained by engineering higher orders of the Magnus expansion and constructed efficient pulse sequences that approximate the target Hamiltonian and state preparation. These tools can be utilized to encode logical information in the Majorana zero modes that can be adiabatically created and controlled with our effective Hamiltonian approach, providing a blueprint for exploring non-abelian phases of matter using Rydberg atoms arrays in the near-term. In particular, the Hamiltonian realization leads to energetic protection against coherent errors, such as control errors or spurious magnetic fields which induce local unitary rotations. In contrast, in a realistic simulation, incoherent errors will build up over time, unless removed by cooling. Developing hardware efficient cooling for the models studied here,

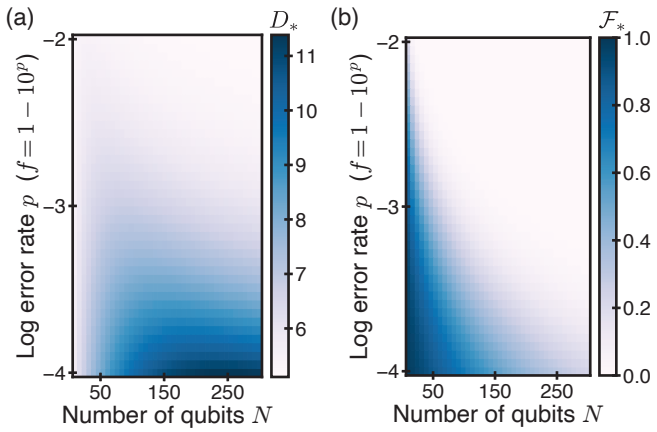


Figure 5.6: Optimal circuit depth and fidelity in near-term devices. (a) The optimal circuit depth D_* maximizing the many-body fidelity during state preparation, balancing the trotterization and gate errors. The corresponding number of gate layers is $3D_*$. (b) The maximal many-body fidelity $\mathcal{F}_*$ at the given two-qubit gate fidelity f and system size N, achieved at the optimal state-preparation circuit depth D_*. We note that the many-body fidelity is a stringent measure and many observables, such as topological readout, should be more robust to errors; see Appendix ?? for further discussion.

for example by mid-circuit readout of stabilizers as in quantum error correction, may be important in practice for stabilizing the topological phase at long times. The addition of such periodic readout intervals can also allow one to combine the present method with recently proposed Floquet quantum error-correcting codes, which dynamically realize topological phases via repeated measurements[704,630]. Exploration of topological order in hybrid models with Hamiltonian evolution and mid-circuit measurements — both of which can be realized using similar experimental controls — is an intriguing future research direction.

The methods developed here can also be applied to study various extensions of the Kitaev model, which are the topic of current research, both theoretical and experimental. Adding external magnetic fields[711,1016,745], Heisenberg interactions[945,745], or more complicated many-body terms[848], may drastically change the behavior of the system.

For example, different topological phases, with new classes of anyonic excitations, have been postulated for some of these extensions while others are especially relevant for real-world materials[957]. Additionally, we can leverage the efficient state preparation of the Kitaev honeycomb ground state and digital Hamiltonian evolution to simulate quenches away from the integrable non-abelian phase to more complicated models, which are difficult to model on a classical computer. Such quenches enable the study of integrability breaking and thermalization near integrable points[560,627,1023]. Furthermore, it could also be used to probe excitations of the quenched Hamiltonian[982], which is especially interesting due to the underlying topological order of the non-abelian phase.

Our approach can be extended to efficiently simulate other, more exotic models. For instance, an important class of lattice gauge theories can be efficiently simulated by implementing three-body interactions[730], using a family of gates $\mathcal{G}_3(\theta) = \exp\left(i\theta Z_i Z_j Z_k\right)$ combined with sublattice rotations (see Appendix ??). Such a family of three-qubit gates can be implemented as a natural extension of $\mathcal{G}_2(\theta)$[661] since arranging atoms in a triangle guarantees a symmetric blockade, as discussed in Appendix ??. The speed and robustness to errors for such operations can likely be improved further using optimal control methods[736]. In the absence of an exact solution, several of the methods employed in this work would have to be modified. For example, the variational state preparation relies on the ability to calculate the many-body overlap in order to minimize the cost function. Instead, one would need to resort to the adiabatic state preparation or variational methods involving a quantum-classical feedback loop[885]. Simplifying these requirements and optimizing these methods is another interesting direction for future research.

We thank D. Bluvstein, X. Gao, C. Kokail, R. Sahay, R. Samajdar, D. Sels, K.

Xiang, and P. Zoller for useful discussions. This work was supported by the US Department of Energy [DE-SC0021013 and DOE Quantum Systems Accelerator Center (contract no. 7568717)], the Defense Advanced Research Projects Agency (grant no. W911NF2010021), the National Science Foundation, and the Harvard-MIT Center for Ultracold Atoms. N.M. acknowledges support from the Department of Energy Computational Science Graduate Fellowship under Award Number DE-SC0021110.

6

Probing topological matter and fermion dynamics on a neutral-atom quantum computer

Quantum computers have the potential to fundamentally advance our ability to simulate strongly correlated many-body quantum systems, which can be challenging to simulate classically[669]. Fermionic models are especially important due to their central role in understanding phenomena across chemistry, materials science, and fundamental physics[533]. Recently, analog quantum simulators[691] based on fermionic atoms in

optical lattices have been advancing our understanding of the Fermi-Hubbard model[1003,939,595]. However, digital quantum simulation approaches offer new possibilities with improved control and programmability, providing access to a much wider range of models and, eventually, to fault-tolerant operation. Early experiments demonstrated key building blocks[548,539,842] of digital fermionic encodings, and recent studies have extended the work to two dimensions[617,869].

Implementing fermionic models on gate-based quantum computers presents unique challenges associated with encoding the non-local nature of fermions within qubit systems. As a result, fermion-to-qubit encodings require either macroscopic operators to represent local fermion hopping[741] or rely on long-range entangled ancilla states to preserve the locality of operations[978,635,604]. The latter case requires preserving topological order throughout computations to accurately represent fermionic particles, and can additionally be related to models that host exotic states of matter with topological order[978]. A paradigmatic case is Kitaev's honeycomb model[761], which features a non-Abelian chiral spin liquid with a topologically non-trivial energy band. While certain Abelian and non-Abelian states have recently been prepared in analog and digital systems[933,912,535,729], the Kitaev model and its extensions[957,640] constitute a promising platform for exploring both static and dynamic properties of such exotic phases of matter, including the dynamical interplay between topological order and strongly correlated fermions.

Here, we realize digital quantum simulations of Kitaev's honeycomb model using a reconfigurable atom array processor. Leveraging measurement-based topological state preparation, tunable Floquet circuits, and error detection, we probe the phase diagram and dynamics of this model. In particular, we prepare and characterize several low-energy states, including that of the non-Abelian spin liquid phase. We fur-

ther utilize this model as an efficient fermion-to-qubit encoding, investigating fermion properties through quench dynamics and engineering strong interactions to realize the Fermi-Hubbard model on a square lattice.

6.1 Hardware-efficient digital quantum simulations

The key idea behind our approach is the use of long-range entanglement to encode fermionic statistics[978]. In particular, while conventional fermion encodings[741] require high-weight qubit operators, topologically ordered states contain long-range correlations that can natively encode these properties. The Kitaev model is a paradigmatic example of such a fermion encoding based on topological order[761]. Here qubits are located on the vertices of the honeycomb lattice (Fig. 8.1a) and are effectively coupled through anisotropic two-qubit interactions,

$$K_{ij}^{\mathrm{X}} = -J_{\mathrm{X}}\mathrm{X}_i\mathrm{X}_j, \qquad K_{ij}^{\mathrm{Y}} = -J_{\mathrm{Y}}\mathrm{Y}_i\mathrm{Y}_j, \qquad K_{ij}^{Z} = -J_{\mathrm{Z}}\mathrm{Z}_i\mathrm{Z}_j, \tag{6.1}$$

acting along the three distinct link directions, as defined in Fig. 8.1a. The X_i,Y_i,Z_i are the Pauli operators acting on qubit i, and we refer to the three link orientations as XX, YY, and ZZ links, respectively. In such a system, there are long-range entangled states which correspond to the common eigenstates of the conserved, mutually commuting plaquette operators, W_p=$\mathrm{X}_1\mathrm{Z}_2\mathrm{Y}_3\mathrm{X}_4\mathrm{Z}_5\mathrm{Y}_6$ (Fig. 8.1a). When acting on such states, the spin interactions in Eq. (6.1) can be described as Majorana hopping operators, ic_ic_j, along appropriate links. The resulting system of Majorana fermions, located on the vertices of the lattice, realizes the fermionic mapping of Kitaev's model[761].

For the experimental realization of this model, we utilize a neutral-atom quantum computer based on a dynamically reconfigurable atom array composed of 72

data qubits and 32 ancilla qubits (Fig. 8.1). Using the apparatus described previously in Refs.[645,569,659,566], qubits are encoded in the long-lived hyperfine levels of ^{87}Rb atoms, individually trapped in optical tweezers, and can be reconfigured during computation while maintaining qubit coherence[569]. Fully programmable global and local single-qubit gates are implemented via fast Raman transitions[566], while high-fidelity entangling gates are achieved by exciting atoms to interacting Rydberg states[659]. A key new element involves the parallel implementation of a family of gates, $\mathrm{ZZ}(\theta) = \exp(i\pi\theta[\mathrm{Z}\otimes\mathrm{Z}]/4)$, with tunable angle θ (Fig. 8.1d). We intersperse these gates with atom motion and single-qubit rotations to realize Floquet circuits (Fig. 8.1c), which consist of repeated digital evolution under the two-qubit interactions in Eq. (6.1) applied along appropriate links.

To efficiently create the topological order[811], ancilla qubits are used to project data qubits into the target long-range entangled state with cylindrical boundary conditions (Fig. 8.1b). This is achieved by measuring commuting plaquette operators W_p in two steps (Fig. 8.2a). First, ancilla qubits are used to measure weight-4 operators on one sublattice of the data qubits, initially all prepared in $|0\rangle$. Such a mid-circuit measurement projects the system into a toric code state[759]. In the second step, the two sublattices are entangled with parallel controlled-Y gates, completing the weight-6 plaquette operators required for this fermion encoding. Although the ancilla measurement outcomes are random ± 1 values, we apply conditional (feedforward) local single-qubit Z gates to deterministically prepare all plaquettes to have $+1$ value in the absence of errors (Fig. 8.2a).

To characterize the resulting state, we measure the plaquette operators W_p, finding an average parity of 0.444(4) (Fig. 8.2b). Furthermore, we measure longer closed-loop operators, enclosing up to four hexagons, and observe finite parity in all cases

(Fig. 8.2d). We can improve the quality of this topological order by performing error detection, by noting that for the cylindrical geometry used here, the product of ancilla values in a given column must have even parity in the absence of errors. Using this decoding postselection method (Fig. 8.2c), we observe an improvement in the plaquette parity to 0.57(1).

6.2 Exploring the Kitaev model

The highly anisotropic interaction structure of the Kitaev model, Eq. (6.1), gives rise to a rich phase diagram, featuring several distinct topological phases (Fig. 8.3a). Of particular interest is the non-Abelian spin liquid phase, known as phase B, which emerges when the three coupling strengths J_X,J_Y,J_Z are sufficiently uniform[761]. The fermionic description of the model results in its low-energy states being characterized by the underlying spin-liquid order and effective fermion correlations[761]. The initial state after feedforward corresponds to a fixed-point state A_Z^I of the Abelian A_Z phase ($J_{X/Y}$=0), where all ZZ-link operators should be +1. We observe a mean ZZ-link parity of 0.883(8), and the measured plaquette operators characterize the spin-liquid nature of the prepared state (Fig. 8.2b).

To evolve from this initial state (A_Z^I) to target states of interest in the phase diagram, we apply a numerically optimized version of a Floquet unitary circuit[747] constructed from repeated application of the nearest-neighbor gates as illustrated in Fig. 8.1c, with optimized entangling phases. We find that a circuit depth of 6, as shown in Fig. 8.3b, is sufficient to probe all points of interest on the phase diagram (Methods), consistent with the slow gap closing with system size[747]. We measure the plaquette parity values to verify the preservation of the topological order and observe

that they decay with increasing circuit depth (Fig. 8.3b), as expected due to accumulating incoherent errors. To mitigate this, we utilize a new type of state-selective readout, which converts atomic state into spatial position[1000,567], allowing us to differentiate between lost atoms and the two computational states[918,816]. By detecting atom loss and employing the error-detecting technique based on ancilla results, we observe that we can better preserve the plaquette expectation values during computation (Fig. 8.3b).

To characterize states across the phase diagram, we measure two-point Majorana fermion correlations, $\langle c_i c_j \rangle$, which are constructed as products of the link operators along the path connecting the two sites (Fig. 8.3d). Therefore, all fermion correlations can be measured as open Pauli strings. Fig. 8.3c shows the measured expectation values of strings up to length 6, for three points in the phase diagram: the initial state after feedforward state preparation $\mathrm{A}_{\mathrm{Z}}^{\mathrm{I}}$, another point in the Abelian phase $\mathrm{A}_{\mathrm{Z}}^{\mathrm{II}}$, and a point in the non-Abelian phase B. We observe a buildup of string correlations as the system is moved towards phase B and find good agreement with theory predictions, under a noise model consisting of single-qubit Pauli errors and atom loss (Methods), across all prepared states.

We probe the nature of phase B by extracting the Chern number—a topological invariant that characterizes the curvature of the system's energy bands[558,528,622]. Noting that the prepared state should correspond to a low-energy state of a free-fermion Hamiltonian, we infer the momentum-space parent Hamiltonian H_{k} from the measured real-space correlations of the state (Fig. 8.3e). Because the unit cell of the honeycomb lattice consists of two sites, the system possesses two Bloch bands and their Chern number can be numerically evaluated from the learned Hamiltonian. As the system transitions from the Abelian to the non-Abelian phase, we observe a change

from a zero (C=0) to a non-zero (C=1) Chern number of the lowest-energy band (Fig. 8.3f). In phase B, an odd Chern number, combined with the underlying topological order (Fig. 8.2b), provides strong evidence of the phase's non-Abelian character (Methods). In particular, it guarantees that, in the presence of a flux, a non-Abelian, unpaired Majorana mode must be present in the spectrum at zero energy[761,532].

6.3 Floquet evolution of fermion systems

Having explored the topological properties in the Kitaev phase diagram, we now leverage them to simulate quench dynamics[631,950,1011] of fermionic particles. We focus on conventional fermions characterized by complex-valued operators, which can be realized by pairing two Majorana fermions, $a_i=(c_i+ic_{i'})/2$. In our realization, we pair them along the ZZ links, such that the resulting complex fermions form a square-lattice geometry (Methods), and the $Z_iZ_{i'}$ operator along an (i,i') link is related to local fermion density, $n_i=(1-Z_iZ_{i'})/2$, with $Z_iZ_{i'}=+1$ denoting particle absence, $n_i=0$. In this framework, the ZZ-link operators in Fig. 8.2b characterize the initial vacuum state, corresponding to a background fermion density of 5.9(5)%.

To initialize real-space configurations of complex fermions, we start from the state A_Z^I and create a fermion pair by applying an open Pauli string (e.g YXXY in Fig. 8.4a) that commutes with the plaquette operators but flips the desired $Z_iZ_{i'}$ operators such that $n_i=1$. Individual complex fermions can, in principle, be created by connecting such strings to the open boundary.

The dynamics of complex fermions is inherited from that of the Majorana operators, where the Kitaev interactions in Eq. (6.1) correspond to nearest-neighbor Majorana hopping terms c_ic_j. We first study the dynamics of the two localized fermions un-

der two different depth-12 Floquet circuits (Fig. 8.4b), focusing on the role of anisotropy between the couplings. Setting two directions to be equal, J_X=J_Y=J, and tuning the strength of the third direction J_Z, we find that for J_Z=J the number of particles grows quickly, because the Majorana hopping terms do not naturally preserve the complex-fermion particle number (Fig. 8.4c). By contrast, for J_Z=8J, background particle creation is suppressed and the total particle number returns close to the initial value for a full effective Floquet cycle (around depths 6 and 12). This emergent particle conservation is the result of strong K^Z_{ij} terms, which corresponds to the total particle number, projecting the dynamics into approximate particle-conserving evolution[520,657]. Indeed, unitary dynamics result in an effective Floquet Hamiltonian closely resembling that of complex fermions, and the intermediate rise in particle number can be interpreted as Floquet micromotion.

Focusing on the particle number conserving (J_Z=8J) case, we evolve two initial states (Fig. 8.4d), with a complex fermion pair either one (d=1) or two (d=2) sites apart, and investigate the final fermion configuration at depth 11. We probe their hopping by measuring density-density correlations G_{ij}=$\langle n_i n_j\rangle$−$\langle n_i\rangle\langle n_j\rangle$. Such correlations capture hopping since a transported particle should be anticorrelated with its initial position (Methods). For free-fermion states, the G_{ij} correlation is equal to the (negative) magnitude of the hopping operator between sites i and j (Methods). In Fig. 8.4e, we explore these correlations with respect to one of the initially occupied sites, normalized by its density. For the d=1 initial separation, we observe a strong asymmetry in the hopping direction, owing to the fermions hopping away from each other, consistent with Pauli exclusion. As expected, the asymmetry is greatly reduced for the d=2 separation.

Fermion exchange

A defining characteristic of fermionic particles is their non-trivial exchange statistics, with the many-body wavefunction being antisymmetric under particle exchange. We directly probe the exchange statistics of the complex fermions through deterministic hopping, realized by a gate sequence designed to preserve particle number. Because the exchange statistics manifest as a global phase, we perform a Ramsey-type experiment (Fig. 8.4f) in which we first apply a partial pair-creation operator $R \propto \sqrt{\mathrm{X} \otimes \mathrm{Z} \otimes \mathrm{Y}}$ to prepare a superposition state, $(|\emptyset\rangle + |\bullet_{\bullet}\rangle)/\sqrt{2}$, where $|\emptyset\rangle$ is the initial vacuum state and $|\bullet_{\bullet}\rangle$ is the two-fermion state (Methods). Then, we compare two different fermion movement patterns: (i) fully exchanging the two fermions with each other and (ii) hopping once and then hopping back to the original configuration. Finally, we apply the partial creation operator R again and measure the resulting fermion density. When the fermions are returned to their original positions, the state remains unchanged, and the second R operator completes the fermion-pair creation, yielding $|\bullet_{\bullet}\rangle$ as expected. However, when the particles are exchanged, we observe the absence of fermions at the end, consistent with the system returning to the vacuum state, $|\emptyset\rangle$. This represents direct demonstration of the superposition state transforming into $(|\emptyset\rangle - |\bullet_{\bullet}\rangle)/\sqrt{2}$ due to the particle exchange, which leads to destructive interference with the final creation operation.

To quantify this process, we evaluate the difference in average density on the target sites between the outcomes of the two protocols, corresponding to the contrast resulting from the fermionic Ramsey sequence, under varying levels of error detection (Fig. 8.4g). We find that the accuracy of the exchange statistics improves as the quality of fermion encoding is enhanced through decoding postselection.

Simulating the Fermi-Hubbard model

The Fermi-Hubbard model is one of the most important strongly interacting fermionic systems. In its simplest form it consists of spin-1/2 particles with contact interactions between different fermionic spin states,

$$H_{\mathrm{FH}} = \sum_{\sigma\in\uparrow,\downarrow} \sum_{\langle i,j\rangle} (a^{\dagger}_{\sigma,i} a_{\sigma,j} + a^{\dagger}_{\sigma,j} a_{\sigma,i}) + U n_{\uparrow} n_{\downarrow}, \tag{6.2}$$

where σ denotes the spin state and $\langle i,j\rangle$ is the set of edges encoding the system connectivity. This model, and its various extensions, provides a description of real-world materials and is believed to underpin some of the most puzzling phenomena in condensed matter, such as high-temperature superconductivity[785].

To simulate this model, we split our array into two halves, representing spin up on the left side and spin down on the right side, and engineer interactions by realizing parallel gates between the two halves (Fig. 6.5a). After the initial encoding step, we omit the hopping terms across the boundary during evolution, enabling independent dynamics of the two spin states. Furthermore, we extend our Floquet cycle by adding a fermion interaction term (Fig. 6.5b). Effectively, this realizes a Fermi-Hubbard model on a 16-site square lattice.

More specifically, to implement onsite density-density interactions, $H_{\mathrm{int}} \propto n_{\uparrow} n_{\downarrow}$, we take advantage of long-range atom motion to couple distant parts of the system (Fig. 6.5c). We apply two parallel CNOT gates across the two halves of the array, interleaved with evolution under the K^{Z}_{ij} interaction on the target half only. This K^{Z}_{ij} term is proportional to $\mathrm{Z}_{\uparrow}\mathrm{Z}_{\uparrow}$, and the CNOT gates propagate it to a four-body $(\mathrm{Z}_{\uparrow}\mathrm{Z}_{\uparrow})\times(\mathrm{Z}_{\downarrow}\mathrm{Z}_{\downarrow})$ term across the two halves, which effectively realizes contact interactions $(4n_{\downarrow}n_{\uparrow} - 2n_{\downarrow} - 2n_{\uparrow})$

between the two fermion species.

We initialize an antiferromagnetic checkerboard spin ordering (Fig. 6.5d) with local single-qubit gates, and study its dynamics with varying interaction strength. In the absence of interactions (U=0), we observe that the staggered magnetization of the initial state quickly decreases after a few Floquet cycles, due to the independent fermion hopping (Fig. 6.5e). However, by increasing the interactions, we observe suppressed particle transport and significantly slower decay of the staggered magnetization (Fig. 6.5e). We measure the staggered magnetization after the final Floquet round for a range of interaction strengths (Fig. 6.5f), and find good agreement with numerical simulations of our circuit (Methods), including a non-monotonic behavior as a function of interaction strength.

Outlook

Our experiments demonstrate key building blocks for digital quantum simulations of complex fermionic and topological systems. Utilizing measurement-based preparation of long-range entanglement, efficient Floquet dynamics, and error detection, they pave the way for explorations of complex and practically relevant quantum systems. These studies can be extended in a number of interesting directions. For instance, properties of the non-Abelian excitations[747] can be explored in the Kitaev model, including fusion and braiding properties[761]. Moreover, the stability of spin liquid phases can be probed in challenging-to-simulate regimes by adding different types of interactions, which can be implemented with additional atom moves. Such simulations have the potential to provide new insights into the understanding of so-called Kitaev materials[957]. Similar methods can be extended to study a broad range of physics and

chemistry models, including those relevant to materials and molecules[833,616], lattice gauge theories[617], and quantum gravity[820,907]. Other fermionic encodings can also be explored, either using qubits[869] or hybrid analog-digital architectures with fermionic atoms[701,687].

While the methods used in this work can readily be scaled up to thousands of qubits[822,803], the achievable circuit depths in digital quantum simulations will be limited due to errors. Our experiments demonstrate that error detection approaches can be used to suppress errors in near-term simulations. Eventually, error correction will need to be integrated to further extend achievable circuit depths. The topological state-preparation circuit can be realized with encoded logical qubits using transversal operations[1019], while implementation of specialized error-correcting codes could further reduce resource overheads[1004]. The techniques developed and demonstrated in this work provide the foundation for co-designing such simulation approaches in a hardware-efficient manner.

During the completion of this work, we became aware of related work studying Kitaev's honeycomb model on a superconducting quantum computer[897].

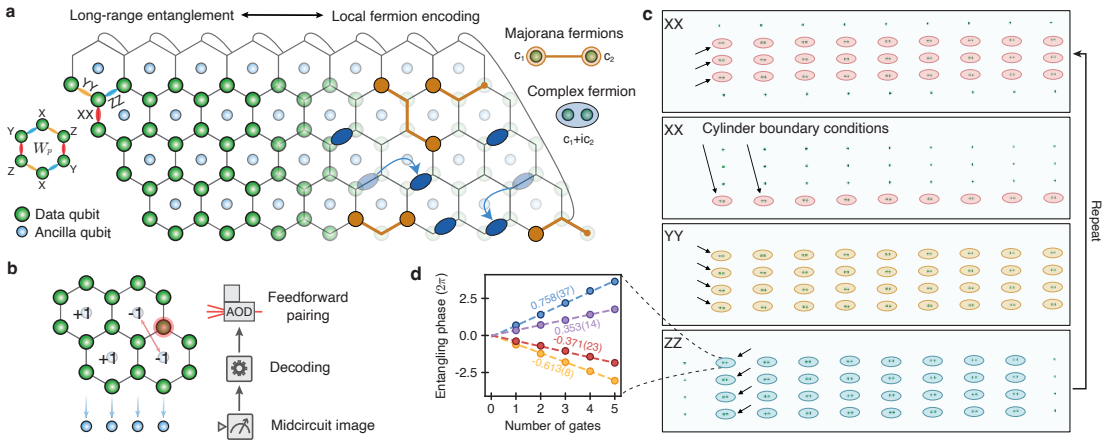


Figure 6.1: Digital quantum simulations with reconfigurable atom arrays. a, The honeycomb lattice used in this work with 104 total atomic qubits and periodic boundary conditions along the shorter direction, forming a cylinder. The qubits are encoded in ^{87}Rb atoms and entangling gates are realized through excitation to interacting Rydberg states. To encode fermion statistics, we prepare a long-range entangled state characterized by hexagonal plaquette operators W_p=$X_1Z_2Y_3X_4Z_5Y_6$ that commute with the unitary evolution and are therefore conserved. The encoded Majorana fermions live on vertices, at the ends of operator strings, and conventional (complex) fermions are formed by combining two Majoranas along a chosen link orientation. b, The long-range entangled state is prepared using mid-circuit measurement of ancilla qubits, and plaquettes are deterministically flipped to be +1 using conditional single-qubit gates (red circle). c, The Floquet evolution cycle consists of atom reconfiguration interspersed with tunable entangling gates and global basis changes. d, Accumulated entangling phase upon repeated application of $\exp(i\pi\theta[Z\otimes Z]/4)$ gates with a variable angle θ realized through fast, parameterized laser pulses. The values show extracted values of θ, and error bars represent one standard deviation.

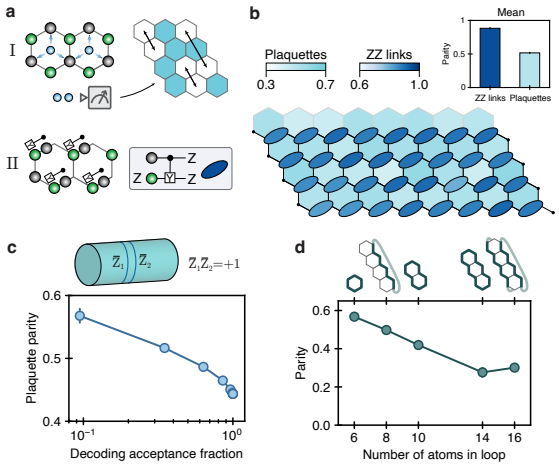


Figure 6.2: Measurement-based preparation of topological order. a, A long-range entangled state of the toric-code type is prepared using a depth-3 circuit, independent of the system size, accompanied by midcircuit readout of the ancilla qubits (I). The measurement results are random up to parity constraints along the periodic direction. A feedforward step realized through FPGA-triggered single-qubit Z rotations pairs the -1 outcomes (white hexagons). Finally, a parallel controlled-Y operation creates the weight-6 plaquettes (hexagons) and initializes the ZZ-link operators (ovals) to all be +1 (II). b, Expectation values of the weight-6 plaquettes and weight-2 ZZ-links across the array of 72 data and 32 ancilla qubits with cylindrical boundary conditions. The inset shows values averaged across the system. c, The product of plaquette operators in each column is equivalent to loops enclosing the cylinder, which are +1 in the absence of errors. Postselection based on the parity of the measured ancilla values within each column improves the plaquette expectation values and the quality of the resulting fermion encoding. d, Parity expectation values of increasingly large loops, including loops that enclose 1, 2, 3, and 4 hexagons within a column and the loop around the cylinder (plotted for maximum decoding postselection). The largest operator is equivalent to the product of two loops enclosing the cylinder. Error bars represent 68% confidence intervals.

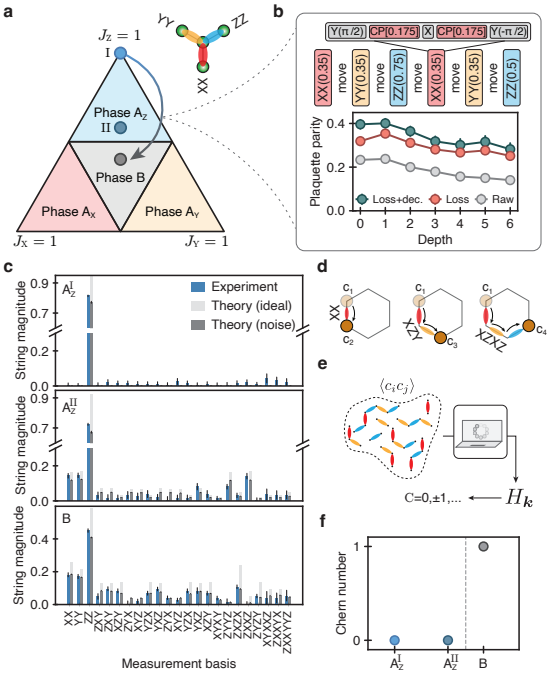


Figure 6.3: Kitaev model on a honeycomb lattice. a, The honeycomb model, consisting of anisotropic spin interactions along the three directions of the honeycomb lattice (J_X+J_Y+J_Z=1), exhibits topological order with three Abelian (A) phases and a single non-Abelian phase B. The toric code state in Fig. 8.2 is the fixed-point state A_Z^I of the Abelian A_Z phase (J_Z=1). b, Starting from this initial state, we prepare different states on the phase diagram. Top: numerically optimized sequence of two-qubit gates used to prepare the non-Abelian phase B. Each circuit layer includes CPHASE (CP) gates and global single-qubit rotations. Bottom: plaquette parity during the evolution, with postselection based on atom loss and decoding. c, Pauli strings of different lengths measured on the three studied states and averaged over the bulk of the system. Error bars represent 68% confidence intervals. d, In the fermion representation, the link operators are proportional to nearest-neighbor Majorana hoppings, $K_{ij}^{X/Y/Z} \propto ic_ic_j$. Longer Pauli strings constructed from their products result in longer-range hopping operators. e, The free-fermion parent Hamiltonian $\mathcal{H}_k$ can be reconstructed from measured two-point Majorana correlations. f, The Chern number C is evaluated using the learned parent Hamiltonians of the string distributions in c, resulting in C=0 in phase A and C=1 in phase B; the robustness of this procedure is explored in Methods. The non-Abelian phase B is characterized by the underlying topological order and an odd Chern number [761].

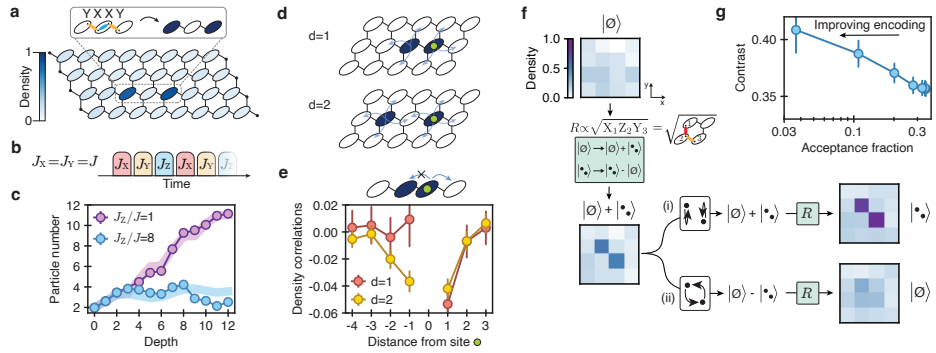


Figure 6.4: Probing fermion dynamics and statistics. a, System initialized in a two-particle state with complex fermions defined along the ZZ links. An open Pauli string is used to create a fermion pair out of the initial vacuum state. b, Digital evolution under two-qubit interactions in Eq. (6.1), realizing Majorana fermion hopping between connected vertices. The hopping strength along the XX and YY links is fixed, J_X=J_Y=J, while the value of J_Z/J is tuned. c, Total number of complex fermions in the system during a quench under two different Floquet drives, for J_Z/J=1 and J_Z/J=8. The K_{ij}^Z term corresponds to the fermion particle number and increasing it enforces particle number conservation. The initial background fermion number resulting from state preparation errors is subtracted for clarity and the solid lines are the result of noisy numerical simulations (Methods). d, System initialized with two fermions at distances d=1 or d=2 is evolved under the Floquet Hamiltonian with J_Z/J=8. e, A horizontal cut of the two-point density-density correlation relative to the marked site (green dot) at depth-11. The directional asymmetry in hopping is consistent with Pauli exclusion, which prevents fermions from occupying the same site. f, Direct measurement of the fermion exchange phase. A superposition of vacuum and fermion-pair states is created with a sequence of local entangling gates, which realizes a partial creation unitary R (Methods). The system is evolved under two different particle-hopping protocols: (i) exchanging the two fermions and (ii) hopping to an intermediate site and hopping back. The evolution is followed by a second application of R, which maps the exchange phase to fermion presence. Color plots show the mean fermion density at each site in a 4x4 region embedded in the full lattice. g, Contrast between protocols (i) and (ii) as a function of decoding postselection. Error bars represent 68% confidence intervals.

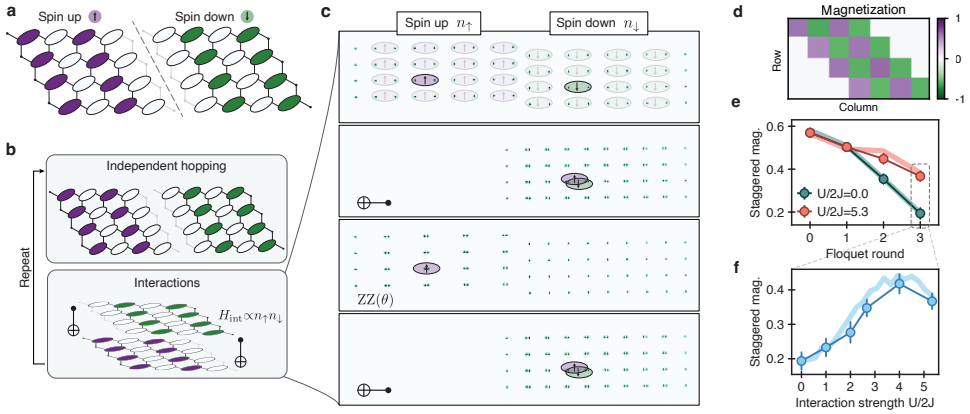


Figure 6.5: Two-component strongly interacting fermions. a, Two independent species of fermions, labeled "spin-up" and "spin-down", are realized by dividing the system into two halves. The XX and YY links across the boundary are turned off to facilitate independent hopping dynamics; this system realizes a 4x4 lattice with two fermion species. b, Floquet evolution consists of independent hopping within the two halves followed by density-density interactions between the two spin states. c, The interactions are realized through a parallel entangling operation connecting the two halves of the system. Two parallel CNOT gates propagate a ZZ(θ) operator, applied to the spin-up half, into the interaction term. d, The initial state is a checkerboard pattern, staggered between the two fermion spin states. e, Staggered magnetization dynamics during a quench with and without the interactions. f, Final staggered magnetization as a function of interaction strength. Increasing interactions suppress the spin mixing dynamics. The solid lines are the result of noisy numerical simulations of the circuit (Methods). Error bars represent 68% confidence intervals.

7

Digital simulation for chemistry and materials

A major thrust of quantum chemistry and material science involves the quantitative prediction of electronic structure properties of molecules and materials. While powerful computational techniques have been developed over the past decades, especially for weakly correlated systems[954,550,825,587], the development of tools for understanding and predicting the properties of materials that feature strongly correlated electrons remains a challenge[538,697,525]. Quantum computing is a promising route to efficiently capturing such quantum correlations[531,551,837], and algorithms for Hamiltonian sim-

ulation and energy estimation[801] with good asymptotic scaling have been developed. However, existing methods for simulating large-scale electronic structure problems are prohibitively expensive to run on near-term quantum hardware[562], highlighting the need for more efficient approaches.

One approach to capturing the complexity of strongly correlated systems utilizes model Hamiltonians[541], such as the generalized Ising, Heisenberg, and Hubbard models, which describe the interactions between the active degrees of freedom at low temperatures. Like other coarse-graining or effective Hamiltonian approaches[553], model parameters can be computed from an ab initio electronic structure problem using a number of classical techniques[575,834,835,896,771,601]. Furthermore, model Hamiltonians exhibit features such as low-degree connectivity that simplify implementation, making them particularly promising candidates for quantum simulation[748,607,961,991,552,813]. Though approximate, simplified model Hamiltonians have proved valuable in analyzing strongly correlated problems[774,775,821] for small system sizes, where accurate but costly classical methods can be applied. However, as the system size increases, classical numerical methods struggle to reliably solve strongly correlated model systems, as the relevant low-energy states often exhibit a large degree of entanglement. In this Article, we focus on the programmable quantum simulations of spin models. These correspond to a class of Hamiltonians that describe compounds where unpaired electrons become localized at low-temperatures and can therefore be represented as effective local spins with $S \geq 1/2$. These include many polynuclear transition metal compounds and materials containing d- and f-block elements, which play a central role in chemical catalysis and magnetism[941,775,879,821,589,797,601,895].

Recent advances in quantum simulation[855,628] have enabled the study of paradigmatic model Hamiltonians with local connectivity. In particular, experiments have

probed non-equilibrium quantum dynamics[557,752,572], exotic forms of emergent magnetism[781,645,916,600], and long-range entangled topological matter[933,912], in regimes that push the limits of state-of-the-art classical simulations[758]. The model Hamiltonians describing realistic molecules and materials however often contain more complex features, including anisotropy, non-locality, and higher-order interactions[821], demanding a higher degree of programmability[896]. While universal quantum computers can in principle simulate such systems, standard implementations based on local two-qubit gates require large circuit depths[961] to realize complex interactions and long-range connectivity. Thus, for optimal performance in devices with limited coherence, it is essential to utilize hardware-efficient capabilities to simulate such systems.

In what follows we introduce a framework to simulate model spin Hamiltonians (Fig. 7.1) on reconfigurable quantum devices. The approach combines two elements. First, we describe a hybrid digital-analog simulation toolbox for realizing complex spin interactions, which combines the programmability of digital simulation with the efficiency of hardware-optimized multi-qubit analog operations. Then, we introduce an algorithm, dubbed "many-body spectroscopy" that leverages time-dynamics and snapshot measurements to extract detailed spectral information of the model Hamiltonian in a resource-efficient way[596]. We describe in detail how these methods can be implemented using Rydberg atom arrays[549,621,814,947,738], and discuss its applicability to other emerging platforms which can support multi-qubit control and dynamic, programmable connectivity[750], such as the ion QCCD architecture[726,859]. Finally, we illustrate potential applications of the framework on model Hamiltonians describing a prototypical biochemical catalyst and 2D materials.

7.1 Engineering spin Hamiltonians

The general Hamiltonian we consider is

$$H = \sum_{i,\alpha} B_i^\alpha \hat{S}_i^\alpha + \sum_{ij,\alpha\beta} J_{ij}^{\alpha\beta} \hat{S}_i^\alpha \hat{S}_j^\beta + \sum_{ijk,\alpha\beta\gamma} K_{ijk}^{\alpha\beta\gamma} \hat{S}_i^\alpha \hat{S}_j^\beta \hat{S}_k^\gamma + \text{higher order}, \tag{7.1}$$

where $\hat{S}_i^\alpha, \alpha = x, y, z$ are spin-S_i operators of the i-th spin ($S_i \geq 1/2$ can vary between sites), and the interaction coefficients ($J_{ij}^{\alpha\beta}$, $K_{ijk}^{\alpha\beta}$, etc.) are potentially long-range. Hamiltonians of this form can capture the effects of many processes arising in physical compounds, including super-exchange, spin-orbit coupling, ring-exchange, and more[821]. In our approach, spin-S variables are encoded into the collective spin of $2S$ qubits, such that the i-th spin in (7.1) is rewritten as

$$\hat{S}_i^\alpha = \sum_{a=1}^{2S_i} \hat{s}_{i,a}^\alpha, \tag{7.2}$$

where $\hat{s}_{i,a}^\alpha$ are the spin-1/2 operators of the a-th qubit in the i-th spin. Valid spin-S_i states live in the symmetric subspace with maximum total spin per site $\langle (\hat{\mathbf{S}}_i)^2 \rangle = S_i(S_i+1)$. While several alternate approaches to encoding spins with hardware-native qudits have been proposed recently[777,606,719,688], the cluster approach introduced here uses the same controls as qubit-based computations ensuring compatibility with existing setups[659], and naturally supports simulation of models with mixed on-site spin.

The core of our protocol involves applying a K step sequential evolution under

simpler interaction Hamiltonians $H_i = \sum_{g \in G_i} h_{i,g}$, $i = 1, ..., K$, acting on disconnected groups G_i of a few qubits each. The combined sequence realizes an effective Floquet Hamiltonian H_F which approximates (7.1). To controllably generate effective Hamiltonians, we use the average Hamiltonian approach. In the limit of small step-sizes $\tau \ll 1/K$, the evolution is well-approximated by $H_F^{(0)} = \frac{1}{K} \sum_{i=1}^{K} H_i$ to leading order, and contributions from higher-order terms are bounded[520].

In general, the performance of this approach will be limited by simulation errors, characterized by the difference between H_F and the target Hamiltonian H, and gate errors, determined by the hardware overhead required to implement individual evolutions $e^{-ih_{i,g}\tau}$. To mitigate the leading sources of error, we next develop Hamiltonian engineering protocols that leverage multi-qubit spin operations to realize (7.1) with short periodic sequences.

7.2 Dynamical projection with digital Floquet engineering

Our Hamiltonian engineering approach is based on the cluster encoding (7.2). The key idea is to first generate interactions in the full Hilbert space using a spin-1/2 (qubit) version H_I of (7.1), and then dynamically project back onto the encoding space. We select H_I such that projection recovers the target Hamiltonian, by mapping each n-body large spin interaction in (7.1) onto an equivalent n-body qubit interaction acting on representatives from the n-clusters (see Methods and Fig. 7.2a). We further decompose H_I into D non-overlapping groups H_{I_j}, such that each term can be applied sequentially.

While this generates the target interactions between spin clusters, it also moves encoded states out of the symmetric subspace. Therefore, to prevent evolution under

H_I from destroying the encoding, we alternately apply evolution under

$$H_P = \lambda \sum_i (1 - P[(\hat{\mathbf{S}}_i)]), \tag{7.3}$$

composed of projectors $P[(\hat{\mathbf{S}}_i)]$ onto the symmetric spin states, by applying multi-qubit gates within spin clusters. The symmetric states are zero-energy ground-states of H_P, and non-symmetric states are separated by an energy gap λ. Alternating H_I and H_P enables Trotter simulation of the static Hamiltonian $H_I + H_P$. For $\lambda \gg J_{ij}$, the system is effectively projected into the ground-space of H_P at low-energies, realizing H. However, accurate Trotter simulation in this regime, by alternating H_I and H_P, requires two separations of time-scale between the step-size and the target interactions $\tau \ll \lambda^{-1} \ll J_{ij}^{-1}$, leading to a large number of gates.

Instead, we develop an approach which enables projection of H_I onto the ground-state of H_P with significantly fewer gates, using ideas inspired by dynamical decoupling[610]. This is achieved by using large-angle rotations $e^{-i\tau H_P}$, where $\tau\lambda \sim 1$, to generate a time-dependent phase on the parts of H_I that couple encoded states to non-symmetric states. These phases cancel out on average, leaving the symmetric part which commutes with H_P. More precisely, the combined evolution is described by

$$\begin{aligned} U_F &= \prod_{p=1}^{N_p} \left(e^{-i\vartheta_p \lambda^{-1} H_P} \prod_{j=1}^{D} e^{-i\tau H_{I,j}} \right) \\ &= \prod_{p=1}^{N_p} \prod_{j=1}^{D} e^{-i\tau H_{I,j}(p)} = e^{-iK\tau H_F}, \end{aligned} \tag{7.4}$$

where $K = N_p D$ is the full length of the sequence, and $\theta_p \lambda^{-1}, \tau$ parameterize the evolution times. In the second line, we transform into an interaction picture, such that intermediate terms are evolved by H_P with a cumulative phase $\Theta_p = \sum_{p'<p} \theta_{p'}$; for the rotating frame to be periodic, we require $\Theta_{N_p+1} \pmod{2\pi} = 0$.

Then the transformed interactions can be written as (see Methods):

$$\begin{aligned} H_{I,j}(p) &= e^{i\Theta_p \lambda^{-1} H_P} H_{I,j} e^{-i\Theta_p \lambda^{-1} H_P} \\ &= \underbrace{H_{I,j}^{(0)}}_{\text{symmetric}} + \underbrace{\left(\sum_{n=1}^{n_{\max}} e^{in\Theta_p} H_{I,j}^{(n)} + h.c. \right)}_{\text{symmetry violating}}. \end{aligned} \tag{7.5}$$

Here, $H_{I,j}^{(n)}$ captures unwanted terms that change the total spin on n sites, while the symmetric terms comprise the target Hamiltonian $\sum_j H_{I,j}^{(0)} = H_T$. To cancel out symmetry-violating terms at leading order in τ, we choose an appropriate sequence of cumulative phases, such that $\sum_p e^{in\Theta_p} = 0$ for $n = 1, ..., n_{max}$. When $n_{\max} = 2$, i. e., up to two-spin interactions, the sequence $\Theta = (0, 2\pi/3, 4\pi/3)$ satisfies this condition. This sequence, having constant θ_p, produces a Floquet Hamiltonian which commutes with H_P in a dressed frame[657], and therefore preserves the encoding up to exponentially long times in τ^{-1} (see Methods).

This approach provides significant benefits in simulating complex spin-models, where the number of overlapping terms in H grows rapidly with parameters such as the spin-size S, number of interactions per spin d, and interaction weight $n_{\max}$. In this regime, a Trotter decomposition of H into non-overlapping terms $h_{i,g}$ would require a sequence of length $K \geq d(2S)^{n_{\max}-1}$, where d measures the number of interactions each spin S_i is involved in. Instead, the projection approach produces decompositions of H

into sequences of length $K = (n_{\max}+1)\left\lceil \frac{d}{2S} \right\rceil$ (see Methods), leading to performance improvements of several orders of magnitude for models with large spins and higher-order interactions.

Similar tools can also be used realize a large class of spin circuits, by generating different evolutions $H_F^{(i)}$ during each cycle. This effectively implements discrete time-dependent evolution

$$U_{\text{circ}} = \prod_{i=1}^{T} e^{-i\tau_i H_F^{(i)}}. \tag{7.6}$$

Variational optimization can be further used to engineer higher-order terms in H_F, enabling generation of more complex spin gates at no additional cost (see Extended Data Fig. 9). Although the classical variational optimization procedure is limited to small circuits, Hamiltonian learning protocols could be used to perform larger-scale optimization on a quantum device directly[590,554]. Such circuits can be used for operations besides Hamiltonian simulation, including state-preparation[748].

7.3 Hardware-efficient implementation

The digital Hamiltonian engineering sequence can, in principle, be realized on any universal quantum processor, but it is especially well suited for reconfigurable processors with native multi-qubit interactions[569,859,750,805]. Neutral atom arrays are a particularly promising candidate for realizing these techniques, for which we develop a detailed implementation proposal. In this platform, two long-lived atomic states encode the qubit degree of freedom $\{|0\rangle,|1\rangle\}$, which can be individually manipulated with fidelity above 99.99%[943,793]. Strong interactions between qubits are realized by cou-

pling to a Rydberg state $|r\rangle$ [732,796], which enables parallel multi-qubit operations [796], with state-of-the-art two-qubit gate fidelities exceeding 99.5% [659]. Further, qubits can be transported with high fidelity by moving optical tweezers [569], to realize arbitrary groupings G_i. By placing atoms sufficiently close together, atoms within a group can undergo strong all-to-all interactions, while interactions between groups can be made negligible by placing them far apart.

The key ingredient required for efficiently implementing H_I and H_P are hardware-efficient multi-qubit spin operations. We show how these can be realized by using pulse engineering to transform the native Rydberg-blockade interaction [732,969] into the desired form. We illustrate this on two families of representative spin operations

$$U_S(\theta) = e^{-i\theta(\hat{\mathbf{S}}_\mathbf{i}^{\,2}/2S)}, \quad U_P(\theta) = e^{-i\theta P[\hat{\mathbf{S}}_\mathbf{i}^{\,2}]} \tag{7.7}$$

where $\hat{\mathbf{S}}_\mathbf{i}^{\,2}$ is the total-spin operator for a cluster of $2S_i$ atoms, and $P[\hat{\mathbf{S}}_\mathbf{i}^{\,2}]$ are the projectors appearing in (7.3).

One approach to engineering these operations is based on an ansatz which naturally extends Ref. [659], where U_S and U_P are found by optimizing an alternating sequence of diagonal phase gates and single-qubit rotations. As in prior works [737,878,659], the pulse profiles generating symmetric diagonal operations can be obtained with numerical optimization via GrAPE [753]. For this alternating ansatz, we find a roughly linear scaling of total gate time T_{gate} with size of the cluster (see Fig. 7.2b). Similar gates can also be implemented in ion-trap architectures, where coupling to collective motional modes can be used to implement diagonal phase gates [949,749].

However, Rydberg atom arrays offer additional control, which allows us to go be-

yond the alternating ansatz. Specifically, we consider simultaneously driving the qubit transition $\Omega_q(t)$ in addition to the usual Rydberg transition $\Omega_r(t)$. We find that this dual driving enables significantly faster realizations of U_S and U_P. After optimizing with GrAPE to identify approximate gates with noise-free simulated fidelities above 99.9% (i.e. assuming no experimental error), we find total gate times below $\Omega T_{\text{gate}}/2\pi = 6.0$ up to cluster sizes $n = 8$ and nearly constant scaling with n (see Fig. 7.2b and Methods). The fact that the evolution is so short, implies these gates generate complex interactions in a very hardware-efficient way, making them ideal for accelerating spin-Hamiltonian simulations. Finally, we develop optimized decompositions of target spin operations into two-qubit gates, and find they are still orders of magnitude more costly than the hardware-efficient implementation (Fig. 7.2c).

In Fig. 7.3, we illustrate the performance of this method on four representative examples that lie within the family of Hamiltonians (7.1). To quantify the performance of the simulation, we present heuristic estimates of the accessible coherent simulation time, measured in units of the target Hamiltonian's local energy scale. We leverage access to multi-qubit spin operations of the form $e^{-i\sum_n \theta_n \mathbf{S}^n}$, and estimate gate errors (arising from experimental imperfections) based on the physical evolution time necessary to realize the target operation. The step-size τ is chosen to to maximize coherent simulation time, balancing simulation and gate errors (see Methods). In the representative examples, we find the combination of dynamical projection and optimized multi-qubit gates outperforms a similarly constructed implementation based on Trotterized interactions and two-qubit gate decomposition. Our approach significantly extends the available simulation time (up to two orders of magnitude), and enables much more efficient generation of complex spin Hamiltonians.

7.4 Spectral information from dynamics

Having described a toolbox for implementing a large class of spin-circuits, enabling time-evolution and state-preparation, we next present a general-purpose algorithm for calculating chemically relevant information. The approach, dubbed "many-body spectroscopy", leverages dynamical snapshot measurements and classical co-processing[596] to compute a wide variety of spectral quantities including low-lying states and finite-temperature properties. The procedure, combining insights from statistical phase estimation[802,810,948,876] and shadow tomography[721], is noise-resilient and sample-efficient, making it especially promising for near-term experiments.

Specifically, the quantity we extract is an operator-resolved density of states

$$D^{A}(\omega) = \sum_{n} \langle n|A|n\rangle \delta(\omega - \varepsilon_n), \tag{7.8}$$

where ε_n and $|n\rangle$ are the energies and eigenstates of the evolution Hamiltonian H, and A denotes an arbitrary operator. Spectral functions like equation (7.8) can be used to access detailed information about the properties of H: the location of peaks provides information about energies[802,948,876], and properties of eigenstates can be computed by choosing A appropriately[810]. For example, we can compute total-spin of an eigenstate using $A = (\sum_i \hat{\mathrm{S}}_i)^2$, or the local spin polarization with $A = \hat{\mathbf{S}}_i$.

The output of the quantum computation are projective measurements (snapshots), produced by the circuit depicted in Fig. 7.4a. First, we initialize a system of N qubits and apply a state-preparation procedure to prepare a reference state $|S\rangle = S|0^N\rangle$. Next, we use a single ancilla qubit in the $|+\rangle$ state to apply a controlled perturbation, prepar-

ing an entangled superposition of $|0\rangle|S\rangle$ and a probe state $|1\rangle|R\rangle$ where $|R\rangle = R|S\rangle$. The system is then evolved under H for time t (see also (7.34)). Finally each qubit is projectively measured, producing a sequence of $N+1$ bits — a snapshot. By measuring the ancilla in the X or Y basis, this circuit effectively performs an interferometry experiment between the reference and probe states. The resulting snapshot measurements enable parallel estimation of two-time correlation functions of the form $C_{O,R}(t) = \langle S|e^{iHt}Oe^{-iHt}R|S\rangle$ for all 2^N operators O that are diagonal in the measurement basis. Crucially, $D^A(\omega)$ can be determined from the same set of snapshots for various A and ω, by changing the classical processing.

To estimate the spectral function $D^A(\omega)$, we use a hybrid quantum-classical computation based on the following expression,

$$D^A(\omega) = \underbrace{\tilde{\mathbb{E}}_{R\sim\mathcal{R}} \int dt}_{\text{circuit average}} \underbrace{e^{i\omega t} \sum_s \langle S|R^\dagger A\, O_s e^{-iHt}|S\rangle}_{\text{classical processing}} \times \underbrace{\langle S|e^{iHt}O_s e^{-iHt}R|S\rangle}_{\text{quantum evolution (Fig. 7.4)}} . \tag{7.9}$$

For this to be formally equivalent to (7.8), the distribution over perturbations $\mathcal{R}$ and ensemble of observables $\{O_s\}$ must couple uniformly to all eigenstates, to ensure unbiased estimation (see Methods). For example, given a polarized reference state $|0\rangle^{\otimes N}$, X-basis measurements are sufficient.

To realize the distributional average and time-integral, the quantum circuit has to be executed (Fig. 7.4a) for randomly sampled perturbations R and evolution times t. In order to efficiently evaluate the classical part of (7.9), we require efficient clas-

sical representations of $|R\rangle$ and $e^{-iHt}|S\rangle$. A good choice is to select $|S\rangle$ to be a known eigenstate of H, such that the time-evolution is trivial, and preferentially sample $|R\rangle$ to maximize the overlap with relevant target states. In contrast, the quantum part of (7.9) includes time-evolution of $|R\rangle$, which has overlap with unknown eigenstates, and often includes large amounts of entanglement. Therefore, this is estimated from snapshot measurements produced by quantum simulation (see Methods).

As an example, consider two interacting spin-3/2 particles, described by $H_2 = J\mathbf{S}_1 \cdot \mathbf{S}_2$. We prepare a polarized reference eigenstate $|S\rangle = |0\rangle^{\otimes 6}$, and sample perturbations R from an ensemble of random single-spin rotations. This corresponds to a trivial state-preparation circuit and a simple controlled-perturbation composed of two-qubit gates in Fig. 7.4. Next, we measure the system in the X-basis, which provides access to the full spectrum for this choice of $|S\rangle$ (Methods). Finally, during classical processing, the bare density of states is obtained by choosing $A = 1$, and evaluating (7.9). The result contains peaks at frequencies ω associated with eigenstates of H_2 (see Fig. 7.4b). Further, we can isolate individual contributions of total spin sectors by instead choosing $A = P_S$, the projectors onto $S = 0, 1, 2$, and 3. This not only allows us to identify the total spin of the eigenstates, but also increases the effective spectral resolution in the presence of noise as it sparsifies the signal. Finite-temperature response functions[530], like the z-component of the zero-field magnetic susceptibility $\chi(T) = \frac{1}{Z}\,\mathrm{tr}\left[\frac{1}{T}(S_z)^2 e^{-H/T}\right]$, can also be computed from the same dataset, by integrating the S_z-projected density-of-states $D^{S_z}(\omega)$ (see Methods). To illustrate this, the magnetic susceptibility is extracted from the same dataset and shown in Fig. 7.4c. The algorithm is especially promising for near-term devices, having favorable resource requirements quantified by the number of snapshots (sample complexity) and maximum evolution time (coherence) required for accurate spectral computation (see Methods

for further discussion).

7.5 Application to transition metal clusters and magnetic solids

As an illustration of a relevant computation in chemical catalysis, we consider the Mn_4O_5Ca core of the oxygen-evolving complex (OEC), a transition metal catalyst central to photosynthesis which is still not fully understood[540,881]. Classical chemistry calculations have been used to fit model Heisenberg Hamiltonians, containing three spin-3/2 sites and one spin-2 site[774,775,776] (Fig. 7.5a). While this spin representation cannot directly capture chemical reactions, it can capture the ground and low-lying spin-states, i. e., the spin-ladder, which are important in catalysis because reaction pathways depend critically on the spin multiplicity[938]. We simulate our framework applied to the S_2H-1b structural model from Ref.[775], by first computing the bare density-of-states $D^1(\mathcal{A})$ (Fig. 7.5b). Then, we identify a low-lying cluster of eigenstates, and compute spin-projected densities $D^{P_z}(\mathcal{A})$ to resolve the spin ladder (Fig. 7.5c). The spin ladder can also be measured experimentally, providing a way to evaluate candidate models of reaction intermediates. To highlight this, we simulate the Heisenberg model for an alternate pathway (S_2H-2b)[775], and observe the modification reverses the ordering of the spin ladder, indicating S_2H-1b is more consistent with measurements (see Fig. 7.5d).

The framework can also be applied to study low-energy properties of extended systems, including strongly correlated materials. We illustrate this on the ferromagnetic, square lattice Heisenberg model (Fig. 7.6). For such large systems, we envision utilizing an approximate ground-state preparation method for $|S\rangle$, so that low-energy properties can be accessed in a noise resilient manner via local controlled-perturbations R.

Then, local Green's functions — two-point operators at different positions and times — can be measured to access properties of low-lying quasi-particle excitations, such as the dispersion relation of single-particle excitations (see Methods, 2D Heisenberg, for details).

7.6 Outlook

These considerations indicate that reconfigurable quantum processors enable a powerful, hardware-efficient framework for quantum simulation of problems from chemistry and materials science, illustrating potential directions for the search for useful quantum advantage. Specifically, in addition to the OEC, other organometallic catalysts could be studied with this approach, including iron-sulfur clusters[798,961], for which bi-quadratic terms appear in the model Hamiltonian to capture higher-order perturbative charge fluctuation effects[940]. Another promising direction involves quantum simulation of low-energy properties of 2D and 3D frustrated spin systems, including model Hamiltonians for Kitaev materials[739,1001,958] and molecular magnets[574,999]. The ability to realize non-local interactions further opens the door to simulation of spin-Hamiltonians defined on non-Euclidean interaction geometries[537,900].

The efficiency of the Hamiltonian engineering approach originates from co-designing Floquet engineering and hardware-specific multi-qubit gates. Extending this approach to larger classes of strongly-correlated model Hamiltonians is an outstanding and exciting frontier. In particular, it would be especially interesting to further develop the toolbox to incorporate charge transport and electron-phonon interactions. This could enable simulation of more complex model Hamiltonians, such as the t-J, Hubbard, and Hubbard-Holstein models, and expand the class of accessible chemistry prob-

lems[551,860]. Application to other settings, including lattice gauge theories[593,1012] and quantum optimization problems[644] are also of interest. Incorporation of error mitigation and correction into the Hamiltonian simulation should be considered; specifically, the present method can potentially be generalized to control logical, encoded degrees of freedom in a hardware-efficient way[565].

Finally, characterization and development of the model Hamiltonian approach itself is an interesting and challenging problem. Key challenges include development of efficient schemes to compute parameters for higher-order interactions[940], estimation of corrections arising from coupling to states outside the model space[692], and validation of the model Hamiltonian approximation[771]. Feedback between the classical and quantum parts of the computation is an important part of these developments[552,984,724]. For these reasons, the large-scale simulation of model Hamiltonians on quantum processors will be invaluable for testing approximations by comparing simulation outputs with experimental measurements. Hence, the approach proposed in this work facilitates exciting directions in computational chemistry and quantum simulation, aiming towards constructing a novel ab initio simulation pipeline that utilizes hybrid quantum-classical resources.

Acknowledgments. We thank A. Aldossary, T. Betley, D. Bluvstein, M. Cain, L. Cunha, J. Feldmeier, C. Kokail, J. Lee, N. Leitao, S. Gant, J. Haber, S. Hollerith, T. Manovitz, J. Neaton, S. Sachdev, A. Schuckert, K. Seetharam, and P. Zoller for insightful discussions. This work was supported by the US Department of Energy [DE-SC0021013 and DOE Quantum Systems Accelerator Center (contract no. 7568717)], the Defense Advanced Research Projects Agency (grant no. W911NF2010021), the National Science Foundation (via CUA PFC, Q-IDEAS HDR, PHY-2207972), the Department of Defense Multidisciplinary University Research Initiative (ARO MURI, grant no.

W911NF2010082), Wellcome Leap under the Q for Bio program, the DARPA IMPAQT programme (grant number HR0011-23-3-0030) and the Harvard-MIT Center for Ultracold Atoms. N.M. acknowledges support from the Department of Energy Computational Science Graduate Fellowship under Award Number DE-SC0021110. A.M.G and R.A.B acknowledges support from the NSF through the Graduate Research Fellowships Program, and A.M.G also acknowledges support through the Theodore H. Ashford Fellowships in the Sciences. A.I.K. acknowledges support from the U.S. Defense Advanced Research Projects Agency (DARPA) Quantum Benchmarking Program (Contract No. HR001122C0063). J. S. and M. H.-G. acknowledge support from the NSF QCLI program through grant number QMA-2016345.

Author Contributions: N.M., S.O., M.K., M.D.L., S.F.Y. contributed to the conception and design of Hamiltonian simulation tools. N.M., J.S., M.H.G. contributed to conception and design of spectroscopy algorithms. N.M., S.O., M.K., A.M.G, R.A.B, performed theoretical and numerical analysis. S.O., J.S. R.A.B., D.W., A.K., N.Y., M.H.G., M.D.L., S.F.Y. contributed to conception of model Hamiltonian approach. M.H.G., M.D.L., S.F.Y. supervised the work. All authors discussed the results and contributed to the manuscript.

Competing interests: A.I.K. is the president and a part-owner of Q-Chem, Inc., M.H.G. is a part-owner of Q-Chem Inc., M.D.L. is a co-founder and shareholder of QuEra Computing Inc.. The remaining authors declare no competing interests.

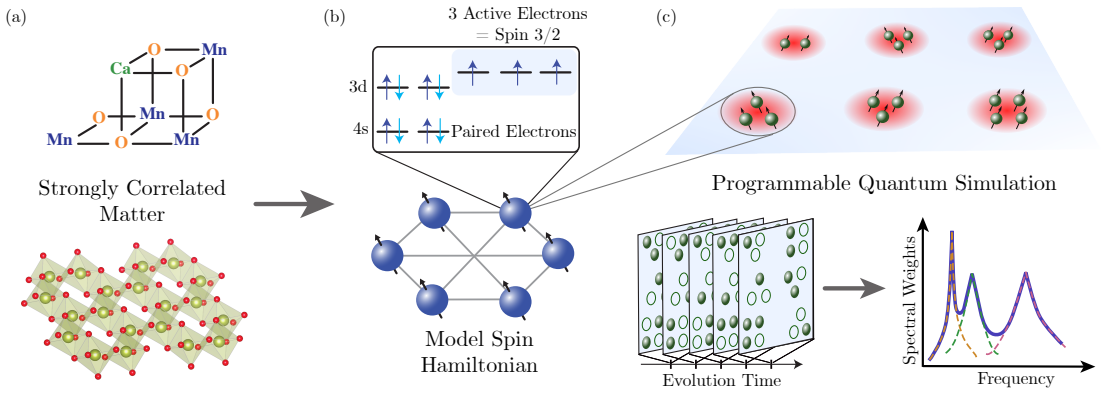


Figure 7.1: Model Hamiltonian approach to quantum simulation of strongly-correlated matter. (a) The procedure starts with a description of the target molecule or material structure, whose electronic structure problem is reduced using classical computational chemistry techniques to a simpler effective Hamiltonian that captures the relevant low-energy behaviors. (b) Here we study problems which are modeled by spin Hamiltonians with potentially non-local connectivity and generic on-site spin $S \geq 1/2$, where each spin is comprised of localized, unpaired electrons in the original molecule. The key simplification comes from capturing charge fluctuations perturbatively, which is a good approximation in certain contexts. (c) Programmable quantum simulation is then used to calculate properties of the model Hamiltonian. We develop a simulation framework, based on encoding spins into clusters of qubits, that can be readily implemented on existing hardware. The toolbox enables efficient generation of complex spin interactions by leveraging dynamical reconfigurability and hardware-optimized multi-qubit gates (Figs. 7.2 and 7.3). The quantum simulator performs time-evolution under the spin Hamiltonian for various simulation times t, and each qubit is projectively measured to produce an set of snapshots. Subsequent classical processing extracts properties like the low-lying excitation spectrum and magnetic susceptibilities, all from the same dataset (see Figs. 7.4-7.6).

7.7 Methods

7.7.1 Hamiltonian Engineering

The Hamiltonian engineering toolbox introduced here is based on the average Hamiltonian approach. This approach uses the fact that in the high-frequency limit, the effective Floquet cycle period $K\tau$ is much smaller than the inverse local energy scales of $H_{i,j}(p)$, and the Floquet Hamiltonian H_F can be well-approximated by expanding in

a small parameter $\frac{K\tau}{||H(p)||_{\text{local}}}$ [520]. The leading contribution is the average Hamiltonian

$$H_F^{(0)} = \frac{1}{K}\sum_{k=0}^{K-1} H(k). \tag{7.10}$$

The second order term also takes a simple form,

$$H_F^{(1)} = \frac{\tau}{2K}\sum_{k<k'} \left[H(k), H(k')\right]. \tag{7.11}$$

The results presented in the main text involve engineering the average Hamiltonian $H_F^{(0)}$ to reproduce the target (7.1). In the setting where θ_p is constant, one can apply the results of Ref.[657] to construct an alternative asymptotic expansion, where each term in the Floquet Hamiltonian commutes with H_P, implying the encoding is preserved to exponentially long times $e^{O(||H(p)||_{\text{local}}/K)}$. However, in this setting, the second order term is non-zero, and generates simulation errors at order $O(\tau)$. It can be cancelled by selecting time-reversal symmetric sequences of length $2K$, where the second half of the pulse is defined by $\Theta_k = \Theta_{K-1-k}$. This reduces simulation errors to order $O(\tau^2)$, but might potentially alter the pre-thermal properties of the Floquet Hamiltonian[657], which is an interesting problem for further research.

Going beyond average Hamiltonian engineering is also possible by optimizing the Floquet sequence[747,554,962]. We demonstrate engineering of higher-order terms for a small system composed of two interacting spin-3/2's, to controllably engineer up to bi-cubic terms $(\hat{\mathbf{S}}_i \cdot \hat{\mathbf{S}}_j)^3$ using only two- and three-qubit operations in Extended Data Fig. 7.7 and the first section in the Supplementary Information (SI).

7.7.2 High-spin Hamiltonian engineering with dynamical Floquet projection

To compute the form of the interaction Hamiltonian in the rotated frame $H_I(k) = e^{i\Theta_k H_P} H_I e^{-i\Theta_k H_P}$ as used in (7.5) let's consider a single spin-1/2 particle belonging to a spin-S_i cluster, and define projectors $P_i = P[\hat{\mathbf{S}}_i^2]$ onto the symmetric space and $Q_i = 1 - P_i$ onto its complement. The spin-1/2 term can be split into four parts

$$\hat{\mathbf{s}}_{i,1} = \underbrace{P_i \hat{\mathbf{s}}_{i,1} P_i + Q_i \hat{\mathbf{s}}_{i,1} Q_i}_{\text{symmetric}} + \underbrace{P_i \hat{\mathbf{s}}_{i,1} Q_i + Q_i \hat{\mathbf{s}}_{i,1} P_i}_{\text{non-symmetric}} \tag{7.12}$$

where the first two terms preserve the on-site total spin, and the second two change the on-site total spin. Since H_P acts as $1 - P_i$ on the i-th spin, we label terms by how they change the expectation value of $(1 - P_i)$

$$\hat{\mathbf{s}}_{i,1}^{(0)} = P_i \hat{\mathbf{s}}_{i,1} P_i + Q_i \hat{\mathbf{s}}_{i,1} Q_i \tag{7.13}$$

$$\hat{\mathbf{s}}_{i,1}^{(+1)} = Q_i \hat{\mathbf{s}}_{i,1} P_i \tag{7.14}$$

$$\hat{\mathbf{s}}_{i,1}^{(-1)} = P_i \hat{\mathbf{s}}_{i,1} Q_i \tag{7.15}$$

This decomposition ensures that each term transforms under conjugation by H_P, as

in (7.5), by picking up a global phase. Specifically, using the following identifies

$$e^{-i\theta P_i} P_i = P_i e^{-i\theta P_i} = e^{-i\theta} P_i \tag{7.16}$$

$$e^{-i\theta Q_i} P_i = P_i e^{-i\theta Q_i} = P_i \tag{7.17}$$

$$e^{-i\theta P_i} Q_i = Q_i e^{-i\theta P_i} = Q_i \tag{7.18}$$

$$e^{-i\theta Q_i} Q_i = Q_i e^{-i\theta Q_i} = e^{-i\theta} Q_i \tag{7.19}$$

one can show that

$$e^{i\theta\lambda^{-1}H_P} \hat{\mathbf{s}}_{i,1}^{(n)} e^{-i\theta\lambda^{-1}H_P} = e^{i\theta n} \hat{\mathbf{s}}_{i,1}^{(n)}. \tag{7.20}$$

This rule can be extended to higher-weight operators. For example, two-spin interactions between clusters $h_{ij} = \hat{\mathbf{s}}_{i,1} \cdot \hat{\mathbf{s}}_{j,1}$ decompose into five parts $h_{ij}^{(n)}, n = -2, -1, 0, 1, 2,$

$$h_{ij} = \underbrace{\hat{\mathbf{s}}_{i,1}^{(0)} \cdot \hat{\mathbf{s}}_{j,1}^{(0)} + \hat{\mathbf{s}}_{i,1}^{(+1)} \cdot \hat{\mathbf{s}}_{j,1}^{(-1)} + \hat{\mathbf{s}}_{i,1}^{(+1)} \cdot \hat{\mathbf{s}}_{j,1}^{(-1)}}_{h_{ij}^{(0)}} \tag{7.21}$$

$$+ \underbrace{\left(\hat{\mathbf{s}}_{i,1}^{(+1)} \cdot \hat{\mathbf{s}}_{j,1}^{(0)} + \hat{\mathbf{s}}_{i,1}^{(0)} \cdot \hat{\mathbf{s}}_{j,1}^{(+1)}\right)}_{h_{ij}^{(+1)}} + h.c. \tag{7.22}$$

$$+ \underbrace{\left(\hat{\mathbf{s}}_{i,1}^{(+1)} \cdot \hat{\mathbf{s}}_{j,1}^{(+1)}\right)}_{h_{ij}^{(+2)}} + h.c., \tag{7.23}$$

corresponding to the different ways to change the expectation value of $Q_i + Q_j$. The n-spin interactions will have terms running from $h^{(-n)}$ to $h^{(+n)}$. Therefore, in the ro-

tating frame, the Hamiltonian terms transform as

$$h_{ij}^{(n)}(p) = e^{i\Theta_p \lambda^{-1} H_P} h_{ij}^{(n)} e^{-i\Theta_p \lambda^{-1} H_P} \tag{7.24}$$

$$= e^{i\Theta_k n} h_{ij}^{(n)} \tag{7.25}$$

$$h_{ij}(p) = \sum_{n=-n_{\max}}^{n_{\max}} e^{i\Theta_k n} h^{(n)}. \tag{7.26}$$

We further choose a sequence of Θ_k's such that only the $h^{(0)}$ contribution is non-zero on average. The simplest sequence which satisfies these conditions are a family of cyclic pulses of order P.

$$\Theta_p = \frac{2\pi i}{P} p \qquad\qquad p = 0, ..., P-1 \tag{7.27}$$

which satisfy the cancellation condition as long as $n_{\max} < P$. In the two-body case, of the terms which contribute to $h_{ij}^{(0)}$, only $\hat{\mathbf{s}}_{i,1}^{(0)} \cdot \hat{\mathbf{s}}_{j,1}^{(0)}$ acts non-trivially in the symmetric subspace, so we focus on this term. An explicit form can be computed by decomposing $\hat{\mathbf{s}}_{i,1}$ into its permutation-symmetric and orthogonal components,

$$\hat{\mathbf{s}}_{i,1} = \underbrace{\frac{1}{2S_i} \sum_{a=1}^{2S_i} \hat{\mathbf{s}}_{i,a}}_{\text{symmetric}} + \underbrace{\left(\frac{2S_i - 1}{2S_i} \hat{\mathbf{s}}_{i,1} - \frac{1}{2S_i} \sum_{a'=2}^{2S_i} \hat{\mathbf{s}}_{i,a'} \right)}_{\text{non-symmetric}}. \tag{7.28}$$

Therefore, the symmetric part $\hat{\mathbf{s}}_{i,1}^{(0)} = \frac{1}{2S_i} \hat{\mathbf{S}}_i$ is proportional to the collective spin.

With this understanding, we can construct a spin-1/2 interaction Hamiltonian H_I that recovers (7.1) under projection, by replacing each n-site high-spin interaction

with an analagous spin-1/2 one. For example, for $n = 2$ the replacement proceeds as

$$\begin{aligned} J_{ij}^{\alpha\beta}\hat{S}_i^{\alpha}\hat{S}_j^{\beta} &\to \overline{J_{ij}}^{\alpha\beta}\hat{s}_{i,a}^{\alpha}\hat{s}_{j,b}^{\beta} \\ \overline{J_{ij}}^{\alpha\beta} &= 4S_iS_jJ_{ij}^{\alpha\beta}, \end{aligned} \tag{7.29}$$

where intra-cluster indexes a, b encode which representative from spin's i and j are used to generate the interaction. The interaction strength is further boosted to $\overline{J_{ij}}$, to account for the $\frac{1}{2S}$ factor in (7.28). A straightforward calculation shows that for higher-weight interactions (e.g. $n_{\max}$), the interaction should also be boosted (e.g. $\overline{K_{ijk}} = 8S_iS_jS_kK_{ijk}$) to recover the target large-spin operator under projection.

In general, it may not be feasible to uniquely assign each spin-S_i interaction in H to qubits in H_I especially when a spin-S_i is involved in more than $2S$ interactions. In this case, H_I can be implemented by splitting it into a sequence of non-overlapping groups $H_{I,1}, ..., H_{I,D}$ that approximate H_I on average. Each sequence can handle up to $D(2S)$ interactions per spin, so if d is the interaction degree then we require a sequence of length $D = \lceil \frac{d}{2S} \rceil$. While manual decompositions sufficed for the models studied here, automated methods to determine efficient decompositions will have to be developed for more complex systems.

7.7.3 Multi-qubit gates with Rydberg blockade

The Rydberg Hamiltonian governing a cluster of N atoms is

$$H_{\text{cluster}} = \frac{\Omega_q(t)}{2}\sum_i |1\rangle_i\langle 0| + \frac{\Omega_r(t)}{2}\sum_i |r\rangle_i\langle 1| + h.c.$$
$$+ \sum_{i<j} V_{ij}|r\rangle_i\langle r| \otimes |r\rangle_j\langle r| \tag{7.30}$$

where $\Omega_q(t), \Omega_r(t)$ are complex valued driving fields. In the blockade approximation, which is valid when $V_{ij} \gg \Omega_r$, there is at most one atom in state $|r\rangle$. Therefore, at leading order in Ω_r/V_{ij}, H_{cluster} is approximated by projecting into the manifold of blockade consistent states. This produces an interacting model with an emergent permutation symmetry (see equation (S5) in the SI). This symmetry allows us to write H_{cluster} in a low-dimensional representation of the Hilbert space scaling as $O(NN_S)$ for a representation including the N_S largest total-spin sectors (see SI).

Figure 7.2b shows optimization results for an alternating ansatz with separate $\Omega_r(t)$ and $\Omega_q(t)$ applications (solid lines) versus a dual driving scheme with simultaneous field control (dashed lines). For the alternating ansatz the optimization process begins with finding short sequences of symmetric diagonal gates $D(\varphi)$ and global single-qubit rotations $Q(\theta)$ that combined realize U_S and U_P (see Eq. (S11) in the SI). While $Q(\theta)$ uses global $\Omega_q(t)$ control, $D(\varphi)$ involves multi-qubit interactions, and the pulse sequences to realize $D(\varphi)$ can be optimized through gradient ascent pulse engineering (GrAPE)[753,737,659]. Numerical optimization is feasible due to the manageable size of the low-dimensional basis. We find that the maximum gate time $T^*(n)$ for generic phases (see Supplementary Figure 1). Gate times in Fig. 7.2 are computed by multiplying $T^*(n)$ with the shortest sequence length determined in the first step. The operations $Q(\theta)$ and $D(\varphi)$ can also be promoted to controlled operations (see SI), as

required for the controlled perturbation in Fig. 7.4a.

Dual driving gate profiles are directly optimized using GrAPE, with an added smoothness regularization to ensure driving profiles can be implemented with available classical controls (see Eq. (S8) in the SI and Extended data Fig. 7.7). Interestingly the optimized fidelity remains roughly independent of the system size, when tolerating noise-free error rates around 10^{-3}. We select this fidelity threshold, and plot the resulting gate times in Fig. 7.2b (dotted lines). However, for more stringent noise-free thresholds, such as 10^{-6}, we observe an approximately linear dependence in n, producing gate times comparable to the alternating decomposition. Theoretical characterization of the asymptotic scaling of gate time with cluster size and error threshold remains an intriguing open question.

For comparison, we estimate gate counts for a decomposition of U_S and U_P into single and two qubit gates (see Fig. 7.2c). Using the Qiskit transpiler[899], we find two-qubit decompositions into single qubit rotations and CPhase gates for U_P. For U_S, the diagonal gates $D(\varphi)$ found numerically in the alternating ansatz only require two-qubit interactions, and can be decomposed into $\binom{n}{2}$ two-qubit CPhase gates, outperforming the Qiskit result for $n \geq 3$. Finally, we show in the SI that symmetric operations like U_S and U_P can be implemented with poly(n) two-qubit gates using ancilla qubits, by constructing an efficient MPO representation of arbitrary n-spin operations.

The fidelity of the multi-qubit gates is subject to errors like spontaneous emission and dephasing due to a finite T_2^*, as seen in current Rydberg gates[659]. In general, errors accumulate with gate time, hence shorter gates tend to produce higher-fidelity implementations. Certain errors can also be mitigated by improving the excitation schemes. Specifically, single-photon schemes as used in as in Refs.[817,919], avoiding

intermediate-state scattering, may enhance performance for bigger clusters. This is because the rate of decay from the Rydberg state does not depend on cluster size, since the number of Rydberg excitations is never larger than one. In contrast, the rate of scattering from the intermediate state grows linearly with cluster size.

7.7.4 Estimating simulation time

The simulation time is defined as the maximum evolution time, before which the typical error-per-qubit is below some target threshold ε. We account for both coherent Hamiltonian simulation errors and incoherent gate errors. For a symmetrized sequence, we estimate the scaling of both contributions to be

$$\varepsilon_{\text{sim}} = (c_2\tau^2)^2 T^2, \varepsilon_{\text{gate}} = \frac{gT}{\tau}, \tag{7.31}$$

with target evolution time T and step-size τ. Here, the coefficient c_2 depends on the detail of the Hamiltonian simulation protocol, and can be estimated from numerics or the third order term in the Magnus expansion (see Eq. (S18) in the SI). The coefficient g measures the gate error probability per cycle, and is determined by assuming each multi-qubit gate has a fixed probability of failure $T_{\text{gate}}g_0$ which scales linearly in the time of the gate. Such a scaling is valid, when errors are dominated by spontaneous emission from the Rybderg state. For simplicity, we utilize the estimated T_{gate} for large-angle unitary U_P with $\theta = \pi$. Both c_2 and g are estimated to grow extensively in system size. Thus, we work instead with the intensive version of these quantities, $\tilde{c}_2 = c_2/L$ and $\tilde{g} = g/L$.

Optimizing the step-size τ to minimize error (see SI), the maximum evolution time

scales as

$$T_{\text{opt}} = \frac{2^{2/3}}{5^{5/6}} \frac{\varepsilon^{5/6}/L}{(\tilde{c}_2 \tilde{g}^2)^{1/3}} \tag{7.32}$$

for a target error rate ε.

In Fig. 7.3, we use this formula, along with numerical estimates for c_2 in models (i) and (ii), and heuristic estimates for models (iii) and (iv). We further estimate g using the simultaneous driving gate times of Fig. 7.2b, and select an error per Rabi cycle of $g_0 = 10^{-3}$. The target error we select is $\varepsilon^{5/6}/L = 0.1$, which grows approximately extensively with system size.

We illustrate the benefits of our approach on four example Hamiltonians (Fig. 7.3). First we consider the spin-1/2 Heisenberg model on a Kagome lattice (i). The standard two-qubit decomposition involves applying a sequence of six-steps, each applying a $e^{-i\theta \mathbf{s}_i \cdot \mathbf{s}_j}$ gate along an edge (i,j) (solid lines in Fig. 7.3). However, using native three-qubit Heisenberg gates, we group the interactions into upwards and downwards facing triangles (dotted lines Fig. 7.3), reducing the sequence to only two-steps, improving c_2. The three-qubit gate also generates interactions more efficiently, further improving g. Note that four-qubit version of this scheme could simulate the spin-1/2 Heisenberg model on a pyrochlore lattice using $K = 2$ [710].

The second model (ii) are two interacting high-spins with $S_i = 5/2$, which interact via a mix of Heisenberg and Dzyaloshinskii–Moriya (DM) interactions,

$$J_{ij}^{\alpha\beta} = J\delta_{\alpha\beta} + D\sum_{\gamma} \varepsilon_{\alpha\beta\gamma}.$$

The conventional decomposition splits the 25 pairwise interactions into five groups of five, which are applied sequentially. In contrast, there is a dynamical projection scheme for this model with $K = 2$ (see Eq. (S25) and the discussion thereafter in the SI). This improvement in Floquet engineering efficiency compensates the overhead from introducing a five-qubit gate, leading to slightly higher accessible simulation times. Scaling with S_i is summarized in Table IV in the SI.

The final two models (iii and iv) are composed of spin-2 particles on a square lattice. (see Eq. (S26) in the SI) In model (iii), nearest-neighbor spins interact via a Heisenberg and bi-quadratic interaction, $\sum_{k=1}^{2} J_k(\mathbf{S}_i \cdot \mathbf{S}_j)^k$. The conventional Trotter approach requires realizing many four-qubit interactions per spin-2 producing very long Floquet periods. In contrast, dynamical projection can be implemented by applying a single four-qubit gate per edge, resulting in smaller K. The multi-qubit implementation is also signficantly more efficient, as the two-qubit decomposition of a four-qubit interaction comes with large overhead, as illustrated in Fig. 7.2c. To highlight the separate contribution from Floquet projection and multi-qubit gates, we compute the effective simulation time for four cases in the table below.

Finally, we consider a model including up to bi-quartic terms $k \leq 4$. Here, we further consider using an eight-qubit multi-qubit gate to directly realize the interaction between two large-spins (iv). This interaction naturally preserves the symmetry, so dynamical projection is not needed in this case. As such, the speedup comes entirely from the efficiency of the optimized eight-qubit operation, compared against the large overhead associated with a two-qubit decomposition of an eight-qubit interaction.

7.7.5 Many-body Spectroscopy

To complete our simulation framework, we also develop tools for resource-efficient readout of Hamiltonian properties. First, we illustrate how to compute two-time correlation functions of the form

$$C_{O,R}(t) = \langle S|O(t)R(0)|S\rangle, \tag{7.33}$$

using the circuit in Fig. 7.4a. The real and imaginary parts of $C_{O,R}(t)$ are independently accessed by measuring the ancilla in the X and Y basis, respectively[802,876,810,985]. More concretely, consider the state of the system right before measurement, including both the ancilla qubit and the system,

$$|\psi_{\mathrm{f}}\rangle = \frac{1}{\sqrt{2}}\left(|0\rangle \otimes U(t)\,|S\rangle + |1\rangle \otimes U(t)R\,|S\rangle\right), \tag{7.34}$$

where U is the time-evolution operator. Measuring $X \otimes O$ or $Y \otimes O$ results in

$$\langle X \otimes O\rangle_{\psi_{\mathrm{f}}} = \frac{1}{2}\left(\langle S|\,R^{\dagger}O(t)\,|S\rangle + \langle S|\,O(t)R\,|S\rangle\right), \tag{7.35}$$

$$\langle Y \otimes O\rangle_{\psi_{\mathrm{f}}} = \frac{i}{2}\left(\langle S|\,R^{\dagger}O(t)\,|S\rangle - \langle S|\,O(t)R\,|S\rangle\right), \tag{7.36}$$

which together gives the full complex-valued $C_{O,R}(t)$ by taking a linear combination of the two,

$$C_{O,R} = \langle (X + iY) \otimes O \rangle_{\psi_f}. \tag{7.37}$$

For observables O diagonal in the measurement basis, $C_{O,R}$ can be efficiently estimated in parallel from snapshots. During the i-th run, let $\mu^{(i)} = \{x, y\}$ be the randomly sampled ancilla measurement basis, and $a^{(i)} = \{0, 1\}$, and $|b^{(i)}\rangle$ be the ancilla and system measurement outcomes respectively. Then, the estimator can be written as

$$\overline{C_{O,R}(t)} = \frac{1}{M} \sum_{i=1}^{M} 2\sigma(\mu^{(i)}, a^{(i)}) \langle b^{(i)}|O|b^{(i)}\rangle \tag{7.38}$$

where σ is a function taking on the values

$$\begin{aligned} \sigma(x, 0) &= +1, & \sigma(x, 1) &= -1, \\ \sigma(y, 0) &= +i, & \sigma(y, 1) &= -i. \end{aligned} \tag{7.39}$$

and $|b^{(i)}\rangle$ is the measured projected state.

These measurements can be used to compute the operator-resolved density of states (7.8), which can be rewritten as follows

$$D^{A}(\omega) = \int dt\, e^{i\omega t} \sum_{n} \mathrm{tr}\left[A|n\rangle e^{-i\varepsilon_n t}\langle n|\right]$$
$$= \int dt\, e^{i\omega t}\, \mathrm{tr}[AU(t)], \tag{7.40}$$

where we have replaced $\delta(\omega - \varepsilon_n) \to \int dt\, e^{i(\omega-\varepsilon_n)t}$. In practice, we will sample evolution times t from a probability distribution $p(t)$, such that the integral is normalized to one when $\omega = \varepsilon_n$, i. e., $\int dt = \int_{-\infty}^{\infty} p(t)dt = 1$. To arrive at (7.9), we can replace the trace with an average over probe states[1022]

$$\mathrm{tr}[AU(t)] = \tilde{\mathbb{E}}_{R\sim\mathcal{R}}\langle R|AU(t)|R\rangle, \tag{7.41}$$

where $\tilde{\mathbb{E}}_{R\sim\mathcal{R}} = \mathrm{Tr}[1]\mathbb{E}_{R\sim\mathcal{R}}$ is a normalized expectation value, and $\mathrm{Tr}[1]$ is the dimensionality of the Hilbert space. This is valid, as long as the ensemble forms a 2-design,

$$\mathbb{E}_{R\sim\mathcal{R}}|R\rangle\langle R| = \frac{1}{\mathrm{tr}[1]}, \tag{7.42}$$

For example, we can sample perturbations R from the ensemble of random single-qubit rotations. Such perturbations can be implemented using the techniques from Fig. 7.2, by applying a sequence of two-qubit gates between an ancilla qubit, and the system qubits. In general, convergence properties of the estimator depend on higher-moments of $\mathcal{R}$ (see Eq. (S27) in the SI).

Observables such as (7.41) can in principle be computed via a modified Hadamard

test by applying controlled-time evolution (see Ref.[810]). Since time-evolution is generally the most costly step, we avoid the overhead associated with controlled-evolution and instead utilize a reference state $|S\rangle$ with simple time-evolution. In particular, we select an ensemble of observables O_s such that

$$\frac{1}{\mathcal{N}(O_s)} \sum_s O_s U(t)|S\rangle\langle S|U^\dagger(t) O_s = 1. \tag{7.43}$$

The normalization factor $\mathcal{N}(O_s)$ depends on the choice of ensemble. Then, we can insert this resolution of the identity into (7.41) to get (7.9). In Fig. 7.4 and Fig. 7.5, we consider the polarized reference state $|S\rangle = |0\rangle^{\otimes N}$ which is an exact eigenstate of the Heisenberg Hamiltonian, and the ensemble of Pauli-X operators $O_s = X_s = \bigotimes_{i=1}^N (X_i)^{s_i}$ where s is an N-bit string. This satisfies the condition, and has $\mathcal{N}(X_s) = 1$ since $X_s|0\rangle^{\otimes N}$ is an orthonormal basis. For generic reference states $|S\rangle$ prepared by applying S to $|0\rangle^{\otimes N}$, the ensemble $O_s = SX_sS^\dagger$ satisfies the condition, and can be measured by applying the inverse preparation circuit $S^\dagger$ before measuring in the X-basis. Lastly, an ensemble which is independent of the reference state, is the set of Pauli strings $P_s = \bigotimes_{i=1}^N \sigma_i^{s_i}$, where s is a base-four string, and σ^{s_i} denotes the four Pauli operators I, X, Y, Z; this can be accessed with randomized measurements (see Eqs. (S56)-(S57) in the SI), and has a normalization factor $\mathcal{N}(P_s) = 2^N$.

Efficient estimation of $D_R^A(t)$ from snapshots

One of the key advantages of our approach, is the ability to compute many estimators $D_R^A(t)$ from one dataset, including complex operators such as projectors onto spin-sectors $A = P_S$. This enhances the sample efficiency and reduces simulation time

requirements, which are crucial limited resources in quantum computation.

To estimate density-of-states in a sample efficient way, we introduce a classical co-processing algorithm which utilizes knowledge of the prepared reference state. In particular, we discuss the estimation procedure for

$$\begin{aligned} D_R^A(t) &= \sum_s \underbrace{\langle R|AO_sU(t)|S\rangle}_{\text{classical}} \underbrace{\langle S|U^\dagger(t)O_sU(t)|R\rangle}_{\text{quantum}} \\ &= e^{-iE_St} \sum_s \langle R|AO_s|S\rangle\langle S|O_s(t)|R\rangle \end{aligned} \tag{7.44}$$

which becomes (7.9) after averaging over times t and perturbations R. In the second line, we assumed $|S\rangle$ is a known eigenstate, so $U(t)|S\rangle = e^{-iE_St}|S\rangle$, and the classical part becomes equivalent to a zero-time correlation function. One challenge is that the sum in (7.44) involves exponentially many observables. However, by using the estimator (7.38) this reduces to a sum over M snapshots. In particular, for the polarized reference state, and Pauli-X measurements, a simple calculation (see Eq. (S36) in the SI) shows that

$$\overline{D_R^A(t)} = \frac{1}{M}\sum_{i=1}^{M} e^{-iE_St} 2^{N/2} \sigma(\mu^{(i)}, a^{(i)}) \langle R|A|b^{(i)}\rangle \tag{7.45}$$

is an unbiased estimator. The standard error of this estimator is independent of system size for appropriately chosen ensembles $\mathcal{R}$, and scales as $O(1/\sqrt{M})$. While $C^*_{O_s,AR}(0)$ could instead be estimated by measuring the unevolved state, this would produce an estimator that converges very slowly, leading to a sample complexity that is exponential in N. However, classical methods can compute $C^*_{O_s,AR}(0)$ with no error, making

the procedure much more sample-efficient. In the discussion below Eq. (S46) in the SI, we discuss how such calculations can be efficiently performed for any pair of reference and probe states with an efficient matrix product state (MPS) description, and any observable A with a matrix product operator (MPO) description. Further, we show that projectors P_S onto spin-sectors can be written as MPOS with poly(N) bond-dimension, making evaluation of $D^{P_S}(\omega)$ classically efficient and scalable. We further discuss how entangled measurements between two systems could be used to estimate these correlators efficiently, even when $|S\rangle$ does not have a known classical description.

Thermal expectation values

The operator-resolved density of states can be used to compute thermal expectation values via[810]

$$\langle A\rangle_\beta = \frac{\int e^{-\beta\omega} D^A(\omega) d\omega}{\int e^{-\beta\omega} D^1(\omega) d\omega}. \tag{7.46}$$

For example, to compute the magnetic susceptibility, we simply select the operator $A = \beta(S^z)^2$, where $\beta = 1/T$ is the inverse temperature. Interestingly, this method of estimating thermal expectation values is insensitive to uniform spectral broadening of each peak, due to a cancellation between the numerator and denominator (see discussion resulting in Eq. (S69) in the SI). However, it is highly sensitive to noise at low ω, which is exponentially amplified by $e^{-\beta\omega}$. To address this, we estimate the SNR for each $D^A(\omega)$ independently, and zero-out all points with SNR below three times the average SNR. This potentially introduces some bias by eliminating peaks with low-signal, but ensures the effects of shot-noise are well controlled.

7.7.6 Noise Modelling

To quantify the effect of noise on the engineered time-dynamics, we simulate a microscopic error model by applying a local depolarizing channel with an error probability p at each gate. This results in a decay of the obtained signals for the correlator $D_R^A(t)$. The rate of the exponential decay grows roughly linearly with the weight of the measured operators (see Extended Data Fig. 7.8). This scaling with operator weight can be captured by instead applying a single depolarizing channel at the end of the time-evolution, with a per-site error probability of γt with an effective noise rate γ. This effective γ also scales roughly linear as a function of the single-qubit error rate per gate p (see Extended Data Fig. 7.8).

7.7.7 Scaling the approach

Quantum simulations are constrained by the required number of samples and the simulation time needed to reach a certain target accuracy. These factors are crucial for determining the size of Hamiltonians which can be accessed for particular quantum hardware.

Focusing on a single gapped eigenstate we determine the number of snapshots C_M needed to distinguish a spectral peak from noise (Fig. 7.10). The signal arises from the overlap of the probe states with the target eigenstate. The noise is given by the variance of the estimator (7.45), and decays as $\varepsilon \sim M^{-1/2}$. For certain ensembles of probe states, the variance can be made system size independent (see Eq. (S52) in the SI). However, a random probe state will have exponentially vanishing overlap with any specific eigenstate. One approach to mitigate this, is to initialize probe states with higher overlap. In Fig. 7.9b we show that for a spin-1 AFM chain a simple bond-

dimension two MPS can outperform product states by orders-of-magnitude in ground-state estimation. While bond-dimension two states can be efficiently prepared with simple circuits of two qubit gates, more general ansatze can also be efficiently realized using the simulation techniques described here[696,671]. Optimized ansatze could be further combined with importance sampling[839], to improve the sample-efficiency of computing finite-temperature or excited state properties (see Supplementary Figure 3).

The simulation time $T_{\max}$ will depend on the required spectral resolution, which does not scale with system size for a gapped eigenstate. However, the rate of spectral broadening depends sensitively on the weight of measured observables (Fig. 7.8). When the reference state is high in energy, such as the polarized state for an AFM chain, the relevant observables typically have extensive weight, requiring $T_{\max} \sim N$ to maintain constant spectral resolution. In contrast, preparing a low-energy reference state, such as the ground-state $|S\rangle = |GS\rangle$, allows coupling to other low-energy states using low-weight operators. This results in a noise-resilient and system-size independent procedure (Fig. 7.9). We further note that ground-state preparation can be approximate, which would result in additional spectral broadening in the computation of $D^A(\omega)$. While the spectral resolution requirements should also grow as the gap shrinks, we have illustrated that operator-resolution can mitigate this in certain settings (e.g. Fig. 7.5 and Fig. 7.6). As such, understanding the general capabilities of this approach is an interesting direction for continued research.

7.7.8 OEC Hamiltonians

The two candidates for the closed S2 state of the oxygen evolving complex (OEC) are parameterized with Heisenberg models $H = -\sum_{ij} J_{ij} \hat{\mathbf{S}}_i \cdot \hat{\mathbf{S}}_j$[774,776], and the parameters

used are summarized in the SI (OEC parameters). In addition to their energies, additional information about eigenstates can be calculated by choosing the operator A in the operator resolved density of states appropriately, and multiplying by a narrow "band-pass" filter in Fourier space to isolate a small set of frequencies[810,927]. For example, we investigate the total spin of the cubane sub-unit, i. e., the three magnetic sites supported on opposite vertices of the cube, using $A = (\hat{\mathbf{S}}_1 + \hat{\mathbf{S}}_2 + \hat{\mathbf{S}}_3)^2$, and compute

$$\mathcal{A}(\omega) = \frac{D^A(\omega)}{D^1(\omega)} \tag{7.47}$$

evaluated at energies ω_n of the eigenstates, which can be extract from peaks in the spectral functions (Extended data fig. 7.11). We further use spin-projection to improve the estimate in the presence of broadening. For example, if the peak at ω_n occurs in spin-sector P_S, we insert the projector P_S in the numerator and denominator, $\mathcal{A}(\omega_n) = \frac{D^{AP_S}(\omega_n)}{D^{P_S}(\omega_n)}$.

7.7.9 2D Heisenberg calculations

The square lattice Heisenberg calculation was performed on a large $(L \times L)$ system, with Hamiltonian

$$H_{2D} = -J \sum_{\mathbf{r}} \left(\hat{\mathbf{S}}_{\mathbf{r}} \cdot \hat{\mathbf{S}}_{\mathbf{r}+\hat{x}} + \hat{\mathbf{S}}_{\mathbf{r}} \cdot \hat{\mathbf{S}}_{\mathbf{r}+\hat{y}} \right) \tag{7.48}$$

We measure the Green's function $G(\mathbf{r}, t) = \langle S | X_{\mathbf{r}}(t) X_0 | S \rangle$ from a polarized reference

$|S\rangle^{\otimes L^2}$ [766]. Since S^z is conserved under the dynamics $G(\mathbf{r},t)$ is classically simulated by restricting it to the space containing the $|S\rangle$ and single spin-flip states $X_\mathbf{r}|S\rangle$, which has dimension L^2+1. We evolve under equally spaced times up to $JT_{\max}=8$, and select $L=23$ which is large enough such that $G(r,t)$ vanishes far from the boundaries. Therefore, by letting $G(r,t)=0$ outside the simulated region, this provides a good approximation for the $L\to\infty$ limit. As such, we define projectors onto (unnormalized) plane-wave states $P_\mathbf{k}=|\mathbf{k}\rangle\langle\mathbf{k}|$, where $\langle\mathbf{k}|X_\mathbf{r}|S\rangle = e^{-i\mathbf{k}\cdot\mathbf{r}}$. Then, $D^{P_\mathbf{k}}(\omega)$ can be written as

$$D^{P_\mathbf{k}}(\omega)=\int dt e^{i(\omega-\omega_0)t}\sum_\mathbf{r}\underbrace{\langle S|X_0P_kX_\mathbf{r}|S\rangle}_{e^{i\mathbf{k}\cdot(\mathbf{r}-0)}}\underbrace{\langle S|X_\mathbf{r}(t)X_0|S\rangle}_{G(r,t)} \tag{7.49}$$

which reduces to the Fourier transform $G(k,\omega)$ when the energy of the polarized state ω_0 is set to zero. Plotting this for a continuous set of k and ω produces the spectral weight depicted in Fig. 7.6. This further shows that finite-size systems are sufficient to simulate extended systems at finite evolution times.

By computing the peak value of ω for each k in the vicinity of the single-particle excitations, we estimate the dispersion relation $\omega(k)$ associated with a single spin-flip excitation. Computations of the many-particle Green's function could be performed similarly by applying multi-site perturbations, to extract finite-temperature properties and characterize the interactions between the quasi-particles.

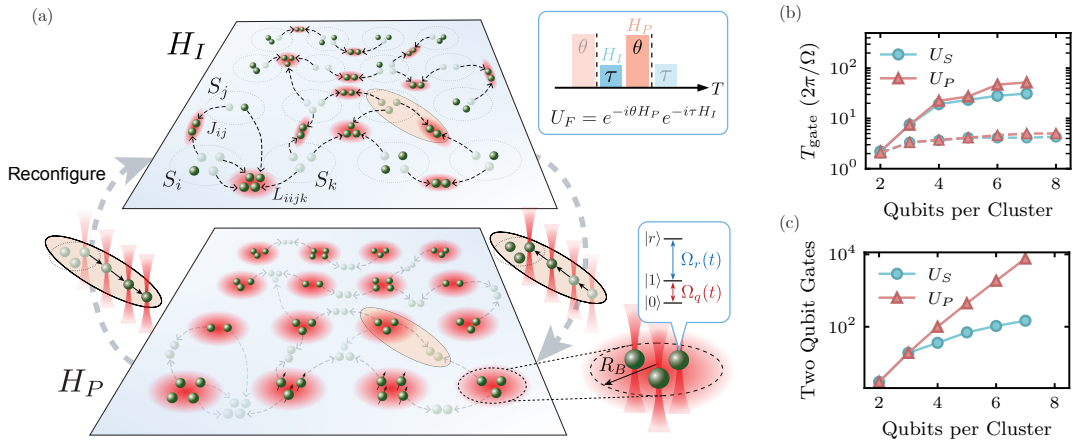


Figure 7.2: Hardware-efficient implementation with neutral-atom tweezer arrays. (a) Our protocol for programmable simulation of generic spin Hamiltonian is based on applying sequences of interactions between non-overlapping few-qubit groups. Here, we illustrate an implementation of a complex spin model using the dynamical projection approach. Spin-S_i variables are encoded in the collective spin of a cluster of $2S_i$ qubits. Then, interactions between spins are generated by evolving pairs of qubits from each cluster under an interaction Hamiltonian H_I. Second-order interactions J_{ij} act on two qubits, while higher-order interactions act on multiple qubits, such as the fourth-order coefficient L_{iijk} of $\hat{S}_i^{\alpha}\hat{S}_i^{\beta}\hat{S}_j\hat{S}_k$. Then, interactions are dynamically projected into the symmetric encoding space within each cluster by evolving under Hamiltonian H_P. The target large spin Hamiltonian H is simulated by alternately evolving under H_I and H_P. This protocol can be realized in any reconfigurable quantum processor. Here, we present an implementation for Rydberg atom arrays, which has two long-lived qubit states $|0\rangle, |1\rangle$, and an excited Rydberg state $|r\rangle$ with strong interactions. The interaction connectivity is dynamically changed by moving optical tweezers[569], and interactions are generated using all-to-all Rydberg blockade interactions within each cluster and simultaneous global driving of the qubit $\Omega_q(t)$ and Rydberg $\Omega_r(t)$ transitions. (b) Fast and efficient multi-qubit spin operations U_S, U_P are identified using optimal control to optimize pulse sequences. Gates times are measured in units of the Rydberg driving frequency ΩT, where the two-qubit CZ gate from Ref.[659] takes $\Omega T/2\pi \approx 1.2$. The alternating ansatz (solid lines) decomposes the target operations into symmetric diagonal gates and single qubit rotations, which can be are individually optimized (see Methods). Simultaneous (dual) driving of both transitions (dotted lines) enables even faster realization of approximate U_S and U_P gates with noise-free error rates below $\sim 10^{-3}$. (c) We compare against decomposition of U_S and U_P into a two-qubit gate set composed of CPhase gates and single-qubit rotations. Such a decomposition rapidly becomes very costly as the cluster size grows, in contrast to the optimized hardware-native operation.

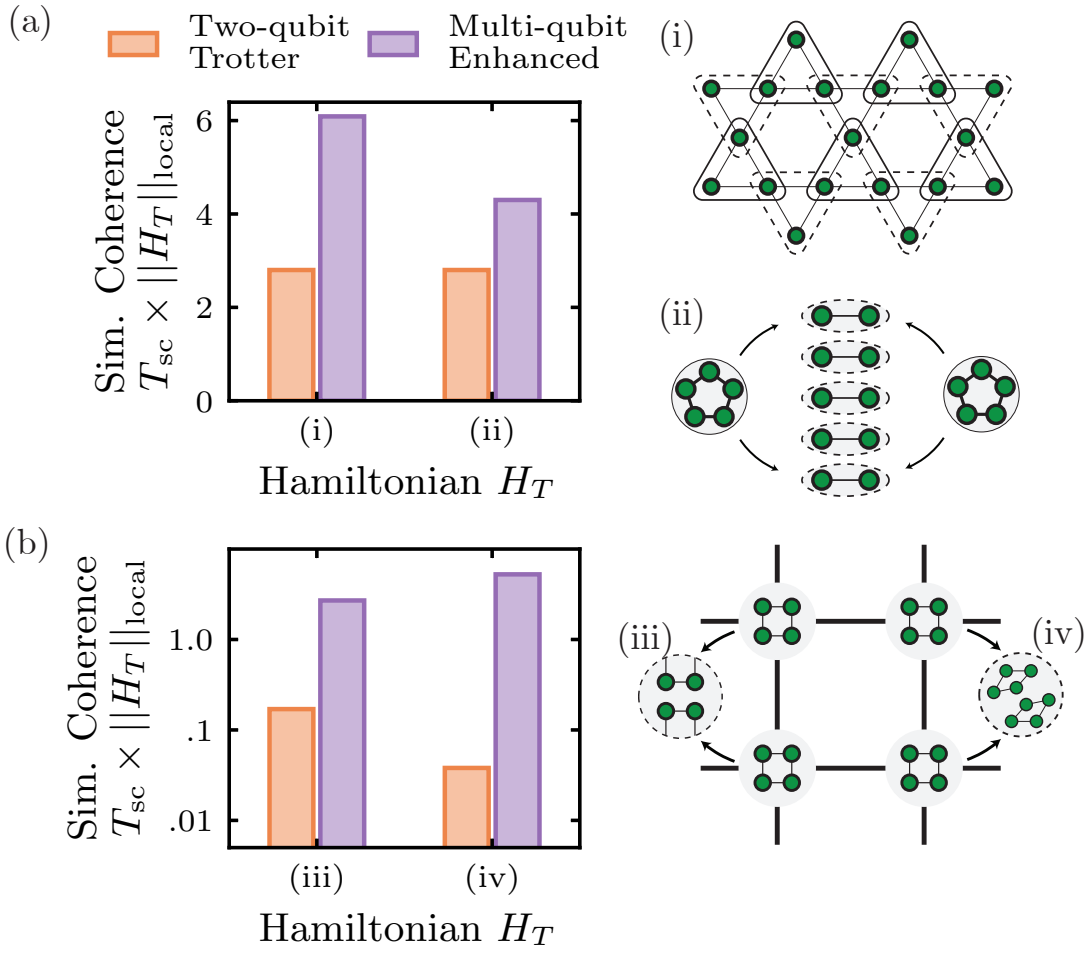


Figure 7.3: Efficiency of Hamiltonian simulation framework. Estimates of the quantum simulation's coherence time T_{sc}, in the target Hamiltonian's units $||H_T||_{local}$ for various models. We consider Hamiltonian simulation implemented using the dual driving gates from Fig. 7.2b, and assume a depolarizing error probability proportional to the gate time, such that $\Omega T/2\pi = 1$ incurs an error of 0.1%, which is projected to be achievable with neutral atoms [659,919,817]. Analogous estimates can be performed straightforwardly for different hardware-dependent error rates using (7.32), which rescales T_{sc} but does not change the trend. In all cases, we compare against an implementation using two-qubit CPhase gates with fidelity 99.9% and perfect single-qubit rotations (see Methods for detailed descriptions of the heuristic estimation procedure). (a) The first two two models are (i) the spin-1/2 Kagome Heisenberg model, and (ii) two interacting spin-5/2's with Heisenberg and Dzyaloshinskii–Moriya (DM) terms, both of which are composed of only two-qubit interactions. In (i), a significant speedup is achieved by utilizing three-qubit multi-qubit gates $e^{-i\pi \mathbf{S}^2}$, which more efficiently generates Heisenberg interactions and reduces the period of the Floquet cycle from $K = 4$ to $K = 2$. In (ii) improvement is achieved using dynamical projection, which reduces K from $2S$ to 2 but at the cost of additional multi-qubit gates. (b) Two complex spin-models which include spin-interactions up to (iii) bi-quadratic interactions $J_1(\mathbf{S}_i \cdot \mathbf{S}_j) + J_2(\mathbf{S}_i \cdot \mathbf{S}_j)^2$ and (iv) bi-quartic interactions $(\mathbf{S}_i \cdot \mathbf{S}_j)^4$. These correspond to four-body and eight-body qubit interactions respectively. In (iii), the dramatic speedup originates from using dynamical projection to significantly reduce the Floquet period, as well as the hardware-efficiency of a native four-qubit gate. The individual contribution to the speedup from both sources is also analyzed in Methods. In (iv), the speedup arises fully from the hardware-efficiency of native eight-qubit operations.

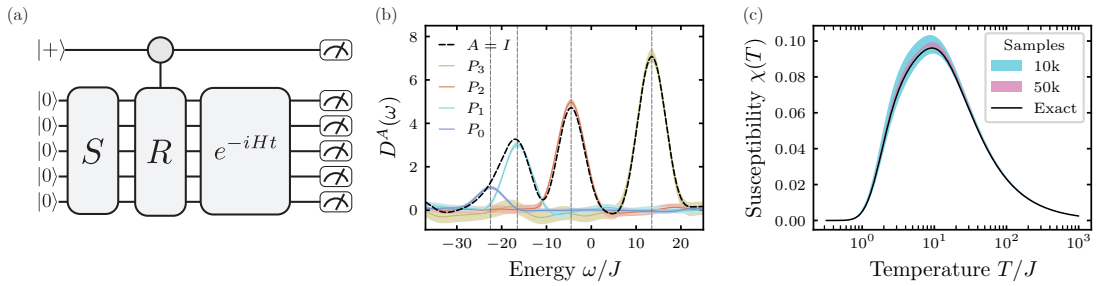


Figure 7.4: Many-body spectroscopy of model Hamiltonians. (a) Schematic quantum circuit diagram for the algorithm. The first step is to apply a state-preparation circuit S to prepare a reference state $|S\rangle = S|0\rangle$, followed by an ancilla-controlled perturbation R preparaing a superposition of $|S\rangle$ and the probe state $|R\rangle = R|S\rangle$. This superposition is time-evolved by the target Hamiltonian, and then each qubit is projectively measured to produce a snapshot. By repeating the procedure for various evolution times t, different perturbations R, and potentially different measurement bases, this setup provides access to detailed information about the spectrum of H. (b) Consider a spin Hamiltonian H_2 with two anti-ferromagnetically coupled spin-3/2's. We simulate 20,000 snapshot measurements and classical processing to calculate the density-of-states $D^{\mathbb{1}}(\omega)$ (black line), and total-spin resolved versions $D^{P_S}(\omega)$ (colored lines). Vertical dashed lines correspond to exact energies and colored regions represent 95% confidence intervals. Peaks are broadened due to finite (coherent) simulation time $JT_{\text{sim}} = 0.26$, which sets the spectral resolution. Hardware-efficient simulation schemes, which extend the simulation time (e.g. Fig. 7.3), are favorable because they improve spectral resolution. Many-body spectroscopy further improves the effective spectral resolution, by leveraging multiple observables to distinguish overlapping peaks. Here, we see that spin-resolution significantly sparsifies the signal, enabling accurate peak detection and energy estimation, while the bare spectrum $D^{\mathbb{1}}(\omega)$ is too broad to resolve all states. (c) The magnetic susceptibility χ, can also be computed from snapshot measurements using S^x-resolved density-of-states (here $JT_{\text{sim}} = 1.04$). For these calculations, it is important to prevent exponential amplification of shot-noise. We therefore use a simple empirical truncation procedure which introduces a small amount of bias (see Methods), but enables rapid convergence with number of snapshots to the ideal value (black line).

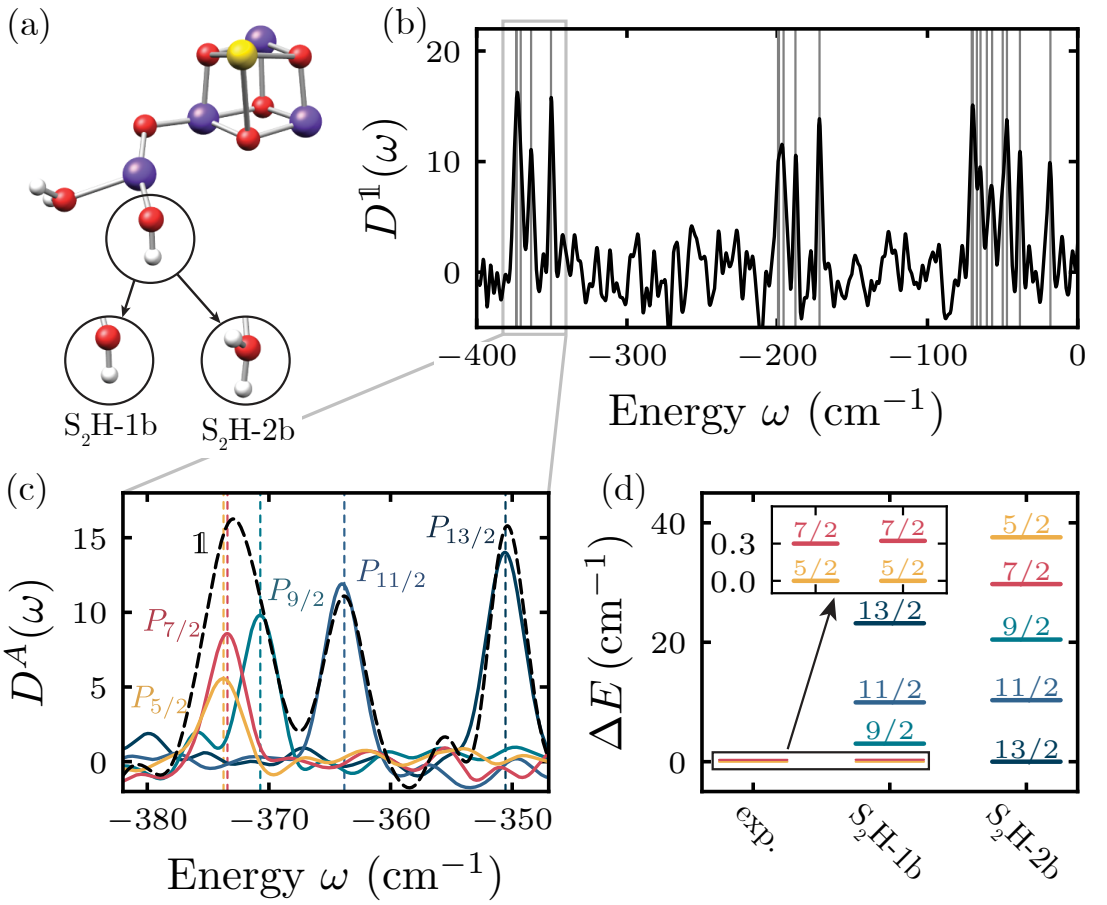


Figure 7.5: Application to the oxygen-evolving complex (OEC). Our programmable quantum simulation framework can be used to compute detailed model spin Hamiltonian properties. (a) Here, we illustrate the procedure on the OEC, an organometallic catalyst with strong spin correlations. In particular, we simulate model spin Hamiltonians for two structures S_2H-1b and S_2H-2b, which have three spin-3/2 and one spin-2 Mn (purple) active sites (reproduced from Ref.[775] with permission from the Royal Society of Chemistry). Model Heisenberg coefficients for both hypothetical structures have been computed from broken-symmetry DFT[775]. (b) A density of states $D^1(\omega)$ calculation is simulated for the S_2H-1b model spin Hamiltonian. Here, we use a polarized reference state $|S\rangle = |0\rangle^{\otimes 13}$ a probe states $|R\rangle$ generated by random single-site rotations, and a evolution times t. We select 50,000 circuits with independently chosen $|R\rangle, t$ pairs, and draw 10 snapshots from each circuit. (c) Focusing on the lowest-lying states, we see three distinct peaks in $D^1(\omega)$. However, by evaluating spin-resolved quantities $D^{P_i}(\omega)$ on the same set of measurements, we identify three additional peaks, whose energies and total-spin match exact diagonalization results (vertical dotted lines). (d) This information is known as the spin-ladder, and can be computed using many-body spectroscopy for both the 1b and 2b states. Importantly, the spin-ladder can also be measured experimentally, and therefore can be used to help determine which structure appears in nature. In this example, experimental measurements indicate a spin-5/2 ground state and spin-7/2 first excited state. However, the ordering of low-energy states is flipped in the 2b configuration, indicating the S2H-1b hypothesis is more likely[775]. We note that quantities beyond total-spin can also be readily evaluated in low-lying eigenstates by inserting different operators A (see Methods).

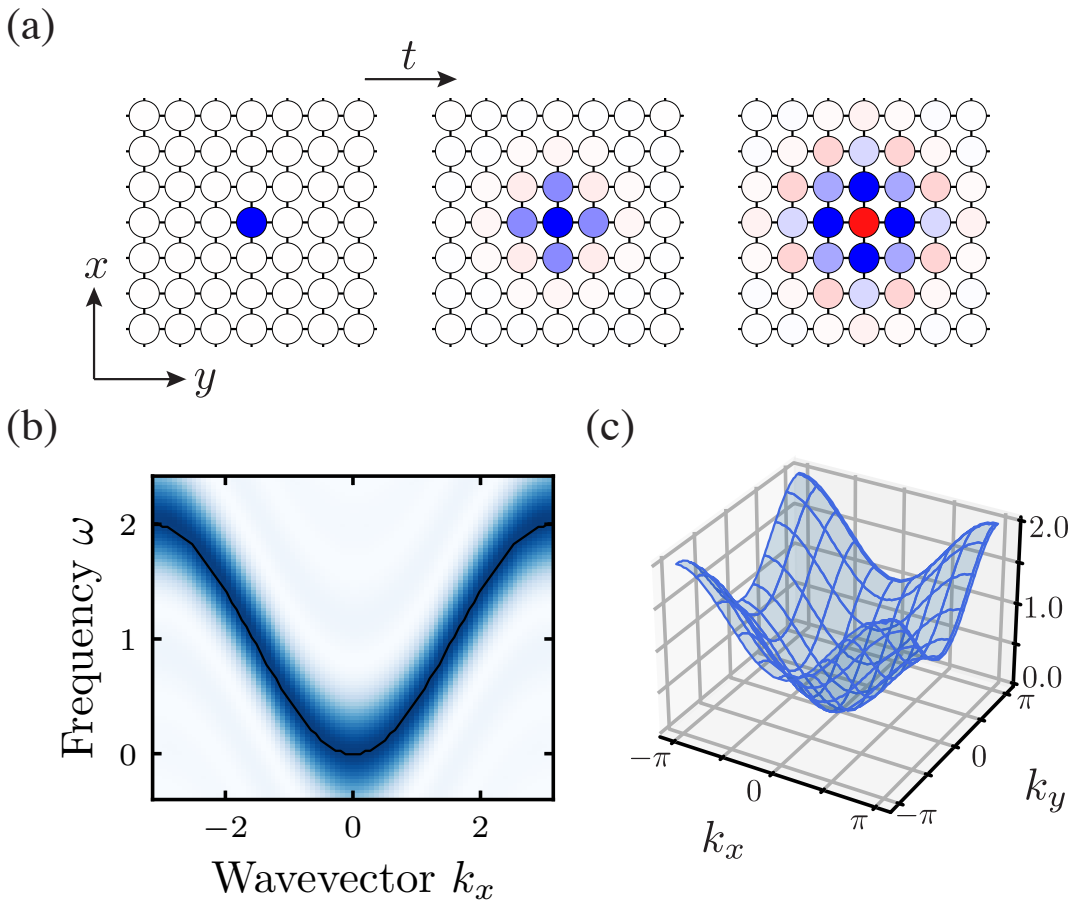


Figure 7.6: Application to 2D magnetic materials. (a) Properties of extended materials can also be investigated using our quantum simulation framework. As an example, we study the square-lattice ferromagnetic ($J > 0$) Heisenberg model $H_{\text{2D}} = -J\sum_{\langle ij\rangle} \hat{\mathbf{s}}_i \cdot \hat{\mathbf{s}}_j$. By preparing the polarized ground state $|S\rangle = |0\rangle^{\otimes N}$, applying a single-site perturbation $R = X_0$ on the central site, and measuring the system in the X-basis after time evolution, we can estimate the single-particle Green's function $G(\mathbf{r}, t) = \langle S|X_{\mathbf{r}}(t)X_0|S\rangle$. Therefore we select $O = X_{\mathbf{r}}$ for various positions $\mathbf{r}$ as the observables in (7.9), all of which are diagonal in the measurement basis. We visualize the real-part of $G(\mathbf{r}, t)$, where the plotted intensity and color denotes the magnitude and sign at $Jt = 0, 0.5$, and 1.0. (b) The structure of excited states is extracted by classical processing of these measurements. Even though the spectrum is continuous, additional structure can be identified by computing the momentum-resolved density of states $D^{P_{\mathbf{k}}}(\omega)$, where $P_{\mathbf{k}}$ is a projector onto plane-wave states (see Methods). Restricting to $k_y = 0$ and evolving to maximum time $JT_{\text{max}} = 8.0$, we see $D^{P_{\mathbf{k}}}(\omega)$ forms a band-like structure, from which a peak ω can be estimated for each $\mathbf{k}$ (black line). (c) This peak extraction allows us to directly estimate the single-particle dispersion $\omega(\mathbf{k})$ across the 2D Brillouin zone.

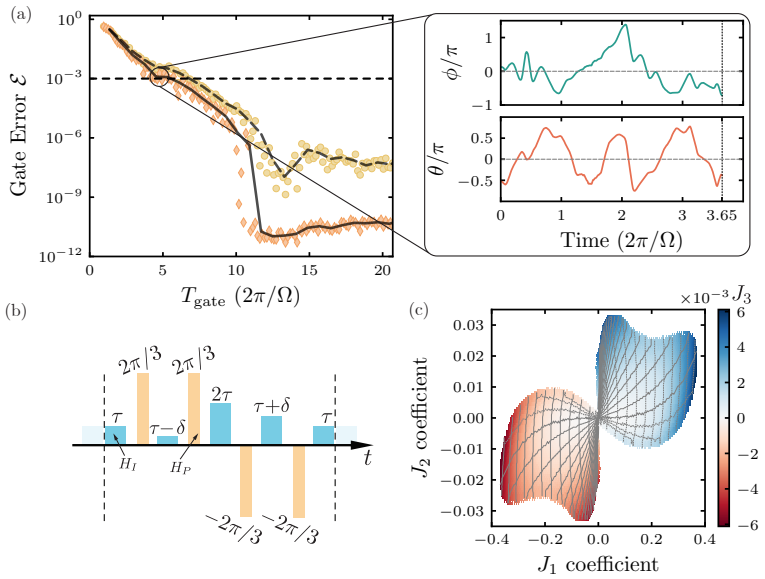


Figure 7.7: Gate optimization procedure and variational Hamiltonian Engineering. (a) To find smooth gates we perform the GrAPE optimization procedure in two steps. In the first step, we penalize rapid changes in the pulse profile by introducing an extra term in the cost-function. In this case, the resulting relationship between noise-free gate-error vs. time (yellow circles) saturates around 10^{-6}. For the second step we initialize the search with the smooth gates found in the previous step, which are re-optimized by removing the smooth penalty. This significantly reduces the noise-free gate error (orange). The data are shown for a $N = 4$ qubit cluster. Since the first step already confined the problem into a subspace of the search space with smooth gates, the resultant pulses also remain smooth after the second step. On the right we show an example smoothened pulse profile for the hyperfine angle θ and the Rydberg phase φ (see Methods) with an noise-free gate error rate $\mathcal{E} = 10^{-3}$. (b) Higher order interaction terms can be controllably engineered via a simple modification of the $K = 6$ Floquet projection sequence. For example, reducing the second time-step and increasing the fourth time-step by the same amount, δ preserves the target Hamiltonian at leading order. (c) By tuning τ and δ, for a system of two interacting spin-3/2's, a very large family of coefficients J_1,J_2,J_3 in the general Hamiltonian $H_T = J_1(\mathbf{S}_1\cdot\mathbf{S}_2)+J_2(\mathbf{S}_1\cdot\mathbf{S}_2)^2+J_3(\mathbf{S}_1\cdot\mathbf{S}_2)^3$ can be engineered. In particular, the roughly horizontal gray lines correspond to constant δ grid lines, and roughly vertical gray lines correspond to values with constant τ. We see that changing δ primarily modifies J_2 and J_3, while changing τ primarily modifies J_1, consistent with our analysis that δ picks out certain higher-order terms. We further note that the especially interesting AKLT family, with $J_2/J_1 = 116/243$ and $J_3/J_1 = 16/243$ lies among the family of efficiently engineerable interactions.

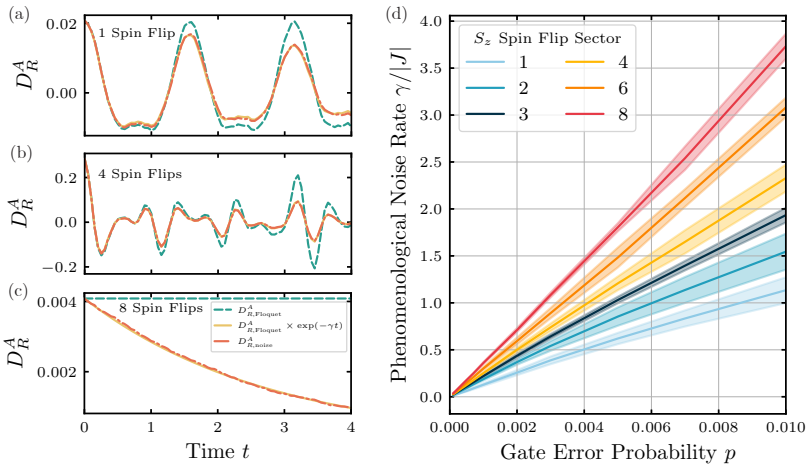


Figure 7.8: Gate-level noise simulations. (a)-(c) Time evolution of the correlations $D_R^{\mathcal{A}}(t)$ for a polarized reference state $|S\rangle = |0\rangle$ and $\mathcal{A}$ chosen to be projectors onto different S^z sectors. This involves measuring operators of fixed weight. We see that the simulation of gate-level noise modelled as a depolarizing channel with a gate error probability $p = 0.001$ (orange dash dotted curve) matches well with the dynamics obtained by adding an additional phenomenological noise $\propto \exp(-\gamma t)$ with rate $\gamma = (0.128, 0.251, 0.36)$ for $N_{\text{spin flip}} = (1, 4, 8)$ (solid yellow lines) to the loss-less time evolution $D^{\mathcal{A}}_{R,\text{Floquet}}$ (green dashed). (d) Relationship between the optimal phenomenological noise rate γ and the gate error probability p for different spin flip sectors. We see a roughly linear-relationship of the decay rate γ with the gate error rate p and operator weight S_z. All data are obtained using time-steps $J\tau = 0.05$.

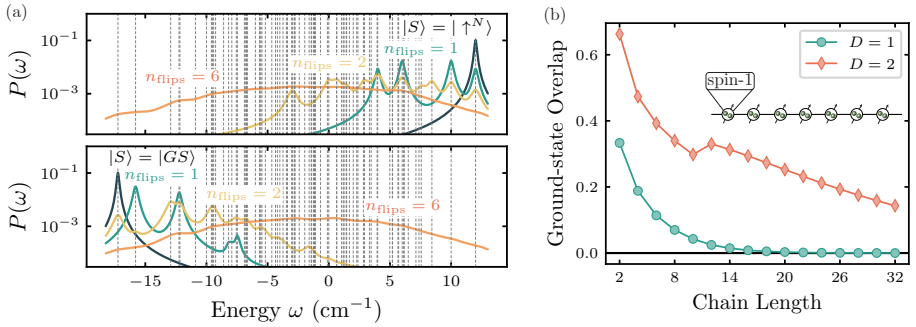


Figure 7.9: Noise susceptibility and eigenstate overlaps. (a) Density-of-states for a spin-1 AFM chain, computed from a polarized reference state $|S\rangle = |0\rangle^{\otimes N}$ (top), and ground state reference $|S\rangle = |GS\rangle$ (bottom). The spectrum is separated into sectors distinguished by their operator weight from $|S\rangle$. For the polarized state, these correspond to sectors with well-defined S^z. For the ground-state, each sector is orthogonalized with respect to lower-weight sectors. Each sector is phenomenologically broadened by $e^{-\gamma t n_{\text{flips}}}$ to simulate the operator-weight dependence of decoherence. When computing low-energy properties, the ground-state reference is more robust to noise, since the low-energy eigenstates can be reached with lower-weight operators. (b) The amplitude of the corresponding spectral peak is determined by the eigenstate overlap. We analyze the ground-state overlap for an AFM spin-1 chain performing DMRG for low bond dimensions ($D = 1, 2$) and find that it is significantly larger for bond-dimension $D = 2$ matrix product states (red diamonds) compared to bond-dimension $D = 1$, i. e., mean-field states (green circles). Interestingly, the ground state overlap decays slower with the chain length for $D = 2$ indicating that the fidelity density is large. This feature makes low bond dimension states a promising direction for efficient state preparation within our scheme since they can efficiently be decomposed into short circuits.

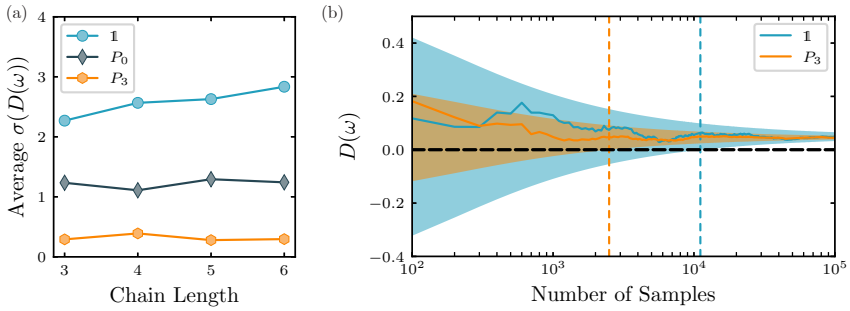


Figure 7.10: Shot noise scaling with system size and convergence with number of snapshots. (a) Numerically computed standard deviations of the estimator (7.9) for the density of states $D^A(\omega)$ of a spin-1 AFM chain, for different chain lengths and observables. Here, we consider a polarized reference state $|S\rangle$ and random single-qubit rotations R for the controlled-perturbation. For the bare density of states the standard deviation slowly scales with the chain length (blue circles). For the projectors into the zero (gray diamonds) and three (orange circles) spin-flip sectors the standard deviation is consistent with being independent of system size. (b) Convergence of estimator with number of samples for two different observables. Shaded regions correspond to 2σ error bars around the mean, and decrease with the number of measurements as $1/\sqrt{M}$. Dark lines are running averages for a specific sampled dataset. The sample complexity is defined as the number of samples needed such that the error bars around the mean do not include zero. After this point, spectral peaks can be reliably distinguished from noise.

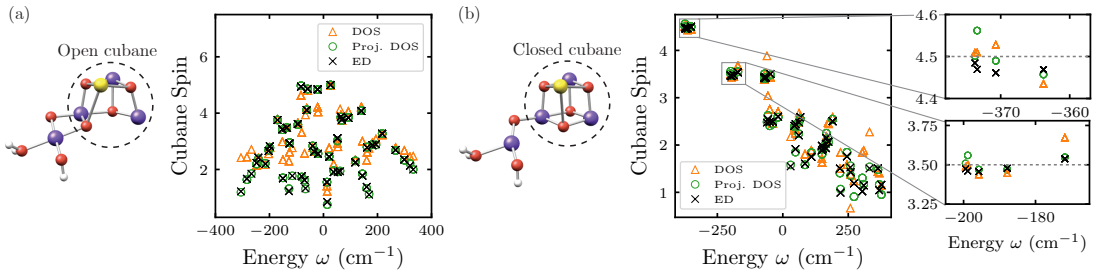


Figure 7.11: Additional observables calculated for OEC. By choosing A to be the local cubane spin S^2_{123}, and calculating $D^A(\omega)$ at each of the peaks in the density of states, we can infer the local structure of spin correlations within each eigenstate. (a) The cubane spin for each eigenstate for the open cubane configuration (S_2H-1a). This model has coefficients: $J_{12} = -15.8, J_{13} = 1.9, J_{14}, J_{23} = 23.1, J_{24} = 1.9, J_{34} = -13.9$ in cm^{-1}, and spin-sizes $S_1 = 2, S_2 = S_3 = S_4 = 3/2$. The triangles, circles and crosses are obtained using three different methods. The crosses indicate the exact value obtained via exact diagonalization (ED), the green circles indicate the values obtained via the spin resolved (projected) density of states (DOS), and the orange triangles are obtained by the bare DOS. The projected DOS, which is able to resolve individual eigenstates, matches well with the ED result. In contrast the bare DOS, which has overlapping peaks (see Fig. 7.5), does not capture the expectation values accurately. (b) Same as in (a) but for the closed cubane configuration S_2H-1b. This model has $S_1 = S_2 = S_3 = 3/2$ and $S_4 = 2$. We see that for the lowest-lying cluster, all spins in the cubane subunit are approximately polarized with a total spin value $S = 9/2 = 4.5$. In contrast, the second cluster of eigenstates seems to differ by a single spin flip as indicated by the value $S = 7/2 = 3.5$.

8

Qubits can simulate fermions without signficant overhead

8.1 Introduction

Quantum mechanical objects come in two distinct flavors, fermions and bosons, distinguished by their mutual statistics. A long-standing open question concerns the gap in computational power between systems composed of these two different types of particles[580]. While it has long been known that fermions can simulate bosons through pairing, generating fermionic statistics from bosonic particles is considerably more challenging. Providing a resolution to this question is of paramount importance in the

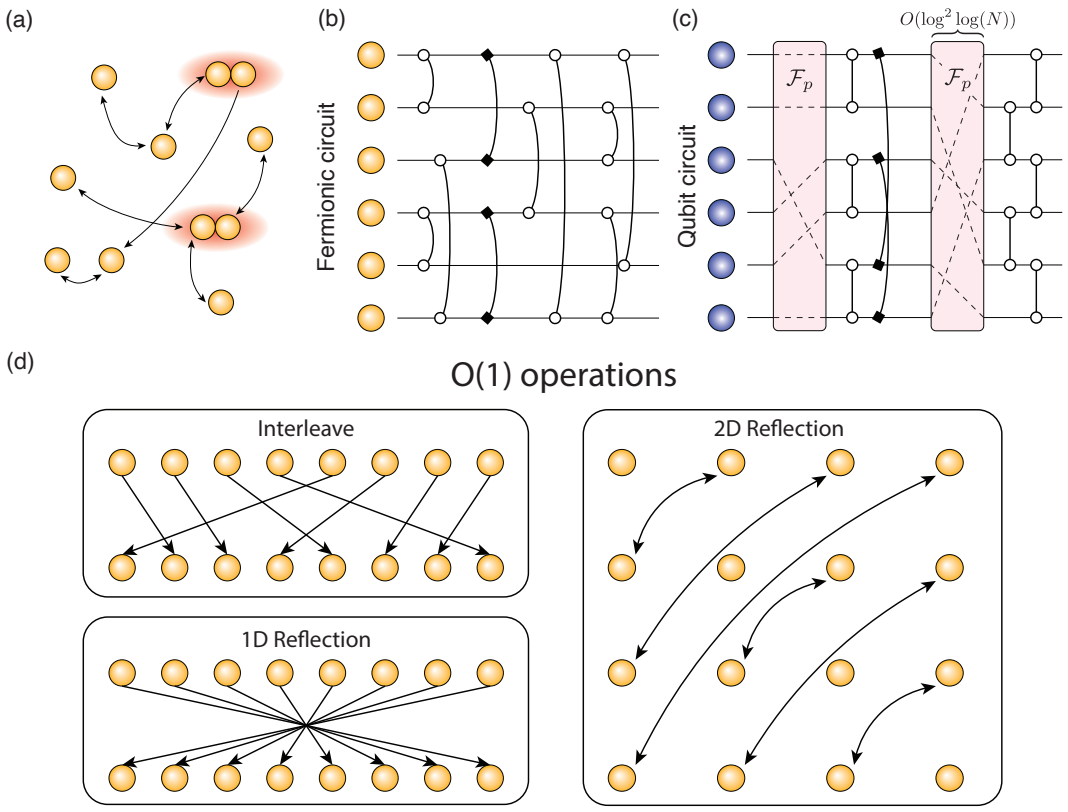


Figure 8.1: Dynamic fermion encoding with log-logarithmic overhead. (a) Fermionic evolution consisting of arbitrary hopping and interactions. (b) Direct implementation with fermionic particles. (c) Encoding fermions in qubits incurs overhead associated with exchange statistics. Encoded fermionic modes can be arbitrarily permuted with worst-case $O(\log^2 \log \mathrm{N})$ depth and (d) depth-1 in certain classes of permutations, realizing arbitrary connectivity with sub-linear overhead.

context of quantum simulation of many-body fermionic systems[524], since most quantum computing platforms encode and process information using bosonic qubits[533]. While quantum algorithms can in principle simulate nature efficiently[669], current approaches require substantial resource overheads to capture non-local fermionic statistics[742], limiting their practical application to relevant problems in material science[616], quantum chemistry[837] and particle physics[637].

Over the past 20 years, insights from condensed matter and quantum information

theory have led to a precise understanding of how fermionic excitations can emerge at low-energies in qubit-based devices, with deep connections to the emergence of long-range entanglement and topological order in quantum matter[994]. As such, it is now widely accepted that local fermionic matter can be simulated by local bosonic matter under the right conditions[978,635,604]. However, for computations involving non-local fermionic operations, it has remained unclear whether an efficient mapping to non-local bosonic operations existed. Although at the fundamental level fermions interact locally [], non-local fermionic interactions appear in effective low energy descriptions of electronic systems[837]. More generally, quantum algorithms need not be restricted by locality constraints, and the ability to implement non-local fermionic circuits can considerably speed up quantum simulation protocols[979,542,765,809].

In this work, we provide a resolution to this long-standing challenge, by presenting a qubit-based architecture for efficient fermionic simulation (Fig. 8.1). Our key insight is to use a dynamical fermionic encoding where the nature of the mapping from fermions to qubits is modified dynamically at every step, permuting the order of the fermionic modes. While previous approaches to implement fermionic permutations require $\mathcal{O}(N)$-depth circuits, here we develop a general approach which can compile any fermionic circuit to asymptotic depth $O(\log^2 \log(N))$.

We showcase the advantages of our approach by discussing two possible applications involving non-local fermionic circuits. First, we discuss simulation of sparse Sachdev-Ye-Kitaev (SYK) models[905,763,1005], which have non-local Majorana interactions, exhibit strong quantum chaos, and are believed to be holographically dual to toy models of quantum gravity. Second, we show how quantum simulations of electronic structure can be accelerated by implementing the fermionic fast Fourier transform (FFFT)[978] with $\mathcal{O}(1)$ overhead, a factor of $O(N/\log(N))$ improvement over

existing methods. These examples highlight how our novel approach generates exponentially shorter circuits then existing techniques, leading to orders-of-magnitude reduction in the implementation cost.

8.2 Dynamical Fermionic Encoding

We consider a model for a fermionic quantum computer[580] defined as follows (see Fig. 8.1a). During one step of the computation, hopping operations and density-interactions can be applied in parallel between disjoint pairs of modes. Then, the connectivity of the fermionic device is changed, such that a different set of pairwise interactions can be applied at the next step. This architecture is the analog of standard qubit-based models of quantum computation, with the additional feature that the constituent modes natively support fermionic statistics. Further, it captures key features of existing and proposed hardware for programmable fermionic quantum devices[686,1013,683,928,875,955], and can run parallel fermionic quantum computation (see Fig. 8.1b).

Our key result is a general procedure for mapping such a fermionic quantum computation to an analogous qubit computation of comparable size.

Theorem 5. (informal) Given an arbitrary fermionic circuit C_F consisting of n-modes and T layers of pairwise gates, there is an analagous circuit C_Q consisting of $O(n)$ qubits, $O(1)$-time reconfiguration, and $O(1)$-time measurement and classical feedback, that can simulate C_F in depth $O(T\log^2\log(n))$.

To achieve this, we use a dynamical fermion-to-qubit mapping. At each step of the computation, we use the Jordan-Wigner encoding to encode N fermionic modes into N qubits[742]. The fermionic creation and annihilation operators are mapped to qubit

operators based on the relation

$$a_{m_t(i)} = \frac{X_i - Y_i}{2} \prod_{i'<i} Z_{i'}, a^\dagger_{m_t(i)} = \frac{X_i - Y_i}{2} \prod_{i'<i} Z_{i'}, \tag{8.1}$$

where $m_t(i)$ is a permutation that establishes the mode ordering at step t. Importantly, the mapping is non-local, as it takes a single-site fermionic operator to a qubit one affecting, potentially, $O(N)$ sites. This non-local structure is what ensures any pair of fermion operators anti-commute. In particular, the corresponding Pauli operators obey the canonical fermionic anti-commutation relations

$$\{a_i, a_j\} = 0, \qquad \{a_i^\dagger, a_j^\dagger\} = 0, \qquad \{a_i^\dagger, a_j\} = \delta_{ij}. \tag{8.2}$$

Even though the JW encoding is non-local, operations between adjacent modes can be efficiently implemented using two-qubit gates. In particular, the two-fermion hopping $a^\dagger_{m_t(i)} a_{m_t(i+1)} + a^\dagger_{m_t(i+1)} a_{m_t(i)} \to X_i X_{i+1} + Y_i Y_{i+1}$ maps to a local two-qubit exchange operation. Hence, by changing the mapping $m_t(i)$, we can control which fermionic interactions are easy to implement.

To switch between different encodings, we define a fermionic permutation operator $\mathcal{F}_p$, which switches the encoding at step t to the encoding at step $t+1$ (see Fig. 8.1c). While general fermionic permutations, as defined here, have been discussed in previous works[765], the prior state-of-the-art implementation involved $O(N^2)$ two-qubit gates arranged in a depth $O(N)$ quantum circuit. In contrast, the analogous operation takes $O(1)$ time in a native fermionic processor. Our key technical innovation, described in detail below, is to show that an arbitrary $\mathcal{F}_p$ can be realized with $O(N \log^2 \log(N))$ two-qubit gates, arranged in a circuit of $O(N)$ qubits and depth $O(\log^2 \log(N))$.

8.3 Constant-overhead structured permutations

The first step to implementing arbitrary permutations $\mathcal{F}_p$, is to identify a subset of permutations with enough structure that an $O(1)$-depth qubit implementation is possible. Consider permutations which involve "interleaving" two groups of qubits. Formally, for an interleave permutation $\mathcal{I}_p$, the modes can be partitioned into two groups, A and B, such that the order within each group remains the same before and after the permutation.

For our implementation of $\mathcal{I}_p$ to be correct, it needs to permute the fermionic modes in a manner that is consistent with fermionic statistics, enforced by the Jordwa-Wigner enconding described above. In particular, the goal of $\mathcal{I}_p$ is to transform one mapping m_t to another m_{t+1}, such that $m_{t+1}(p(i)) = m_t(i)$. Hence, the fermionic mode originally at qubit site i is moved to qubit site $p(i)$. This corresponds to modifying the Jordan-Wigner strings as follows.

$$\mathcal{I}_p \left[X_i \prod_{i'<i} Z_{i'} \right] = X_{p(i)} \prod_{i'<p(i)} Z_{i'} \tag{8.3}$$

The standard approach to achieve this transformation, is to permute the physical qubits $i \to p(i)$, and apply a CZ gate between any pair of qubits (i,j) with $i < j$, such that $p(i) > p(j)$, i.e. pairs of modes which cross during the permutation. This is known as a fermionic swap network, and in general involves $O(N^2)$ Clifford gates.

Here, we show how to achieve an equivalent transformation, but with only $O(N)$ Clifford gates arranged in $O(1)$ depth, by leveraging the circuit in Fig. 8.2. For simplicity of presentation, we assume the partition of modes A, B is contiguous, such that $A = \{1, .., k\}$ and $B = \{k+1, ..., n\}$. In the first step of the circuit, we apply a CNOT

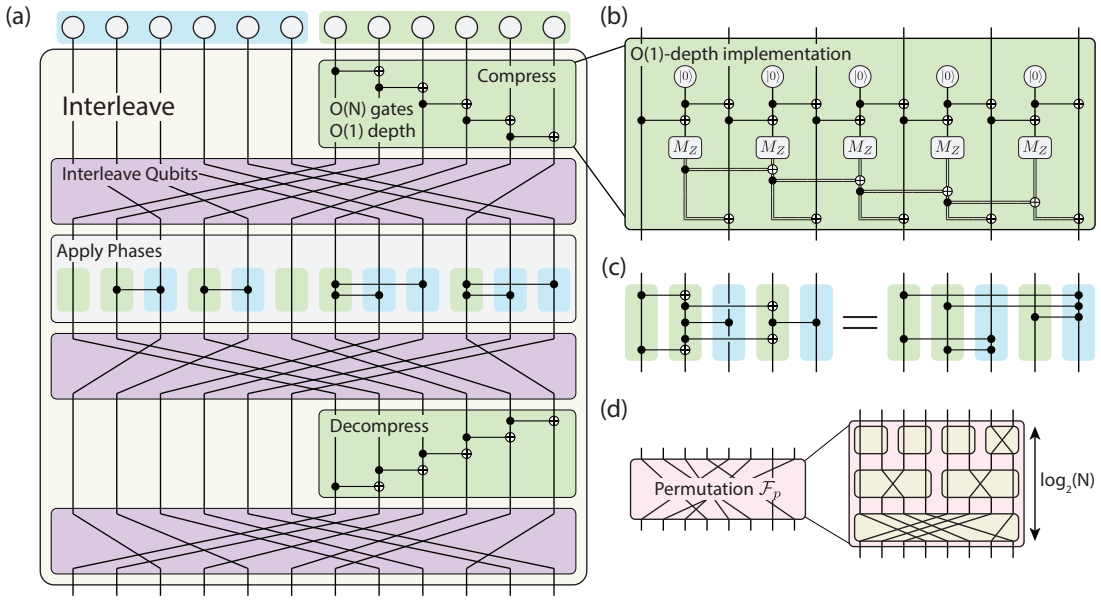


Figure 8.2: Changing fermionic encoding with minimal overhead. A key subroutine of our architecture is the interleaving operation, where two partitions of the encoded fermionic modes A (blue) and B (green) can be arbitrarily permuted with O(N) gates, as long as the ordering within the partitions is preserved. (a) The first step is to compress the information encoded in the modes in B, by applying a CNOT cascade. Then, the qubits are reconfigured based on the structure of the target interleave. Next, a layer of CZ gates is applied, connecting each mode in A to it's closest mode in B on the left. Then, the reconfiguration is inverted, and the CNOT cascade is inverted to decompress the information. Finally, the permutation is applied one more time, placing qubits in their final position. (b) While the CNOT cascade as drawn is composed of $O(N)$ gates arranged in a depth $O(N)$ circuit, this can be reduced to $O(1)$ depth using one ancilla-qubit per mode and measurement, and non-local classical feed-forward. (c) In the circuit picture, the CNOT cascades transform in parallel the CZ gates, such that effectively a CZ gate is applied between each mode in A and all of the modes in B to it's left. This ensures a CZ gate is applied between any pair of modes that cross during the permutation, realizing the correct transformation of the Jordan-Wigner encoding. (d) An arbitrary permutation of the fermionic modes can be efficiently compiled into a sequence of interleave operations, via a recursive construction. The resulting circuit structure involves performing $\log(N)$ layers of interleaves.

cascade to qubits in group B. This compresses the information of modes in B, in a manner which will significantly simplify the implementation of $\mathcal{I}_p$. Then, we reconfigure the qubits, based on the target permutation, and apply a layer of CZ gates between each qubit in group A, and the qubit from B closest and to its left. Then, we reverse the compression step, by permuting qubits and applying the inverse CNOT cascade. Then, we perform a final permutation of qubits, such that they arrive at their final locations.

While the CNOT cascade is naively a depth $O(N)$ circuit, we can introduce a single-ancilla per CNOT, perform a depth-2 CNOT circuit, and use measurement and classical Pauli-feedforward, to perform the same operation (see Fig. 8.2b). We note more generally that any Clifford circuit with $O(N)$ gates can be parallelized efficiently into a constant-depth circuit with $O(1)$ ancilla's per qubit[901,970]. Hence, the key metric we emphasize is the total number of Clifford gates per qubit.

This circuit acheives the same transformation as the fermionic swap network, with asymptotically fewer gates, because the CNOT cascade compresses information in region B such that $O(N)$ CZ gates is sufficient. When the layer of CZ gates is conjugated by the CNOT cascade, it makes it so each CZ gate coupling a mode in A to it's rightward-adjacent mode in B is broadcasted into $O(N)$ CZ gates coupling modes in A to all rightward-modes in B (see Fig. 8.2c). Due to the special structure of the interleave, only modes in A and B cross, and hence, this realizes all of the CZ's in the fermionic swap network.

8.4 Arbitrary Fermionic Permutations

Arbitrary permutations can be implemented by short sequences of $O(1)$-time operations. For example, the interleave operation can be applied $\log(N)$ times to compile an arbitrary N-qubit permutation $\mathcal{F}_p$ (see Fig. 8.2d). The idea is to use a recursive construction. Assume we can apply smaller permutations that sort the first $N/2$ and second $N/2$ modes separately. This ensures that the ordering within each group is fixed, such that the target permutation can be generated with one additional interleave operation. Since each recursion layer divides the system in half, $\log_2(N)$ layers is sufficient. Further, in practice, this approach is remarkably efficient, requiring less than $N/2$ ancillas, and leverages highly parallel operations, making it especially appealing for implementation.

The interleave is one of a variety of $O(1)$ operations we have identified (see Fig. 8.1c). All the operations leverage the same high-level structure, where a CNOT cascade is carefully constructed to compress the fermionic swap network of $O(N^2)$ CZ gates to an efficient one with $O(N)$ Clifford gates (see SI for more details). Of particular interest are the 1D and 2D reflections, which belong to a qualitatively different class, as they cannot be compiled using a constant number of interleave operations.

This enhanced set of operations unlocks our asymptotically sub-logarithmic procedure for implementing arbitrary permutations, which is used for proving Theorem 5. Intuitively, we achieve $O(\log^2 \log(N))$ scaling by partitioning the N modes into $O(\sqrt{N})$ groups of size $O(\sqrt{N})$ each. Then, we recursively sort the smaller groups before and after a 2D reflection. Hence, we can use $\mathcal{F}_p$ to efficiently switch fermionic encodings, enabling fermionic computation with qubits with minimal overhead. In the SI, we further present a heuristic numerical optimization, which identifies more efficient circuits

for compiling $\mathcal{F}_p$ at practical circuit sizes of $N = 100 - 1000$.

8.5 Random graphs and sparse SYK

One application of being able to efficiently emulate non-local fermionic circuits is quantum simulation of unstructured and sparse fermionic models. One important class are the Sachdev-Ye-Kitaev models, which are known to exhibit quantum chaos, and conjectured to be dual to simple toy-models of gravity[905,763]. The SYK models take the general form of an interacting fermionic model

$$H_{SYK} = \frac{1}{K} \sum_{ijkl} J_{ijkl} \chi_i \chi_j \chi_k \chi_l \tag{8.4}$$

where χ_i are majorana fermion operators, which are related to standard fermionic operators by $\chi_{2i} = (a_i + a_i^\dagger)/\sqrt{2}$ and $\chi_{2i+1} = (a_i - a_i^\dagger)/\sqrt{2}$. A majorana permutation can be implemented by a simple modification of the equivalent fermionic permutation (see SI), allowing Theorem ?? to be directly extended.

To compile a circuit for Hamiltonian simulation, we consider a standard procedure where we start by dividing the interactions into non-overlapping groups $H_{SYK} = \sum_\alpha H_{SYK}^\alpha$ by solving a graph coloring problem[608] (see Fig. 8.3a), such that the α-th step of a simulation cycle will involve H_{SYK}^α. In a trotter-based method, we evolve under $e^{-iH_{SYK}^\alpha dt}$ and for a QSP-based method we query a block-encoding of H_{SYK}^α (see SI). For both of these approaches, we transition from step α to $\alpha + 1$ by applying a majorana permutation, such that H_{SYK}^α becomes a local qubit Hamiltonian. Local four-majorana interactions take the form

$$\chi_{2i}\chi_{2i+1}\chi_{2i+2}\chi_{2i+3} = Z_i Z_{i+1} \tag{8.5}$$

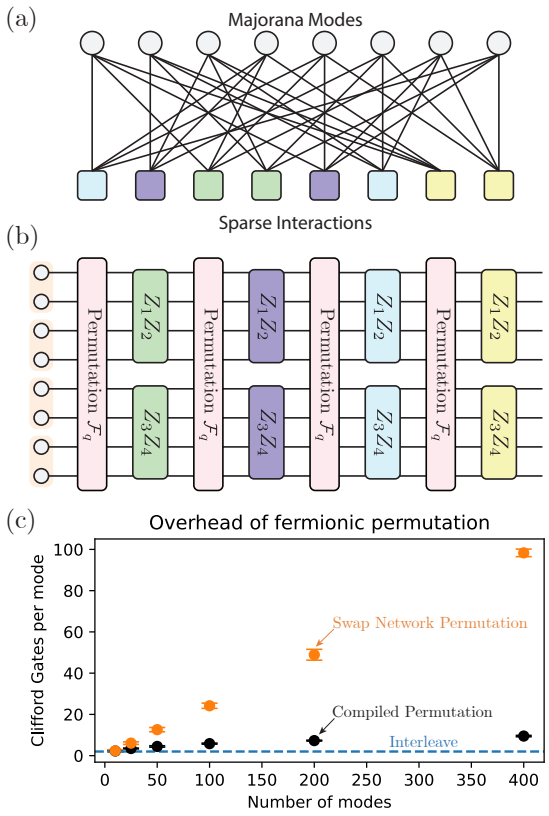


Figure 8.3: Compiling non-local, SYK models. (a) We consider non-local models where each modes is involved in d distinct four-majorana interactions, described by a constant-degree and d-colorable interaction graph. (b) A single trotter cycle or block encoding of these Hamiltonians can be implemented by alternating Majorana permutations (see SI), and two-qubit Ising interactions. (c) We use numerical optimization to compute explicit CNOT circuits for randomly sampled permutations, and present the corresponding Clifford overhead per mode, after optimization (black), and for the standard swap network (orange). Further, random interleaves produce constant-overhead circuits (blue dotted line), and the corresponding models still exhibit signatures of strong chaos (see SI).

and so by alternating majorana permutations and Ising interactions, we can implement generic quartic majorana models (see Fig. 8.3b).

An especially interesting case for quantum simulation are sparsified versions of the SYK model[1005], where the degree of the interaction graph d is independent of the total number of modes N. We consider two settings, and how our techniques can be applied. In the first setting, we estimate the resources required to compile a randomly generated sparse-SYK instance. Numerical results suggest that despite this compilation overhead, one simulation cycle on $N = 400$ modes can be performed with $\leq 10 \times d$ CNOTs per mode per cycle. In the second setting, we introduce a special class of SYK models, generated by inserting a random majorana interleave between Ising interactions. Our numerics suggest these models still exhibit chaos, and the overall cost reduces to just d CNOTs per mode per cycle. In contrast, if we were to implement the sparse SYK models using standard fermionic swap networks, the cost would grows linearly with system size, representing multiple orders-of-magnitude higher cost for interesting instances with hundreds of modes.

8.6 Quantum simulation with the FFFT

The ability to efficiently encode non-local fermionic circuits has signficant implications for the cost of state-preparation and Hamiltonian simulation of quantum materials. The key subroutine we leverage is a fermionic version of the fast fourier transform (FFFT)[979], which enables us to transform from position-space to momentum-space using a $\log(N)$-depth fermionic circuit. Starting with the 1D FFFT (see Fig. 8.4a), we see that the non-local reconfiguration at each step is a special case of the interleave operation, and hence can be implemented with one application of $\mathcal{I}_p$ and $O(1)$ over-

head. Higher-dimensional FFFT can be implemented by combining the 1D FFFT with reflection operations (see Fig. 8.4b). This represents an exponential improvement in scaling of circuit volume with N compared to prior approaches (see Table 8.1).

scalings	1D FFFT	2D Reflection	2D FFFT
swap network[765]	$O(L)$	$O(L^2)$	$O(L^2)$
compact encoding[635]	$O(L)$	N/A	$O(L)$
dynamic JW	$O(\log L)$	O(1)	$O(\log L)$

Table 8.1: Asymptotic scalings of the Clifford gates per qubit required to implement a 2D FFFT, for a $N = L \times L$ square lattice. The dynamic JW represents the scheme developed in this work, and the compact encoding is a mapping with local gates in 2D.

Arbitrary, translation-invariant free-fermion states can be prepared in momentum space, and then transformed via the FFFT to real-space, providing a remarkably efficient route to preparing various forms of long-range ordered quantum states (Fig. 8.4c). For example, complex states such as a chiral superconductors, critical states, and fermi-surfaces, can be exactly prepared using this technique, with a total circuit depth $O(\log_2(N))$ (see SI). In contrast, a device with strictly local fermionic operations in D-dimensions, would require at least $O(N^{1/D})$ time to prepare this class of states, representing an exponential speedup.

State-prep with FFFT can be further combined with techniques for preparing topologically ordered states with measurement and feedforward, to prepare exotic phases such as chiral non-abelian spin-liquids (Fig. 8.4d), which arise by combining a chiral $p + ip$ superconducting state with toric-code order (see SI)[761]. Understanding the full family of states which are preparable in $O(\log(N))$ depth using dynamical encodings, remains an exciting direction for continued research.

The FFFT also enables us to speed up quantum simulation algorithms. In particu-

lar, we consider simulation of a generalized Hubbard Hamiltonian

$$\begin{aligned} H &= \sum_{x,y,\sigma} t_{x-y,\sigma} a^\dagger_{x,\sigma} a_{y,\sigma} + \sum_{x,\sigma} U_{x,\sigma} n_{x,\sigma} \\ &+ \sum_{x,y,\sigma,\sigma'} V_{x-y,\sigma\sigma'} n_{x,\sigma} n_{y,\sigma'} \\ &\equiv T + U + V \end{aligned} \tag{8.6}$$

consisting of three parts: a kinetic term T, on-site interaction term U, and two-fermion interaction V, which is also assumed to be translationally-invariant. In Ref.[542], it was shown how a generic electronic structure Hamiltonian can be written in this form, using the plane-wave dual basis. Further, in Ref.[809], it was shown how the diagonal terms $(U + V)$ can be implemented with asymptotic circuit depth scaling as $O(\log(n))$. The key intuition is to use a classical fourier-transform to diagonalize the density operator $n_{x,\sigma} \rightarrow n_{k,\sigma}$. Similarly, the T operator can be diagonalized, using the FFFT. However, in prior work, the FFFT was the bottleneck in terms of circuit-depth. Hence, putting it together with our results, we have shown a single trotter-step or block-encoding query of (8.6) can be implemented with asymptotic depth $O(\log(N))$, an improvement of $O(N/\log(N))$.

8.7 Conclusion

Efficiently simulating non-local fermionic operations on qubit-based quantum computers unlocks a variety of new possibilities in quantum simulation and quantum algorithm design. In particular, we showed how to simulate sparse, random fermionic models, and efficiently implement the FFFT for materials simulation. The fast-nonlocal fermionic permutations we develop could also be useful for a variety of other algorith-

mic techniques, which deserve further research. For example, it could be interesting to develop improved techniques for readout of fermionic simulations, by e.g. implementing matchgate shadows very efficiently[986]. We could also construct a variety of fermionic ansatz states using these techniques, based on e.g. fermionic tensor networks like MERA[623], iso-TNS[625], and more.

It would also be interesting to begin implementing and exploring fermionic simulation, using these techniques, in near-term quantum computers. This will likely require a few additional simplifications. For example, when simulating (8.6), the classical Fourier transform required to simulate a generic V is likely the most costly step. Instead, initial explorations could use the Hubbard model, which only has on-site interactions. The phase diagram of even these simplified models is of wide-spread interest, and has been studied extensively using both state-of-the-art numerical methods and analog quantum simulation, for the purpose of understanding and discovering novel forms of super-conductivity, inspired by experiments in the cuprates. Further, while we assume access to arbitrary qubit permutations here, real devices often have further restrictions. Co-designing efficient fermionic permutation with hardware-specific constraints is a promising direction to develop optimized architectures for fermionic simulation.

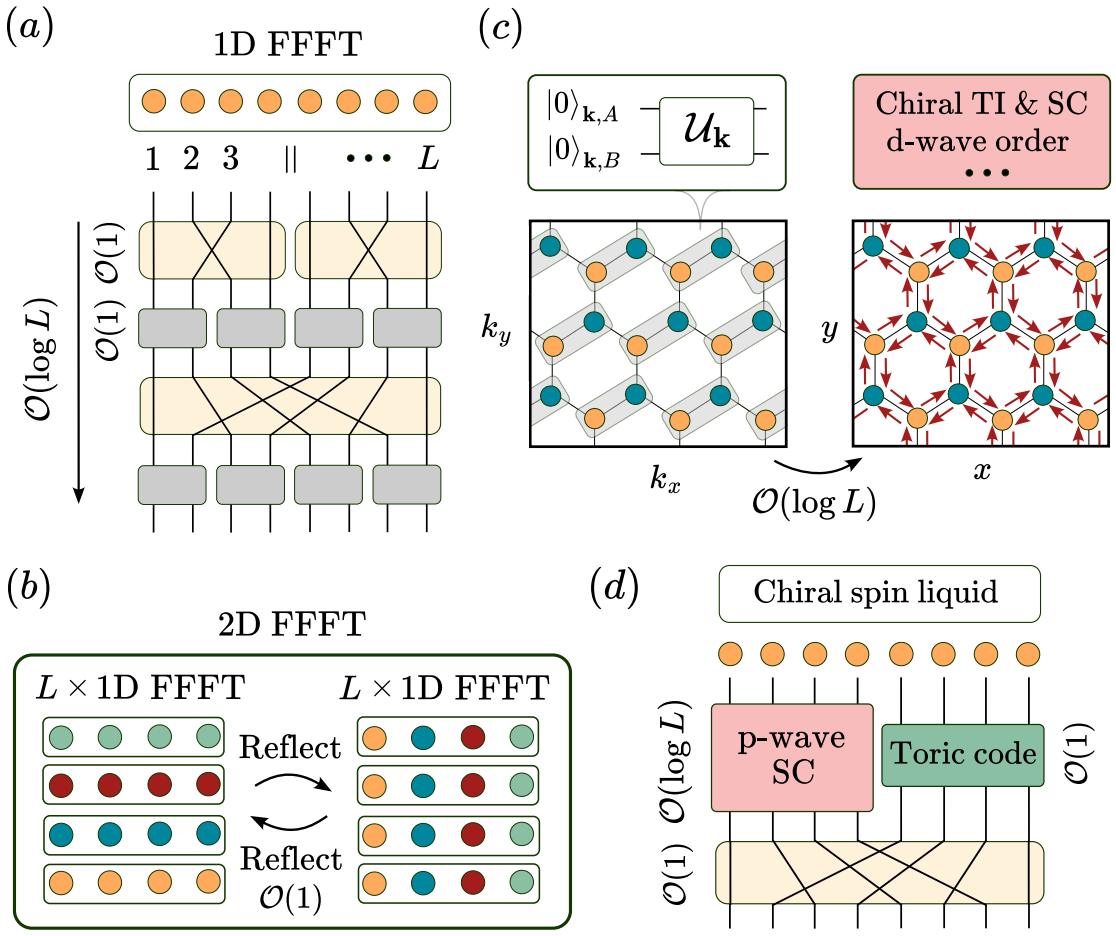


Figure 8.4: Free-fermion state preparation. (a) The 1D FFFT on L fermionic modes can be implemented in $\log L$ steps of $\mathcal{O}(1)$ depth, each of them consisting on parallel interleave operations [Fig. 8.1(d)] followed by one layer of entangling gates (as detailed in Ref.[979]). (b) The 2D FFFT on a $L \times L$ lattice can be implemented by first applying L 1D FFFT. The order is then modified with a $\mathcal{O}(1)$-depth 2D reflection operation [Fig. 8.1(d)]. After applying another set of L 1D FFFT, the original order is finally restored. (c) Translational-invariant free-fermion states can be prepared with a $\mathcal{O}(\log L)$-depth circuit, by first preparing them in k-space, and then transforming to real-space using the FFFT supplemented with $\mathcal{O}(1)$ permutations (see main text). In the figure, we exemplify the protocol for the case of a two-site unit cell, as required to prepare e.g. a chiral topological insulator, but it can be equally applied to more complicated periodic structures, as well as to superconducting states. (d) A non-abelian chiral spin liquid can also be prepared exactly in $\mathcal{O}(\log L)$ depth by interleaving a p-wave superconductor with a Toric code state.

References

[sup] See supplemental online material.

[SOM] See supplemental online material, which also includes references[740,613,966,844,570,968,902,518,658,702,706,871].

[516] Abanin, D., De Roeck, W., Ho, W. W., & Huveneers, F. (2017a). A Rigorous Theory of Many-Body Prethermalization for Periodically Driven and Closed Quantum Systems. Communications in Mathematical Physics, 354(3), 809–827.

[517] Abanin, D., De Roeck, W., Ho, W. W., & Huveneers, F. (2017b). A Rigorous Theory of Many-Body Prethermalization for Periodically Driven and Closed Quantum Systems. Communications in Mathematical Physics, 354(3), 809–827.

[518] Abanin, D., De Roeck, W., Ho, W. W., & Huveneers, F. (2017c). A rigorous theory of many-body prethermalization for periodically driven and closed quantum systems. Communications in Mathematical Physics, 354(3), 809–827.

[519] Abanin, D. A., Altman, E., Bloch, I., & Serbyn, M. (2019). Colloquium: Many-body localization, thermalization, and entanglement. Rev. Mod. Phys., 91, 021001.

[520] Abanin, D. A., De Roeck, W., Ho, W. W., & Huveneers, F. (2017d). Effective Hamiltonians, prethermalization, and slow energy absorption in periodically driven many-body systems. Phys. Rev. B, 95(1), 014112.

[521] Abanin, D. A., De Roeck, W., Ho, W. W., & Huveneers, F. m. c. (2017e). Effective Hamiltonians, prethermalization, and slow energy absorption in periodically driven many-body systems. Phys. Rev. B, 95, 014112.

[522] Abanin, D. A., De Roeck, W., Ho, W. W., & Huveneers, F. m. c. (2017f). Effective Hamiltonians, prethermalization, and slow energy absorption in periodically driven many-body systems. Phys. Rev. B, 95, 014112.

[523] Abanin, D. A., De Roeck, W., & Huveneers, F. (2015). Exponentially Slow Heating in Periodically Driven Many-Body Systems. Phys. Rev. Lett., 115, 256803.

[524] Abrams, D. S. & Lloyd, S. (1997). Simulation of Many-Body Fermi Systems on a Universal Quantum Computer. Phys. Rev. Lett., 79(13), 2586–2589. Publisher: American Physical Society.

[525] Ahn, C., Cavalleri, A., Georges, A., Ismail-Beigi, S., Millis, A. J., & Triscone, J.-M. (2021). Designing and controlling the properties of transition metal oxide quantum materials. Nat. Mater., 20(11), 1462–1468.

[526] Aidelsburger, M., Atala, M., Lohse, M., Barreiro, J. T., Paredes, B., & Bloch, I. (2013). Realization of the Hofstadter Hamiltonian with Ultracold Atoms in Optical Lattices. Phys. Rev. Lett., 111, 185301.

[527] Aidelsburger, M., Barbiero, L., Bermudez, A., Chanda, T., Dauphin, A., González-Cuadra, D., Grzybowski, P. R., Hands, S., Jendrzejewski, F., Jüne-

mann, J., Juzeliūnas, G., Kasper, V., Piga, A., Ran, S.-J., Rizzi, M., Sierra, G., Tagliacozzo, L., Tirrito, E., Zache, T. V., Zakrzewski, J., Zohar, E., & Lewenstein, M. (2022). Cold atoms meet lattice gauge theory. Philosophical Transactions of the Royal Society A, 380(2216), 20210064.

[528] Aidelsburger, M., Lohse, M., Schweizer, C., Atala, M., Barreiro, J. T., Nascimbène, S., Cooper, N. R., Bloch, I., & Goldman, N. (2015). Measuring the Chern number of Hofstadter bands with ultracold bosonic atoms. Nat. Phys., 11(2), 162–166.

[529] Alcaraz, F. C. & Bariev, R. Z. (1999). An Exactly Solvable Constrained XXZ Chain.

[530] Alessio, M. & Krylov, A. I. (2021). Equation-of-Motion Coupled-Cluster Protocol for Calculating Magnetic Properties: Theory and Applications to Single-Molecule Magnets. J. Chem. Theory Comput., 17(7), 4225–4241.

[531] Alexeev, Y., Bacon, D., Brown, K. R., Calderbank, R., Carr, L. D., Chong, F. T., DeMarco, B., Englund, D., Farhi, E., Fefferman, B., Gorshkov, A. V., Houck, A., Kim, J., Kimmel, S., Lange, M., Lloyd, S., Lukin, M. D., Maslov, D., Maunz, P., Monroe, C., Preskill, J., Roetteler, M., Savage, M. J., & Thompson, J. (2021). Quantum Computer Systems for Scientific Discovery. PRX Quantum, 2(1), 017001.

[532] Alicea, J. (2012). New directions in the pursuit of Majorana fermions in solid state systems. Rep. Prog. Phys., 75(7), 076501.

[533] Altman, E., Brown, K. R., Carleo, G., Carr, L. D., Demler, E., Chin, C., DeMarco, B., Economou, S. E., Eriksson, M. A., Fu, K.-M. C., Greiner, M., Haz-

zard, K. R., Hulet, R. G., Kollár, A. J., Lev, B. L., Lukin, M. D., Ma, R., Mi, X., Misra, S., Monroe, C., Murch, K., Nazario, Z., Ni, K.-K., Potter, A. C., Roushan, P., Saffman, M., Schleier-Smith, M., Siddiqi, I., Simmonds, R., Singh, M., Spielman, I., Temme, K., Weiss, D. S., Vučković, J., Vuletić, V., Ye, J., & Zwierlein, M. (2021). Quantum Simulators: Architectures and Opportunities. PRX Quantum, 2(1), 017003.

[534] Andersen, T. I., Lensky, Y. D., Kechedzhi, K., Drozdov, I., Bengtsson, A., Hong, S., Morvan, A., Mi, X., Opremcak, A., Acharya, R., Allen, R., Ansmann, M., Arute, F., Arya, K., Asfaw, A., Atalaya, J., Babbush, R., Bacon, D., Bardin, J. C., Bortoli, G., Bourassa, A., Bovaird, J., Brill, L., Broughton, M., Buckley, B. B., Buell, D. A., Burger, T., Burkett, B., Bushnell, N., Chen, Z., Chiaro, B., Chik, D., Chou, C., Cogan, J., Collins, R., Conner, P., Courtney, W., Crook, A. L., Curtin, B., Debroy, D. M., Barba, A. D. T., Demura, S., Dunsworth, A., Eppens, D., Erickson, C., Faoro, L., Farhi, E., Fatemi, R., Ferreira, V. S., Burgos, L. F., Forati, E., Fowler, A. G., Foxen, B., Giang, W., Gidney, C., Gilboa, D., Giustina, M., Gosula, R., Dau, A. G., Gross, J. A., Habegger, S., Hamilton, M. C., Hansen, M., Harrigan, M. P., Harrington, S. D., Heu, P., Hilton, J., Hoffmann, M. R., Huang, T., Huff, A., Huggins, W. J., Ioffe, L. B., Isakov, S. V., Iveland, J., Jeffrey, E., Jiang, Z., Jones, C., Juhas, P., Kafri, D., Khattar, T., Khezri, M., Kieferová, M., Kim, S., Kitaev, A., Klimov, P. V., Klots, A. R., Korotkov, A. N., Kostritsa, F., Kreikebaum, J. M., Landhuis, D., Laptev, P., Lau, K.-M., Laws, L., Lee, J., Lee, K., Lester, B. J., Lill, A., Liu, W., Locharla, A., Lucero, E., Malone, F. D., Martin, O., McClean, J. R., McCourt, T., McEwen, M., Miao, K. C., Mieszala, A., Mohseni, M., Montazeri, S., Mount, E., Movas-

sagh, R., Mruczkiewicz, W., Naaman, O., Neeley, M., Neill, C., Nersisyan, A., Newman, M., Ng, J. H., Nguyen, A., Nguyen, M., Niu, M. Y., O'Brien, T. E., Omonije, S., Petukhov, A., Potter, R., Pryadko, L. P., Quintana, C., Rocque, C., Rubin, N. C., Saei, N., Sank, D., Sankaragomathi, K., Satzinger, K. J., Schurkus, H. F., Schuster, C., Shearn, M. J., Shorter, A., Shutty, N., Shvarts, V., Skruzny, J., Smith, W. C., Somma, R., Sterling, G., Strain, D., Szalay, M., Torres, A., Vidal, G., Villalonga, B., Heidweiller, C. V., White, T., Woo, B. W. K., Xing, C., Yao, Z. J., Yeh, P., Yoo, J., Young, G., Zalcman, A., Zhang, Y., Zhu, N., Zobrist, N., Neven, H., Boixo, S., Megrant, A., Kelly, J., Chen, Y., Smelyanskiy, V., Kim, E.-A., Aleiner, I., & Roushan, P. (2022). Observation of non-Abelian exchange statistics on a superconducting processor.

[535] Andersen, T. I., Lensky, Y. D., Kechedzhi, K., Drozdov, I. K., Bengtsson, A., Hong, S., Morvan, A., Mi, X., Opremcak, A., Acharya, R., Allen, R., Ansmann, M., Arute, F., Arya, K., Asfaw, A., Atalaya, J., Babbush, R., Bacon, D., Bardin, J. C., Bortoli, G., Bourassa, A., Bovaird, J., Brill, L., Broughton, M., Buckley, B. B., Buell, D. A., Burger, T., Burkett, B., Bushnell, N., Chen, Z., Chiaro, B., Chik, D., Chou, C., Cogan, J., Collins, R., Conner, P., Courtney, W., Crook, A. L., Curtin, B., Debroy, D. M., Del Toro Barba, A., Demura, S., Dunsworth, A., Eppens, D., Erickson, C., Faoro, L., Farhi, E., Fatemi, R., Ferreira, V. S., Burgos, L. F., Forati, E., Fowler, A. G., Foxen, B., Giang, W., Gidney, C., Gilboa, D., Giustina, M., Gosula, R., Dau, A. G., Gross, J. A., Habegger, S., Hamilton, M. C., Hansen, M., Harrigan, M. P., Harrington, S. D., Heu, P., Hilton, J., Hoffmann, M. R., Huang, T., Huff, A., Huggins, W. J., Ioffe, L. B., Isakov, S. V., Iveland, J., Jeffrey, E., Jiang, Z., Jones, C., Juhas, P., Kafri, D.,

Khattar, T., Khezri, M., Kieferová, M., Kim, S., Kitaev, A., Klimov, P. V., Klots, A. R., Korotkov, A. N., Kostritsa, F., Kreikebaum, J. M., Landhuis, D., Laptev, P., Lau, K.-M., Laws, L., Lee, J., Lee, K. W., Lester, B. J., Lill, A. T., Liu, W., Locharla, A., Lucero, E., Malone, F. D., Martin, O., McClean, J. R., McCourt, T., McEwen, M., Miao, K. C., Mieszala, A., Mohseni, M., Montazeri, S., Mount, E., Movassagh, R., Mruczkiewicz, W., Naaman, O., Neeley, M., Neill, C., Nersisyan, A., Newman, M., Ng, J. H., Nguyen, A., Nguyen, M., Niu, M. Y., O'Brien, T. E., Omonije, S., Petukhov, A., Potter, R., Pryadko, L. P., Quintana, C., Rocque, C., Rubin, N. C., Saei, N., Sank, D., Sankaragomathi, K., Satzinger, K. J., Schurkus, H. F., Schuster, C., Shearn, M. J., Shorter, A., Shutty, N., Shvarts, V., Skruzny, J., Smith, W. C., Somma, R., Sterling, G., Strain, D., Szalay, M., Torres, A., Vidal, G., Villalonga, B., Heidweiller, C. V., White, T., Woo, B. W. K., Xing, C., Yao, Z. J., Yeh, P., Yoo, J., Young, G., Zalcman, A., Zhang, Y., Zhu, N., Zobrist, N., Neven, H., Boixo, S., Megrant, A., Kelly, J., Chen, Y., Smelyanskiy, V., Kim, E.-A., Aleiner, I., Roushan, P., & Google Quantum AI and Collaborators (2023). Non-Abelian braiding of graph vertices in a superconducting processor. Nature, 618(7964), 264–269.

[536] Anderson, P. (1973). Resonating valence bonds: A new kind of insulator? Mater. Res. Bull., 8(2), 153–160.

[537] Anshu, A., Breuckmann, N. P., & Nirkhe, C. (2023). NLTS Hamiltonians from good quantum codes. In Proceedings of the 55th Annual ACM Symposium on Theory of Computing (pp. 1090–1096).

[538] Aoto, Y. A., de Lima Batista, A. P., Kohn, A., & de Oliveira-Filho, A. G. (2017). How to arrive at accurate benchmark values for transition metal com-

pounds: Computation or experiment? J. Chem. Theory Comput., 13(11), 5291–5316.

[539] Arute, F., Arya, K., Babbush, R., Bacon, D., Bardin, J. C., Barends, R., Boixo, S., Broughton, M., Buckley, B. B., Buell, D. A., Burkett, B., Bushnell, N., Chen, Y., Chen, Z., Chiaro, B., Collins, R., Courtney, W., Demura, S., Dunsworth, A., Farhi, E., Fowler, A., Foxen, B., Gidney, C., Giustina, M., Graff, R., Habegger, S., Harrigan, M. P., Ho, A., Hong, S., Huang, T., Huggins, W. J., Ioffe, L., Isakov, S. V., Jeffrey, E., Jiang, Z., Jones, C., Kafri, D., Kechedzhi, K., Kelly, J., Kim, S., Klimov, P. V., Korotkov, A., Kostritsa, F., Landhuis, D., Laptev, P., Lindmark, M., Lucero, E., Martin, O., Martinis, J. M., McClean, J. R., McEwen, M., Megrant, A., Mi, X., Mohseni, M., Mruczkiewicz, W., Mutus, J., Naaman, O., Neeley, M., Neill, C., Neven, H., Niu, M. Y., O'Brien, T. E., Ostby, E., Petukhov, A., Putterman, H., Quintana, C., Roushan, P., Rubin, N. C., Sank, D., Satzinger, K. J., Smelyanskiy, V., Strain, D., Sung, K. J., Szalay, M., Takeshita, T. Y., Vainsencher, A., White, T., Wiebe, N., Yao, Z. J., Yeh, P., & Zalcman, A. (2020). Hartree-Fock on a superconducting qubit quantum computer. Science, 369(6507), 1084–1089.

[540] Askerka, M., Brudvig, G. W., & Batista, V. S. (2017). The o2-evolving complex of photosystem ii: Recent insights from quantum mechanics/molecular mechanics (qm/mm), extended x-ray absorption fine structure (exafs), and femtosecond x-ray crystallography data. Acc. Chem. Res., 50(1), 41–48.

[541] Auerbach, A. (1998). Interacting electrons and quantum magnetism. Springer Science & Business Media.

[542] Babbush, R., Wiebe, N., McClean, J., McClain, J., Neven, H., & Chan, G. K.-L. (2018). Low-Depth Quantum Simulation of Materials. Physical Review X, 8(1), 011044.

[543] Bakalov, B. & Kirillov, A. A. (2001). Lectures on tensor categories and modular functors, volume 21. American Mathematical Soc.

[544] Banerjee, D., Dalmonte, M., Müller, M., Rico, E., Stebler, P., Wiese, U.-J., & Zoller, P. (2012). Atomic Quantum Simulation of Dynamical Gauge Fields Coupled to Fermionic Matter: From String Breaking to Evolution after a Quench. Phys. Rev. Lett., 109, 175302.

[545] Bañuls, M. C., Blatt, R., Catani, J., Celi, A., Cirac, J. I., Dalmonte, M., Fallani, L., Jansen, K., Lewenstein, M., Montangero, S., Muschik, C. A., Reznik, B., Rico, E., Tagliacozzo, L., Van Acoleyen, K., Verstraete, F., Wiese, U.-J., Wingate, M., Zakrzewski, J., & Zoller, P. (2020). Simulating lattice gauge theories within quantum technologies. The European Physical Journal D, 74(8), 165.

[546] Bao, Y., Fan, R., Vishwanath, A., & Altman, E. (2023). Mixed-state topological order and the errorfield double formulation of decoherence-induced transitions.

[547] Barbiero, L., Schweizer, C., Aidelsburger, M., Demler, E., Goldman, N., & Grusdt, F. (2019). Coupling ultracold matter to dynamical gauge fields in optical lattices: From flux attachment to $\mathbb{Z}_2$ lattice gauge theories. Science Advances, 5(10), eaav7444.

[548] Barends, R., Lamata, L., Kelly, J., García-Álvarez, L., Fowler, A. G., Megrant, A., Jeffrey, E., White, T. C., Sank, D., Mutus, J. Y., Campbell, B., Chen, Y.,

Chen, Z., Chiaro, B., Dunsworth, A., Hoi, I.-C., Neill, C., O'Malley, P. J. J., Quintana, C., Roushan, P., Vainsencher, A., Wenner, J., Solano, E., & Martinis, J. M. (2015). Digital quantum simulation of fermionic models with a superconducting circuit. Nat. Commun., 6(1), 7654.

[549] Barredo, D., de Léséleuc, S., Lienhard, V., Lahaye, T., & Browaeys, A. (2016). An atom-by-atom assembler of defect-free arbitrary two-dimensional atomic arrays. Science, 354(6315), 1021–1023.

[550] Bartlett, R. J. & Musiał, M. (2007). Coupled-cluster theory in quantum chemistry. Rev. Mod. Phys., 79(1), 291–352.

[551] Bauer, B., Bravyi, S., Motta, M., & Chan, G. K.-L. (2020). Quantum algorithms for quantum chemistry and quantum materials science. Chem. Rev., 120(22), 12685–12717.

[552] Bauer, B., Wecker, D., Millis, A. J., Hastings, M. B., & Troyer, M. (2016). Hybrid Quantum-Classical Approach to Correlated Materials. Physical Review X, 6(3), 031045.

[553] Bauman, N. P., Low, G. H., & Kowalski, K. (2019). Quantum simulations of excited states with active-space downfolded Hamiltonians. J. Chem. Phys., 151(23), 234114.

[554] Benedetti, M., Fiorentini, M., & Lubasch, M. (2021). Hardware-efficient variational quantum algorithms for time evolution. Physical Review Research, 3(3), 033083. arXiv:2009.12361 [quant-ph].

[555] Bernien, H., Schwartz, S., Keesling, A., Levine, H., Omran, A., Pichler, H., Choi, S., Zibrov, A. S., Endres, M., Greiner, M., Vuletic, V., & Lukin, M. D.

(2017a). Probing many-body dynamics on a 51-atom quantum simulator. Nature, 551, 579.

[556] Bernien, H., Schwartz, S., Keesling, A., Levine, H., Omran, A., Pichler, H., Choi, S., Zibrov, A. S., Endres, M., Greiner, M., Vuletić, V., & Lukin, M. D. (2017b). Probing many-body dynamics on a 51-atom quantum simulator. Nature, 551(7682), 579–584.

[557] Bernien, H., Schwartz, S., Keesling, A., Levine, H., Omran, A., Pichler, H., Choi, S., Zibrov, A. S., Endres, M., Greiner, M., Vuletić, V., & Lukin, M. D. (2017c). Probing many-body dynamics on a 51-atom quantum simulator. Nature, 551(7682), 579–584.

[558] Berry, M. V. (1997). Quantal phase factors accompanying adiabatic changes. Proc. R. Soc. Lond., 392(1802), 45–57.

[559] Berry, M. V. (2009). Transitionless quantum driving. Journal of Physics A: Mathematical and Theoretical, 42(36), 365303.

[560] Bertini, B., Essler, F. H. L., Groha, S., & Robinson, N. J. (2015). Prethermalization and Thermalization in Models with Weak Integrability Breaking. Phys. Rev. Lett., 115, 180601.

[561] Bespalova, T. A. & Kyriienko, O. (2021). Quantum simulation and ground state preparation for the honeycomb Kitaev model.

[562] Beverland, M. E., Murali, P., Troyer, M., Svore, K. M., Hoefler, T., Kliuchnikov, V., Low, G. H., Soeken, M., Sundaram, A., & Vaschillo, A. (2022). Assessing requirements to scale to practical quantum advantage.

[563] Bloch, I., Dalibard, J., & Zwerger, W. (2008). Many-body physics with ultracold gases. Rev. Mod. Phys., 80, 885–964.

[564] Blok, M. S., Ramasesh, V. V., Schuster, T., O'Brien, K., Kreikebaum, J. M., Dahlen, D., Morvan, A., Yoshida, B., Yao, N. Y., & Siddiqi, I. (2021). Quantum Information Scrambling on a Superconducting Qutrit Processor. Phys. Rev. X, 11, 021010.

[565] Bluvstein, D., Evered, S. J., Geim, A. A., Li, S. H., Zhou, H., Manovitz, T., Ebadi, S., Cain, M., Kalinowski, M., Hangleiter, D., Bonilla Ataides, J. P., Maskara, N., Cong, I., Gao, X., Rodriguez, P. S., Karolyshyn, T., Semeghini, G., Gullans, M. J., Greiner, M., Vuletic, V., & Lukin, M. D. Logical quantum processor based on reconfigurable atom arrays. Submitted to Nature.

[566] Bluvstein, D., Evered, S. J., Geim, A. A., Li, S. H., Zhou, H., Manovitz, T., Ebadi, S., Cain, M., Kalinowski, M., Hangleiter, D., Bonilla Ataides, J. P., Maskara, N., Cong, I., Gao, X., Sales Rodriguez, P., Karolyshyn, T., Semeghini, G., Gullans, M. J., Greiner, M., Vuletić, V., & Lukin, M. D. (2024). Logical quantum processor based on reconfigurable atom arrays. Nature, 626(7997), 58–65.

[567] Bluvstein, D., Geim, A. A., et al. In preparation.

[568] Bluvstein, D., Levine, H., Semeghini, G., Wang, T. T., Ebadi, S., Kalinowski, M., Keesling, A., Maskara, N., Pichler, H., Greiner, M., Vuletić, V., & Lukin, M. D. (2022a). A quantum processor based on coherent transport of entangled atom arrays. Nature, 604(7906), 451–456.

[569] Bluvstein, D., Levine, H., Semeghini, G., Wang, T. T., Ebadi, S., Kalinowski, M., Keesling, A., Maskara, N., Pichler, H., Greiner, M., Vuletić, V., & Lukin, M. D. (2022b). A quantum processor based on coherent transport of entangled atom arrays. Nature, 604(7906), 451–456.

[570] Bluvstein, D., Omran, A., Levine, H., Keesling, A., Semeghini, G., Ebadi, S., Wang, T. T., Michailidis, A. A., Maskara, N., Ho, W. W., Choi, S., Serbyn, M., Greiner, M., Vuletić, V., & Lukin, M. D. (2021a). Controlling quantum many-body dynamics in driven rydberg atom arrays. Science.

[571] Bluvstein, D., Omran, A., Levine, H., Keesling, A., Semeghini, G., Ebadi, S., Wang, T. T., Michailidis, A. A., Maskara, N., Ho, W. W., Choi, S., Serbyn, M., Greiner, M., Vuletić, V., & Lukin, M. D. (2021b). Controlling quantum many-body dynamics in driven Rydberg atom arrays. Science, 371(6536), 1355–1359.

[572] Bluvstein, D., Omran, A., Levine, H., Keesling, A., Semeghini, G., Ebadi, S., Wang, T. T., Michailidis, A. A., Maskara, N., Ho, W. W., Choi, S., Serbyn, M., Greiner, M., Vuletić, V., & Lukin, M. D. (2021c). Controlling quantum many-body dynamics in driven Rydberg atom arrays. Science, 371(6536), 1355–1359.

[573] Bluvstein, D., Omran, A., Levine, H., Keesling, A., Semeghini, G., Ebadi, S., Wang, T. T., Michailidis, A. A., Maskara, N., Ho, W. W., Choi, S., Serbyn, M., Greiner, M., Vuletić, V., & Lukin, M. D. (2021d). Controlling quantum many-body dynamics in driven Rydberg atom arrays. Science, 371(6536), 1355–1359.

[574] Bogani, L. & Wernsdorfer, W. (2008). Molecular spintronics using single-molecule magnets. Nature Materials, 7, 179–186.

[575] Bolvin, H. (2003). From ab Initio Calculations to Model Hamiltonians: The Effective Hamiltonian Technique as an Efficient Tool to Describe Mixed-Valence Molecules. J. Phys. Chem. A, 107(25), 5071–5078.

[576] Bombin, H. (2010). Topological Order with a Twist: Ising Anyons from an Abelian Model. Phys. Rev. Lett., 105, 030403.

[577] Bookatz, A. D., Wocjan, P., & Viola, L. (2014). Hamiltonian quantum simulation with bounded-strength controls. New J. Phys., 16(4), 045021.

[578] Bornet, G., Emperauger, G., Chen, C., Ye, B., Block, M., Bintz, M., Boyd, J. A., Barredo, D., Comparin, T., Mezzacapo, F., Roscilde, T., Lahaye, T., Yao, N. Y., & Browaeys, A. (2023). Scalable spin squeezing in a dipolar Rydberg atom array. Nature, 621(7980), 728–733.

[579] Braumüller, J., Karamlou, A. H., Yanay, Y., Kannan, B., Kim, D., Kjaergaard, M., Melville, A., Niedzielski, B. M., Sung, Y., Vepsäläinen, A., Winik, R., Yoder, J. L., Orlando, T. P., Gustavsson, S., Tahan, C., & Oliver, W. D. (2022). Probing quantum information propagation with out-of-time-ordered correlators. Nature Physics, 18(2), 172–178.

[580] Bravyi, S. B. & Kitaev, A. Y. (2002). Fermionic Quantum Computation. Annals of Physics, 298(1), 210–226.

[581] Bricmont, J. & Frölich, J. (1983). An order parameter distinguishing between different phases of lattice gauge theories with matter fields. Physics Letters B, 122(1), 73–77.

[582] Bridgeman, J. C., Flammia, S. T., & Poulin, D. (2016). Detecting topological order with ribbon operators. Physical Review B, 94(20), 205123.

[583] Browaeys, A. & Lahaye, T. (2020a). Many-body physics with individually controlled rydberg atoms. Nature Physics, 16(2), 132–142.

[584] Browaeys, A. & Lahaye, T. (2020b). Many-body physics with individually controlled Rydberg atoms. Nature Physics, 16(2), 132–142.

[585] Brydges, T., Elben, A., Jurcevic, P., Vermersch, B., Maier, C., Lanyon, B. P., Zoller, P., Blatt, R., & Roos, C. F. (2019). Probing Rényi entanglement entropy via randomized measurements. Science, 364(6437), 260–263.

[586] Bull, K., Martin, I., & Papić, Z. (2019). Systematic construction of scarred many-body dynamics in 1d lattice models. Phys. Rev. Lett., 123, 030601.

[587] Burke, K. (2012). Perspective on density functional theory. J. Chem. Phys., 136(15).

[588] Cain, M., Chattopadhyay, S., Liu, J.-G., Samajdar, R., Pichler, H., & Lukin, M. D. (2023). Quantum speedup for combinatorial optimization with flat energy landscapes.

[589] Calzado, C. J., Clemente-Juan, J. M., Coronado, E., Gaita-Arino, A., & Suaud, N. (2008). Role of the Electron Transfer and Magnetic Exchange Interactions in the Magnetic Properties of Mixed-Valence Polyoxovanadate Complexes. Inorg. Chem., 47(13), 5889–5901.

[590] Carrasco, J., Elben, A., Kokail, C., Kraus, B., & Zoller, P. (2021). Theoretical and Experimental Perspectives of Quantum Verification. PRX Quantum, 2(1), 010102.

[591] Castelnovo, C. & Chamon, C. (2008). Quantum topological phase transition at the microscopic level. Physical Review B, 77(5), 054433.

[592] Celi, A., Vermersch, B., Viyuela, O., Pichler, H., Lukin, M. D., & Zoller, P. (2020a). Emerging Two-Dimensional Gauge Theories in Rydberg Configurable Arrays. Phys. Rev. X, 10, 021057.

[593] Celi, A., Vermersch, B., Viyuela, O., Pichler, H., Lukin, M. D., & Zoller, P. (2020b). Emerging Two-Dimensional Gauge Theories in Rydberg Configurable Arrays. Phys. Rev. X, 10(2), 021057.

[594] Cepaite, I., Polkovnikov, A., Daley, A. J., & Duncan, C. W. (2023). Counterdiabatic Optimized Local Driving. PRX Quantum, 4, 010312.

[595] Chalopin, T., Bojović, P., Wang, S., Franz, T., Sinha, A., Wang, Z., Bourgund, D., Obermeyer, J., Grusdt, F., Bohrdt, A., Pollet, L., Wietek, A., Georges, A., Hilker, T., & Bloch, I. (2024). Probing the magnetic origin of the pseudogap using a Fermi-Hubbard quantum simulator.

[596] Chan, H. H. S., Meister, R., Goh, M. L., & Koczor, B. (2023). Algorithmic shadow spectroscopy.

[597] Chandrasekharan, S. & Wiese, U.-J. (1997). Quantum link models: A discrete approach to gauge theories. Nuclear Physics B, 492(1), 455–471.

[598] Chattopadhyay, S., Pichler, H., Lukin, M. D., & Ho, W. W. (2020). Quantum many-body scars from virtual entangled pairs. Phys. Rev. B, 101, 174308.

[599] Chen, C., Bornet, G., Bintz, M., Emperauger, G., Leclerc, L., Liu, V. S., Scholl, P., Barredo, D., Hauschild, J., Chatterjee, S., Schuler, M., Läuchli, A. M., Zale-

tel, M. P., Lahaye, T., Yao, N. Y., & Browaeys, A. (2023a). Continuous symmetry breaking in a two-dimensional Rydberg array. Nature, 616(7958), 691–695.

[600] Chen, C., Bornet, G., Bintz, M., Emperauger, G., Leclerc, L., Liu, V. S., Scholl, P., Barredo, D., Hauschild, J., Chatterjee, S., Schuler, M., Läuchli, A. M., Zaletel, M. P., Lahaye, T., Yao, N. Y., & Browaeys, A. (2023b). Continuous symmetry breaking in a two-dimensional Rydberg array. Nature, 616(7958), 691–695.

[601] Chen, D.-T., Helms, P., Hale, A. R., Lee, M., Li, C., Gray, J., Christou, G., Zapf, V. S., Chan, G. K.-L., & Cheng, H.-P. (2022). Using Hyperoptimized Tensor Networks and First-Principles Electronic Structure to Simulate the Experimental Properties of the Giant {Mn84} Torus. J. Phys. Chem. Lett., 13(10), 2365–2370.

[602] Chen, X., Gu, Z.-C., & Wen, X.-G. (2010). Local unitary transformation, long-range quantum entanglement, wave function renormalization, and topological order. Physical Review B, 82(15), 155138.

[603] Chen, X., Gu, Z.-C., & Wen, X.-G. (2011). Classification of gapped symmetric phases in one-dimensional spin systems. Phys. Rev. B, 83, 035107.

[604] Chen, Y.-A. & Xu, Y. (2023). Equivalence between Fermion-to-Qubit Mappings in two Spatial Dimensions. PRX Quantum, 4(1), 010326.

[605] Cheng, Y., Li, C., & Zhai, H. (2021). Variational approach to quantum spin liquid in a Rydberg atom simulator.

[606] Chi, Y., Huang, J., Zhang, Z., Mao, J., Zhou, Z., Chen, X., Zhai, C., Bao, J., Dai, T., Yuan, H., Zhang, M., Dai, D., Tang, B., Yang, Y., Li, Z., Ding, Y., Oxenløwe, L. K., Thompson, M. G., O'Brien, J. L., Li, Y., Gong, Q., & Wang, J.

(2022). A programmable qudit-based quantum processor. Nat. Commun., 13(1), 1166.

[607] Chiesa, A., Tacchino, F., Grossi, M., Santini, P., Tavernelli, I., Gerace, D., & Carretta, S. (2019). Quantum hardware simulating four-dimensional inelastic neutron scattering. Nat. Phys., 15(5), 455–459.

[608] Childs, A. M., Cleve, R., Deotto, E., Farhi, E., Gutmann, S., & Spielman, D. A. (2003). Exponential algorithmic speedup by quantum walk. In Proceedings of the thirty-fifth annual ACM symposium on Theory of computing (pp. 59–68). arXiv:quant-ph/0209131.

[609] Choi, J., Zhou, H., Knowles, H. S., Landig, R., Choi, S., & Lukin, M. D. (2020a). Robust Dynamic Hamiltonian Engineering of Many-Body Spin Systems. Phys. Rev. X, 10, 031002.

[610] Choi, J., Zhou, H., Knowles, H. S., Landig, R., Choi, S., & Lukin, M. D. (2020b). Robust Dynamic Hamiltonian Engineering of Many-Body Spin Systems. Phys. Rev. X, 10(3), 031002.

[611] Choi, S., Choi, J., Landig, R., Kucsko, G., Zhou, H., Isoya, J., Jelezko, F., Onoda, S., Sumiya, H., Khemani, V., Keyserlingk, C. v., Yao, N. Y., Demler, E., & Lukin, M. D. (2017). Observation of discrete time-crystalline order in a disordered dipolar many-body system. Nature, 543(7644), 221–225.

[612] Choi, S., Choi, J., Landig, R., Kucsko, G., Zhou, H., Isoya, J., Jelezko, F., Onoda, S., Sumiya, H., Khemani, V., von Keyserlingk, C., Yao, N. Y., Demler, E., & Lukin, M. D. (2016). Observation of discrete time-crystalline order in a disordered dipolar many-body system. ArXiv e-prints.

[613] Choi, S., Turner, C. J., Pichler, H., Ho, W. W., Michailidis, A. A., Papić, Z., Serbyn, M., Lukin, M. D., & Abanin, D. A. (2019). Emergent su(2) dynamics and perfect quantum many-body scars. Phys. Rev. Lett., 122, 220603.

[614] Cirac, J. I., Pérez-García, D., Schuch, N., & Verstraete, F. (2021). Matrix product states and projected entangled pair states: Concepts, symmetries, theorems. Rev. Mod. Phys., 93, 045003.

[615] Claeys, P. W., Pandey, M., Sels, D., & Polkovnikov, A. (2019). Floquet-Engineering Counterdiabatic Protocols in Quantum Many-Body Systems. Phys. Rev. Lett., 123, 090602.

[616] Clinton, L., Cubitt, T., Flynn, B., Gambetta, F. M., Klassen, J., Montanaro, A., Piddock, S., Santos, R. A., & Sheridan, E. (2024). Towards near-term quantum simulation of materials. Nat. Commun., 15(1), 211.

[617] Cochran, T. A., Jobst, B., Rosenberg, E., Lensky, Y. D., Gyawali, G., Eassa, N., Will, M., Abanin, D., Acharya, R., Beni, L. A., Andersen, T. I., Ansmann, M., Arute, F., Arya, K., Asfaw, A., Atalaya, J., Babbush, R., Ballard, B., Bardin, J. C., Bengtsson, A., Bilmes, A., Bourassa, A., Bovaird, J., Broughton, M., Browne, D. A., Buchea, B., Buckley, B. B., Burger, T., Burkett, B., Bushnell, N., Cabrera, A., Campero, J., Chang, H.-S., Chen, Z., Chiaro, B., Claes, J., Cleland, A. Y., Cogan, J., Collins, R., Conner, P., Courtney, W., Crook, A. L., Curtin, B., Das, S., Demura, S., De Lorenzo, L., Di Paolo, A., Donohoe, P., Drozdov, I., Dunsworth, A., Eickbusch, A., Elbag, A. M., Elzouka, M., Erickson, C., Ferreira, V. S., Burgos, L. F., Forati, E., Fowler, A. G., Foxen, B., Ganjam, S., Gasca, R., Genois, ., Giang, W., Gilboa, D., Gosula, R., Dau, A. G., Grau-

mann, D., Greene, A., Gross, J. A., Habegger, S., Hansen, M., Harrigan, M. P., Harrington, S. D., Heu, P., Higgott, O., Hilton, J., Huang, H.-Y., Huff, A., Huggins, W. J., Jeffrey, E., Jiang, Z., Jones, C., Joshi, C., Juhas, P., Kafri, D., Kang, H., Karamlou, A. H., Kechedzhi, K., Khaire, T., Khattar, T., Khezri, M., Kim, S., Klimov, P. V., Kobrin, B., Korotkov, A. N., Kostritsa, F., Kreikebaum, J. M., Kurilovich, V. D., Landhuis, D., Lange-Dei, T., Langley, B. W., Lau, K.-M., Ledford, J., Lee, K., Lester, B. J., Guevel, L. L., Li, W. Y., Lill, A. T., Livingston, W. P., Locharla, A., Lundahl, D., Lunt, A., Madhuk, S., Maloney, A., Mandrà, S., Martin, L. S., Martin, O., Maxfield, C., McClean, J. R., McEwen, M., Meeks, S., Megrant, A., Miao, K. C., Molavi, R., Molina, S., Montazeri, S., Movassagh, R., Neill, C., Newman, M., Nguyen, A., Nguyen, M., Ni, C.-H., Niu, M. Y., Oliver, W. D., Ottosson, K., Pizzuto, A., Potter, R., Pritchard, O., Quintana, C., Ramachandran, G., Reagor, M. J., Rhodes, D. M., Roberts, G., Sankaragomathi, K., Satzinger, K. J., Schurkus, H. F., Shearn, M. J., Shorter, A., Shutty, N., Shvarts, V., Sivak, V., Small, S., Smith, W. C., Springer, S., Sterling, G., Suchard, J., Szasz, A., Sztein, A., Thor, D., Torunbalci, M. M., Vaishnav, A., Vargas, J., Vdovichev, S., Vidal, G., Heidweiller, C. V., Waltman, S., Wang, S. X., Ware, B., White, T., Wong, K., Woo, B. W. K., Xing, C., Yao, Z. J., Yeh, P., Ying, B., Yoo, J., Yosri, N., Young, G., Zalcman, A., Zhang, Y., Zhu, N., Zobris, N., Boixo, S., Kelly, J., Lucero, E., Chen, Y., Smelyanskiy, V., Neven, H., Gammon-Smith, A., Pollmann, F., Knap, M., & Roushan, P. (2024). Visualizing Dynamics of Charges and Strings in (2+1)D Lattice Gauge Theories.

[618] Colombo, S., Pedrozo-Peñafiel, E., Adiyatullin, A. F., Li, Z., Mendez, E., Shu,

C., & Vuletić, V. (2022a). Time-reversal-based quantum metrology with many-body entangled states. Nature Physics, 18(8), 925–930.

[619] Colombo, S., Pedrozo-Peñafiel, E., Adiyatullin, A. F., Li, Z., Mendez, E., Shu, C., & Vuletić, V. (2022b). Time-reversal-based quantum metrology with many-body entangled states. Nature Physics, 18(8), 925–930.

[620] Cong, I., Choi, S., & Lukin, M. D. (2019). Quantum convolutional neural networks. Nature Physics, 15(12), 1273–1278. Publisher: Nature Publishing Group.

[621] Cooper, A., Covey, J. P., Madjarov, I. S., Porsev, S. G., Safronova, M. S., & Endres, M. (2018). Alkaline-Earth Atoms in Optical Tweezers. Phys. Rev. X, 8(4), 041055.

[622] Cooper, N., Dalibard, J., & Spielman, I. (2019). Topological bands for ultracold atoms. Rev. Mod. Phys., 91(1), 015005.

[623] Corboz, P. & Vidal, G. (2009). Fermionic multiscale entanglement renormalization ansatz. Phys. Rev. B, 80(16), 165129. Publisher: American Physical Society.

[624] Dai, H.-N., Yang, B., Reingruber, A., Sun, H., Xu, X.-F., Chen, Y.-A., Yuan, Z.-S., & Pan, J.-W. (2017). Four-body ring-exchange interactions and anyonic statistics within a minimal toric-code Hamiltonian. Nature Physics, 13(12), 1195–1200.

[625] Dai, Z., Wu, Y., Wang, T., & Zaletel, M. P. (2025). Fermionic Isometric Tensor Network States in Two Dimensions. Phys. Rev. Lett., 134(2), 026502. Publisher: American Physical Society.

[626] D'Alessio, L., Kafri, Y., Polkovnikov, A., & Rigol, M. (2016a). From quantum chaos and eigenstate thermalization to statistical mechanics and thermodynamics. Advances in Physics, 65(3), 239.

[627] D'Alessio, L., Kafri, Y., Polkovnikov, A., & Rigol, M. (2016b). From quantum chaos and eigenstate thermalization to statistical mechanics and thermodynamics. Adv. Phys, 65(3), 239–362.

[628] Daley, A. J., Bloch, I., Kokail, C., Flannigan, S., Pearson, N., Troyer, M., & Zoller, P. (2022). Practical quantum advantage in quantum simulation. Nature, 607(7920), 667–676.

[629] Dalmonte, M. & Montangero, S. (2016). Lattice gauge theory simulations in the quantum information era. Contemporary Physics, 57(3), 388–412.

[630] Davydova, M., Tantivasadakarn, N., & Balasubramanian, S. (2022). Floquet codes without parent subsystem codes.

[631] de Léséleuc, S., Lienhard, V., Scholl, P., Barredo, D., Weber, S., Lang, N., Büchler, H. P., Lahaye, T., & Browaeys, A. (2019). Observation of a symmetry-protected topological phase of interacting bosons with Rydberg atoms. Science, 365(6455), 775–780.

[632] Demirplak, M. & Rice, S. A. (2003a). Adiabatic population transfer with control fields. The Journal of Physical Chemistry A, 107(46), 9937–9945.

[633] Demirplak, M. & Rice, S. A. (2003b). Adiabatic Population Transfer with Control Fields. The Journal of Physical Chemistry A, 107(46), 9937–9945.

[634] Dennis, E., Kitaev, A., Landahl, A., & Preskill, J. (2002). Topological quantum memory. Journal of Mathematical Physics, 43(9), 4452–4505. Publisher: American Institute of Physics.

[635] Derby, C., Klassen, J., Bausch, J., & Cubitt, T. (2021). Compact fermion to qubit mappings. Phys. Rev. B, 104(3), 035118.

[636] Desaules, J.-Y., Pietracaprina, F., Papić, Z., Goold, J., & Pappalardi, S. (2022). Extensive Multipartite Entanglement from su(2) Quantum Many-Body Scars. Phys. Rev. Lett., 129, 020601.

[637] Di Meglio, A., Jansen, K., Tavernelli, I., Alexandrou, C., Arunachalam, S., Bauer, C. W., Borras, K., Carrazza, S., Crippa, A., Croft, V., de Putter, R., Delgado, A., Dunjko, V., Egger, D. J., Fernández-Combarro, E., Fuchs, E., Funcke, L., González-Cuadra, D., Grossi, M., Halimeh, J. C., Holmes, Z., Kühn, S., Lacroix, D., Lewis, R., Lucchesi, D., Martinez, M. L., Meloni, F., Mezzacapo, A., Montangero, S., Nagano, L., Pascuzzi, V. R., Radescu, V., Ortega, E. R., Roggero, A., Schuhmacher, J., Seixas, J., Silvi, P., Spentzouris, P., Tacchino, F., Temme, K., Terashi, K., Tura, J., Tüysüz, C., Vallecorsa, S., Wiese, U.-J., Yoo, S., & Zhang, J. (2024). Quantum Computing for High-Energy Physics: State of the Art and Challenges. PRX Quantum, 5(3), 037001. Publisher: American Physical Society.

[638] Dooley, S., Pappalardi, S., & Goold, J. (2023). Entanglement enhanced metrology with quantum many-body scars. Phys. Rev. B, 107, 035123.

[639] Duan, L. M., Demler, E., & Lukin, M. D. (2003a). Controlling Spin Exchange Interactions of Ultracold Atoms in Optical Lattices. Phys. Rev. Lett., 91(9),

090402.

[640] Duan, L. M., Demler, E., & Lukin, M. D. (2003b). Controlling spin exchange interactions of ultracold atoms in optical lattices. Phys. Rev. Lett., 91.

[641] Duclos-Cianci, G. & Poulin, D. (2013). Fault-tolerant renormalization group decoder for abelian topological codes.

[642] Duivenvoorden, K., Iqbal, M., Haegeman, J., Verstraete, F., & Schuch, N. (2017). Entanglement phases as holographic duals of anyon condensates. Phys. Rev. B, 95, 235119.

[643] Ebadi, S., Keesling, A., Cain, M., Wang, T. T., Levine, H., Bluvstein, D., Semeghini, G., Omran, A., Liu, J.-G., Samajdar, R., Luo, X.-Z., Nash, B., Gao, X., Barak, B., Farhi, E., Sachdev, S., Gemelke, N., Zhou, L., Choi, S., Pichler, H., Wang, S.-T., Greiner, M., Vuletić, V., & Lukin, M. D. (2022a). Quantum optimization of maximum independent set using Rydberg atom arrays. Science, 376(6598), 1209–1215.

[644] Ebadi, S., Keesling, A., Cain, M., Wang, T. T., Levine, H., Bluvstein, D., Semeghini, G., Omran, A., Liu, J.-G., Samajdar, R., Luo, X.-Z., Nash, B., Gao, X., Barak, B., Farhi, E., Sachdev, S., Gemelke, N., Zhou, L., Choi, S., Pichler, H., Wang, S.-T., Greiner, M., Vuletić, V., & Lukin, M. D. (2022b). Quantum optimization of maximum independent set using Rydberg atom arrays. Science, 376(6598), 1209–1215.

[645] Ebadi, S., Wang, T. T., Levine, H., Keesling, A., Semeghini, G., Omran, A., Bluvstein, D., Samajdar, R., Pichler, H., Ho, W. W., Choi, S., Sachdev, S.,

Greiner, M., Vuletic, V., & Lukin, M. D. (2021a). Quantum Phases of Matter on a 256-Atom Programmable Quantum Simulator. Nature, 595(7866), 227–232.

[646] Ebadi, S., Wang, T. T., Levine, H., Keesling, A., Semeghini, G., Omran, A., Bluvstein, D., Samajdar, R., Pichler, H., Ho, W. W., Choi, S., Sachdev, S., Greiner, M., Vuletić, V., & Lukin, M. D. (2021b). Quantum phases of matter on a 256-atom programmable quantum simulator. Nature, 595(7866), 227–232.

[647] Ebadi, S., Wang, T. T., Levine, H., Keesling, A., Semeghini, G., Omran, A., Bluvstein, D., Samajdar, R., Pichler, H., Ho, W. W., Choi, S., Sachdev, S., Greiner, M., Vuletić, V., & Lukin, M. D. (2021c). Quantum phases of matter on a 256-atom programmable quantum simulator. Nature, 595(7866), 227–232.

[648] Ebadi, S., Wang, T. T., Levine, H., Keesling, A., Semeghini, G., Omran, A., Bluvstein, D., Samajdar, R., Pichler, H., Ho, W. W., Choi, S., Sachdev, S., Greiner, M., Vuletić, V., & Lukin, M. D. (2021d). Quantum phases of matter on a 256-atom programmable quantum simulator. Nature, 595(7866), 227–232.

[649] Eckardt, A. (2017). Colloquium: Atomic quantum gases in periodically driven optical lattices. Rev. Mod. Phys., 89, 011004.

[650] Eckner, W. J., Darkwah Oppong, N., Cao, A., Young, A. W., Milner, W. R., Robinson, J. M., Ye, J., & Kaufman, A. M. (2023). Realizing spin squeezing with Rydberg interactions in an optical clock. Nature, 621(7980), 734–739.

[651] Else, D. V., Bauer, B., & Nayak, C. (2016a). Floquet time crystals. Phys. Rev. Lett., 117, 090402.

[652] Else, D. V., Bauer, B., & Nayak, C. (2016b). Floquet Time Crystals. Phys. Rev. Lett., 117, 090402.

[653] Else, D. V., Bauer, B., & Nayak, C. (2017a). Prethermal phases of matter protected by time-translation symmetry. Phys. Rev. X, 7, 011026.

[654] Else, D. V., Bauer, B., & Nayak, C. (2017b). Prethermal Phases of Matter Protected by Time-Translation Symmetry. Phys. Rev. X, 7, 011026.

[655] Else, D. V., Bauer, B., & Nayak, C. (2017c). Prethermal Phases of Matter Protected by Time-Translation Symmetry. Phys. Rev. X, 7, 011026.

[656] Else, D. V., Bauer, B., & Nayak, C. (2017d). Prethermal Phases of Matter Protected by Time-Translation Symmetry. Phys. Rev. X, 7(1), 011026.

[657] Else, D. V., Bauer, B., & Nayak, C. (2017e). Prethermal Phases of Matter Protected by Time-Translation Symmetry. Phys. Rev. X, 7(1), 011026.

[658] Else, D. V., Ho, W. W., & Dumitrescu, P. T. (2020). Long-lived interacting phases of matter protected by multiple time-translation symmetries in quasiperiodically driven systems. Phys. Rev. X, 10, 021032.

[659] Evered, S. J., Bluvstein, D., Kalinowski, M., Ebadi, S., Manovitz, T., Zhou, H., Li, S. H., Geim, A. A., Wang, T. T., Maskara, N., Levine, H., Semeghini, G., Greiner, M., Vuletic, V., & Lukin, M. D. (2023a). High-fidelity parallel entangling gates on a neutral atom quantum computer. Nature, 622(7982), 268–272.

[660] Evered, S. J., Bluvstein, D., Kalinowski, M., Ebadi, S., Manovitz, T., Zhou, H., Li, S. H., Geim, A. A., Wang, T. T., Maskara, N., Levine, H., Semeghini, G., Greiner, M., Vuletić, V., & Lukin, M. D. (2023b). High-fidelity parallel entangling gates on a neutral-atom quantum computer. Nature, 622(7982), 268–272.

[661] Evered, S. J., Bluvstein, D., Kalinowski, M., Ebadi, S., Manovitz, T., Zhou, H., Li, S. H., Geim, A. A., Wang, T. T., Maskara, N., Levine, H., Semeghini, G., Greiner, M., Vuletić, V., & Lukin, M. D. (2023c). High-fidelity parallel entangling gates on a neutral atom quantum computer.

[662] Fan, R., Bao, Y., Altman, E., & Vishwanath, A. (2023). Diagnostics of mixed-state topological order and breakdown of quantum memory.

[663] Feldmeier, J., Maskara, N., Köylüoğlu, N. U., & Lukin, M. D. (2024). Quantum simulation of dynamical gauge theories in periodically driven Rydberg atom arrays.

[664] Feldmeier, J., Pollmann, F., & Knap, M. (2019). Emergent Glassy Dynamics in a Quantum Dimer Model. Phys. Rev. Lett., 123, 040601.

[665] Fendley, P., Sengupta, K., & Sachdev, S. (2004a). Competing density-wave orders in a one-dimensional hard-boson model. Phys. Rev. B, 69, 075106.

[666] Fendley, P., Sengupta, K., & Sachdev, S. (2004b). Competing density-wave orders in a one-dimensional hard-boson model. Phys. Rev. B, 69, 075106.

[667] Feng, L., Katz, O., Haack, C., Maghrebi, M., Gorshkov, A. V., Gong, Z., Cetina, M., & Monroe, C. (2023). Continuous symmetry breaking in a trapped-ion spin chain. Nature, 623(7988), 713–717.

[668] Feynman, R. P. (1982a). Simulating physics with computers. Int. J. Theor. Phys, 21(6/7).

[669] Feynman, R. P. (1982b). Simulating physics with computers. Int. J. Theor. Phys., 21(6), 467–488.

[670] Fläschner, N., Rem, B. S., Tarnowski, M., Vogel, D., Lühmann, D.-S., Sengstock, K., & Weitenberg, C. (2016). Experimental reconstruction of the Berry curvature in a Floquet Bloch band. Science, 352(6289), 1091–1094.

[671] Foss-Feig, M., Hayes, D., Dreiling, J. M., Figgatt, C., Gaebler, J. P., Moses, S. A., Pino, J. M., & Potter, A. C. (2021). Holographic quantum algorithms for simulating correlated spin systems. Physical Review Research, 3(3), 033002.

[672] Fowler, A. G., Mariantoni, M., Martinis, J. M., & Cleland, A. N. (2012). Surface codes: Towards practical large-scale quantum computation. Phys. Rev. A, 86, 032324.

[673] Fredenhagen, K. & Marcu, M. (1983). Charged states in $\mathbb{Z}_2$ gauge theories. Communications in Mathematical Physics, 92(1), 81–119.

[674] Frölian, A., Chisholm, C. S., Neri, E., Cabrera, C. R., Ramos, R., Celi, A., & Tarruell, L. (2022). Realizing a 1D topological gauge theory in an optically dressed BEC. Nature, 608(7922), 293–297.

[675] Fukuhara, T., Hild, S., Zeiher, J., Schauß, P., Bloch, I., Endres, M., & Gross, C. (2015). Spatially Resolved Detection of a Spin-Entanglement Wave in a Bose-Hubbard Chain. Phys. Rev. Lett., 115, 035302.

[676] Funcke, L., Hartung, T., Jansen, K., & Kühn, S. (2023). Review on quantum computing for lattice field theory.

[677] Gärttner, M., Bohnet, J. G., Safavi-Naini, A., Wall, M. L., Bollinger, J. J., & Rey, A. M. (2017). Measuring out-of-time-order correlations and multiple quantum spectra in a trapped-ion quantum magnet. Nature Physics, 13(8), 781–786.

[678] Geier, S., Braemer, A., Braun, E., Müllenbach, M., Franz, T., Gärttner, M., Zürn, G., & Weidemüller, M. (2024). Time-reversal in a dipolar quantum many-body spin system.

[679] Geier, S., Thaicharoen, N., Hainaut, C., Franz, T., Salzinger, A., Tebben, A., Grimshandl, D., Zürn, G., & Weidemüller, M. (2021). Floquet Hamiltonian engineering of an isolated many-body spin system. Science, 374(6571), 1149–1152.

[680] Georgescu, I. M., Ashhab, S., & Nori, F. (2014). Quantum simulation. Rev. Mod. Phys., 86, 153–185.

[681] Gilmore, K. A., Affolter, M., Lewis-Swan, R. J., Barberena, D., Jordan, E., Rey, A. M., & Bollinger, J. J. (2021). Quantum-enhanced sensing of displacements and electric fields with two-dimensional trapped-ion crystals. Science, 373(6555), 673–678.

[682] Giudici, G., Lukin, M. D., & Pichler, H. (2022). Dynamical preparation of quantum spin liquids in Rydberg atom arrays.

[683] Gkritsis, F., Dux, D., Zhang, J., Jain, N., Gogolin, C., & Preiss, P. M. (2024). Simulating Chemistry with Fermionic Optical Superlattices. _eprint: 2409.05663.

[684] Glaetzle, A. W., Dalmonte, M., Nath, R., Rousochatzakis, I., Moessner, R., & Zoller, P. (2014). Quantum Spin-Ice and Dimer Models with Rydberg Atoms. Phys. Rev. X, 4, 041037.

[685] Goldman, N. & Dalibard, J. (2014). Periodically Driven Quantum Systems: Effective Hamiltonians and Engineered Gauge Fields. Phys. Rev. X, 4, 031027.

[686] González-Cuadra, D., Bluvstein, D., Kalinowski, M., Kaubruegger, R., Maskara, N., Naldesi, P., Zache, T. V., Kaufman, A. M., Lukin, M. D., Pichler, H., Vermersch, B., Ye, J., & Zoller, P. (2023a). Fermionic quantum processing with programmable neutral atom arrays. Proceedings of the National Academy of Sciences, 120(35), e2304294120.

[687] González-Cuadra, D., Bluvstein, D., Kalinowski, M., Kaubruegger, R., Maskara, N., Naldesi, P., Zache, T. V., Kaufman, A. M., Lukin, M. D., Pichler, H., Vermersch, B., Ye, J., & Zoller, P. (2023b). Fermionic quantum processing with programmable neutral atom arrays. Proc. Natl. Acad. Sci., 120.

[688] González-Cuadra, D., Zache, T. V., Carrasco, J., Kraus, B., & Zoller, P. (2022). Hardware Efficient Quantum Simulation of Non-Abelian Gauge Theories with Qudits on Rydberg Platforms. Phys. Rev. Lett., 129(16), 160501.

[689] Gregor, K., Huse, D. A., Moessner, R., & Sondhi, S. L. (2011). Diagnosing deconfinement and topological order. New Journal of Physics, 13(2), 025009.

[690] Gritsev, V. & Polkovnikov, A. (2017). Integrable Floquet dynamics. SciPost Phys., 2(3), 021.

[691] Gross, C. & Bloch, I. (2017). Quantum simulations with ultracold atoms in optical lattices. Science, 357(6355), 995–1001.

[692] Günther, J., Baiardi, A., Reiher, M., & Christandl, M. (2023). More quantum chemistry with fewer qubits.

[693] Haah, J. (2016). An invariant of topologically ordered states under local unitary transformations. Communications in Mathematical Physics, 342(3), 771–801. Publisher: Springer.

[694] Haah, J., Harrow, A. W., Ji, Z., Wu, X., & Yu, N. (2017). Sample-optimal tomography of quantum states. IEEE Transactions on Information Theory, 63(9), 5628–5641.

[695] Haegeman, J., Van Acoleyen, K., Schuch, N., Cirac, J. I., & Verstraete, F. (2015). Gauging quantum states: From global to local symmetries in many-body systems. Phys. Rev. X, 5, 011024.

[696] Haghshenas, R., Gray, J., Potter, A. C., & Chan, G. K.-L. (2022). The Variational Power of Quantum Circuit Tensor Networks. Physical Review X, 12(1), 011047. arXiv:2107.01307 [cond-mat, physics:quant-ph].

[697] Hait, D., Tubman, N. M., Levine, D. S., Whaley, K. B., & Head-Gordon, M. (2019). What levels of coupled cluster theory are appropriate for transition metal systems? a study using near-exact quantum chemical values for 3d transition metal binary compounds. J. Chem. Theory Comput., 15(10), 5370–5385.

[698] Haldane, F. D. M. (1988). Model for a Quantum Hall Effect without Landau Levels: Condensed-Matter Realization of the "Parity Anomaly". Phys. Rev. Lett., 61(18), 2015–2018. Publisher: American Physical Society.

[699] Halimeh, J. C. & Hauke, P. (2022). Stabilizing gauge theories in quantum simulators: a brief review.

[700] Halimeh, J. C., Homeier, L., Bohrdt, A., & Grusdt, F. (2023). Spin exchange-enabled quantum simulator for large-scale non-Abelian gauge theories.

[701] Hartke, T., Oreg, B., Jia, N., & Zwierlein, M. (2022). Quantum register of fermion pairs. Nature, 601(7894), 537–541.

[702] Hastings, M. B. (2010). Locality in quantum systems.

[703] Hastings, M. B. (2011). Topological order at nonzero temperature. Phys. Rev. Lett., 107, 210501.

[704] Hastings, M. B. & Haah, J. (2021). Dynamically generated logical qubits. Quantum, 5, 564.

[705] Hastings, M. B. & Wen, X.-G. (2005a). Quasiadiabatic continuation of quantum states: The stability of topological ground-state degeneracy and emergent gauge invariance. Phys. Rev. B, 72(4), 045141. Publisher: American Physical Society.

[706] Hastings, M. B. & Wen, X.-G. (2005b). Quasiadiabatic continuation of quantum states: The stability of topological ground-state degeneracy and emergent gauge invariance. Physical Review B, 72(4).

[707] Hauschild, J. & Pollmann, F. (2018a). Efficient Numerical Simulations with Tensor Networks: Tensor Network Python (TeNPy). SciPost Physics Lecture Notes, (pp.5).

[708] Hauschild, J. & Pollmann, F. (2018b). Efficient numerical simulations with Tensor Networks: Tensor Network Python (TeNPy). SciPost Phys. Lect. Notes, (pp.5).

[709] Heller, E. J. (1984). Bound-state eigenfunctions of classically chaotic hamiltonian systems: Scars of periodic orbits. Phys. Rev. Lett., 53, 1515.

[710] Hermele, M., Fisher, M. P. A., & Balents, L. (2004). Pyrochlore photons: The U (1) spin liquid in a S = 1 2 three-dimensional frustrated magnet. Physical Review B, 69(6), 064404.

[711] Hickey, C. & Trebst, S. (2019). Emergence of a field-driven U(1) spin liquid in the Kitaev honeycomb model. Nat. Commun., 10(1), 530.

[712] Hines, J. A., Rajagopal, S. V., Moreau, G. L., Wahrman, M. D., Lewis, N. A., Marković, O., & Schleier-Smith, M. (2023). Spin Squeezing by Rydberg Dressing in an Array of Atomic Ensembles. Phys. Rev. Lett., 131, 063401.

[713] Ho, W. W., Choi, S., Lukin, M. D., & Abanin, D. A. (2017). Critical time crystals in dipolar systems. Phys. Rev. Lett., 119, 010602.

[714] Ho, W. W., Choi, S., Pichler, H., & Lukin, M. D. (2019). Periodic orbits, entanglement, and quantum many-body scars in constrained models: Matrix product state approach. Phys. Rev. Lett., 122, 040603.

[715] Homeier, L., Bohrdt, A., Linsel, S., Demler, E., Halimeh, J. C., & Grusdt, F. (2023). Realistic scheme for quantum simulation of Z2 lattice gauge theories with dynamical matter in (2 + 1)D. Communications Physics, 6(1), 127.

[716] Horn, D. (1981). Finite matrix models with continuous local gauge invariance. Physics Letters B, 100(2), 149–151.

[717] Horodecki, M., Horodecki, P., & Horodecki, R. (1996). Separability of mixed states: necessary and sufficient conditions. Physics Letters A, 223(1), 1–8.

[718] Horodecki, R., Horodecki, P., Horodecki, M., & Horodecki, K. (2009). Quantum entanglement. Rev. Mod. Phys., 81, 865–942.

[719] Hrmo, P., Wilhelm, B., Gerster, L., van Mourik, M. W., Huber, M., Blatt, R., Schindler, P., Monz, T., & Ringbauer, M. (2023). Native qudit entanglement in a trapped ion quantum processor. Nat. Commun., 14(1), 2242.

[720] Huang, B., Wu, Y.-H., & Liu, W. V. (2018). Clean floquet time crystals: Models and realizations in cold atoms. Physical Review Letters, 120(11).

[721] Huang, H.-Y., Kueng, R., & Preskill, J. (2020). Predicting many properties of a quantum system from very few measurements. Nat. Phys., 16(10), 1050–1057.

[722] Huang, H.-Y., Kueng, R., Torlai, G., Albert, V. V., & Preskill, J. (2022). Provably efficient machine learning for quantum many-body problems. Science, 377(6613), eabk3333.

[723] Hudomal, A., Desaules, J.-Y., Mukherjee, B., Su, G.-X., Halimeh, J. C., & Papić, Z. (2022). Driving quantum many-body scars in the PXP model. Phys. Rev. B, 106, 104302.

[724] Huggins, W. J., O'Gorman, B. A., Rubin, N. C., Reichman, D. R., Babbush, R., & Lee, J. (2022). Unbiasing fermionic quantum Monte Carlo with a quantum computer. Nature, 603(7901), 416–420.

[725] Hyllus, P., Laskowski, W., Krischek, R., Schwemmer, C., Wieczorek, W., Weinfurter, H., Pezzé, L., & Smerzi, A. (2012). Fisher information and multiparticle entanglement. Phys. Rev. A, 85, 022321.

[726] Häffner, H., Roos, C. F., & Blatt, R. (2008). Quantum computing with trapped ions. Phys. Rep., 469(4), 155–203.

[727] Iqbal, M. & Schuch, N. (2021). Entanglement Order Parameters and Critical Behavior for Topological Phase Transitions and Beyond. Physical Review X, 11(4), 041014.

[728] Iqbal, M., Tantivasadakarn, N., Gatterman, T. M., Gerber, J. A., Gilmore, K., Gresh, D., Hankin, A., Hewitt, N., Horst, C. V., Matheny, M., Mengle, T., Neyenhuis, B., Vishwanath, A., Foss-Feig, M., Verresen, R., & Dreyer, H. (2023). Topological Order from Measurements and Feed-Forward on a Trapped Ion Quantum Computer.

[729] Iqbal, M., Tantivasadakarn, N., Verresen, R., Campbell, S. L., Dreiling, J. M., Figgatt, C., Gaebler, J. P., Johansen, J., Mills, M., Moses, S. A., Pino, J. M., Ransford, A., Rowe, M., Siegfried, P., Stutz, R. P., Foss-Feig, M., Vishwanath, A., & Dreyer, H. (2024). Non-Abelian topological order and anyons on a trapped-ion processor. Nature, 626(7999), 505–511.

[730] Irmejs, R., Banuls, M. C., & Cirac, J. I. (2022). Quantum Simulation of Z2 Lattice Gauge theory with minimal requirements.

[731] Islam, R., Ma, R., Preiss, P. M., Eric Tai, M., Lukin, A., Rispoli, M., & Greiner, M. (2015). Measuring entanglement entropy in a quantum many-body system. Nature, 528(7580), 77–83.

[732] Jaksch, D., Cirac, J. I., Zoller, P., Rolston, S. L., Côté, R., & Lukin, M. D. (2000). Fast Quantum Gates for Neutral Atoms. Phys. Rev. Lett., 85(10), 2208–2211.

[733] Jamadagni, A., Kazemi, J., & Weimer, H. (2022). Learning of error statistics for the detection of quantum phases.

[734] Jamadagni, A. & Weimer, H. (2022). Operational definition of topological order. Phys. Rev. B, 106, 085143.

[735] Jandura, S. & Pupillo, G. (2022a). Time-Optimal Two- and Three-Qubit Gates for Rydberg Atoms. Quantum, 6, 712.

[736] Jandura, S. & Pupillo, G. (2022b). Time-Optimal Two- and Three-Qubit Gates for Rydberg Atoms. Quantum, 6, 712.

[737] Jandura, S. & Pupillo, G. (2022c). Time-Optimal Two- and Three-Qubit Gates for Rydberg Atoms. Quantum, 6, 712.

[738] Jenkins, A., Lis, J. W., Senoo, A., McGrew, W. F., & Kaufman, A. M. (2022). Ytterbium Nuclear-Spin Qubits in an Optical Tweezer Array. Physical Review X, 12(2), 021027.

[739] Jin, H.-K., Natori, W. M. H., Pollmann, F., & Knolle, J. (2022). Unveiling the S=3/2 Kitaev honeycomb spin liquids. Nat. Commun., 13(1), 3813.

[740] Johansson, J., Nation, P., & Nori, F. (2013). Qutip 2: A python framework for the dynamics of open quantum systems. Computer Physics Communications, 184(4), 1234–1240.

[741] Jordan, P. & Wigner, E. (1928a). über das Paulische äquivalenzverbot. Z. Phys., 47(9-10), 631–651.

[742] Jordan, P. & Wigner, E. (1928b). Über das Paulische Äquivalenzverbot. Zeitschrift für Physik, 47(9), 631–651. ISBN: 0044-3328.

[743] Joshi, M. K., Kokail, C., van Bijnen, R., Kranzl, F., Zache, T. V., Blatt, R., Roos, C. F., & Zoller, P. (2023). Exploring large-scale entanglement in quantum simulation. Nature, 624(7992), 539–544.

[744] Jotzu, G., Messer, M., Desbuquois, R., Lebrat, M., Uehlinger, T., Greif, D., & Esslinger, T. (2014). Experimental realization of the topological Haldane model with ultracold fermions. Nature, 515(7526), 237–240.

[745] Joy, A. P. & Rosch, A. (2022). Dynamics of visons and thermal hall effect in perturbed kitaev models. Phys. Rev. X, 12, 041004.

[746] Kalinowski, M., Maskara, N., & Lukin, M. D. (2023a). Non-Abelian Floquet Spin Liquids in a Digital Rydberg Simulator. Phys. Rev. X, 13, 031008.

[747] Kalinowski, M., Maskara, N., & Lukin, M. D. (2023b). Non-Abelian Floquet Spin Liquids in a Digital Rydberg Simulator. Phys. Rev. X, 13(3), 031008.

[748] Kandala, A., Mezzacapo, A., Temme, K., Takita, M., Brink, M., Chow, J. M., & Gambetta, J. M. (2017). Hardware-efficient variational quantum eigensolver for small molecules and quantum magnets. Nature, 549(7671), 242–246.

[749] Katz, O., Cetina, M., & Monroe, C. (2022). N-body interactions between trapped ion qubits via spin-dependent squeezing. Phys. Rev. Lett., 129(6), 063603.

[750] Katz, O., Feng, L., Risinger, A., Monroe, C., & Cetina, M. (2023). Demonstration of three- and four-body interactions between trapped-ion spins. Nat. Phys., 19(10), 1452–1458.

[751] Kaufman, A. M., Tai, M. E., Lukin, A., Rispoli, M., Schittko, R., Preiss, P. M., & Greiner, M. (2016). Quantum thermalization through entanglement in an isolated many-body system. Science, 353(6301), 794.

[752] Keesling, A., Omran, A., Levine, H., Bernien, H., Pichler, H., Choi, S., Samajdar, R., Schwartz, S., Silvi, P., Sachdev, S., Zoller, P., Endres, M., Greiner, M., Vuletić, V., & Lukin, M. D. (2019). Quantum Kibble–Zurek mechanism and critical dynamics on a programmable Rydberg simulator. Nature, 568(7751), 207–211.

[753] Khaneja, N., Reiss, T., Kehlet, C., Schulte-Herbrüggen, T., & Glaser, S. J. (2005). Optimal control of coupled spin dynamics: design of NMR pulse sequences by gradient ascent algorithms. J. Magn. Reson., 172(2), 296–305.

[754] Khemani, V., Laumann, C. R., & Chandran, A. (2019). Signatures of integrability in the dynamics of Rydberg-blockaded chains. Phys. Rev. B, 99, 161101.

[755] Khemani, V., Lazarides, A., Moessner, R., & Sondhi, S. L. (2016a). Phase structure of driven quantum systems. Phys. Rev. Lett., 116, 250401.

[756] Khemani, V., Lazarides, A., Moessner, R., & Sondhi, S. L. (2016b). Phase Structure of Driven Quantum Systems. Phys. Rev. Lett., 116, 250401.

[757] Khemani, V., Moessner, R., & Sondhi, S. L. (2020). Comment on "quantum time crystals from hamiltonians with long-range interactions".

[758] Kim, Y., Eddins, A., Anand, S., Wei, K. X., Van Den Berg, E., Rosenblatt, S., Nayfeh, H., Wu, Y., Zaletel, M., Temme, K., & Kandala, A. (2023). Evidence for the utility of quantum computing before fault tolerance. Nature, 618(7965), 500–505.

[759] Kitaev, A. (2003a). Fault-tolerant quantum computation by anyons. Annals of Physics, 303(1), 2–30. Publisher: Elsevier BV.

[760] Kitaev, A. (2003b). Fault-tolerant quantum computation by anyons. Ann. Phys., 303(1), 2–30.

[761] Kitaev, A. (2006a). Anyons in an exactly solved model and beyond. Ann. Phys., 321(1), 2–111.

[762] Kitaev, A. (2006b). Anyons in an exactly solved model and beyond. Ann. Phys., 321(1), 2–111.

[763] Kitaev, A. (2015). A simple model of quantum holography.

[764] Kitaev, A. & Preskill, J. (2006). Topological Entanglement Entropy. Phys. Rev. Lett., 96(11), 110404. Publisher: American Physical Society.

[765] Kivlichan, I. D., McClean, J., Wiebe, N., Gidney, C., Aspuru-Guzik, A., Chan, G. K.-L., & Babbush, R. (2018). Quantum Simulation of Electronic Structure with Linear Depth and Connectivity. Physical Review Letters, 120(11), 110501.

[766] Knap, M., Kantian, A., Giamarchi, T., Bloch, I., Lukin, M. D., & Demler, E. (2013). Probing real-space and time resolved correlation functions with many-body Ramsey interferometry. Physical Review Letters, 111(14), 147205. arXiv:1307.0006 [cond-mat, physics:quant-ph].

[767] Kokail, C., Maier, C., van Bijnen, R., Brydges, T., Joshi, M. K., Jurcevic, P., Muschik, C. A., Silvi, P., Blatt, R., Roos, C. F., & Zoller, P. (2019). Self-verifying variational quantum simulation of lattice models. Nature, 569(7756), 355–360.

[768] Kokail, C., Sundar, B., Zache, T. V., Elben, A., Vermersch, B., Dalmonte, M., van Bijnen, R., & Zoller, P. (2021). Quantum Variational Learning of the Entanglement Hamiltonian. Phys. Rev. Lett., 127, 170501.

[769] König, R., Reichardt, B. W., & Vidal, G. (2009). Exact entanglement renormalization for string-net models. Phys. Rev. B, 79, 195123.

[770] Kornjaca, M., Samajdar, R., Macrì, T., Gemelke, N., Wang, S.-T., & Liu, F. (2023). Trimer quantum spin liquid in a honeycomb array of Rydberg atoms. Communications Physics, 6(1), 358.

[771] Kotaru, S., Kähler, S., Alessio, M., & Krylov, A. I. (2023). Magnetic exchange interactions in binuclear and tetranuclear iron (iii) complexes described by spin-flip dft and heisenberg effective hamiltonians. J. Comput. Chem., 44(3), 367–380.

[772] Kozin, V. K. & Kyriienko, O. (2019). Quantum time crystals from hamiltonians with long-range interactions. Phys. Rev. Lett., 123, 210602.

[773] Kraus, C. V. & Cirac, J. I. (2010). Generalized Hartree–Fock theory for interacting fermions in lattices: numerical methods. New J. Phys., 12(11), 113004.

[774] Krewald, V., Neese, F., & Pantazis, D. A. (2013). On the Magnetic and Spectroscopic Properties of High-Valent Mn $_3$ CaO $_4$ Cubanes as Structural Units of Natural and Artificial Water-Oxidizing Catalysts. J. Am. Chem. Soc., 135(15), 5726–5739.

[775] Krewald, V., Retegan, M., Cox, N., Messinger, J., Lubitz, W., DeBeer, S., Neese, F., & Pantazis, D. A. (2015). Metal oxidation states in biological water splitting. Chem. Sci., 6(3), 1676–1695.

[776] Krewald, V., Retegan, M., Neese, F., Lubitz, W., Pantazis, D. A., & Cox, N. (2016). Spin State as a Marker for the Structural Evolution of Nature's Water-Splitting Catalyst. Inorg. Chem., 55(2), 488–501.

[777] Kruckenhauser, A., Bijnen, R. v., Zache, T. V., Liberto, M. D., & Zoller, P. (2022). High-dimensional SO(4)-symmetric Rydberg manifolds for quantum simulation. Quantum Sci. Technol., 8(1), 015020.

[778] Kuwahara, T., Mori, T., & Saito, K. (2016). Floquet–Magnus theory and generic transient dynamics in periodically driven many-body quantum systems. Annals of Physics, 367, 96–124.

[779] Köylüoğlu, N. U., Maskara, N., Feldmeier, J., & Lukin, M. D. (2024). Floquet engineering of interactions and entanglement in periodically driven Rydberg chains.

[780] Labuhn, H., Barredo, D., Ravets, S., de Léséleuc, S., Macrì, T., Lahaye, T., & Browaeys, A. (2016a). Tunable two-dimensional arrays of single Rydberg atoms for realizing quantum Ising models. Nature, 534(7609), 667–670.

[781] Labuhn, H., Barredo, D., Ravets, S., de Léséleuc, S., Macrì, T., Lahaye, T., & Browaeys, A. (2016b). Tunable two-dimensional arrays of single Rydberg atoms for realizing quantum Ising models. Nature, 534(7609), 667–670.

[782] Lan, Z., van Horssen, M., Powell, S., & Garrahan, J. P. (2018). Quantum Slow Relaxation and Metastability due to Dynamical Constraints. Phys. Rev. Lett., 121, 040603.

[783] Langen, T., Erne, S., Geiger, R., Rauer, B., Schweigler, T., Kuhnert, M., Rohringer, W., Mazets, I. E., Gasenzer, T., & Schmiedmayer, J. (2015). Ex-

perimental observation of a generalized Gibbs ensemble. Science, 348(6231), 207–211.

[784] Lazarides, A., Das, A., & Moessner, R. (2014). Periodic Thermodynamics of Isolated Quantum Systems. Phys. Rev. Lett., 112(15), 150401.

[785] Lee, P. A., Nagaosa, N., & Wen, X.-G. (2006). Doping a Mott insulator: Physics of high-temperature superconductivity. Rev. Mod. Phys., 78(1), 17–85.

[786] Lee, Y. A. & Vidal, G. (2013). Entanglement negativity and topological order. Physical Review A, 88(4), 042318.

[787] Lensky, Y. D., Kechedzhi, K., Aleiner, I., & Kim, E.-A. (2022). Graph gauge theory of mobile non-Abelian anyons in a qubit stabilizer code.

[788] Lerose, A., Marino, J., Gambassi, A., & Silva, A. (2019). Prethermal quantum many-body kapitza phases of periodically driven spin systems. Physical Review B, 100(10).

[789] Lesanovsky, I. & Katsura, H. (2012). Interacting Fibonacci anyons in a Rydberg gas. Phys. Rev. A, 86, 041601.

[790] Levin, M. & Wen, X.-G. (2006). Detecting Topological Order in a Ground State Wave Function. Phys. Rev. Lett., 96(11), 110405. Publisher: American Physical Society.

[791] Levin, M. A. & Wen, X.-G. (2005). String-net condensation: A physical mechanism for topological phases. Phys. Rev. B, 71, 045110.

[792] Levine, H., Bluvstein, D., Keesling, A., Wang, T. T., Ebadi, S., Semeghini, G., Omran, A., Greiner, M., Vuletić, V., & Lukin, M. D. (2022a). Dispersive optical

systems for scalable Raman driving of hyperfine qubits. Phys. Rev. A, 105, 032618.

[793] Levine, H., Bluvstein, D., Keesling, A., Wang, T. T., Ebadi, S., Semeghini, G., Omran, A., Greiner, M., Vuletić, V., & Lukin, M. D. (2022b). Dispersive optical systems for scalable raman driving of hyperfine qubits. Phys. Rev. A, 105, 032618.

[794] Levine, H., Keesling, A., Semeghini, G., Omran, A., Wang, T. T., Ebadi, S., Bernien, H., Greiner, M., Vuletić, V., Pichler, H., & Lukin, M. D. (2019a). Parallel Implementation of High-Fidelity Multiqubit Gates with Neutral Atoms. Phys. Rev. Lett., 123, 170503.

[795] Levine, H., Keesling, A., Semeghini, G., Omran, A., Wang, T. T., Ebadi, S., Bernien, H., Greiner, M., Vuletić, V., Pichler, H., & Lukin, M. D. (2019b). Parallel Implementation of High-Fidelity Multiqubit Gates with Neutral Atoms. Phys. Rev. Lett., 123(17), 170503.

[796] Levine, H., Keesling, A., Semeghini, G., Omran, A., Wang, T. T., Ebadi, S., Bernien, H., Greiner, M., Vuletić, V., Pichler, H., & Lukin, M. D. (2019c). Parallel Implementation of High-Fidelity Multiqubit Gates with Neutral Atoms. Phys. Rev. Lett., 123(17), 170503.

[797] Li, X., Yu, H., Lou, F., Feng, J., Whangbo, M.-H., & Xiang, H. (2021). Spin Hamiltonians in Magnets: Theories and Computations. Molecules, 26(4), 803.

[798] Li, Z., Guo, S., Sun, Q., & Chan, G. K.-L. (2019). Electronic landscape of the P-cluster of nitrogenase as revealed through many-electron quantum wavefunction simulations. Nat. Chem., 11(11), 1026–1033.

[799] Lieb, E. H. (1994). Flux phase of the half-filled band. Phys. Rev. Lett., 73, 2158–2161.

[800] Lin, C.-J., Chandran, A., & Motrunich, O. I. (2020). Slow thermalization of exact quantum many-body scar states under perturbations. Phys. Rev. Research, 2, 033044.

[801] Lin, L. (2022). Lecture notes on quantum algorithms for scientific computation.

[802] Lin, L. & Tong, Y. (2022). Heisenberg-limited ground state energy estimation for early fault-tolerant quantum computers. PRX Quantum, 3(1), 010318. arXiv:2102.11340 [quant-ph].

[803] Lin, R., Zhong, H.-S., Li, Y., Zhao, Z.-R., Zheng, L.-T., Hu, T.-R., Wu, H.-M., Wu, Z., Ma, W.-J., Gao, Y., Zhu, Y.-K., Su, Z.-F., Ouyang, W.-L., Zhang, Y.-C., Rui, J., Chen, M.-C., Lu, C.-Y., & Pan, J.-W. (2024). AI-enabled rapid assembly of thousands of defect-free neutral atom arrays with constant-time-overhead.

[804] Linnemann, D., Strobel, H., Muessel, W., Schulz, J., Lewis-Swan, R. J., Kheruntsyan, K. V., & Oberthaler, M. K. (2016). Quantum-Enhanced Sensing Based on Time Reversal of Nonlinear Dynamics. Phys. Rev. Lett., 117, 013001.

[805] Lis, J. W., Senoo, A., McGrew, W. F., Rönchen, F., Jenkins, A., & Kaufman, A. M. (2023). Mid-circuit operations using the omg-architecture in neutral atom arrays. arXiv:2305.19266 [cond-mat, physics:physics, physics:quant-ph].

[806] Liu, S. & Xue, Z.-Y. (2013). Probing non-Abelian anyonic statistics with cold atoms in an optical lattice. J. Opt. Soc. Am. B, 30(6), 1720.

[807] Ljubotina, M., Roos, B., Abanin, D. A., & Serbyn, M. (2022a). Optimal Steering of Matrix Product States and Quantum Many-Body Scars. PRX Quantum, 3, 030343.

[808] Ljubotina, M., Roos, B., Abanin, D. A., & Serbyn, M. (2022b). Optimal Steering of Matrix Product States and Quantum Many-Body Scars. PRX Quantum, 3, 030343.

[809] Low, G. H. & Chuang, I. L. (2019). Hamiltonian Simulation by Qubitization. Quantum, 3, 163.

[810] Lu, S., Bañuls, M. C., & Cirac, J. I. (2021). Algorithms for quantum simulation at finite energies. PRX Quantum, 2(2), 020321.

[811] Lu, T.-C., Lessa, L. A., Kim, I. H., & Hsieh, T. H. (2022). Measurement as a Shortcut to Long-Range Entangled Quantum Matter. PRX Quantum, 3(4), 040337.

[812] Lu, T.-C. & Vijay, S. (2022). Characterizing long-range entanglement in a mixed state through an emergent order on the entangling surface.

[813] Ma, H., Govoni, M., & Galli, G. (2020). Quantum simulations of materials on near-term quantum computers. npj Computational Materials, 6(1), 85.

[814] Ma, S., Burgers, A. P., Liu, G., Wilson, J., Zhang, B., & Thompson, J. D. (2022). Universal Gate Operations on Nuclear Spin Qubits in an Optical Tweezer Array of ^{171}Yb Atoms. Phys. Rev. X, 12(2), 021028.

[815] Ma, S., Liu, G., Peng, P., Zhang, B., Jandura, S., Claes, J., Burgers, A. P., Pupillo, G., Puri, S., & Thompson, J. D. (2023a). High-fidelity gates and mid-circuit erasure conversion in an atomic qubit. Nature, 622(7982), 279–284.

[816] Ma, S., Liu, G., Peng, P., Zhang, B., Jandura, S., Claes, J., Burgers, A. P., Pupillo, G., Puri, S., & Thompson, J. D. (2023b). High-fidelity gates and mid-circuit erasure conversion in an atomic qubit. Nature, 622(7982), 279–284.

[817] Ma, S., Liu, G., Peng, P., Zhang, B., Jandura, S., Claes, J., Burgers, A. P., Pupillo, G., Puri, S., & Thompson, J. D. (2023c). High-fidelity gates and mid-circuit erasure conversion in an atomic qubit. Nature, 622(7982), 279–284.

[818] Machado, F., Else, D. V., Kahanamoku-Meyer, G. D., Nayak, C., & Yao, N. Y. (2020). Long-Range Prethermal Phases of Nonequilibrium Matter. Phys. Rev. X, 10(1), 011043.

[819] Magnus, W. (1954). On the exponential solution of differential equations for a linear operator. Comm. Pure Appl. Math., 7(4), 649–673.

[820] Maldacena, J. (2023). A simple quantum system that describes a black hole.

[821] Malrieu, J. P., Caballol, R., Calzado, C. J., de Graaf, C., & Guihéry, N. (2014). Magnetic Interactions in Molecules and Highly Correlated Materials: Physical Content, Analytical Derivation, and Rigorous Extraction of Magnetic Hamiltonians. Chem. Rev., 114(1), 429–492.

[822] Manetsch, H. J., Nomura, G., Bataille, E., Leung, K. H., Lv, X., & Endres, M. (2024). A tweezer array with 6100 highly coherent atomic qubits.

[823] Manmana, S. R., Stoudenmire, E. M., Hazzard, K. R. A., Rey, A. M., & Gorshkov, A. V. (2013). Topological phases in ultracold polar-molecule quantum magnets. Phys. Rev. B, 87(8), 081106(R).

[824] Manovitz, T., Li, S. H., Ebadi, S., Samajdar, R., Geim, A. A., Evered, S. J., Bluvstein, D., Zhou, H., Köylüoğlu, N. U., Feldmeier, J., Dolgirev, P. E., Maskara, N., Kalinowski, M., Sachdev, S., Huse, D. A., Greiner, M., Vuletić, V., & Lukin, M. D. (2024). Quantum coarsening and collective dynamics on a programmable quantum simulator.

[825] Mardirossian, N. & Head-Gordon, M. (2017). Thirty years of density functional theory in computational chemistry: an overview and extensive assessment of 200 density functionals. Mol. Phys., 115(19), 2315–2372.

[826] Marin Bukov, L. D. & Polkovnikov, A. (2015). Universal high-frequency behavior of periodically driven systems: from dynamical stabilization to Floquet engineering. Advances in Physics, 64(2), 139–226.

[827] Martinez, E. A., Muschik, C. A., Schindler, P., Nigg, D., Erhard, A., Heyl, M., Hauke, P., Dalmonte, M., Monz, T., Zoller, P., & Blatt, R. (2016). Real-time dynamics of lattice gauge theories with a few-qubit quantum computer. Nature, 534(7608), 516–519.

[828] Martyn, J. M., Rossi, Z. M., Tan, A. K., & Chuang, I. L. (2021). Grand Unification of Quantum Algorithms. PRX Quantum, 2(4), 040203.

[829] Maskara, N., Michailidis, A. A., Ho, W. W., Bluvstein, D., Choi, S., Lukin, M. D., & Serbyn, M. (2021a). Discrete Time-Crystalline Order Enabled by

Quantum Many-Body Scars: Entanglement Steering via Periodic Driving. Phys. Rev. Lett., 127, 090602.

[830] Maskara, N., Michailidis, A. A., Ho, W. W., Bluvstein, D., Choi, S., Lukin, M. D., & Serbyn, M. (2021b). Discrete Time-Crystalline Order Enabled by Quantum Many-Body Scars: Entanglement Steering via Periodic Driving. Phys. Rev. Lett., 127, 090602.

[831] Maskara, N., Ostermann, S., Shee, J., Kalinowski, M., Gomez, A. M., Bravo, R. A., Wang, D. S., Krylov, A. I., Yao, N. Y., Head-Gordon, M., Lukin, M. D., & Yelin, S. F. (2023a). Programmable simulations of molecules and materials with reconfigurable quantum processors.

[832] Maskara, N., Ostermann, S., Shee, J., Kalinowski, M., Gomez, A. M., Bravo, R. A., Wang, D. S., Krylov, A. I., Yao, N. Y., Head-Gordon, M., Lukin, M. D., & Yelin, S. F. (2023b). Programmable Simulations of Molecules and Materials with Reconfigurable Quantum Processors.

[833] Maskara, N., Ostermann, S., Shee, J., Kalinowski, M., Gomez, A. M., Bravo, R. A., Wang, D. S., Krylov, A. I., Yao, N. Y., Head-Gordon, M., Lukin, M. D., & Yelin, S. F. (2023c). Programmable Simulations of Molecules and Materials with Reconfigurable Quantum Processors.

[834] Mayhall, N. J. & Head-Gordon, M. (2014). Computational quantum chemistry for single Heisenberg spin couplings made simple: Just one spin flip required. J. Chem. Phys., 141(13), 134111.

[835] Mayhall, N. J. & Head-Gordon, M. (2015). Computational Quantum Chemistry for Multiple-Site Heisenberg Spin Couplings Made Simple: Still Only One Spin–Flip Required. J. Phys. Chem. Lett., 6(10), 1982–1988.

[836] Mazurenko, A., Chiu, C. S., Ji, G., Parsons, M. F., Kanász-Nagy, M., Schmidt, R., Grusdt, F., Demler, E., Greif, D., & Greiner, M. (2017). A cold-atom Fermi–Hubbard antiferromagnet. Nature, 545(7655), 462–466.

[837] McArdle, S., Endo, S., Aspuru-Guzik, A., Benjamin, S. C., & Yuan, X. (2020). Quantum computational chemistry. Rev. Mod. Phys., 92(1), 015003.

[838] McClean, J. R., Boixo, S., Smelyanskiy, V. N., Babbush, R., & Neven, H. (2018). Barren plateaus in quantum neural network training landscapes. Nature communications, 9(1), 1–6.

[839] McClean, J. R., Romero, J., Babbush, R., & Aspuru-Guzik, A. (2016). The theory of variational hybrid quantum-classical algorithms. New Journal of Physics, 18(2), 023023.

[840] Meinert, F., Mark, M. J., Lauber, K., Daley, A. J., & Nägerl, H.-C. (2016). Floquet Engineering of Correlated Tunneling in the Bose-Hubbard Model with Ultracold Atoms. Phys. Rev. Lett., 116, 205301.

[841] Mi, X., Ippoliti, M., Quintana, C., Greene, A., Chen, Z., Gross, J., Arute, F., Arya, K., Atalaya, J., Babbush, R., Bardin, J. C., Basso, J., Bengtsson, A., Bilmes, A., Bourassa, A., Brill, L., Broughton, M., Buckley, B. B., Buell, D. A., Burkett, B., Bushnell, N., Chiaro, B., Collins, R., Courtney, W., Debroy, D., Demura, S., Derk, A. R., Dunsworth, A., Eppens, D., Erickson, C., Farhi, E.,

Fowler, A. G., Foxen, B., Gidney, C., Giustina, M., Harrigan, M. P., Harrington, S. D., Hilton, J., Ho, A., Hong, S., Huang, T., Huff, A., Huggins, W. J., Ioffe, L. B., Isakov, S. V., Iveland, J., Jeffrey, E., Jiang, Z., Jones, C., Kafri, D., Khattar, T., Kim, S., Kitaev, A., Klimov, P. V., Korotkov, A. N., Kostritsa, F., Landhuis, D., Laptev, P., Lee, J., Lee, K., Locharla, A., Lucero, E., Martin, O., McClean, J. R., McCourt, T., McEwen, M., Miao, K. C., Mohseni, M., Montazeri, S., Mruczkiewicz, W., Naaman, O., Neeley, M., Neill, C., Newman, M., Niu, M. Y., O'Brien, T. E., Opremcak, A., Ostby, E., Pato, B., Petukhov, A., Rubin, N. C., Sank, D., Satzinger, K. J., Shvarts, V., Su, Y., Strain, D., Szalay, M., Trevithick, M. D., Villalonga, B., White, T., Yao, Z. J., Yeh, P., Yoo, J., Zalcman, A., Neven, H., Boixo, S., Smelyanskiy, V., Megrant, A., Kelly, J., Chen, Y., Sondhi, S. L., Moessner, R., Kechedzhi, K., Khemani, V., & Roushan, P. (2022a). Time-crystalline eigenstate order on a quantum processor. Nature, 601(7894), 531–536.

[842] Mi, X., Sonner, M., Niu, M. Y., Lee, K. W., Foxen, B., Acharya, R., Aleiner, I., Andersen, T. I., Arute, F., Arya, K., Asfaw, A., Atalaya, J., Bardin, J. C., Basso, J., Bengtsson, A., Bortoli, G., Bourassa, A., Brill, L., Broughton, M., Buckley, B. B., Buell, D. A., Burkett, B., Bushnell, N., Chen, Z., Chiaro, B., Collins, R., Conner, P., Courtney, W., Crook, A. L., Debroy, D. M., Demura, S., Dunsworth, A., Eppens, D., Erickson, C., Faoro, L., Farhi, E., Fatemi, R., Flores, L., Forati, E., Fowler, A. G., Giang, W., Gidney, C., Gilboa, D., Giustina, M., Dau, A. G., Gross, J. A., Habegger, S., Harrigan, M. P., Hoffmann, M., Hong, S., Huang, T., Huff, A., Huggins, W. J., Ioffe, L. B., Isakov, S. V., Iveland, J., Jeffrey, E., Jiang, Z., Jones, C., Kafri, D., Kechedzhi, K.,

Khattar, T., Kim, S., Kitaev, A. Y., Klimov, P. V., Klots, A. R., Korotkov, A. N., Kostritsa, F., Kreikebaum, J. M., Landhuis, D., Laptev, P., Lau, K.-M., Lee, J., Laws, L., Liu, W., Locharla, A., Martin, O., McClean, J. R., McEwen, M., Meurer Costa, B., Miao, K. C., Mohseni, M., Montazeri, S., Morvan, A., Mount, E., Mruczkiewicz, W., Naaman, O., Neeley, M., Neill, C., Newman, M., O'Brien, T. E., Opremcak, A., Petukhov, A., Potter, R., Quintana, C., Rubin, N. C., Saei, N., Sank, D., Sankaragomathi, K., Satzinger, K. J., Schuster, C., Shearn, M. J., Shvarts, V., Strain, D., Su, Y., Szalay, M., Vidal, G., Villalonga, B., Vollgraff-Heidweiller, C., White, T., Yao, Z., Yeh, P., Yoo, J., Zalcman, A., Zhang, Y., Zhu, N., Neven, H., Bacon, D., Hilton, J., Lucero, E., Babbush, R., Boixo, S., Megrant, A., Chen, Y., Kelly, J., Smelyanskiy, V., Abanin, D. A., & Roushan, P. (2022b). Noise-resilient edge modes on a chain of superconducting qubits. Science, 378(6621), 785–790.

[843] Michailidis, A. A., Turner, C. J., Papić, Z., Abanin, D. A., & Serbyn, M. (2020a). Slow quantum thermalization and many-body revivals from mixed phase space. Phys. Rev. X, 10, 011055.

[844] Michailidis, A. A., Turner, C. J., Papić, Z., Abanin, D. A., & Serbyn, M. (2020b). Stabilizing two-dimensional quantum scars by deformation and synchronization. Phys. Rev. Research, 2, 022065.

[845] Micheli, A., Brennen, G. K., & Zoller, P. (2006). A toolbox for lattice-spin models with polar molecules. Nat. Phys., 2(5), 341–347.

[846] Mil, A., Zache, T. V., Hegde, A., Xia, A., Bhatt, R. P., Oberthaler, M. K., Hauke, P., Berges, J., & Jendrzejewski, F. (2020). A scalable realization of local

U(1) gauge invariance in cold atomic mixtures. Science, 367(6482), 1128–1130.

[847] Mildenberger, J., Mruczkiewicz, W., Halimeh, J. C., Jiang, Z., & Hauke, P. (2022). Probing confinement in a $\mathbb{Z}_2$ lattice gauge theory on a quantum computer.

[848] Minami, K. (2019). Honeycomb lattice Kitaev model with Wen–Toric-code interactions, and anyon excitations. Nuclear Physics B, 939, 465–484.

[849] Misguich, G., Serban, D., & Pasquier, V. (2002a). Quantum Dimer Model on the Kagome Lattice: Solvable Dimer-Liquid and Ising Gauge Theory. Phys. Rev. Lett., 89, 137202.

[850] Misguich, G., Serban, D., & Pasquier, V. (2002b). Quantum Dimer Model on the Kagome Lattice: Solvable Dimer-Liquid and Ising Gauge Theory. Phys. Rev. Lett., 89(13), 137202. Publisher: American Physical Society.

[851] Miyake, H., Siviloglou, G. A., Kennedy, C. J., Burton, W. C., & Ketterle, W. (2013). Realizing the Harper Hamiltonian with Laser-Assisted Tunneling in Optical Lattices. Phys. Rev. Lett., 111, 185302.

[852] Mizuta, K., Takasan, K., & Kawakami, N. (2020). Exact Floquet quantum many-body scars under Rydberg blockade. Phys. Rev. Research, 2, 033284.

[853] Moessner, R., Sondhi, S. L., & Chandra, P. (2001a). Phase diagram of the hexagonal lattice quantum dimer model. Phys. Rev. B, 64, 144416.

[854] Moessner, R., Sondhi, S. L., & Fradkin, E. (2001b). Short-ranged resonating valence bond physics, quantum dimer models, and Ising gauge theories. Phys. Rev. B, 65, 024504.

[855] Monroe, C., Campbell, W., Duan, L.-M., Gong, Z.-X., Gorshkov, A., Hess, P., Islam, R., Kim, K., Linke, N., Pagano, G., Richerme, P., Senko, C., & Yao, N. (2021). Programmable quantum simulations of spin systems with trapped ions. Rev. Mod. Phys., 93(2), 025001.

[856] Monz, T., Schindler, P., Barreiro, J. T., Chwalla, M., Nigg, D., Coish, W. A., Harlander, M., Hänsel, W., Hennrich, M., & Blatt, R. (2011). 14-Qubit Entanglement: Creation and Coherence. Phys. Rev. Lett., 106, 130506.

[857] Morgado, M. & Whitlock, S. (2021). Quantum simulation and computing with Rydberg-interacting qubits. AVS Quantum Science, 3(2), 023501.

[858] Mori, T., Kuwahara, T., & Saito, K. (2016). Rigorous Bound on Energy Absorption and Generic Relaxation in Periodically Driven Quantum Systems. Phys. Rev. Lett., 116, 120401.

[859] Moses, S. A., Baldwin, C. H., Allman, M. S., Ancona, R., Ascarrunz, L., Barnes, C., Bartolotta, J., Bjork, B., Blanchard, P., Bohn, M., Bohnet, J. G., Brown, N. C., Burdick, N. Q., Burton, W. C., Campbell, S. L., au2, J. P. C. I., Carron, C., Chambers, J., Chan, J. W., Chen, Y. H., Chernoguzov, A., Chertkov, E., Colina, J., Curtis, J. P., Daniel, R., DeCross, M., Deen, D., Delaney, C., Dreiling, J. M., Ertsgaard, C. T., Esposito, J., Estey, B., Fabrikant, M., Figgatt, C., Foltz, C., Foss-Feig, M., Francois, D., Gaebler, J. P., Gatterman, T. M., Gilbreth, C. N., Giles, J., Glynn, E., Hall, A., Hankin, A. M., Hansen, A., Hayes, D., Higashi, B., Hoffman, I. M., Horning, B., Hout, J. J., Jacobs, R., Johansen, J., Jones, L., Karcz, J., Klein, T., Lauria, P., Lee, P., Liefer, D., Lytle, C., Lu, S. T., Lucchetti, D., Malm, A., Matheny, M., Mathewson, B.,

Mayer, K., Miller, D. B., Mills, M., Neyenhuis, B., Nugent, L., Olson, S., Parks, J., Price, G. N., Price, Z., Pugh, M., Ransford, A., Reed, A. P., Roman, C., Rowe, M., Ryan-Anderson, C., Sanders, S., Sedlacek, J., Shevchuk, P., Siegfried, P., Skripka, T., Spaun, B., Sprenkle, R. T., Stutz, R. P., Swallows, M., Tobey, R. I., Tran, A., Tran, T., Vogt, E., Volin, C., Walker, J., Zolot, A. M., & Pino, J. M. (2023). A race track trapped-ion quantum processor.

[860] Motta, M. & Rice, J. E. (2022). Emerging quantum computing algorithms for quantum chemistry. Wiley Interdiscip. Rev. Comput. Mol. Sci., 12(3), e1580.

[861] Moudgalya, S., Bernevig, B. A., & Regnault, N. (2020). Quantum many-body scars in a landau level on a thin torus. Physical Review B, 102(19).

[862] Moudgalya, S., Rachel, S., Bernevig, B. A., & Regnault, N. (2018). Exact excited states of nonintegrable models. Physical Review B, 98(23).

[863] Mukherjee, B., Nandy, S., Sen, A., Sen, D., & Sengupta, K. (2020). Collapse and revival of quantum many-body scars via Floquet engineering. Phys. Rev. B, 101, 245107.

[864] Nandkishore, R. & Huse, D. A. (2015). Many-body localization and thermalization in quantum statistical mechanics. Annu. Rev. Condens. Matter Phys., 6(1), 15–38.

[865] Napp, J. C., La Placa, R. L., Dalzell, A. M., Brandão, F. G. S. L., & Harrow, A. W. (2022). Efficient classical simulation of random shallow 2d quantum circuits. Phys. Rev. X, 12, 021021.

[866] Nayak, C., Simon, S. H., Stern, A., Freedman, M., & Das Sarma, S. (2008a). Non-abelian anyons and topological quantum computation. Rev. Mod. Phys., 80, 1083–1159.

[867] Nayak, C., Simon, S. H., Stern, A., Freedman, M., & Das Sarma, S. (2008b). Non-Abelian anyons and topological quantum computation. Rev. Mod. Phys., 80(3), 1083–1159.

[868] Nguyen, M.-T., Liu, J.-G., Wurtz, J., Lukin, M. D., Wang, S.-T., & Pichler, H. (2023). Quantum Optimization with Arbitrary Connectivity Using Rydberg Atom Arrays. PRX Quantum, 4, 010316.

[869] Nigmatullin, R., Hemery, K., Ghanem, K., Moses, S., Gresh, D., Siegfried, P., Mills, M., Gatterman, T., Hewitt, N., Granet, E., & Dreyer, H. (2024). Experimental Demonstration of Break-Even for the Compact Fermionic Encoding.

[870] Nishad, N., Keselman, A., Lahaye, T., Browaeys, A., & Tsesses, S. (2023). Quantum simulation of generic spin-exchange models in Floquet-engineered Rydberg-atom arrays. Phys. Rev. A, 108, 053318.

[871] Omran, A., Levine, H., Keesling, A., Semeghini, G., Wang, T. T., Ebadi, S., Bernien, H., Zibrov, A. S., Pichler, H., Choi, S., Cui, J., Rossignolo, M., Rembold, P., Montangero, S., Calarco, T., Endres, M., Greiner, M., Vuletić, V., & Lukin, M. D. (2019a). Generation and manipulation of Schrödinger cat states in Rydberg atom arrays. Science, 365(6453), 570–574.

[872] Omran, A., Levine, H., Keesling, A., Semeghini, G., Wang, T. T., Ebadi, S., Bernien, H., Zibrov, A. S., Pichler, H., Choi, S., Cui, J., Rossignolo, M., Rembold, P., Montangero, S., Calarco, T., Endres, M., Greiner, M., Vuletić, V., &

Lukin, M. D. (2019b). Generation and manipulation of Schrödinger cat states in Rydberg atom arrays. Science, 365(6453), 570–574.

[873] Orland, P. & Rohrlich, D. (1990). Lattice gauge magnets: Local isospin from spin. Nuclear Physics B, 338(3), 647–672.

[874] Orús, R. (2014). A practical introduction to tensor networks: Matrix product states and projected entangled pair states. Annals of Physics, 349, 117–158.

[875] Ott, R., González-Cuadra, D., Zache, T. V., Zoller, P., Kaufman, A. M., & Pichler, H. (2024). Error-corrected fermionic quantum processors with neutral atoms.

[876] O'Brien, T. E., Tarasinski, B., & Terhal, B. M. (2019). Quantum phase estimation of multiple eigenvalues for small-scale (noisy) experiments. New J. Phys., 21(2), 023022.

[877] Pagano, A., Weber, S., Jaschke, D., Pfau, T., Meinert, F., Montangero, S., & Büchler, H. P. (2022a). Error budgeting for a controlled-phase gate with strontium-88 rydberg atoms. Phys. Rev. Res., 4, 033019.

[878] Pagano, A., Weber, S., Jaschke, D., Pfau, T., Meinert, F., Montangero, S., & Büchler, H. P. (2022b). Error budgeting for a controlled-phase gate with strontium-88 rydberg atoms. Phys. Rev. Res., 4, 033019.

[879] Pantazis, D. A., Orio, M., Petrenko, T., Zein, S., Lubitz, W., Messinger, J., & Neese, F. (2009). Structure of the oxygen-evolving complex of photosystem II: information on the S2 state through quantum chemical calculation of its magnetic properties. Phys. Chem. Chem. Phys., 11(31), 6788.

[880] Pastori, L., Olsacher, T., Kokail, C., & Zoller, P. (2022). Characterization and Verification of Trotterized Digital Quantum Simulation Via Hamiltonian and Liouvillian Learning. PRX Quantum, 3(3), 030324.

[881] Paul, S., Neese, F., & Pantazis, D. A. (2017). Structural models of the biological oxygen-evolving complex: achievements, insights, and challenges for biomimicry. Green Chem., 19(10), 2309–2325.

[882] Pedrozo-Peñafiel, E., Colombo, S., Shu, C., Adiyatullin, A. F., Li, Z., Mendez, E., Braverman, B., Kawasaki, A., Akamatsu, D., Xiao, Y., & Vuletić, V. (2020). Entanglement on an optical atomic-clock transition. Nature, 588(7838), 414–418.

[883] Peng, P., Huang, X., Yin, C., Joseph, L., Ramanathan, C., & Cappellaro, P. (2022). Deep Reinforcement Learning for Quantum Hamiltonian Engineering. Phys. Rev. Appl., 18, 024033.

[884] Peres, A. (1996). Separability Criterion for Density Matrices. Physical Review Letters, 77(8), 1413–1415.

[885] Peruzzo, A., McClean, J., Shadbolt, P., Yung, M.-H., Zhou, X.-Q., Love, P. J., Aspuru-Guzik, A., & O'Brien, J. L. (2014). A variational eigenvalue solver on a photonic quantum processor. Nat. Commun., 5(1), 4213.

[886] Pesah, A., Cerezo, M., Wang, S., Volkoff, T., Sornborger, A. T., & Coles, P. J. (2021). Absence of barren plateaus in quantum convolutional neural networks. Phys. Rev. X, 11, 041011.

[887] Pezzè, L., Smerzi, A., Oberthaler, M. K., Schmied, R., & Treutlein, P. (2018). Quantum metrology with nonclassical states of atomic ensembles. Rev. Mod. Phys., 90, 035005.

[888] Pichler, H., Wang, S.-T., Zhou, L., Choi, S., & Lukin, M. D. (2018a). Quantum Optimization for Maximum Independent Set Using Rydberg Atom Arrays.

[889] Pichler, H., Wang, S.-T., Zhou, L., Choi, S., & Lukin, M. D. (2018b). Quantum optimization for maximum independent set using Rydberg atom arrays.

[890] Pino, J. M., Dreiling, J. M., Figgatt, C., Gaebler, J. P., Moses, S. A., Allman, M., Baldwin, C., Foss-Feig, M., Hayes, D., Mayer, K., et al. (2021). Demonstration of the trapped-ion quantum ccd computer architecture. Nature, 592(7853), 209–213.

[891] Pizzi, A., Knolle, J., & Nunnenkamp, A. (2021). Higher-order and fractional discrete time crystals in clean long-range interacting systems. Nature Communications, 12(1).

[892] Pizzi, A., Malz, D., De Tomasi, G., Knolle, J., & Nunnenkamp, A. (2020). Time crystallinity and finite-size effects in clean floquet systems. Phys. Rev. B, 102, 214207.

[893] Po, H. C., Fidkowski, L., Vishwanath, A., & Potter, A. C. (2017). Radical chiral Floquet phases in a periodically driven Kitaev model and beyond. Phys. Rev. B, 96(24), 245116.

[894] Poilblanc, D., Schuch, N., Pérez-García, D., & Cirac, J. I. (2012). Topological and entanglement properties of resonating valence bond wave functions. Phys. Rev. B, 86(1), 014404. Publisher: American Physical Society.

[895] Pokhilko, P., Bezrukov, D. S., & Krylov, A. I. (2021). Is Solid Copper Oxalate a Spin Chain or a Mixture of Entangled Spin Pairs? J. Phys. Chem. C, 125(13), 7502–7510.

[896] Pokhilko, P. & Krylov, A. I. (2020). Effective Hamiltonians derived from equation-of-motion coupled-cluster wave functions: Theory and application to the Hubbard and Heisenberg Hamiltonians. J. Chem. Phys., 152(9), 094108.

[897] Pollman, F. (2025). Private communication.

[898] Potirniche, I.-D., Potter, A. C., Schleier-Smith, M., Vishwanath, A., & Yao, N. Y. (2017). Floquet Symmetry-Protected Topological Phases in Cold-Atom Systems. Phys. Rev. Lett., 119(12), 123601.

[899] Qiskit contributors (2023). Qiskit: An open-source framework for quantum computing.

[900] Rakovszky, T. & Khemani, V. (2023). The physics of (good) ldpc codes i. gauging and dualities.

[901] Raussendorf, R., Browne, D. E., & Briegel, H. J. (2003). Measurement-based quantum computation on cluster states. Physical Review A, 68(2), 022312.

[902] Russomanno, A., Iemini, F., Dalmonte, M., & Fazio, R. (2017). Floquet time crystal in the lipkin-meshkov-glick model. Physical Review B, 95(21).

[903] Sachdev, S. (1992). Kagome- and triangular-lattice Heisenberg antiferromagnets: Ordering from quantum fluctuations and quantum-disordered ground states with unconfined bosonic spinons. Phys. Rev. B, 45(21), 12377–12396. Publisher: American Physical Society.

[904] Sachdev, S. (2018). Topological order, emergent gauge fields, and Fermi surface reconstruction. Rep. Prog. Phys., 82(1), 014001.

[905] Sachdev, S. & Ye, J. (1993). Gapless spin-fluid ground state in a random quantum Heisenberg magnet. Phys. Rev. Lett., 70(21), 3339–3342. Publisher: American Physical Society.

[906] Saffman, M., Walker, T. G., & Mølmer, K. (2010). Quantum information with rydberg atoms. Rev. Mod. Phys., 82, 2313–2363.

[907] Sahay, R., Lukin, M. D., & Cotler, J. (2024). Emergent Holographic Forces from Tensor Networks and Criticality.

[908] Saleh, A. M. E., Arashi, M., & Kibria, B. G. (2019). Theory of ridge regression estimation with applications. John Wiley & Sons.

[909] Samajdar, R., Ho, W. W., Pichler, H., Lukin, M. D., & Sachdev, S. (2021). Quantum phases of Rydberg atoms on a kagome lattice. Proceedings of the National Academy of Sciences, 118(4), e2015785118.

[910] Samajdar, R., Joshi, D. G., Teng, Y., & Sachdev, S. (2022). Emergent $\mathbb{Z}_2$ gauge theories and topological excitations in Rydberg atom arrays.

[911] Samajdar, R., Joshi, D. G., Teng, Y., & Sachdev, S. (2023). Emergent $\mathbb{Z}_2$ Gauge Theories and Topological Excitations in Rydberg Atom Arrays. Phys. Rev. Lett., 130, 043601.

[912] Satzinger, K., Liu, Y.-J., Smith, A., Knapp, C., Newman, M., Jones, C., Chen, Z., Quintana, C., Mi, X., Dunsworth, A., et al. (2021a). Realizing topologically ordered states on a quantum processor. Science, 374(6572), 1237–1241.

[913] Satzinger, K. J., Liu, Y.-J., Smith, A., Knapp, C., Newman, M., Jones, C., Chen, Z., Quintana, C., Mi, X., Dunsworth, A., Gidney, C., Aleiner, I., Arute, F., Arya, K., Atalaya, J., Babbush, R., Bardin, J. C., Barends, R., Basso, J., Bengtsson, A., Bilmes, A., Broughton, M., Buckley, B. B., Buell, D. A., Burkett, B., Bushnell, N., Chiaro, B., Collins, R., Courtney, W., Demura, S., Derk, A. R., Eppens, D., Erickson, C., Faoro, L., Farhi, E., Fowler, A. G., Foxen, B., Giustina, M., Greene, A., Gross, J. A., Harrigan, M. P., Harrington, S. D., Hilton, J., Hong, S., Huang, T., Huggins, W. J., Ioffe, L. B., Isakov, S. V., Jeffrey, E., Jiang, Z., Kafri, D., Kechedzhi, K., Khattar, T., Kim, S., Klimov, P. V., Korotkov, A. N., Kostritsa, F., Landhuis, D., Laptev, P., Locharla, A., Lucero, E., Martin, O., McClean, J. R., McEwen, M., Miao, K. C., Mohseni, M., Montazeri, S., Mruczkiewicz, W., Mutus, J., Naaman, O., Neeley, M., Neill, C., Niu, M. Y., O'Brien, T. E., Opremcak, A., Pató, B., Petukhov, A., Rubin, N. C., Sank, D., Shvarts, V., Strain, D., Szalay, M., Villalonga, B., White, T. C., Yao, Z., Yeh, P., Yoo, J., Zalcman, A., Neven, H., Boixo, S., Megrant, A., Chen, Y., Kelly, J., Smelyanskiy, V., Kitaev, A., Knap, M., Pollmann, F., & Roushan, P. (2021b). Realizing topologically ordered states on a quantum processor. Science, 374(6572), 1237–1241.

[914] Schindler, P. M. & Bukov, M. (2024). Counterdiabatic Driving for Periodically Driven Systems.

[915] Schleier-Smith, M. H., Leroux, I. D., & Vuletić, V. (2010). States of an Ensemble of Two-Level Atoms with Reduced Quantum Uncertainty. Phys. Rev. Lett., 104, 073604.

[916] Scholl, P., Schuler, M., Williams, H. J., Eberharter, A. A., Barredo, D.,

Schymik, K.-N., Lienhard, V., Henry, L.-P., Lang, T. C., Lahaye, T., Läuchli, A. M., & Browaeys, A. (2021a). Quantum simulation of 2D antiferromagnets with hundreds of Rydberg atoms. Nature, 595(7866), 233–238.

[917] Scholl, P., Schuler, M., Williams, H. J., Eberharter, A. A., Barredo, D., Schymik, K.-N., Lienhard, V., Henry, L.-P., Lang, T. C., Lahaye, T., Läuchli, A. M., & Browaeys, A. (2021b). Quantum simulation of 2D antiferromagnets with hundreds of Rydberg atoms. Nature, 595(7866), 233–238.

[918] Scholl, P., Shaw, A. L., Tsai, R. B.-S., Finkelstein, R., Choi, J., & Endres, M. (2023a). Erasure conversion in a high-fidelity Rydberg quantum simulator. Nature, 622(7982), 273–278.

[919] Scholl, P., Shaw, A. L., Tsai, R. B.-S., Finkelstein, R., Choi, J., & Endres, M. (2023b). Erasure conversion in a high-fidelity Rydberg quantum simulator. Nature, 622(7982), 273–278.

[920] Scholl, P., Williams, H. J., Bornet, G., Wallner, F., Barredo, D., Henriet, L., Signoles, A., Hainaut, C., Franz, T., Geier, S., Tebben, A., Salzinger, A., Zürn, G., Lahaye, T., Weidemüller, M., & Browaeys, A. (2022a). Microwave Engineering of Programmable *XXZ* Hamiltonians in Arrays of Rydberg Atoms. PRX Quantum, 3, 020303.

[921] Scholl, P., Williams, H. J., Bornet, G., Wallner, F., Barredo, D., Henriet, L., Signoles, A., Hainaut, C., Franz, T., Geier, S., Tebben, A., Salzinger, A., Zürn, G., Lahaye, T., Weidemüller, M., & Browaeys, A. (2022b). Microwave Engineering of Programmable XXZ Hamiltonians in Arrays of Rydberg Atoms. PRX Quantum, 3(2), 020303.

[922] Schollwöck, U. (2011). The density-matrix renormalization group in the age of matrix product states. Annals of Physics, 326(1), 96–192.

[923] Schreiber, M., Hodgman, S. S., Bordia, P., Lüschen, H. P., Fischer, M. H., Vosk, R., Altman, E., Schneider, U., & Bloch, I. (2015). Observation of many-body localization of interacting fermions in a quasirandom optical lattice. Science, 349(6250), 842–845.

[924] Schuch, N., Pérez-García, D., & Cirac, I. (2011). Classifying quantum phases using matrix product states and projected entangled pair states. Phys. Rev. B, 84, 165139.

[925] Schuch, N., Poilblanc, D., Cirac, J. I., & Pérez-García, D. (2012). Resonating valence bond states in the PEPS formalism. Phys. Rev. B, 86(11), 115108. Publisher: American Physical Society.

[926] Schuch, N., Wolf, M. M., Verstraete, F., & Cirac, J. I. (2007). Computational complexity of projected entangled pair states. Phys. Rev. Lett., 98, 140506.

[927] Schuckert, A., Bohrdt, A., Crane, E., & Knap, M. (2022). Probing finite-temperature observables in quantum simulators with short-time dynamics. arXiv:2206.01756 [cond-mat, physics:quant-ph].

[928] Schuckert, A., Crane, E., Gorshkov, A. V., Hafezi, M., & Gullans, M. J. (2024). Fermion-qubit fault-tolerant quantum computing. _eprint: 2411.08955.

[929] Schweizer, C., Grusdt, F., Berngruber, M., Barbiero, L., Demler, E., Goldman, N., Bloch, I., & Aidelsburger, M. (2019a). Floquet approach to $\mathbb{Z}_2$ lattice gauge theories with ultracold atoms in optical lattices. Nature Physics, 15(11), 1168–1173.

[930] Schweizer, C., Grusdt, F., Berngruber, M., Barbiero, L., Demler, E., Goldman, N., Bloch, I., & Aidelsburger, M. (2019b). Floquet approach to $\mathbb{Z}_2$ lattice gauge theories with ultracold atoms in optical lattices. Nat. Phys., 15(11), 1168–1173.

[931] Sels, D. & Polkovnikov, A. (2017a). Minimizing irreversible losses in quantum systems by local counterdiabatic driving. Proceedings of the National Academy of Sciences, 114(20), E3909–E3916.

[932] Sels, D. & Polkovnikov, A. (2017b). Minimizing irreversible losses in quantum systems by local counterdiabatic driving. Proceedings of the National Academy of Sciences, 114(20), E3909–E3916.

[933] Semeghini, G., Levine, H., Keesling, A., Ebadi, S., Wang, T. T., Bluvstein, D., Verresen, R., Pichler, H., Kalinowski, M., Samajdar, R., et al. (2021a). Probing topological spin liquids on a programmable quantum simulator. Science, 374(6572), 1242–1247.

[934] Semeghini, G., Levine, H., Keesling, A., Ebadi, S., Wang, T. T., Bluvstein, D., Verresen, R., Pichler, H., Kalinowski, M., Samajdar, R., Omran, A., Sachdev, S., Vishwanath, A., Greiner, M., Vuletić, V., & Lukin, M. D. (2021b). Probing topological spin liquids on a programmable quantum simulator. Science, 374(6572), 1242–1247.

[935] Semeghini, G., Levine, H., Keesling, A., Ebadi, S., Wang, T. T., Bluvstein, D., Verresen, R., Pichler, H., Kalinowski, M., Samajdar, R., Omran, A., Sachdev, S., Vishwanath, A., Greiner, M., Vuletić, V., & Lukin, M. D. (2021c). Probing topological spin liquids on a programmable quantum simulator. Science, 374(6572), 1242–1247.

[936] Semeghini, G., Levine, H., Keesling, A., Ebadi, S., Wang, T. T., Bluvstein, D., Verresen, R., Pichler, H., Kalinowski, M., Samajdar, R., Omran, A., Sachdev, S., Vishwanath, A., Greiner, M., Vuletić, V., & Lukin, M. D. (2021d). Probing topological spin liquids on a programmable quantum simulator. Science, 374(6572), 1242–1247.

[937] Serbyn, M., Abanin, D. A., & Papić, Z. (2020). Quantum Many-Body Scars and Weak Breaking of Ergodicity. arXiv e-prints, (pp. arXiv:2011.09486).

[938] Shaik, S., Hirao, H., & Kumar, D. (2007). Reactivity of high-valent iron–oxo species in enzymes and synthetic reagents: a tale of many states. Acc. Chem. Res., 40(7), 532–542.

[939] Shao, H. J., Wang, Y. X., Zhu, D. Z., Zhu, Y. S., Sun, H. N., Chen, S. Y., Zhang, C., Fan, Z. J., Deng, Y., Yao, X. C., Chen, Y. A., & Pan, J. W. (2024). Antiferromagnetic phase transition in a 3d fermionic hubbard model. Nature, 632, 267–272.

[940] Sharma, S., Sivalingam, K., Neese, F., & Chan, G. K.-L. (2014). Low-energy spectrum of iron–sulfur clusters directly from many-particle quantum mechanics. Nat. Chem., 6(10), 927–933.

[941] Shee, J., Loipersberger, M., Hait, D., Lee, J., & Head-Gordon, M. (2021). Revealing the nature of electron correlation in transition metal complexes with symmetry breaking and chemical intuition. J. Chem. Phys., 154(19), 194109.

[942] Sheng, C., He, X., Xu, P., Guo, R., Wang, K., Xiong, Z., Liu, M., Wang, J., & Zhan, M. (2018a). High-Fidelity Single-Qubit Gates on Neutral Atoms in a

Two-Dimensional Magic-Intensity Optical Dipole Trap Array. Phys. Rev. Lett., 121(24), 240501.

[943] Sheng, C., He, X., Xu, P., Guo, R., Wang, K., Xiong, Z., Liu, M., Wang, J., & Zhan, M. (2018b). High-fidelity single-qubit gates on neutral atoms in a two-dimensional magic-intensity optical dipole trap array. Phys. Rev. Lett., 121, 240501.

[944] Shi, T., Demler, E., & Cirac, J. I. (2018). Variational study of fermionic and bosonic systems with non-Gaussian states: Theory and applications. Ann. Phys., 390, 245–302.

[945] Shinjo, K., Sota, S., & Tohyama, T. (2015). Density-matrix renormalization group study of the extended Kitaev-Heisenberg model. Phys. Rev. B, 91(5), 054401.

[946] Shiraishi, N. & Mori, T. (2017). Systematic construction of counterexamples to the eigenstate thermalization hypothesis. Phys. Rev. Lett., 119, 030601.

[947] Singh, K., Anand, S., Pocklington, A., Kemp, J. T., & Bernien, H. (2022). Dual-Element, Two-Dimensional Atom Array with Continuous-Mode Operation. Phys. Rev. X, 12(1), 011040.

[948] Somma, R. D. (2019). Quantum eigenvalue estimation via time series analysis. New J. Phys., 21(12), 123025.

[949] Sørensen, A. & Mølmer, K. (1999). Quantum computation with ions in thermal motion. Phys. Rev. Lett., 82, 1971–1974.

[950] Spar, B. M., Guardado-Sanchez, E., Chi, S., Yan, Z. Z., & Bakr, W. S. (2022). Realization of a Fermi-Hubbard Optical Tweezer Array. Phys. Rev. Lett., 128(22), 223202.

[951] Stricker, R., Vodola, D., Erhard, A., Postler, L., Meth, M., Ringbauer, M., Schindler, P., Monz, T., Müller, M., & Blatt, R. (2020). Experimental deterministic correction of qubit loss. Nature, 585(7824), 207–210.

[952] Sun, B.-Y., Goldman, N., Aidelsburger, M., & Bukov, M. (2022). Engineering and probing non-Abelian chiral spin liquids using periodically driven ultracold atoms.

[953] Surace, F. M., Mazza, P. P., Giudici, G., Lerose, A., Gambassi, A., & Dalmonte, M. (2020). Lattice Gauge Theories and String Dynamics in Rydberg Atom Quantum Simulators. Phys. Rev. X, 10, 021041.

[954] Szabo, A. & Ostlund, N. S. (2012). Modern quantum chemistry: introduction to advanced electronic structure theory. Courier Corporation.

[955] Tabares, C., Kokail, C., Zoller, P., González-Cuadra, D., & González-Tudela, A. (2025). Programming optical-lattice Fermi-Hubbard quantum simulators. _eprint: 2502.05067.

[956] Tagliacozzo, L., Celi, A., Zamora, A., & Lewenstein, M. (2013). Optical Abelian lattice gauge theories. Annals of Physics, 330, 160–191.

[957] Takagi, H., Takayama, T., Jackeli, G., Khaliullin, G., & Nagler, S. E. (2019a). Concept and realization of Kitaev quantum spin liquids. Nat. Rev. Phys., 1(4), 264–280.

[958] Takagi, H., Takayama, T., Jackeli, G., Khaliullin, G., & Nagler, S. E. (2019b). Concept and realization of Kitaev quantum spin liquids. Nat. Rev. Phys., 1(4), 264–280.

[959] Tarabunga, P. S., Surace, F. M., Andreoni, R., Angelone, A., & Dalmonte, M. (2022a). Gauge-Theoretic Origin of Rydberg Quantum Spin Liquids. Phys. Rev. Lett., 129, 195301.

[960] Tarabunga, P. S., Surace, F. M., Andreoni, R., Angelone, A., & Dalmonte, M. (2022b). Gauge-theoretic origin of rydberg quantum spin liquids.

[961] Tazhigulov, R. N., Sun, S.-N., Haghshenas, R., Zhai, H., Tan, A. T., Rubin, N. C., Babbush, R., Minnich, A. J., & Chan, G. K.-L. (2022). Simulating Models of Challenging Correlated Molecules and Materials on the Sycamore Quantum Processor. PRX Quantum, 3(4), 040318.

[962] Tepaske, M. S. J., Luitz, D. J., & Hahn, D. (2023). Optimal compression of constrained quantum time evolution. arXiv:2311.06347 [cond-mat, physics:quant-ph].

[963] Terhal, B. M. (2015). Quantum error correction for quantum memories. Rev. Mod. Phys., 87, 307–346.

[964] Tóth, G. (2012). Multipartite entanglement and high-precision metrology. Phys. Rev. A, 85, 022322.

[965] Turner, C. J., Desaules, J.-Y., Bull, K., & Papić, Z. (2020). Correspondence principle for many-body scars in ultracold Rydberg atoms.

[966] Turner, C. J., Michailidis, A. A., Abanin, D. A., Serbyn, M., & Papić, Z. (2018a). Weak ergodicity breaking from quantum many-body scars. Nat. Phys., 14, 745.

[967] Turner, C. J., Michailidis, A. A., Abanin, D. A., Serbyn, M., & Papić, Z. (2018b). Weak ergodicity breaking from quantum many-body scars. Nature Physics, 14(7), 745–749.

[968] Turner, C. J., Michailidis, A. A., Abanin, D. A., Serbyn, M., & Papić, Z. (2018c). Quantum scarred eigenstates in a Rydberg atom chain: Entanglement, breakdown of thermalization, and stability to perturbations. Phys. Rev. B, 98, 155134.

[969] Urban, E., Johnson, T. A., Henage, T., Isenhower, L., Yavuz, D. D., Walker, T. G., & Saffman, M. (2009). Observation of Rydberg blockade between two atoms. Nat. Phys., 5(2), 110–114.

[970] Van Den Nest, M., Dehaene, J., & De Moor, B. (2004). Graphical description of the action of local Clifford transformations on graph states. Physical Review A, 69(2), 022316.

[971] Verresen, R., Lukin, M. D., & Vishwanath, A. (2021a). Prediction of Toric Code Topological Order from Rydberg Blockade. Phys. Rev. X, 11, 031005.

[972] Verresen, R., Lukin, M. D., & Vishwanath, A. (2021b). Prediction of Toric Code Topological Order from Rydberg Blockade. Phys. Rev. X, 11, 031005.

[973] Verresen, R., Lukin, M. D., & Vishwanath, A. (2021c). Prediction of toric code topological order from Rydberg blockade. Phys. Rev. X, 11, 031005.

[974] Verresen, R., Tantivasadakarn, N., & Vishwanath, A. (2021d). Efficiently preparing Schrödinger's cat, fractons and non-abelian topological order in quantum devices.

[975] Verresen, R. & Vishwanath, A. (2022a). Unifying Kitaev Magnets, Kagomé Dimer Models, and Ruby Rydberg Spin Liquids. Phys. Rev. X, 12, 041029.

[976] Verresen, R. & Vishwanath, A. (2022b). Unifying Kitaev magnets, kagome dimer models and ruby Rydberg spin liquids.

[977] Verresen, R., Vishwanath, A., & Pollmann, F. (2019). Stable Luttinger liquids and emergent $U(1)$ symmetry in constrained quantum chains.

[978] Verstraete, F. & Cirac, J. I. (2005). Mapping local Hamiltonians of fermions to local Hamiltonians of spins. J. Stat. Mech.: Theory Exp., 2005(09), P09012.

[979] Verstraete, F., Cirac, J. I., & Latorre, J. I. (2009). Quantum circuits for strongly correlated quantum systems. Phys. Rev. A, 79(3), 032316. Publisher: American Physical Society.

[980] Verstraete, F., Murg, V., & Cirac, J. I. (2008). Matrix product states, projected entangled pair states, and variational renormalization group methods for quantum spin systems. Advances in Physics, 57(2), 143–224.

[981] Vidal, G. (2008). Class of quantum many-body states that can be efficiently simulated. Phys. Rev. Lett., 101, 110501.

[982] Villa, L., Despres, J., & Sanchez-Palencia, L. (2019). Unraveling the excitation spectrum of many-body systems from quantum quenches. Phys. Rev. A, 100(6), 063632.

[983] von Keyserlingk, C. W., Khemani, V., & Sondhi, S. L. (2016). Absolute stability and spatiotemporal long-range order in floquet systems. Physical Review B, 94(8).

[984] Vorwerk, C., Sheng, N., Govoni, M., Huang, B., & Galli, G. (2022). Quantum embedding theories to simulate condensed systems on quantum computers. Nature Computational Science, 2(7), 424–432.

[985] Wan, K., Berta, M., & Campbell, E. T. (2022). Randomized Quantum Algorithm for Statistical Phase Estimation. Physical Review Letters, 129(3), 030503.

[986] Wan, K., Huggins, W. J., Lee, J., & Babbush, R. (2023). Matchgate Shadows for Fermionic Quantum Simulation. Communications in Mathematical Physics, 404(2), 629–700. ISBN: 1432-0916.

[987] Wang, C., Harrington, J., & Preskill, J. (2003). Confinement-higgs transition in a disordered gauge theory and the accuracy threshold for quantum memory. Annals of Physics, 303(1), 31–58.

[988] Wang, Z. (2010). Topological quantum computation. Number 112. American Mathematical Soc.

[989] Wang, Z., Ge, Z.-Y., Xiang, Z., Song, X., Huang, R.-Z., Song, P., Guo, X.-Y., Su, L., Xu, K., Zheng, D., & Fan, H. (2022). Observation of emergent $\mathbb{Z}_2$ gauge invariance in a superconducting circuit. Phys. Rev. Res., 4, L022060.

[990] Waugh, J. S., Huber, L. M., & Haeberlen, U. (1968). Approach to High-Resolution nmr in Solids. Phys. Rev. Lett., 20, 180–182.

[991] Wecker, D., Hastings, M. B., Wiebe, N., Clark, B. K., Nayak, C., & Troyer, M. (2015). Solving strongly correlated electron models on a quantum computer. Physical Review A, 92(6), 062318.

[992] Wei, K. X., Ramanathan, C., & Cappellaro, P. (2018). Exploring Localization in Nuclear Spin Chains. Phys. Rev. Lett., 120, 070501.

[993] Weidinger, S. A. (2018). Non-equilibrium Field Theory of Condensed Matter Systems – Periodic Driving and Quantum Quenches. Phd thesis, Technischen Universität München.

[994] Wen, X.-G. (2007). Quantum Field Theory of Many-Body Systems: From the Origin of Sound to an Origin of Light and Electrons. Oxford University Press.

[995] Wen, X.-G. (2017). Colloquium: Zoo of quantum-topological phases of matter. Rev. Mod. Phys., 89(4), 041004. Publisher: American Physical Society.

[996] Wiese, U.-J. (2013). Ultracold quantum gases and lattice systems: quantum simulation of lattice gauge theories. Annalen der Physik, 525(10-11), 777–796.

[997] Wilczek (1992). Disassembling anyons. Phys. Rev. Lett., 69(1), 132–135.

[998] Wilson, K. G. (1974). Confinement of quarks. Physical Review D, 10(8), 2445–2459.

[999] Woodruff, D. N., Winpenny, R. E. P., & Lay, R. A. (2013). Lanthanide Single-Molecule Magnets. Chem. Rev., 113, 5110.

[1000] Wu, T.-Y., Kumar, A., Mejia, F. G., & Weiss, D. S. (2019). Stern-Gerlach detection of neutral atom qubits in a state dependent optical lattice. Nat. Phys., 15(6), 538–542.

[1001] Xu, C., Feng, J., Kawamura, M., Yamaji, Y., Nahas, Y., Prokhorenko, S., Qi, Y., Xiang, H., & Bellaiche, L. (2020a). Possible Kitaev Quantum Spin Liquid State in 2D Materials with S = 3 / 2. Phys. Rev. Lett., 124(8), 087205.

[1002] Xu, H. & Taylor, J. M. (2011). Developing a robust approach to implementing non-Abelian anyons and topological quantum computing in a modified Kitaev honeycomb lattice model.

[1003] Xu, M., Kendrick, L. H., Kale, A., Gang, Y., Ji, G., Scalettar, R. T., Lebrat, M., & Greiner, M. (2023). Frustration- and doping-induced magnetism in a fermi–hubbard simulator. Nature, 620, 971–976.

[1004] Xu, Q., Zhou, H., Zheng, G., Bluvstein, D., Ataides, J. P. B., Lukin, M. D., & Jiang, L. (2024). Fast and Parallelizable Logical Computation with Homological Product Codes.

[1005] Xu, S., Susskind, L., Su, Y., & Swingle, B. (2020b). A Sparse Model of Quantum Holography. _eprint: 2008.02303.

[1006] Yang, B., Sun, H., Ott, R., Wang, H.-Y., Zache, T. V., Halimeh, J. C., Yuan, Z.-S., Hauke, P., & Pan, J.-W. (2020). Observation of gauge invariance in a 71-site Bose–Hubbard quantum simulator. Nature, 587(7834), 392–396.

[1007] Yao, N., Potter, A., Potirniche, I.-D., & Vishwanath, A. (2017a). Discrete time crystals: Rigidity, criticality, and realizations. Physical Review Letters, 118(3).

[1008] Yao, N. Y., Potter, A. C., Potirniche, I.-D., & Vishwanath, A. (2017b). Discrete Time Crystals: Rigidity, Criticality, and Realizations. Phys. Rev. Lett., 118, 030401.

[1009] Yao, N. Y., Potter, A. C., Potirniche, I.-D., & Vishwanath, A. (2017c). Discrete Time Crystals: Rigidity, Criticality, and Realizations. Phys. Rev. Lett., 118(3), 030401.

[1010] Yarloo, H., Emami Kopaei, A., & Langari, A. (2020). Homogeneous floquet time crystal from weak ergodicity breaking. Phys. Rev. B, 102, 224309.

[1011] Young, A. W., Eckner, W. J., Schine, N., Childs, A. M., & Kaufman, A. M. (2022). Tweezer-programmable 2D quantum walks in a Hubbard-regime lattice. Science, 377(6608), 885–889.

[1012] Zache, T. V., González-Cuadra, D., & Zoller, P. (2023a). Fermion-qudit quantum processors for simulating lattice gauge theories with matter. Quantum, 7, 1140.

[1013] Zache, T. V., González-Cuadra, D., & Zoller, P. (2023b). Fermion-qudit quantum processors for simulating lattice gauge theories with matter. Quantum, 7, 1140. Publisher: Verein zur Förderung des Open Access Publizierens in den Quantenwissenschaften.

[1014] Zeng, Z., Giudici, G., & Pichler, H. (2024). Quantum dimer models with Rydberg gadgets.

[1015] Zhang, J., Hess, P. W., Kyprianidis, A., Becker, P., Lee, A., Smith, J., Pagano, G., Potirniche, I. D., Potter, A. C., Vishwanath, A., Yao, N. Y., & Monroe, C. (2017). Observation of a discrete time crystal. Nature, 543(7644), 217–220.

[1016] Zhang, S.-S., Halász, G. B., & Batista, C. D. (2022). Theory of the Kitaev model in a [111] magnetic field. Nat. Commun., 13(1), 399.

[1017] Zhou, H., Choi, J., Choi, S., Landig, R., Douglas, A. M., Isoya, J., Jelezko, F., Onoda, S., Sumiya, H., Cappellaro, P., Knowles, H. S., Park, H., & Lukin, M. D. (2020). Quantum Metrology with Strongly Interacting Spin Systems. Phys. Rev. X, 10, 031003.

[1018] Zhou, H., Martin, L. S., Tyler, M., Makarova, O., Leitao, N., Park, H., & Lukin, M. D. (2023). Robust Higher-Order Hamiltonian Engineering for Quantum Sensing with Strongly Interacting Systems. Phys. Rev. Lett., 131, 220803.

[1019] Zhou, H., Zhao, C., Cain, M., Bluvstein, D., Duckering, C., Hu, H.-Y., Wang, S.-T., Kubica, A., & Lukin, M. D. (2024). Algorithmic Fault Tolerance for Fast Quantum Computing.

[1020] Zhu, G., Lavasani, A., & Barkeshli, M. (2020). Universal logical gates on topologically encoded qubits via constant-depth unitary circuits. Phys. Rev. Lett., 125, 050502.

[1021] Zhu, G.-Y. & Zhang, G.-M. (2019). Gapless coulomb state emerging from a self-dual topological tensor-network state. Phys. Rev. Lett., 122, 176401.

[1022] Zintchenko, I. & Wiebe, N. (2016). Randomized gap and amplitude estimation. Physical Review A, 93(6), 062306. arXiv:1603.03672 [quant-ph].

[1023] Znidaric, M. (2020). Weak Integrability Breaking: Chaos with Integrability Signature in Coherent Diffusion. Phys. Rev. Lett., 125, 180605.

[1024] Zohar, E., Cirac, J. I., & Reznik, B. (2013). Simulating (2+1)-Dimensional Lattice QED with Dynamical Matter Using Ultracold Atoms. Phys. Rev. Lett., 110, 055302.

[1025] Zohar, E., Cirac, J. I., & Reznik, B. (2015). Quantum simulations of lattice gauge theories using ultracold atoms in optical lattices. Reports on Progress in Physics, 79(1), 014401.

[1026] Zohar, E., Farace, A., Reznik, B., & Cirac, J. I. (2017). Digital Quantum Simulation of Z2 Lattice Gauge Theories with Dynamical Fermionic Matter. Phys. Rev. Lett., 118(7), 070501.

References

[sup] See supplemental online material.

[SOM] See supplemental online material, which also includes references[740,613,966,844,570,968,902,518,658,702,706,871].

[516] Abanin, D., De Roeck, W., Ho, W. W., & Huveneers, F. (2017a). A Rigorous Theory of Many-Body Prethermalization for Periodically Driven and Closed Quantum Systems. Communications in Mathematical Physics, 354(3), 809–827.

[517] Abanin, D., De Roeck, W., Ho, W. W., & Huveneers, F. (2017b). A Rigorous Theory of Many-Body Prethermalization for Periodically Driven and Closed Quantum Systems. Communications in Mathematical Physics, 354(3), 809–827.

[518] Abanin, D., De Roeck, W., Ho, W. W., & Huveneers, F. (2017c). A rigorous theory of many-body prethermalization for periodically driven and closed quantum systems. Communications in Mathematical Physics, 354(3), 809–827.

[519] Abanin, D. A., Altman, E., Bloch, I., & Serbyn, M. (2019). Colloquium: Many-body localization, thermalization, and entanglement. Rev. Mod. Phys., 91, 021001.

[520] Abanin, D. A., De Roeck, W., Ho, W. W., & Huveneers, F. (2017d). Effective Hamiltonians, prethermalization, and slow energy absorption in periodically driven many-body systems. Phys. Rev. B, 95(1), 014112.

[521] Abanin, D. A., De Roeck, W., Ho, W. W., & Huveneers, F. m. c. (2017e). Effective Hamiltonians, prethermalization, and slow energy absorption in periodically driven many-body systems. Phys. Rev. B, 95, 014112.

[522] Abanin, D. A., De Roeck, W., Ho, W. W., & Huveneers, F. m. c. (2017f). Effective Hamiltonians, prethermalization, and slow energy absorption in periodically driven many-body systems. Phys. Rev. B, 95, 014112.

[523] Abanin, D. A., De Roeck, W., & Huveneers, F. (2015). Exponentially Slow Heating in Periodically Driven Many-Body Systems. Phys. Rev. Lett., 115, 256803.

[524] Abrams, D. S. & Lloyd, S. (1997). Simulation of Many-Body Fermi Systems on a Universal Quantum Computer. Phys. Rev. Lett., 79(13), 2586–2589. Publisher: American Physical Society.

[525] Ahn, C., Cavalleri, A., Georges, A., Ismail-Beigi, S., Millis, A. J., & Triscone, J.-M. (2021). Designing and controlling the properties of transition metal oxide quantum materials. Nat. Mater., 20(11), 1462–1468.

[526] Aidelsburger, M., Atala, M., Lohse, M., Barreiro, J. T., Paredes, B., & Bloch, I. (2013). Realization of the Hofstadter Hamiltonian with Ultracold Atoms in Optical Lattices. Phys. Rev. Lett., 111, 185301.

[527] Aidelsburger, M., Barbiero, L., Bermudez, A., Chanda, T., Dauphin, A., González-Cuadra, D., Grzybowski, P. R., Hands, S., Jendrzejewski, F., Jünemann, J., Juzeliūnas, G., Kasper, V., Piga, A., Ran, S.-J., Rizzi, M., Sierra, G., Tagliacozzo, L., Tirrito, E., Zache, T. V., Zakrzewski, J., Zohar, E., & Lewenstein, M. (2022). Cold atoms meet lattice gauge theory. Philosophical Transactions of the Royal Society A, 380(2216), 20210064.

[528] Aidelsburger, M., Lohse, M., Schweizer, C., Atala, M., Barreiro, J. T., Nascimbène, S., Cooper, N. R., Bloch, I., & Goldman, N. (2015). Measuring the Chern number of Hofstadter bands with ultracold bosonic atoms. Nat. Phys., 11(2), 162–166.

[529] Alcaraz, F. C. & Bariev, R. Z. (1999). An Exactly Solvable Constrained XXZ Chain.

[530] Alessio, M. & Krylov, A. I. (2021). Equation-of-Motion Coupled-Cluster Protocol for Calculating Magnetic Properties: Theory and Applications to Single-Molecule Magnets. J. Chem. Theory Comput., 17(7), 4225–4241.

[531] Alexeev, Y., Bacon, D., Brown, K. R., Calderbank, R., Carr, L. D., Chong, F. T., DeMarco, B., Englund, D., Farhi, E., Fefferman, B., Gorshkov, A. V., Houck, A., Kim, J., Kimmel, S., Lange, M., Lloyd, S., Lukin, M. D., Maslov, D.,

Maunz, P., Monroe, C., Preskill, J., Roetteler, M., Savage, M. J., & Thompson, J. (2021). Quantum Computer Systems for Scientific Discovery. PRX Quantum, 2(1), 017001.

[532] Alicea, J. (2012). New directions in the pursuit of Majorana fermions in solid state systems. Rep. Prog. Phys., 75(7), 076501.

[533] Altman, E., Brown, K. R., Carleo, G., Carr, L. D., Demler, E., Chin, C., DeMarco, B., Economou, S. E., Eriksson, M. A., Fu, K.-M. C., Greiner, M., Hazzard, K. R., Hulet, R. G., Kollár, A. J., Lev, B. L., Lukin, M. D., Ma, R., Mi, X., Misra, S., Monroe, C., Murch, K., Nazario, Z., Ni, K.-K., Potter, A. C., Roushan, P., Saffman, M., Schleier-Smith, M., Siddiqi, I., Simmonds, R., Singh, M., Spielman, I., Temme, K., Weiss, D. S., Vučković, J., Vuletić, V., Ye, J., & Zwierlein, M. (2021). Quantum Simulators: Architectures and Opportunities. PRX Quantum, 2(1), 017003.

[534] Andersen, T. I., Lensky, Y. D., Kechedzhi, K., Drozdov, I., Bengtsson, A., Hong, S., Morvan, A., Mi, X., Opremcak, A., Acharya, R., Allen, R., Ansmann, M., Arute, F., Arya, K., Asfaw, A., Atalaya, J., Babbush, R., Bacon, D., Bardin, J. C., Bortoli, G., Bourassa, A., Bovaird, J., Brill, L., Broughton, M., Buckley, B. B., Buell, D. A., Burger, T., Burkett, B., Bushnell, N., Chen, Z., Chiaro, B., Chik, D., Chou, C., Cogan, J., Collins, R., Conner, P., Courtney, W., Crook, A. L., Curtin, B., Debroy, D. M., Barba, A. D. T., Demura, S., Dunsworth, A., Eppens, D., Erickson, C., Faoro, L., Farhi, E., Fatemi, R., Ferreira, V. S., Burgos, L. F., Forati, E., Fowler, A. G., Foxen, B., Giang, W., Gidney, C., Gilboa, D., Giustina, M., Gosula, R., Dau, A. G., Gross, J. A., Habegger, S., Hamilton, M. C., Hansen, M., Harrigan, M. P., Harrington, S. D., Heu, P., Hilton, J., Hoffmann, M. R., Huang, T., Huff, A., Huggins, W. J., Ioffe, L. B., Isakov, S. V., Iveland, J., Jeffrey, E., Jiang, Z., Jones, C., Juhas, P., Kafri, D., Khattar, T., Khezri, M., Kieferová, M., Kim, S., Kitaev, A., Klimov, P. V., Klots, A. R., Korotkov, A. N., Kostritsa, F., Kreikebaum, J. M., Landhuis, D., Laptev, P., Lau, K.-M., Laws, L., Lee, J., Lee, K., Lester, B. J., Lill, A., Liu, W., Locharla, A., Lucero, E., Malone, F. D., Martin, O., McClean, J. R., McCourt, T., McEwen, M., Miao, K. C., Mieszala, A., Mohseni, M., Montazeri, S., Mount, E., Movassagh, R., Mruczkiewicz, W., Naaman, O., Neeley, M., Neill, C., Nersisyan, A., Newman, M., Ng, J. H., Nguyen, A., Nguyen, M., Niu, M. Y., O'Brien, T. E.,

Omonije, S., Petukhov, A., Potter, R., Pryadko, L. P., Quintana, C., Rocque, C., Rubin, N. C., Saei, N., Sank, D., Sankaragomathi, K., Satzinger, K. J., Schurkus, H. F., Schuster, C., Shearn, M. J., Shorter, A., Shutty, N., Shvarts, V., Skruzny, J., Smith, W. C., Somma, R., Sterling, G., Strain, D., Szalay, M., Torres, A., Vidal, G., Villalonga, B., Heidweiller, C. V., White, T., Woo, B. W. K., Xing, C., Yao, Z. J., Yeh, P., Yoo, J., Young, G., Zalcman, A., Zhang, Y., Zhu, N., Zobrist, N., Neven, H., Boixo, S., Megrant, A., Kelly, J., Chen, Y., Smelyanskiy, V., Kim, E.-A., Aleiner, I., & Roushan, P. (2022). Observation of non-Abelian exchange statistics on a superconducting processor.

[535] Andersen, T. I., Lensky, Y. D., Kechedzhi, K., Drozdov, I. K., Bengtsson, A., Hong, S., Morvan, A., Mi, X., Opremcak, A., Acharya, R., Allen, R., Ansmann, M., Arute, F., Arya, K., Asfaw, A., Atalaya, J., Babbush, R., Bacon, D., Bardin, J. C., Bortoli, G., Bourassa, A., Bovaird, J., Brill, L., Broughton, M., Buckley, B. B., Buell, D. A., Burger, T., Burkett, B., Bushnell, N., Chen, Z., Chiaro, B., Chik, D., Chou, C., Cogan, J., Collins, R., Conner, P., Courtney, W., Crook, A. L., Curtin, B., Debroy, D. M., Del Toro Barba, A., Demura, S., Dunsworth, A., Eppens, D., Erickson, C., Faoro, L., Farhi, E., Fatemi, R., Ferreira, V. S., Burgos, L. F., Forati, E., Fowler, A. G., Foxen, B., Giang, W., Gidney, C., Gilboa, D., Giustina, M., Gosula, R., Dau, A. G., Gross, J. A., Habegger, S., Hamilton, M. C., Hansen, M., Harrigan, M. P., Harrington, S. D., Heu, P., Hilton, J., Hoffmann, M. R., Huang, T., Huff, A., Huggins, W. J., Ioffe, L. B., Isakov, S. V., Iveland, J., Jeffrey, E., Jiang, Z., Jones, C., Juhas, P., Kafri, D., Khattar, T., Khezri, M., Kieferová, M., Kim, S., Kitaev, A., Klimov, P. V., Klots, A. R., Korotkov, A. N., Kostritsa, F., Kreikebaum, J. M., Landhuis, D., Laptev, P., Lau, K.-M., Laws, L., Lee, J., Lee, K. W., Lester, B. J., Lill, A. T., Liu, W., Locharla, A., Lucero, E., Malone, F. D., Martin, O., McClean, J. R., McCourt, T., McEwen, M., Miao, K. C., Mieszala, A., Mohseni, M., Montazeri, S., Mount, E., Movassagh, R., Mruczkiewicz, W., Naaman, O., Neeley, M., Neill, C., Nersisyan, A., Newman, M., Ng, J. H., Nguyen, A., Nguyen, M., Niu, M. Y., O'Brien, T. E., Omonije, S., Petukhov, A., Potter, R., Pryadko, L. P., Quintana, C., Rocque, C., Rubin, N. C., Saei, N., Sank, D., Sankaragomathi, K., Satzinger, K. J., Schurkus, H. F., Schuster, C., Shearn, M. J., Shorter, A., Shutty, N., Shvarts, V., Skruzny, J., Smith, W. C., Somma, R., Sterling, G.,

Strain, D., Szalay, M., Torres, A., Vidal, G., Villalonga, B., Heidweiller, C. V., White, T., Woo, B. W. K., Xing, C., Yao, Z. J., Yeh, P., Yoo, J., Young, G., Zalcman, A., Zhang, Y., Zhu, N., Zobrist, N., Neven, H., Boixo, S., Megrant, A., Kelly, J., Chen, Y., Smelyanskiy, V., Kim, E.-A., Aleiner, I., Roushan, P., & Google Quantum AI and Collaborators (2023). Non-Abelian braiding of graph vertices in a superconducting processor. Nature, 618(7964), 264–269.

[536] Anderson, P. (1973). Resonating valence bonds: A new kind of insulator? Mater. Res. Bull., 8(2), 153–160.

[537] Anshu, A., Breuckmann, N. P., & Nirkhe, C. (2023). NLTS Hamiltonians from good quantum codes. In Proceedings of the 55th Annual ACM Symposium on Theory of Computing (pp. 1090–1096).

[538] Aoto, Y. A., de Lima Batista, A. P., Kohn, A., & de Oliveira-Filho, A. G. (2017). How to arrive at accurate benchmark values for transition metal compounds: Computation or experiment? J. Chem. Theory Comput., 13(11), 5291–5316.

[539] Arute, F., Arya, K., Babbush, R., Bacon, D., Bardin, J. C., Barends, R., Boixo, S., Broughton, M., Buckley, B. B., Buell, D. A., Burkett, B., Bushnell, N., Chen, Y., Chen, Z., Chiaro, B., Collins, R., Courtney, W., Demura, S., Dunsworth, A., Farhi, E., Fowler, A., Foxen, B., Gidney, C., Giustina, M., Graff, R., Habegger, S., Harrigan, M. P., Ho, A., Hong, S., Huang, T., Huggins, W. J., Ioffe, L., Isakov, S. V., Jeffrey, E., Jiang, Z., Jones, C., Kafri, D., Kechedzhi, K., Kelly, J., Kim, S., Klimov, P. V., Korotkov, A., Kostritsa, F., Landhuis, D., Laptev, P., Lindmark, M., Lucero, E., Martin, O., Martinis, J. M., McClean, J. R., McEwen, M., Megrant, A., Mi, X., Mohseni, M., Mruczkiewicz, W., Mutus, J., Naaman, O., Neeley, M., Neill, C., Neven, H., Niu, M. Y., O'Brien, T. E., Ostby, E., Petukhov, A., Putterman, H., Quintana, C., Roushan, P., Rubin, N. C., Sank, D., Satzinger, K. J., Smelyanskiy, V., Strain, D., Sung, K. J., Szalay, M., Takeshita, T. Y., Vainsencher, A., White, T., Wiebe, N., Yao, Z. J., Yeh, P., & Zalcman, A. (2020). Hartree-Fock on a superconducting qubit quantum computer. Science, 369(6507), 1084–1089.

[540] Askerka, M., Brudvig, G. W., & Batista, V. S. (2017). The o2-evolving complex of photosystem ii: Recent insights from quantum mechanics/molecular mechan-

ics (qm/mm), extended x-ray absorption fine structure (exafs), and femtosecond x-ray crystallography data. Acc. Chem. Res., 50(1), 41–48.

[541] Auerbach, A. (1998). Interacting electrons and quantum magnetism. Springer Science & Business Media.

[542] Babbush, R., Wiebe, N., McClean, J., McClain, J., Neven, H., & Chan, G. K.-L. (2018). Low-Depth Quantum Simulation of Materials. Physical Review X, 8(1), 011044.

[543] Bakalov, B. & Kirillov, A. A. (2001). Lectures on tensor categories and modular functors, volume 21. American Mathematical Soc.

[544] Banerjee, D., Dalmonte, M., Müller, M., Rico, E., Stebler, P., Wiese, U.-J., & Zoller, P. (2012). Atomic Quantum Simulation of Dynamical Gauge Fields Coupled to Fermionic Matter: From String Breaking to Evolution after a Quench. Phys. Rev. Lett., 109, 175302.

[545] Bañuls, M. C., Blatt, R., Catani, J., Celi, A., Cirac, J. I., Dalmonte, M., Fallani, L., Jansen, K., Lewenstein, M., Montangero, S., Muschik, C. A., Reznik, B., Rico, E., Tagliacozzo, L., Van Acoleyen, K., Verstraete, F., Wiese, U.-J., Wingate, M., Zakrzewski, J., & Zoller, P. (2020). Simulating lattice gauge theories within quantum technologies. The European Physical Journal D, 74(8), 165.

[546] Bao, Y., Fan, R., Vishwanath, A., & Altman, E. (2023). Mixed-state topological order and the errorfield double formulation of decoherence-induced transitions.

[547] Barbiero, L., Schweizer, C., Aidelsburger, M., Demler, E., Goldman, N., & Grusdt, F. (2019). Coupling ultracold matter to dynamical gauge fields in optical lattices: From flux attachment to $\mathbb{Z}_2$ lattice gauge theories. Science Advances, 5(10), eaav7444.

[548] Barends, R., Lamata, L., Kelly, J., García-Álvarez, L., Fowler, A. G., Megrant, A., Jeffrey, E., White, T. C., Sank, D., Mutus, J. Y., Campbell, B., Chen, Y., Chen, Z., Chiaro, B., Dunsworth, A., Hoi, I.-C., Neill, C., O'Malley, P. J. J., Quintana, C., Roushan, P., Vainsencher, A., Wenner, J., Solano, E., & Martinis,

J. M. (2015). Digital quantum simulation of fermionic models with a superconducting circuit. Nat. Commun., 6(1), 7654.

[549] Barredo, D., de Léséleuc, S., Lienhard, V., Lahaye, T., & Browaeys, A. (2016). An atom-by-atom assembler of defect-free arbitrary two-dimensional atomic arrays. Science, 354(6315), 1021–1023.

[550] Bartlett, R. J. & Musiał, M. (2007). Coupled-cluster theory in quantum chemistry. Rev. Mod. Phys., 79(1), 291–352.

[551] Bauer, B., Bravyi, S., Motta, M., & Chan, G. K.-L. (2020). Quantum algorithms for quantum chemistry and quantum materials science. Chem. Rev., 120(22), 12685–12717.

[552] Bauer, B., Wecker, D., Millis, A. J., Hastings, M. B., & Troyer, M. (2016). Hybrid Quantum-Classical Approach to Correlated Materials. Physical Review X, 6(3), 031045.

[553] Bauman, N. P., Low, G. H., & Kowalski, K. (2019). Quantum simulations of excited states with active-space downfolded Hamiltonians. J. Chem. Phys., 151(23), 234114.

[554] Benedetti, M., Fiorentini, M., & Lubasch, M. (2021). Hardware-efficient variational quantum algorithms for time evolution. Physical Review Research, 3(3), 033083. arXiv:2009.12361 [quant-ph].

[555] Bernien, H., Schwartz, S., Keesling, A., Levine, H., Omran, A., Pichler, H., Choi, S., Zibrov, A. S., Endres, M., Greiner, M., Vuletic, V., & Lukin, M. D. (2017a). Probing many-body dynamics on a 51-atom quantum simulator. Nature, 551, 579.

[556] Bernien, H., Schwartz, S., Keesling, A., Levine, H., Omran, A., Pichler, H., Choi, S., Zibrov, A. S., Endres, M., Greiner, M., Vuletić, V., & Lukin, M. D. (2017b). Probing many-body dynamics on a 51-atom quantum simulator. Nature, 551(7682), 579–584.

[557] Bernien, H., Schwartz, S., Keesling, A., Levine, H., Omran, A., Pichler, H., Choi, S., Zibrov, A. S., Endres, M., Greiner, M., Vuletić, V., & Lukin, M. D.

(2017c). Probing many-body dynamics on a 51-atom quantum simulator. Nature, 551(7682), 579–584.

[558] Berry, M. V. (1997). Quantal phase factors accompanying adiabatic changes. Proc. R. Soc. Lond., 392(1802), 45–57.

[559] Berry, M. V. (2009). Transitionless quantum driving. Journal of Physics A: Mathematical and Theoretical, 42(36), 365303.

[560] Bertini, B., Essler, F. H. L., Groha, S., & Robinson, N. J. (2015). Prethermalization and Thermalization in Models with Weak Integrability Breaking. Phys. Rev. Lett., 115, 180601.

[561] Bespalova, T. A. & Kyriienko, O. (2021). Quantum simulation and ground state preparation for the honeycomb Kitaev model.

[562] Beverland, M. E., Murali, P., Troyer, M., Svore, K. M., Hoefler, T., Kliuchnikov, V., Low, G. H., Soeken, M., Sundaram, A., & Vaschillo, A. (2022). Assessing requirements to scale to practical quantum advantage.

[563] Bloch, I., Dalibard, J., & Zwerger, W. (2008). Many-body physics with ultracold gases. Rev. Mod. Phys., 80, 885–964.

[564] Blok, M. S., Ramasesh, V. V., Schuster, T., O'Brien, K., Kreikebaum, J. M., Dahlen, D., Morvan, A., Yoshida, B., Yao, N. Y., & Siddiqi, I. (2021). Quantum Information Scrambling on a Superconducting Qutrit Processor. Phys. Rev. X, 11, 021010.

[565] Bluvstein, D., Evered, S. J., Geim, A. A., Li, S. H., Zhou, H., Manovitz, T., Ebadi, S., Cain, M., Kalinowski, M., Hangleiter, D., Bonilla Ataides, J. P., Maskara, N., Cong, I., Gao, X., Rodriguez, P. S., Karolyshyn, T., Semeghini, G., Gullans, M. J., Greiner, M., Vuletic, V., & Lukin, M. D. Logical quantum processor based on reconfigurable atom arrays. Submitted to Nature.

[566] Bluvstein, D., Evered, S. J., Geim, A. A., Li, S. H., Zhou, H., Manovitz, T., Ebadi, S., Cain, M., Kalinowski, M., Hangleiter, D., Bonilla Ataides, J. P., Maskara, N., Cong, I., Gao, X., Sales Rodriguez, P., Karolyshyn, T., Semeghini, G., Gullans, M. J., Greiner, M., Vuletić, V., & Lukin, M. D. (2024). Logical

quantum processor based on reconfigurable atom arrays. Nature, 626(7997), 58–65.

[567] Bluvstein, D., Geim, A. A., et al. In preparation.

[568] Bluvstein, D., Levine, H., Semeghini, G., Wang, T. T., Ebadi, S., Kalinowski, M., Keesling, A., Maskara, N., Pichler, H., Greiner, M., Vuletić, V., & Lukin, M. D. (2022a). A quantum processor based on coherent transport of entangled atom arrays. Nature, 604(7906), 451–456.

[569] Bluvstein, D., Levine, H., Semeghini, G., Wang, T. T., Ebadi, S., Kalinowski, M., Keesling, A., Maskara, N., Pichler, H., Greiner, M., Vuletić, V., & Lukin, M. D. (2022b). A quantum processor based on coherent transport of entangled atom arrays. Nature, 604(7906), 451–456.

[570] Bluvstein, D., Omran, A., Levine, H., Keesling, A., Semeghini, G., Ebadi, S., Wang, T. T., Michailidis, A. A., Maskara, N., Ho, W. W., Choi, S., Serbyn, M., Greiner, M., Vuletić, V., & Lukin, M. D. (2021a). Controlling quantum many-body dynamics in driven rydberg atom arrays. Science.

[571] Bluvstein, D., Omran, A., Levine, H., Keesling, A., Semeghini, G., Ebadi, S., Wang, T. T., Michailidis, A. A., Maskara, N., Ho, W. W., Choi, S., Serbyn, M., Greiner, M., Vuletić, V., & Lukin, M. D. (2021b). Controlling quantum many-body dynamics in driven Rydberg atom arrays. Science, 371(6536), 1355–1359.

[572] Bluvstein, D., Omran, A., Levine, H., Keesling, A., Semeghini, G., Ebadi, S., Wang, T. T., Michailidis, A. A., Maskara, N., Ho, W. W., Choi, S., Serbyn, M., Greiner, M., Vuletić, V., & Lukin, M. D. (2021c). Controlling quantum many-body dynamics in driven Rydberg atom arrays. Science, 371(6536), 1355–1359.

[573] Bluvstein, D., Omran, A., Levine, H., Keesling, A., Semeghini, G., Ebadi, S., Wang, T. T., Michailidis, A. A., Maskara, N., Ho, W. W., Choi, S., Serbyn, M., Greiner, M., Vuletić, V., & Lukin, M. D. (2021d). Controlling quantum many-body dynamics in driven Rydberg atom arrays. Science, 371(6536), 1355–1359.

[574] Bogani, L. & Wernsdorfer, W. (2008). Molecular spintronics using single-molecule magnets. Nature Materials, 7, 179–186.

[575] Bolvin, H. (2003). From ab Initio Calculations to Model Hamiltonians: The Effective Hamiltonian Technique as an Efficient Tool to Describe Mixed-Valence Molecules. J. Phys. Chem. A, 107(25), 5071–5078.

[576] Bombin, H. (2010). Topological Order with a Twist: Ising Anyons from an Abelian Model. Phys. Rev. Lett., 105, 030403.

[577] Bookatz, A. D., Wocjan, P., & Viola, L. (2014). Hamiltonian quantum simulation with bounded-strength controls. New J. Phys., 16(4), 045021.

[578] Bornet, G., Emperauger, G., Chen, C., Ye, B., Block, M., Bintz, M., Boyd, J. A., Barredo, D., Comparin, T., Mezzacapo, F., Roscilde, T., Lahaye, T., Yao, N. Y., & Browaeys, A. (2023). Scalable spin squeezing in a dipolar Rydberg atom array. Nature, 621(7980), 728–733.

[579] Braumüller, J., Karamlou, A. H., Yanay, Y., Kannan, B., Kim, D., Kjaergaard, M., Melville, A., Niedzielski, B. M., Sung, Y., Vepsäläinen, A., Winik, R., Yoder, J. L., Orlando, T. P., Gustavsson, S., Tahan, C., & Oliver, W. D. (2022). Probing quantum information propagation with out-of-time-ordered correlators. Nature Physics, 18(2), 172–178.

[580] Bravyi, S. B. & Kitaev, A. Y. (2002). Fermionic Quantum Computation. Annals of Physics, 298(1), 210–226.

[581] Bricmont, J. & Frölich, J. (1983). An order parameter distinguishing between different phases of lattice gauge theories with matter fields. Physics Letters B, 122(1), 73–77.

[582] Bridgeman, J. C., Flammia, S. T., & Poulin, D. (2016). Detecting topological order with ribbon operators. Physical Review B, 94(20), 205123.

[583] Browaeys, A. & Lahaye, T. (2020a). Many-body physics with individually controlled rydberg atoms. Nature Physics, 16(2), 132–142.

[584] Browaeys, A. & Lahaye, T. (2020b). Many-body physics with individually controlled Rydberg atoms. Nature Physics, 16(2), 132–142.

[585] Brydges, T., Elben, A., Jurcevic, P., Vermersch, B., Maier, C., Lanyon, B. P., Zoller, P., Blatt, R., & Roos, C. F. (2019). Probing Rényi entanglement entropy via randomized measurements. Science, 364(6437), 260–263.

[586] Bull, K., Martin, I., & Papić, Z. (2019). Systematic construction of scarred many-body dynamics in 1d lattice models. Phys. Rev. Lett., 123, 030601.

[587] Burke, K. (2012). Perspective on density functional theory. J. Chem. Phys., 136(15).

[588] Cain, M., Chattopadhyay, S., Liu, J.-G., Samajdar, R., Pichler, H., & Lukin, M. D. (2023). Quantum speedup for combinatorial optimization with flat energy landscapes.

[589] Calzado, C. J., Clemente-Juan, J. M., Coronado, E., Gaita-Arino, A., & Suaud, N. (2008). Role of the Electron Transfer and Magnetic Exchange Interactions in the Magnetic Properties of Mixed-Valence Polyoxovanadate Complexes. Inorg. Chem., 47(13), 5889–5901.

[590] Carrasco, J., Elben, A., Kokail, C., Kraus, B., & Zoller, P. (2021). Theoretical and Experimental Perspectives of Quantum Verification. PRX Quantum, 2(1), 010102.

[591] Castelnovo, C. & Chamon, C. (2008). Quantum topological phase transition at the microscopic level. Physical Review B, 77(5), 054433.

[592] Celi, A., Vermersch, B., Viyuela, O., Pichler, H., Lukin, M. D., & Zoller, P. (2020a). Emerging Two-Dimensional Gauge Theories in Rydberg Configurable Arrays. Phys. Rev. X, 10, 021057.

[593] Celi, A., Vermersch, B., Viyuela, O., Pichler, H., Lukin, M. D., & Zoller, P. (2020b). Emerging Two-Dimensional Gauge Theories in Rydberg Configurable Arrays. Phys. Rev. X, 10(2), 021057.

[594] Cepaite, I., Polkovnikov, A., Daley, A. J., & Duncan, C. W. (2023). Counterdiabatic Optimized Local Driving. PRX Quantum, 4, 010312.

[595] Chalopin, T., Bojović, P., Wang, S., Franz, T., Sinha, A., Wang, Z., Bourgund, D., Obermeyer, J., Grusdt, F., Bohrdt, A., Pollet, L., Wietek, A., Georges, A., Hilker, T., & Bloch, I. (2024). Probing the magnetic origin of the pseudogap using a Fermi-Hubbard quantum simulator.

[596] Chan, H. H. S., Meister, R., Goh, M. L., & Koczor, B. (2023). Algorithmic shadow spectroscopy.

[597] Chandrasekharan, S. & Wiese, U.-J. (1997). Quantum link models: A discrete approach to gauge theories. Nuclear Physics B, 492(1), 455–471.

[598] Chattopadhyay, S., Pichler, H., Lukin, M. D., & Ho, W. W. (2020). Quantum many-body scars from virtual entangled pairs. Phys. Rev. B, 101, 174308.

[599] Chen, C., Bornet, G., Bintz, M., Emperauger, G., Leclerc, L., Liu, V. S., Scholl, P., Barredo, D., Hauschild, J., Chatterjee, S., Schuler, M., Läuchli, A. M., Zaletel, M. P., Lahaye, T., Yao, N. Y., & Browaeys, A. (2023a). Continuous symmetry breaking in a two-dimensional Rydberg array. Nature, 616(7958), 691–695.

[600] Chen, C., Bornet, G., Bintz, M., Emperauger, G., Leclerc, L., Liu, V. S., Scholl, P., Barredo, D., Hauschild, J., Chatterjee, S., Schuler, M., Läuchli, A. M., Zaletel, M. P., Lahaye, T., Yao, N. Y., & Browaeys, A. (2023b). Continuous symmetry breaking in a two-dimensional Rydberg array. Nature, 616(7958), 691–695.

[601] Chen, D.-T., Helms, P., Hale, A. R., Lee, M., Li, C., Gray, J., Christou, G., Zapf, V. S., Chan, G. K.-L., & Cheng, H.-P. (2022). Using Hyperoptimized Tensor Networks and First-Principles Electronic Structure to Simulate the Experimental Properties of the Giant {Mn84} Torus. J. Phys. Chem. Lett., 13(10), 2365–2370.

[602] Chen, X., Gu, Z.-C., & Wen, X.-G. (2010). Local unitary transformation, long-range quantum entanglement, wave function renormalization, and topological order. Physical Review B, 82(15), 155138.

[603] Chen, X., Gu, Z.-C., & Wen, X.-G. (2011). Classification of gapped symmetric phases in one-dimensional spin systems. Phys. Rev. B, 83, 035107.

[604] Chen, Y.-A. & Xu, Y. (2023). Equivalence between Fermion-to-Qubit Mappings in two Spatial Dimensions. PRX Quantum, 4(1), 010326.

[605] Cheng, Y., Li, C., & Zhai, H. (2021). Variational approach to quantum spin liquid in a Rydberg atom simulator.

[606] Chi, Y., Huang, J., Zhang, Z., Mao, J., Zhou, Z., Chen, X., Zhai, C., Bao, J., Dai, T., Yuan, H., Zhang, M., Dai, D., Tang, B., Yang, Y., Li, Z., Ding, Y., Oxenløwe, L. K., Thompson, M. G., O'Brien, J. L., Li, Y., Gong, Q., & Wang, J. (2022). A programmable qudit-based quantum processor. Nat. Commun., 13(1), 1166.

[607] Chiesa, A., Tacchino, F., Grossi, M., Santini, P., Tavernelli, I., Gerace, D., & Carretta, S. (2019). Quantum hardware simulating four-dimensional inelastic neutron scattering. Nat. Phys., 15(5), 455–459.

[608] Childs, A. M., Cleve, R., Deotto, E., Farhi, E., Gutmann, S., & Spielman, D. A. (2003). Exponential algorithmic speedup by quantum walk. In Proceedings of the thirty-fifth annual ACM symposium on Theory of computing (pp. 59–68). arXiv:quant-ph/0209131.

[609] Choi, J., Zhou, H., Knowles, H. S., Landig, R., Choi, S., & Lukin, M. D. (2020a). Robust Dynamic Hamiltonian Engineering of Many-Body Spin Systems. Phys. Rev. X, 10, 031002.

[610] Choi, J., Zhou, H., Knowles, H. S., Landig, R., Choi, S., & Lukin, M. D. (2020b). Robust Dynamic Hamiltonian Engineering of Many-Body Spin Systems. Phys. Rev. X, 10(3), 031002.

[611] Choi, S., Choi, J., Landig, R., Kucsko, G., Zhou, H., Isoya, J., Jelezko, F., Onoda, S., Sumiya, H., Khemani, V., Keyserlingk, C. v., Yao, N. Y., Demler, E., & Lukin, M. D. (2017). Observation of discrete time-crystalline order in a disordered dipolar many-body system. Nature, 543(7644), 221–225.

[612] Choi, S., Choi, J., Landig, R., Kucsko, G., Zhou, H., Isoya, J., Jelezko, F., Onoda, S., Sumiya, H., Khemani, V., von Keyserlingk, C., Yao, N. Y., Demler, E., & Lukin, M. D. (2016). Observation of discrete time-crystalline order in a disordered dipolar many-body system. ArXiv e-prints.

[613] Choi, S., Turner, C. J., Pichler, H., Ho, W. W., Michailidis, A. A., Papić, Z., Serbyn, M., Lukin, M. D., & Abanin, D. A. (2019). Emergent su(2) dynamics and perfect quantum many-body scars. Phys. Rev. Lett., 122, 220603.

[614] Cirac, J. I., Pérez-García, D., Schuch, N., & Verstraete, F. (2021). Matrix product states and projected entangled pair states: Concepts, symmetries, theorems. Rev. Mod. Phys., 93, 045003.

[615] Claeys, P. W., Pandey, M., Sels, D., & Polkovnikov, A. (2019). Floquet-Engineering Counterdiabatic Protocols in Quantum Many-Body Systems. Phys. Rev. Lett., 123, 090602.

[616] Clinton, L., Cubitt, T., Flynn, B., Gambetta, F. M., Klassen, J., Montanaro, A., Piddock, S., Santos, R. A., & Sheridan, E. (2024). Towards near-term quantum simulation of materials. Nat. Commun., 15(1), 211.

[617] Cochran, T. A., Jobst, B., Rosenberg, E., Lensky, Y. D., Gyawali, G., Eassa, N., Will, M., Abanin, D., Acharya, R., Beni, L. A., Andersen, T. I., Ansmann, M., Arute, F., Arya, K., Asfaw, A., Atalaya, J., Babbush, R., Ballard, B., Bardin, J. C., Bengtsson, A., Bilmes, A., Bourassa, A., Bovaird, J., Broughton, M., Browne, D. A., Buchea, B., Buckley, B. B., Burger, T., Burkett, B., Bushnell, N., Cabrera, A., Campero, J., Chang, H.-S., Chen, Z., Chiaro, B., Claes, J., Cleland, A. Y., Cogan, J., Collins, R., Conner, P., Courtney, W., Crook, A. L., Curtin, B., Das, S., Demura, S., De Lorenzo, L., Di Paolo, A., Donohoe, P., Drozdov, I., Dunsworth, A., Eickbusch, A., Elbag, A. M., Elzouka, M., Erickson, C., Ferreira, V. S., Burgos, L. F., Forati, E., Fowler, A. G., Foxen, B., Ganjam, S., Gasca, R., Genois, ., Giang, W., Gilboa, D., Gosula, R., Dau, A. G., Graumann, D., Greene, A., Gross, J. A., Habegger, S., Hansen, M., Harrigan, M. P., Harrington, S. D., Heu, P., Higgott, O., Hilton, J., Huang, H.-Y., Huff, A., Huggins, W. J., Jeffrey, E., Jiang, Z., Jones, C., Joshi, C., Juhas, P., Kafri, D., Kang, H., Karamlou, A. H., Kechedzhi, K., Khaire, T., Khattar, T., Khezri, M., Kim, S., Klimov, P. V., Kobrin, B., Korotkov, A. N., Kostritsa, F., Kreikebaum, J. M., Kurilovich, V. D., Landhuis, D., Lange-Dei, T., Langley, B. W., Lau, K.-M., Ledford, J., Lee, K., Lester, B. J., Guevel, L. L., Li, W. Y., Lill, A. T., Livingston, W. P., Locharla, A., Lundahl, D., Lunt, A., Madhuk, S., Maloney, A., Mandrà, S., Martin, L. S., Martin, O., Maxfield, C., McClean, J. R., McEwen, M., Meeks, S., Megrant, A., Miao, K. C., Molavi, R., Molina, S., Montazeri, S., Movassagh, R., Neill, C., Newman, M., Nguyen, A., Nguyen, M., Ni, C.-H., Niu, M. Y., Oliver, W. D., Ottosson, K., Pizzuto, A., Potter, R., Pritchard, O., Quintana, C., Ramachandran, G., Reagor, M. J., Rhodes, D. M., Roberts, G.,

Sankaragomathi, K., Satzinger, K. J., Schurkus, H. F., Shearn, M. J., Shorter, A., Shutty, N., Shvarts, V., Sivak, V., Small, S., Smith, W. C., Springer, S., Sterling, G., Suchard, J., Szasz, A., Sztein, A., Thor, D., Torunbalci, M. M., Vaishnav, A., Vargas, J., Vdovichev, S., Vidal, G., Heidweiller, C. V., Waltman, S., Wang, S. X., Ware, B., White, T., Wong, K., Woo, B. W. K., Xing, C., Yao, Z. J., Yeh, P., Ying, B., Yoo, J., Yosri, N., Young, G., Zalcman, A., Zhang, Y., Zhu, N., Zobris, N., Boixo, S., Kelly, J., Lucero, E., Chen, Y., Smelyanskiy, V., Neven, H., Gammon-Smith, A., Pollmann, F., Knap, M., & Roushan, P. (2024). Visualizing Dynamics of Charges and Strings in (2+1)D Lattice Gauge Theories.

[618] Colombo, S., Pedrozo-Peñafiel, E., Adiyatullin, A. F., Li, Z., Mendez, E., Shu, C., & Vuletić, V. (2022a). Time-reversal-based quantum metrology with many-body entangled states. Nature Physics, 18(8), 925–930.

[619] Colombo, S., Pedrozo-Peñafiel, E., Adiyatullin, A. F., Li, Z., Mendez, E., Shu, C., & Vuletić, V. (2022b). Time-reversal-based quantum metrology with many-body entangled states. Nature Physics, 18(8), 925–930.

[620] Cong, I., Choi, S., & Lukin, M. D. (2019). Quantum convolutional neural networks. Nature Physics, 15(12), 1273–1278. Publisher: Nature Publishing Group.

[621] Cooper, A., Covey, J. P., Madjarov, I. S., Porsev, S. G., Safronova, M. S., & Endres, M. (2018). Alkaline-Earth Atoms in Optical Tweezers. Phys. Rev. X, 8(4), 041055.

[622] Cooper, N., Dalibard, J., & Spielman, I. (2019). Topological bands for ultracold atoms. Rev. Mod. Phys., 91(1), 015005.

[623] Corboz, P. & Vidal, G. (2009). Fermionic multiscale entanglement renormalization ansatz. Phys. Rev. B, 80(16), 165129. Publisher: American Physical Society.

[624] Dai, H.-N., Yang, B., Reingruber, A., Sun, H., Xu, X.-F., Chen, Y.-A., Yuan, Z.-S., & Pan, J.-W. (2017). Four-body ring-exchange interactions and anyonic statistics within a minimal toric-code Hamiltonian. Nature Physics, 13(12), 1195–1200.

[625] Dai, Z., Wu, Y., Wang, T., & Zaletel, M. P. (2025). Fermionic Isometric Tensor Network States in Two Dimensions. Phys. Rev. Lett., 134(2), 026502. Publisher: American Physical Society.

[626] D'Alessio, L., Kafri, Y., Polkovnikov, A., & Rigol, M. (2016a). From quantum chaos and eigenstate thermalization to statistical mechanics and thermodynamics. Advances in Physics, 65(3), 239.

[627] D'Alessio, L., Kafri, Y., Polkovnikov, A., & Rigol, M. (2016b). From quantum chaos and eigenstate thermalization to statistical mechanics and thermodynamics. Adv. Phys, 65(3), 239–362.

[628] Daley, A. J., Bloch, I., Kokail, C., Flannigan, S., Pearson, N., Troyer, M., & Zoller, P. (2022). Practical quantum advantage in quantum simulation. Nature, 607(7920), 667–676.

[629] Dalmonte, M. & Montangero, S. (2016). Lattice gauge theory simulations in the quantum information era. Contemporary Physics, 57(3), 388–412.

[630] Davydova, M., Tantivasadakarn, N., & Balasubramanian, S. (2022). Floquet codes without parent subsystem codes.

[631] de Léséleuc, S., Lienhard, V., Scholl, P., Barredo, D., Weber, S., Lang, N., Büchler, H. P., Lahaye, T., & Browaeys, A. (2019). Observation of a symmetry-protected topological phase of interacting bosons with Rydberg atoms. Science, 365(6455), 775–780.

[632] Demirplak, M. & Rice, S. A. (2003a). Adiabatic population transfer with control fields. The Journal of Physical Chemistry A, 107(46), 9937–9945.

[633] Demirplak, M. & Rice, S. A. (2003b). Adiabatic Population Transfer with Control Fields. The Journal of Physical Chemistry A, 107(46), 9937–9945.

[634] Dennis, E., Kitaev, A., Landahl, A., & Preskill, J. (2002). Topological quantum memory. Journal of Mathematical Physics, 43(9), 4452–4505. Publisher: American Institute of Physics.

[635] Derby, C., Klassen, J., Bausch, J., & Cubitt, T. (2021). Compact fermion to qubit mappings. Phys. Rev. B, 104(3), 035118.

[636] Desaules, J.-Y., Pietracaprina, F., Papić, Z., Goold, J., & Pappalardi, S. (2022). Extensive Multipartite Entanglement from su(2) Quantum Many-Body Scars. Phys. Rev. Lett., 129, 020601.

[637] Di Meglio, A., Jansen, K., Tavernelli, I., Alexandrou, C., Arunachalam, S., Bauer, C. W., Borras, K., Carrazza, S., Crippa, A., Croft, V., de Putter, R., Delgado, A., Dunjko, V., Egger, D. J., Fernández-Combarro, E., Fuchs, E., Funcke, L., González-Cuadra, D., Grossi, M., Halimeh, J. C., Holmes, Z., Kühn, S., Lacroix, D., Lewis, R., Lucchesi, D., Martinez, M. L., Meloni, F., Mezzacapo, A., Montangero, S., Nagano, L., Pascuzzi, V. R., Radescu, V., Ortega, E. R., Roggero, A., Schuhmacher, J., Seixas, J., Silvi, P., Spentzouris, P., Tacchino, F., Temme, K., Terashi, K., Tura, J., Tüysüz, C., Vallecorsa, S., Wiese, U.-J., Yoo, S., & Zhang, J. (2024). Quantum Computing for High-Energy Physics: State of the Art and Challenges. PRX Quantum, 5(3), 037001. Publisher: American Physical Society.

[638] Dooley, S., Pappalardi, S., & Goold, J. (2023). Entanglement enhanced metrology with quantum many-body scars. Phys. Rev. B, 107, 035123.

[639] Duan, L. M., Demler, E., & Lukin, M. D. (2003a). Controlling Spin Exchange Interactions of Ultracold Atoms in Optical Lattices. Phys. Rev. Lett., 91(9), 090402.

[640] Duan, L. M., Demler, E., & Lukin, M. D. (2003b). Controlling spin exchange interactions of ultracold atoms in optical lattices. Phys. Rev. Lett., 91.

[641] Duclos-Cianci, G. & Poulin, D. (2013). Fault-tolerant renormalization group decoder for abelian topological codes.

[642] Duivenvoorden, K., Iqbal, M., Haegeman, J., Verstraete, F., & Schuch, N. (2017). Entanglement phases as holographic duals of anyon condensates. Phys. Rev. B, 95, 235119.

[643] Ebadi, S., Keesling, A., Cain, M., Wang, T. T., Levine, H., Bluvstein, D., Semeghini, G., Omran, A., Liu, J.-G., Samajdar, R., Luo, X.-Z., Nash, B., Gao, X., Barak, B., Farhi, E., Sachdev, S., Gemelke, N., Zhou, L., Choi, S., Pichler, H., Wang, S.-T., Greiner, M., Vuletić, V., & Lukin, M. D. (2022a). Quantum

optimization of maximum independent set using Rydberg atom arrays. Science, 376(6598), 1209–1215.

[644] Ebadi, S., Keesling, A., Cain, M., Wang, T. T., Levine, H., Bluvstein, D., Semeghini, G., Omran, A., Liu, J.-G., Samajdar, R., Luo, X.-Z., Nash, B., Gao, X., Barak, B., Farhi, E., Sachdev, S., Gemelke, N., Zhou, L., Choi, S., Pichler, H., Wang, S.-T., Greiner, M., Vuletić, V., & Lukin, M. D. (2022b). Quantum optimization of maximum independent set using Rydberg atom arrays. Science, 376(6598), 1209–1215.

[645] Ebadi, S., Wang, T. T., Levine, H., Keesling, A., Semeghini, G., Omran, A., Bluvstein, D., Samajdar, R., Pichler, H., Ho, W. W., Choi, S., Sachdev, S., Greiner, M., Vuletic, V., & Lukin, M. D. (2021a). Quantum Phases of Matter on a 256-Atom Programmable Quantum Simulator. Nature, 595(7866), 227–232.

[646] Ebadi, S., Wang, T. T., Levine, H., Keesling, A., Semeghini, G., Omran, A., Bluvstein, D., Samajdar, R., Pichler, H., Ho, W. W., Choi, S., Sachdev, S., Greiner, M., Vuletić, V., & Lukin, M. D. (2021b). Quantum phases of matter on a 256-atom programmable quantum simulator. Nature, 595(7866), 227–232.

[647] Ebadi, S., Wang, T. T., Levine, H., Keesling, A., Semeghini, G., Omran, A., Bluvstein, D., Samajdar, R., Pichler, H., Ho, W. W., Choi, S., Sachdev, S., Greiner, M., Vuletić, V., & Lukin, M. D. (2021c). Quantum phases of matter on a 256-atom programmable quantum simulator. Nature, 595(7866), 227–232.

[648] Ebadi, S., Wang, T. T., Levine, H., Keesling, A., Semeghini, G., Omran, A., Bluvstein, D., Samajdar, R., Pichler, H., Ho, W. W., Choi, S., Sachdev, S., Greiner, M., Vuletić, V., & Lukin, M. D. (2021d). Quantum phases of matter on a 256-atom programmable quantum simulator. Nature, 595(7866), 227–232.

[649] Eckardt, A. (2017). Colloquium: Atomic quantum gases in periodically driven optical lattices. Rev. Mod. Phys., 89, 011004.

[650] Eckner, W. J., Darkwah Oppong, N., Cao, A., Young, A. W., Milner, W. R., Robinson, J. M., Ye, J., & Kaufman, A. M. (2023). Realizing spin squeezing with Rydberg interactions in an optical clock. Nature, 621(7980), 734–739.

[651] Else, D. V., Bauer, B., & Nayak, C. (2016a). Floquet time crystals. Phys. Rev. Lett., 117, 090402.

[652] Else, D. V., Bauer, B., & Nayak, C. (2016b). Floquet Time Crystals. Phys. Rev. Lett., 117, 090402.

[653] Else, D. V., Bauer, B., & Nayak, C. (2017a). Prethermal phases of matter protected by time-translation symmetry. Phys. Rev. X, 7, 011026.

[654] Else, D. V., Bauer, B., & Nayak, C. (2017b). Prethermal Phases of Matter Protected by Time-Translation Symmetry. Phys. Rev. X, 7, 011026.

[655] Else, D. V., Bauer, B., & Nayak, C. (2017c). Prethermal Phases of Matter Protected by Time-Translation Symmetry. Phys. Rev. X, 7, 011026.

[656] Else, D. V., Bauer, B., & Nayak, C. (2017d). Prethermal Phases of Matter Protected by Time-Translation Symmetry. Phys. Rev. X, 7(1), 011026.

[657] Else, D. V., Bauer, B., & Nayak, C. (2017e). Prethermal Phases of Matter Protected by Time-Translation Symmetry. Phys. Rev. X, 7(1), 011026.

[658] Else, D. V., Ho, W. W., & Dumitrescu, P. T. (2020). Long-lived interacting phases of matter protected by multiple time-translation symmetries in quasiperiodically driven systems. Phys. Rev. X, 10, 021032.

[659] Evered, S. J., Bluvstein, D., Kalinowski, M., Ebadi, S., Manovitz, T., Zhou, H., Li, S. H., Geim, A. A., Wang, T. T., Maskara, N., Levine, H., Semeghini, G., Greiner, M., Vuletic, V., & Lukin, M. D. (2023a). High-fidelity parallel entangling gates on a neutral atom quantum computer. Nature, 622(7982), 268–272.

[660] Evered, S. J., Bluvstein, D., Kalinowski, M., Ebadi, S., Manovitz, T., Zhou, H., Li, S. H., Geim, A. A., Wang, T. T., Maskara, N., Levine, H., Semeghini, G., Greiner, M., Vuletić, V., & Lukin, M. D. (2023b). High-fidelity parallel entangling gates on a neutral-atom quantum computer. Nature, 622(7982), 268–272.

[661] Evered, S. J., Bluvstein, D., Kalinowski, M., Ebadi, S., Manovitz, T., Zhou, H., Li, S. H., Geim, A. A., Wang, T. T., Maskara, N., Levine, H., Semeghini, G., Greiner, M., Vuletić, V., & Lukin, M. D. (2023c). High-fidelity parallel entangling gates on a neutral atom quantum computer.

[662] Fan, R., Bao, Y., Altman, E., & Vishwanath, A. (2023). Diagnostics of mixed-state topological order and breakdown of quantum memory.

[663] Feldmeier, J., Maskara, N., Köylüoğlu, N. U., & Lukin, M. D. (2024). Quantum simulation of dynamical gauge theories in periodically driven Rydberg atom arrays.

[664] Feldmeier, J., Pollmann, F., & Knap, M. (2019). Emergent Glassy Dynamics in a Quantum Dimer Model. Phys. Rev. Lett., 123, 040601.

[665] Fendley, P., Sengupta, K., & Sachdev, S. (2004a). Competing density-wave orders in a one-dimensional hard-boson model. Phys. Rev. B, 69, 075106.

[666] Fendley, P., Sengupta, K., & Sachdev, S. (2004b). Competing density-wave orders in a one-dimensional hard-boson model. Phys. Rev. B, 69, 075106.

[667] Feng, L., Katz, O., Haack, C., Maghrebi, M., Gorshkov, A. V., Gong, Z., Cetina, M., & Monroe, C. (2023). Continuous symmetry breaking in a trapped-ion spin chain. Nature, 623(7988), 713–717.

[668] Feynman, R. P. (1982a). Simulating physics with computers. Int. J. Theor. Phys, 21(6/7).

[669] Feynman, R. P. (1982b). Simulating physics with computers. Int. J. Theor. Phys., 21(6), 467–488.

[670] Fläschner, N., Rem, B. S., Tarnowski, M., Vogel, D., Lühmann, D.-S., Sengstock, K., & Weitenberg, C. (2016). Experimental reconstruction of the Berry curvature in a Floquet Bloch band. Science, 352(6289), 1091–1094.

[671] Foss-Feig, M., Hayes, D., Dreiling, J. M., Figgatt, C., Gaebler, J. P., Moses, S. A., Pino, J. M., & Potter, A. C. (2021). Holographic quantum algorithms for simulating correlated spin systems. Physical Review Research, 3(3), 033002.

[672] Fowler, A. G., Mariantoni, M., Martinis, J. M., & Cleland, A. N. (2012). Surface codes: Towards practical large-scale quantum computation. Phys. Rev. A, 86, 032324.

[673] Fredenhagen, K. & Marcu, M. (1983). Charged states in $\mathbb{Z}_2$ gauge theories. Communications in Mathematical Physics, 92(1), 81–119.

[674] Frölian, A., Chisholm, C. S., Neri, E., Cabrera, C. R., Ramos, R., Celi, A., & Tarruell, L. (2022). Realizing a 1D topological gauge theory in an optically dressed BEC. Nature, 608(7922), 293–297.

[675] Fukuhara, T., Hild, S., Zeiher, J., Schauß, P., Bloch, I., Endres, M., & Gross, C. (2015). Spatially Resolved Detection of a Spin-Entanglement Wave in a Bose-Hubbard Chain. Phys. Rev. Lett., 115, 035302.

[676] Funcke, L., Hartung, T., Jansen, K., & Kühn, S. (2023). Review on quantum computing for lattice field theory.

[677] Gärttner, M., Bohnet, J. G., Safavi-Naini, A., Wall, M. L., Bollinger, J. J., & Rey, A. M. (2017). Measuring out-of-time-order correlations and multiple quantum spectra in a trapped-ion quantum magnet. Nature Physics, 13(8), 781–786.

[678] Geier, S., Braemer, A., Braun, E., Müllenbach, M., Franz, T., Gärttner, M., Zürn, G., & Weidemüller, M. (2024). Time-reversal in a dipolar quantum many-body spin system.

[679] Geier, S., Thaicharoen, N., Hainaut, C., Franz, T., Salzinger, A., Tebben, A., Grimshandl, D., Zürn, G., & Weidemüller, M. (2021). Floquet Hamiltonian engineering of an isolated many-body spin system. Science, 374(6571), 1149–1152.

[680] Georgescu, I. M., Ashhab, S., & Nori, F. (2014). Quantum simulation. Rev. Mod. Phys., 86, 153–185.

[681] Gilmore, K. A., Affolter, M., Lewis-Swan, R. J., Barberena, D., Jordan, E., Rey, A. M., & Bollinger, J. J. (2021). Quantum-enhanced sensing of displacements and electric fields with two-dimensional trapped-ion crystals. Science, 373(6555), 673–678.

[682] Giudici, G., Lukin, M. D., & Pichler, H. (2022). Dynamical preparation of quantum spin liquids in Rydberg atom arrays.

[683] Gkritsis, F., Dux, D., Zhang, J., Jain, N., Gogolin, C., & Preiss, P. M. (2024). Simulating Chemistry with Fermionic Optical Superlattices. _eprint: 2409.05663.

[684] Glaetzle, A. W., Dalmonte, M., Nath, R., Rousochatzakis, I., Moessner, R., & Zoller, P. (2014). Quantum Spin-Ice and Dimer Models with Rydberg Atoms. Phys. Rev. X, 4, 041037.

[685] Goldman, N. & Dalibard, J. (2014). Periodically Driven Quantum Systems: Effective Hamiltonians and Engineered Gauge Fields. Phys. Rev. X, 4, 031027.

[686] González-Cuadra, D., Bluvstein, D., Kalinowski, M., Kaubruegger, R., Maskara, N., Naldesi, P., Zache, T. V., Kaufman, A. M., Lukin, M. D., Pichler, H., Vermersch, B., Ye, J., & Zoller, P. (2023a). Fermionic quantum processing with programmable neutral atom arrays. Proceedings of the National Academy of Sciences, 120(35), e2304294120.

[687] González-Cuadra, D., Bluvstein, D., Kalinowski, M., Kaubruegger, R., Maskara, N., Naldesi, P., Zache, T. V., Kaufman, A. M., Lukin, M. D., Pichler, H., Vermersch, B., Ye, J., & Zoller, P. (2023b). Fermionic quantum processing with programmable neutral atom arrays. Proc. Natl. Acad. Sci., 120.

[688] González-Cuadra, D., Zache, T. V., Carrasco, J., Kraus, B., & Zoller, P. (2022). Hardware Efficient Quantum Simulation of Non-Abelian Gauge Theories with Qudits on Rydberg Platforms. Phys. Rev. Lett., 129(16), 160501.

[689] Gregor, K., Huse, D. A., Moessner, R., & Sondhi, S. L. (2011). Diagnosing deconfinement and topological order. New Journal of Physics, 13(2), 025009.

[690] Gritsev, V. & Polkovnikov, A. (2017). Integrable Floquet dynamics. SciPost Phys., 2(3), 021.

[691] Gross, C. & Bloch, I. (2017). Quantum simulations with ultracold atoms in optical lattices. Science, 357(6355), 995–1001.

[692] Günther, J., Baiardi, A., Reiher, M., & Christandl, M. (2023). More quantum chemistry with fewer qubits.

[693] Haah, J. (2016). An invariant of topologically ordered states under local unitary transformations. Communications in Mathematical Physics, 342(3), 771–801. Publisher: Springer.

[694] Haah, J., Harrow, A. W., Ji, Z., Wu, X., & Yu, N. (2017). Sample-optimal tomography of quantum states. IEEE Transactions on Information Theory, 63(9), 5628–5641.

[695] Haegeman, J., Van Acoleyen, K., Schuch, N., Cirac, J. I., & Verstraete, F. (2015). Gauging quantum states: From global to local symmetries in many-body systems. Phys. Rev. X, 5, 011024.

[696] Haghshenas, R., Gray, J., Potter, A. C., & Chan, G. K.-L. (2022). The Variational Power of Quantum Circuit Tensor Networks. Physical Review X, 12(1), 011047. arXiv:2107.01307 [cond-mat, physics:quant-ph].

[697] Hait, D., Tubman, N. M., Levine, D. S., Whaley, K. B., & Head-Gordon, M. (2019). What levels of coupled cluster theory are appropriate for transition metal systems? a study using near-exact quantum chemical values for 3d transition metal binary compounds. J. Chem. Theory Comput., 15(10), 5370–5385.

[698] Haldane, F. D. M. (1988). Model for a Quantum Hall Effect without Landau Levels: Condensed-Matter Realization of the "Parity Anomaly". Phys. Rev. Lett., 61(18), 2015–2018. Publisher: American Physical Society.

[699] Halimeh, J. C. & Hauke, P. (2022). Stabilizing gauge theories in quantum simulators: a brief review.

[700] Halimeh, J. C., Homeier, L., Bohrdt, A., & Grusdt, F. (2023). Spin exchange-enabled quantum simulator for large-scale non-Abelian gauge theories.

[701] Hartke, T., Oreg, B., Jia, N., & Zwierlein, M. (2022). Quantum register of fermion pairs. Nature, 601(7894), 537–541.

[702] Hastings, M. B. (2010). Locality in quantum systems.

[703] Hastings, M. B. (2011). Topological order at nonzero temperature. Phys. Rev. Lett., 107, 210501.

[704] Hastings, M. B. & Haah, J. (2021). Dynamically generated logical qubits. Quantum, 5, 564.

[705] Hastings, M. B. & Wen, X.-G. (2005a). Quasiadiabatic continuation of quantum states: The stability of topological ground-state degeneracy and emergent gauge invariance. Phys. Rev. B, 72(4), 045141. Publisher: American Physical Society.

[706] Hastings, M. B. & Wen, X.-G. (2005b). Quasiadiabatic continuation of quantum states: The stability of topological ground-state degeneracy and emergent gauge invariance. Physical Review B, 72(4).

[707] Hauschild, J. & Pollmann, F. (2018a). Efficient Numerical Simulations with Tensor Networks: Tensor Network Python (TeNPy). SciPost Physics Lecture Notes, (pp.5).

[708] Hauschild, J. & Pollmann, F. (2018b). Efficient numerical simulations with Tensor Networks: Tensor Network Python (TeNPy). SciPost Phys. Lect. Notes, (pp.5).

[709] Heller, E. J. (1984). Bound-state eigenfunctions of classically chaotic hamiltonian systems: Scars of periodic orbits. Phys. Rev. Lett., 53, 1515.

[710] Hermele, M., Fisher, M. P. A., & Balents, L. (2004). Pyrochlore photons: The U (1) spin liquid in a S = 1 2 three-dimensional frustrated magnet. Physical Review B, 69(6), 064404.

[711] Hickey, C. & Trebst, S. (2019). Emergence of a field-driven U(1) spin liquid in the Kitaev honeycomb model. Nat. Commun., 10(1), 530.

[712] Hines, J. A., Rajagopal, S. V., Moreau, G. L., Wahrman, M. D., Lewis, N. A., Marković, O., & Schleier-Smith, M. (2023). Spin Squeezing by Rydberg Dressing in an Array of Atomic Ensembles. Phys. Rev. Lett., 131, 063401.

[713] Ho, W. W., Choi, S., Lukin, M. D., & Abanin, D. A. (2017). Critical time crystals in dipolar systems. Phys. Rev. Lett., 119, 010602.

[714] Ho, W. W., Choi, S., Pichler, H., & Lukin, M. D. (2019). Periodic orbits, entanglement, and quantum many-body scars in constrained models: Matrix product state approach. Phys. Rev. Lett., 122, 040603.

[715] Homeier, L., Bohrdt, A., Linsel, S., Demler, E., Halimeh, J. C., & Grusdt, F. (2023). Realistic scheme for quantum simulation of Z2 lattice gauge theories with dynamical matter in (2 + 1)D. Communications Physics, 6(1), 127.

[716] Horn, D. (1981). Finite matrix models with continuous local gauge invariance. Physics Letters B, 100(2), 149–151.

[717] Horodecki, M., Horodecki, P., & Horodecki, R. (1996). Separability of mixed states: necessary and sufficient conditions. Physics Letters A, 223(1), 1–8.

[718] Horodecki, R., Horodecki, P., Horodecki, M., & Horodecki, K. (2009). Quantum entanglement. Rev. Mod. Phys., 81, 865–942.

[719] Hrmo, P., Wilhelm, B., Gerster, L., van Mourik, M. W., Huber, M., Blatt, R., Schindler, P., Monz, T., & Ringbauer, M. (2023). Native qudit entanglement in a trapped ion quantum processor. Nat. Commun., 14(1), 2242.

[720] Huang, B., Wu, Y.-H., & Liu, W. V. (2018). Clean floquet time crystals: Models and realizations in cold atoms. Physical Review Letters, 120(11).

[721] Huang, H.-Y., Kueng, R., & Preskill, J. (2020). Predicting many properties of a quantum system from very few measurements. Nat. Phys., 16(10), 1050–1057.

[722] Huang, H.-Y., Kueng, R., Torlai, G., Albert, V. V., & Preskill, J. (2022). Provably efficient machine learning for quantum many-body problems. Science, 377(6613), eabk3333.

[723] Hudomal, A., Desaules, J.-Y., Mukherjee, B., Su, G.-X., Halimeh, J. C., & Papić, Z. (2022). Driving quantum many-body scars in the PXP model. Phys. Rev. B, 106, 104302.

[724] Huggins, W. J., O'Gorman, B. A., Rubin, N. C., Reichman, D. R., Babbush, R., & Lee, J. (2022). Unbiasing fermionic quantum Monte Carlo with a quantum computer. Nature, 603(7901), 416–420.

[725] Hyllus, P., Laskowski, W., Krischek, R., Schwemmer, C., Wieczorek, W., Weinfurter, H., Pezzé, L., & Smerzi, A. (2012). Fisher information and multiparticle entanglement. Phys. Rev. A, 85, 022321.

[726] Häffner, H., Roos, C. F., & Blatt, R. (2008). Quantum computing with trapped ions. Phys. Rep., 469(4), 155–203.

[727] Iqbal, M. & Schuch, N. (2021). Entanglement Order Parameters and Critical Behavior for Topological Phase Transitions and Beyond. Physical Review X, 11(4), 041014.

[728] Iqbal, M., Tantivasadakarn, N., Gatterman, T. M., Gerber, J. A., Gilmore, K., Gresh, D., Hankin, A., Hewitt, N., Horst, C. V., Matheny, M., Mengle, T., Neyenhuis, B., Vishwanath, A., Foss-Feig, M., Verresen, R., & Dreyer, H. (2023). Topological Order from Measurements and Feed-Forward on a Trapped Ion Quantum Computer.

[729] Iqbal, M., Tantivasadakarn, N., Verresen, R., Campbell, S. L., Dreiling, J. M., Figgatt, C., Gaebler, J. P., Johansen, J., Mills, M., Moses, S. A., Pino, J. M., Ransford, A., Rowe, M., Siegfried, P., Stutz, R. P., Foss-Feig, M., Vishwanath, A., & Dreyer, H. (2024). Non-Abelian topological order and anyons on a trapped-ion processor. Nature, 626(7999), 505–511.

[730] Irmejs, R., Banuls, M. C., & Cirac, J. I. (2022). Quantum Simulation of Z2 Lattice Gauge theory with minimal requirements.

[731] Islam, R., Ma, R., Preiss, P. M., Eric Tai, M., Lukin, A., Rispoli, M., & Greiner, M. (2015). Measuring entanglement entropy in a quantum many-body system. Nature, 528(7580), 77–83.

[732] Jaksch, D., Cirac, J. I., Zoller, P., Rolston, S. L., Côté, R., & Lukin, M. D. (2000). Fast Quantum Gates for Neutral Atoms. Phys. Rev. Lett., 85(10), 2208–2211.

[733] Jamadagni, A., Kazemi, J., & Weimer, H. (2022). Learning of error statistics for the detection of quantum phases.

[734] Jamadagni, A. & Weimer, H. (2022). Operational definition of topological order. Phys. Rev. B, 106, 085143.

[735] Jandura, S. & Pupillo, G. (2022a). Time-Optimal Two- and Three-Qubit Gates for Rydberg Atoms. Quantum, 6, 712.

[736] Jandura, S. & Pupillo, G. (2022b). Time-Optimal Two- and Three-Qubit Gates for Rydberg Atoms. Quantum, 6, 712.

[737] Jandura, S. & Pupillo, G. (2022c). Time-Optimal Two- and Three-Qubit Gates for Rydberg Atoms. Quantum, 6, 712.

[738] Jenkins, A., Lis, J. W., Senoo, A., McGrew, W. F., & Kaufman, A. M. (2022). Ytterbium Nuclear-Spin Qubits in an Optical Tweezer Array. Physical Review X, 12(2), 021027.

[739] Jin, H.-K., Natori, W. M. H., Pollmann, F., & Knolle, J. (2022). Unveiling the S=3/2 Kitaev honeycomb spin liquids. Nat. Commun., 13(1), 3813.

[740] Johansson, J., Nation, P., & Nori, F. (2013). Qutip 2: A python framework for the dynamics of open quantum systems. Computer Physics Communications, 184(4), 1234–1240.

[741] Jordan, P. & Wigner, E. (1928a). über das Paulische äquivalenzverbot. Z. Phys., 47(9-10), 631–651.

[742] Jordan, P. & Wigner, E. (1928b). Über das Paulische Äquivalenzverbot. Zeitschrift für Physik, 47(9), 631–651. ISBN: 0044-3328.

[743] Joshi, M. K., Kokail, C., van Bijnen, R., Kranzl, F., Zache, T. V., Blatt, R., Roos, C. F., & Zoller, P. (2023). Exploring large-scale entanglement in quantum simulation. Nature, 624(7992), 539–544.

[744] Jotzu, G., Messer, M., Desbuquois, R., Lebrat, M., Uehlinger, T., Greif, D., & Esslinger, T. (2014). Experimental realization of the topological Haldane model with ultracold fermions. Nature, 515(7526), 237–240.

[745] Joy, A. P. & Rosch, A. (2022). Dynamics of visons and thermal hall effect in perturbed kitaev models. Phys. Rev. X, 12, 041004.

[746] Kalinowski, M., Maskara, N., & Lukin, M. D. (2023a). Non-Abelian Floquet Spin Liquids in a Digital Rydberg Simulator. Phys. Rev. X, 13, 031008.

[747] Kalinowski, M., Maskara, N., & Lukin, M. D. (2023b). Non-Abelian Floquet Spin Liquids in a Digital Rydberg Simulator. Phys. Rev. X, 13(3), 031008.

[748] Kandala, A., Mezzacapo, A., Temme, K., Takita, M., Brink, M., Chow, J. M., & Gambetta, J. M. (2017). Hardware-efficient variational quantum eigensolver for small molecules and quantum magnets. Nature, 549(7671), 242–246.

[749] Katz, O., Cetina, M., & Monroe, C. (2022). N-body interactions between trapped ion qubits via spin-dependent squeezing. Phys. Rev. Lett., 129(6), 063603.

[750] Katz, O., Feng, L., Risinger, A., Monroe, C., & Cetina, M. (2023). Demonstration of three- and four-body interactions between trapped-ion spins. Nat. Phys., 19(10), 1452–1458.

[751] Kaufman, A. M., Tai, M. E., Lukin, A., Rispoli, M., Schittko, R., Preiss, P. M., & Greiner, M. (2016). Quantum thermalization through entanglement in an isolated many-body system. Science, 353(6301), 794.

[752] Keesling, A., Omran, A., Levine, H., Bernien, H., Pichler, H., Choi, S., Samajdar, R., Schwartz, S., Silvi, P., Sachdev, S., Zoller, P., Endres, M., Greiner, M., Vuletić, V., & Lukin, M. D. (2019). Quantum Kibble–Zurek mechanism and critical dynamics on a programmable Rydberg simulator. Nature, 568(7751), 207–211.

[753] Khaneja, N., Reiss, T., Kehlet, C., Schulte-Herbrüggen, T., & Glaser, S. J. (2005). Optimal control of coupled spin dynamics: design of NMR pulse sequences by gradient ascent algorithms. J. Magn. Reson., 172(2), 296–305.

[754] Khemani, V., Laumann, C. R., & Chandran, A. (2019). Signatures of integrability in the dynamics of Rydberg-blockaded chains. Phys. Rev. B, 99, 161101.

[755] Khemani, V., Lazarides, A., Moessner, R., & Sondhi, S. L. (2016a). Phase structure of driven quantum systems. Phys. Rev. Lett., 116, 250401.

[756] Khemani, V., Lazarides, A., Moessner, R., & Sondhi, S. L. (2016b). Phase Structure of Driven Quantum Systems. Phys. Rev. Lett., 116, 250401.

[757] Khemani, V., Moessner, R., & Sondhi, S. L. (2020). Comment on "quantum time crystals from hamiltonians with long-range interactions".

[758] Kim, Y., Eddins, A., Anand, S., Wei, K. X., Van Den Berg, E., Rosenblatt, S., Nayfeh, H., Wu, Y., Zaletel, M., Temme, K., & Kandala, A. (2023). Evidence for the utility of quantum computing before fault tolerance. Nature, 618(7965), 500–505.

[759] Kitaev, A. (2003a). Fault-tolerant quantum computation by anyons. Annals of Physics, 303(1), 2–30. Publisher: Elsevier BV.

[760] Kitaev, A. (2003b). Fault-tolerant quantum computation by anyons. Ann. Phys., 303(1), 2–30.

[761] Kitaev, A. (2006a). Anyons in an exactly solved model and beyond. Ann. Phys., 321(1), 2–111.

[762] Kitaev, A. (2006b). Anyons in an exactly solved model and beyond. Ann. Phys., 321(1), 2–111.

[763] Kitaev, A. (2015). A simple model of quantum holography.

[764] Kitaev, A. & Preskill, J. (2006). Topological Entanglement Entropy. Phys. Rev. Lett., 96(11), 110404. Publisher: American Physical Society.

[765] Kivlichan, I. D., McClean, J., Wiebe, N., Gidney, C., Aspuru-Guzik, A., Chan, G. K.-L., & Babbush, R. (2018). Quantum Simulation of Electronic Structure with Linear Depth and Connectivity. Physical Review Letters, 120(11), 110501.

[766] Knap, M., Kantian, A., Giamarchi, T., Bloch, I., Lukin, M. D., & Demler, E. (2013). Probing real-space and time resolved correlation functions with many-body Ramsey interferometry. Physical Review Letters, 111(14), 147205. arXiv:1307.0006 [cond-mat, physics:quant-ph].

[767] Kokail, C., Maier, C., van Bijnen, R., Brydges, T., Joshi, M. K., Jurcevic, P., Muschik, C. A., Silvi, P., Blatt, R., Roos, C. F., & Zoller, P. (2019). Self-verifying variational quantum simulation of lattice models. Nature, 569(7756), 355–360.

[768] Kokail, C., Sundar, B., Zache, T. V., Elben, A., Vermersch, B., Dalmonte, M., van Bijnen, R., & Zoller, P. (2021). Quantum Variational Learning of the Entanglement Hamiltonian. Phys. Rev. Lett., 127, 170501.

[769] König, R., Reichardt, B. W., & Vidal, G. (2009). Exact entanglement renormalization for string-net models. Phys. Rev. B, 79, 195123.

[770] Kornjaca, M., Samajdar, R., Macrì, T., Gemelke, N., Wang, S.-T., & Liu, F. (2023). Trimer quantum spin liquid in a honeycomb array of Rydberg atoms. Communications Physics, 6(1), 358.

[771] Kotaru, S., Kähler, S., Alessio, M., & Krylov, A. I. (2023). Magnetic exchange interactions in binuclear and tetranuclear iron (iii) complexes described by spin-flip dft and heisenberg effective hamiltonians. J. Comput. Chem., 44(3), 367–380.

[772] Kozin, V. K. & Kyriienko, O. (2019). Quantum time crystals from hamiltonians with long-range interactions. Phys. Rev. Lett., 123, 210602.

[773] Kraus, C. V. & Cirac, J. I. (2010). Generalized Hartree–Fock theory for interacting fermions in lattices: numerical methods. New J. Phys., 12(11), 113004.

[774] Krewald, V., Neese, F., & Pantazis, D. A. (2013). On the Magnetic and Spectroscopic Properties of High-Valent Mn $_3$ CaO $_4$ Cubanes as Structural Units of Natural and Artificial Water-Oxidizing Catalysts. J. Am. Chem. Soc., 135(15), 5726–5739.

[775] Krewald, V., Retegan, M., Cox, N., Messinger, J., Lubitz, W., DeBeer, S., Neese, F., & Pantazis, D. A. (2015). Metal oxidation states in biological water splitting. Chem. Sci., 6(3), 1676–1695.

[776] Krewald, V., Retegan, M., Neese, F., Lubitz, W., Pantazis, D. A., & Cox, N. (2016). Spin State as a Marker for the Structural Evolution of Nature's Water-Splitting Catalyst. Inorg. Chem., 55(2), 488–501.

[777] Kruckenhauser, A., Bijnen, R. v., Zache, T. V., Liberto, M. D., & Zoller, P. (2022). High-dimensional SO(4)-symmetric Rydberg manifolds for quantum simulation. Quantum Sci. Technol., 8(1), 015020.

[778] Kuwahara, T., Mori, T., & Saito, K. (2016). Floquet–Magnus theory and generic transient dynamics in periodically driven many-body quantum systems. Annals of Physics, 367, 96–124.

[779] Köylüoğlu, N. U., Maskara, N., Feldmeier, J., & Lukin, M. D. (2024). Floquet engineering of interactions and entanglement in periodically driven Rydberg chains.

[780] Labuhn, H., Barredo, D., Ravets, S., de Léséleuc, S., Macrì, T., Lahaye, T., & Browaeys, A. (2016a). Tunable two-dimensional arrays of single Rydberg atoms for realizing quantum Ising models. Nature, 534(7609), 667–670.

[781] Labuhn, H., Barredo, D., Ravets, S., de Léséleuc, S., Macrì, T., Lahaye, T., & Browaeys, A. (2016b). Tunable two-dimensional arrays of single Rydberg atoms for realizing quantum Ising models. Nature, 534(7609), 667–670.

[782] Lan, Z., van Horssen, M., Powell, S., & Garrahan, J. P. (2018). Quantum Slow Relaxation and Metastability due to Dynamical Constraints. Phys. Rev. Lett., 121, 040603.

[783] Langen, T., Erne, S., Geiger, R., Rauer, B., Schweigler, T., Kuhnert, M., Rohringer, W., Mazets, I. E., Gasenzer, T., & Schmiedmayer, J. (2015). Experimental observation of a generalized Gibbs ensemble. Science, 348(6231), 207–211.

[784] Lazarides, A., Das, A., & Moessner, R. (2014). Periodic Thermodynamics of Isolated Quantum Systems. Phys. Rev. Lett., 112(15), 150401.

[785] Lee, P. A., Nagaosa, N., & Wen, X.-G. (2006). Doping a Mott insulator: Physics of high-temperature superconductivity. Rev. Mod. Phys., 78(1), 17–85.

[786] Lee, Y. A. & Vidal, G. (2013). Entanglement negativity and topological order. Physical Review A, 88(4), 042318.

[787] Lensky, Y. D., Kechedzhi, K., Aleiner, I., & Kim, E.-A. (2022). Graph gauge theory of mobile non-Abelian anyons in a qubit stabilizer code.

[788] Lerose, A., Marino, J., Gambassi, A., & Silva, A. (2019). Prethermal quantum many-body kapitza phases of periodically driven spin systems. Physical Review B, 100(10).

[789] Lesanovsky, I. & Katsura, H. (2012). Interacting Fibonacci anyons in a Rydberg gas. Phys. Rev. A, 86, 041601.

[790] Levin, M. & Wen, X.-G. (2006). Detecting Topological Order in a Ground State Wave Function. Phys. Rev. Lett., 96(11), 110405. Publisher: American Physical Society.

[791] Levin, M. A. & Wen, X.-G. (2005). String-net condensation: A physical mechanism for topological phases. Phys. Rev. B, 71, 045110.

[792] Levine, H., Bluvstein, D., Keesling, A., Wang, T. T., Ebadi, S., Semeghini, G., Omran, A., Greiner, M., Vuletić, V., & Lukin, M. D. (2022a). Dispersive optical systems for scalable Raman driving of hyperfine qubits. Phys. Rev. A, 105, 032618.

[793] Levine, H., Bluvstein, D., Keesling, A., Wang, T. T., Ebadi, S., Semeghini, G., Omran, A., Greiner, M., Vuletić, V., & Lukin, M. D. (2022b). Dispersive optical systems for scalable raman driving of hyperfine qubits. Phys. Rev. A, 105, 032618.

[794] Levine, H., Keesling, A., Semeghini, G., Omran, A., Wang, T. T., Ebadi, S., Bernien, H., Greiner, M., Vuletić, V., Pichler, H., & Lukin, M. D. (2019a). Parallel Implementation of High-Fidelity Multiqubit Gates with Neutral Atoms. Phys. Rev. Lett., 123, 170503.

[795] Levine, H., Keesling, A., Semeghini, G., Omran, A., Wang, T. T., Ebadi, S., Bernien, H., Greiner, M., Vuletić, V., Pichler, H., & Lukin, M. D. (2019b). Parallel Implementation of High-Fidelity Multiqubit Gates with Neutral Atoms. Phys. Rev. Lett., 123(17), 170503.

[796] Levine, H., Keesling, A., Semeghini, G., Omran, A., Wang, T. T., Ebadi, S., Bernien, H., Greiner, M., Vuletić, V., Pichler, H., & Lukin, M. D. (2019c). Parallel Implementation of High-Fidelity Multiqubit Gates with Neutral Atoms. Phys. Rev. Lett., 123(17), 170503.

[797] Li, X., Yu, H., Lou, F., Feng, J., Whangbo, M.-H., & Xiang, H. (2021). Spin Hamiltonians in Magnets: Theories and Computations. Molecules, 26(4), 803.

[798] Li, Z., Guo, S., Sun, Q., & Chan, G. K.-L. (2019). Electronic landscape of the P-cluster of nitrogenase as revealed through many-electron quantum wavefunction simulations. Nat. Chem., 11(11), 1026–1033.

[799] Lieb, E. H. (1994). Flux phase of the half-filled band. Phys. Rev. Lett., 73, 2158–2161.

[800] Lin, C.-J., Chandran, A., & Motrunich, O. I. (2020). Slow thermalization of exact quantum many-body scar states under perturbations. Phys. Rev. Research, 2, 033044.

[801] Lin, L. (2022). Lecture notes on quantum algorithms for scientific computation.

[802] Lin, L. & Tong, Y. (2022). Heisenberg-limited ground state energy estimation for early fault-tolerant quantum computers. PRX Quantum, 3(1), 010318. arXiv:2102.11340 [quant-ph].

[803] Lin, R., Zhong, H.-S., Li, Y., Zhao, Z.-R., Zheng, L.-T., Hu, T.-R., Wu, H.-M., Wu, Z., Ma, W.-J., Gao, Y., Zhu, Y.-K., Su, Z.-F., Ouyang, W.-L., Zhang, Y.-C., Rui, J., Chen, M.-C., Lu, C.-Y., & Pan, J.-W. (2024). AI-enabled rapid assembly of thousands of defect-free neutral atom arrays with constant-time-overhead.

[804] Linnemann, D., Strobel, H., Muessel, W., Schulz, J., Lewis-Swan, R. J., Kheruntsyan, K. V., & Oberthaler, M. K. (2016). Quantum-Enhanced Sensing Based on Time Reversal of Nonlinear Dynamics. Phys. Rev. Lett., 117, 013001.

[805] Lis, J. W., Senoo, A., McGrew, W. F., Rönchen, F., Jenkins, A., & Kaufman, A. M. (2023). Mid-circuit operations using the omg-architecture in neutral atom arrays. arXiv:2305.19266 [cond-mat, physics:physics, physics:quant-ph].

[806] Liu, S. & Xue, Z.-Y. (2013). Probing non-Abelian anyonic statistics with cold atoms in an optical lattice. J. Opt. Soc. Am. B, 30(6), 1720.

[807] Ljubotina, M., Roos, B., Abanin, D. A., & Serbyn, M. (2022a). Optimal Steering of Matrix Product States and Quantum Many-Body Scars. PRX Quantum, 3, 030343.

[808] Ljubotina, M., Roos, B., Abanin, D. A., & Serbyn, M. (2022b). Optimal Steering of Matrix Product States and Quantum Many-Body Scars. PRX Quantum, 3, 030343.

[809] Low, G. H. & Chuang, I. L. (2019). Hamiltonian Simulation by Qubitization. Quantum, 3, 163.

[810] Lu, S., Bañuls, M. C., & Cirac, J. I. (2021). Algorithms for quantum simulation at finite energies. PRX Quantum, 2(2), 020321.

[811] Lu, T.-C., Lessa, L. A., Kim, I. H., & Hsieh, T. H. (2022). Measurement as a Shortcut to Long-Range Entangled Quantum Matter. PRX Quantum, 3(4), 040337.

[812] Lu, T.-C. & Vijay, S. (2022). Characterizing long-range entanglement in a mixed state through an emergent order on the entangling surface.

[813] Ma, H., Govoni, M., & Galli, G. (2020). Quantum simulations of materials on near-term quantum computers. npj Computational Materials, 6(1), 85.

[814] Ma, S., Burgers, A. P., Liu, G., Wilson, J., Zhang, B., & Thompson, J. D. (2022). Universal Gate Operations on Nuclear Spin Qubits in an Optical Tweezer Array of ^{171}Yb Atoms. Phys. Rev. X, 12(2), 021028.

[815] Ma, S., Liu, G., Peng, P., Zhang, B., Jandura, S., Claes, J., Burgers, A. P., Pupillo, G., Puri, S., & Thompson, J. D. (2023a). High-fidelity gates and mid-circuit erasure conversion in an atomic qubit. Nature, 622(7982), 279–284.

[816] Ma, S., Liu, G., Peng, P., Zhang, B., Jandura, S., Claes, J., Burgers, A. P., Pupillo, G., Puri, S., & Thompson, J. D. (2023b). High-fidelity gates and mid-circuit erasure conversion in an atomic qubit. Nature, 622(7982), 279–284.

[817] Ma, S., Liu, G., Peng, P., Zhang, B., Jandura, S., Claes, J., Burgers, A. P., Pupillo, G., Puri, S., & Thompson, J. D. (2023c). High-fidelity gates and mid-circuit erasure conversion in an atomic qubit. Nature, 622(7982), 279–284.

[818] Machado, F., Else, D. V., Kahanamoku-Meyer, G. D., Nayak, C., & Yao, N. Y. (2020). Long-Range Prethermal Phases of Nonequilibrium Matter. Phys. Rev. X, 10(1), 011043.

[819] Magnus, W. (1954). On the exponential solution of differential equations for a linear operator. Comm. Pure Appl. Math., 7(4), 649–673.

[820] Maldacena, J. (2023). A simple quantum system that describes a black hole.

[821] Malrieu, J. P., Caballol, R., Calzado, C. J., de Graaf, C., & Guihéry, N. (2014). Magnetic Interactions in Molecules and Highly Correlated Materials: Physical Content, Analytical Derivation, and Rigorous Extraction of Magnetic Hamiltonians. Chem. Rev., 114(1), 429–492.

[822] Manetsch, H. J., Nomura, G., Bataille, E., Leung, K. H., Lv, X., & Endres, M. (2024). A tweezer array with 6100 highly coherent atomic qubits.

[823] Manmana, S. R., Stoudenmire, E. M., Hazzard, K. R. A., Rey, A. M., & Gorshkov, A. V. (2013). Topological phases in ultracold polar-molecule quantum magnets. Phys. Rev. B, 87(8), 081106(R).

[824] Manovitz, T., Li, S. H., Ebadi, S., Samajdar, R., Geim, A. A., Evered, S. J., Bluvstein, D., Zhou, H., Köylüoğlu, N. U., Feldmeier, J., Dolgirev, P. E., Maskara, N., Kalinowski, M., Sachdev, S., Huse, D. A., Greiner, M., Vuletić, V., & Lukin, M. D. (2024). Quantum coarsening and collective dynamics on a programmable quantum simulator.

[825] Mardirossian, N. & Head-Gordon, M. (2017). Thirty years of density functional theory in computational chemistry: an overview and extensive assessment of 200 density functionals. Mol. Phys., 115(19), 2315–2372.

[826] Marin Bukov, L. D. & Polkovnikov, A. (2015). Universal high-frequency behavior of periodically driven systems: from dynamical stabilization to Floquet engineering. Advances in Physics, 64(2), 139–226.

[827] Martinez, E. A., Muschik, C. A., Schindler, P., Nigg, D., Erhard, A., Heyl, M., Hauke, P., Dalmonte, M., Monz, T., Zoller, P., & Blatt, R. (2016). Real-time dynamics of lattice gauge theories with a few-qubit quantum computer. Nature, 534(7608), 516–519.

[828] Martyn, J. M., Rossi, Z. M., Tan, A. K., & Chuang, I. L. (2021). Grand Unification of Quantum Algorithms. PRX Quantum, 2(4), 040203.

[829] Maskara, N., Michailidis, A. A., Ho, W. W., Bluvstein, D., Choi, S., Lukin, M. D., & Serbyn, M. (2021a). Discrete Time-Crystalline Order Enabled by Quantum Many-Body Scars: Entanglement Steering via Periodic Driving. Phys. Rev. Lett., 127, 090602.

[830] Maskara, N., Michailidis, A. A., Ho, W. W., Bluvstein, D., Choi, S., Lukin, M. D., & Serbyn, M. (2021b). Discrete Time-Crystalline Order Enabled by Quantum Many-Body Scars: Entanglement Steering via Periodic Driving. Phys. Rev. Lett., 127, 090602.

[831] Maskara, N., Ostermann, S., Shee, J., Kalinowski, M., Gomez, A. M., Bravo, R. A., Wang, D. S., Krylov, A. I., Yao, N. Y., Head-Gordon, M., Lukin, M. D., & Yelin, S. F. (2023a). Programmable simulations of molecules and materials with reconfigurable quantum processors.

[832] Maskara, N., Ostermann, S., Shee, J., Kalinowski, M., Gomez, A. M., Bravo, R. A., Wang, D. S., Krylov, A. I., Yao, N. Y., Head-Gordon, M., Lukin, M. D., & Yelin, S. F. (2023b). Programmable Simulations of Molecules and Materials with Reconfigurable Quantum Processors.

[833] Maskara, N., Ostermann, S., Shee, J., Kalinowski, M., Gomez, A. M., Bravo, R. A., Wang, D. S., Krylov, A. I., Yao, N. Y., Head-Gordon, M., Lukin, M. D., & Yelin, S. F. (2023c). Programmable Simulations of Molecules and Materials with Reconfigurable Quantum Processors.

[834] Mayhall, N. J. & Head-Gordon, M. (2014). Computational quantum chemistry for single Heisenberg spin couplings made simple: Just one spin flip required. J. Chem. Phys., 141(13), 134111.

[835] Mayhall, N. J. & Head-Gordon, M. (2015). Computational Quantum Chemistry for Multiple-Site Heisenberg Spin Couplings Made Simple: Still Only One Spin–Flip Required. J. Phys. Chem. Lett., 6(10), 1982–1988.

[836] Mazurenko, A., Chiu, C. S., Ji, G., Parsons, M. F., Kanász-Nagy, M., Schmidt, R., Grusdt, F., Demler, E., Greif, D., & Greiner, M. (2017). A cold-atom Fermi–Hubbard antiferromagnet. Nature, 545(7655), 462–466.

[837] McArdle, S., Endo, S., Aspuru-Guzik, A., Benjamin, S. C., & Yuan, X. (2020). Quantum computational chemistry. Rev. Mod. Phys., 92(1), 015003.

[838] McClean, J. R., Boixo, S., Smelyanskiy, V. N., Babbush, R., & Neven, H. (2018). Barren plateaus in quantum neural network training landscapes. Nature communications, 9(1), 1–6.

[839] McClean, J. R., Romero, J., Babbush, R., & Aspuru-Guzik, A. (2016). The theory of variational hybrid quantum-classical algorithms. New Journal of Physics, 18(2), 023023.

[840] Meinert, F., Mark, M. J., Lauber, K., Daley, A. J., & Nägerl, H.-C. (2016). Floquet Engineering of Correlated Tunneling in the Bose-Hubbard Model with Ultracold Atoms. Phys. Rev. Lett., 116, 205301.

[841] Mi, X., Ippoliti, M., Quintana, C., Greene, A., Chen, Z., Gross, J., Arute, F., Arya, K., Atalaya, J., Babbush, R., Bardin, J. C., Basso, J., Bengtsson, A., Bilmes, A., Bourassa, A., Brill, L., Broughton, M., Buckley, B. B., Buell, D. A., Burkett, B., Bushnell, N., Chiaro, B., Collins, R., Courtney, W., Debroy, D., Demura, S., Derk, A. R., Dunsworth, A., Eppens, D., Erickson, C., Farhi, E., Fowler, A. G., Foxen, B., Gidney, C., Giustina, M., Harrigan, M. P., Harrington, S. D., Hilton, J., Ho, A., Hong, S., Huang, T., Huff, A., Huggins, W. J., Ioffe, L. B., Isakov, S. V., Iveland, J., Jeffrey, E., Jiang, Z., Jones, C., Kafri, D., Khattar, T., Kim, S., Kitaev, A., Klimov, P. V., Korotkov, A. N., Kostritsa, F., Landhuis, D., Laptev, P., Lee, J., Lee, K., Locharla, A., Lucero, E., Martin, O., McClean, J. R., McCourt, T., McEwen, M., Miao, K. C., Mohseni, M., Montazeri, S., Mruczkiewicz, W., Naaman, O., Neeley, M., Neill, C., Newman, M., Niu, M. Y., O'Brien, T. E., Opremcak, A., Ostby, E., Pato, B., Petukhov, A., Rubin, N. C., Sank, D., Satzinger, K. J., Shvarts, V., Su, Y., Strain, D., Szalay, M., Trevithick, M. D., Villalonga, B., White, T., Yao, Z. J., Yeh, P., Yoo, J., Zalcman, A., Neven, H., Boixo, S., Smelyanskiy, V., Megrant, A., Kelly, J., Chen, Y., Sondhi, S. L., Moessner, R., Kechedzhi, K., Khemani, V., & Roushan, P. (2022a). Time-crystalline eigenstate order on a quantum processor. Nature, 601(7894), 531–536.

[842] Mi, X., Sonner, M., Niu, M. Y., Lee, K. W., Foxen, B., Acharya, R., Aleiner, I., Andersen, T. I., Arute, F., Arya, K., Asfaw, A., Atalaya, J., Bardin, J. C., Basso, J., Bengtsson, A., Bortoli, G., Bourassa, A., Brill, L., Broughton, M., Buckley, B. B., Buell, D. A., Burkett, B., Bushnell, N., Chen, Z., Chiaro, B., Collins, R., Conner, P., Courtney, W., Crook, A. L., Debroy, D. M., Demura, S., Dunsworth, A., Eppens, D., Erickson, C., Faoro, L., Farhi, E., Fatemi, R., Flores, L., Forati, E., Fowler, A. G., Giang, W., Gidney, C., Gilboa, D.,

Giustina, M., Dau, A. G., Gross, J. A., Habegger, S., Harrigan, M. P., Hoffmann, M., Hong, S., Huang, T., Huff, A., Huggins, W. J., Ioffe, L. B., Isakov, S. V., Iveland, J., Jeffrey, E., Jiang, Z., Jones, C., Kafri, D., Kechedzhi, K., Khattar, T., Kim, S., Kitaev, A. Y., Klimov, P. V., Klots, A. R., Korotkov, A. N., Kostritsa, F., Kreikebaum, J. M., Landhuis, D., Laptev, P., Lau, K.-M., Lee, J., Laws, L., Liu, W., Locharla, A., Martin, O., McClean, J. R., McEwen, M., Meurer Costa, B., Miao, K. C., Mohseni, M., Montazeri, S., Morvan, A., Mount, E., Mruczkiewicz, W., Naaman, O., Neeley, M., Neill, C., Newman, M., O'Brien, T. E., Opremcak, A., Petukhov, A., Potter, R., Quintana, C., Rubin, N. C., Saei, N., Sank, D., Sankaragomathi, K., Satzinger, K. J., Schuster, C., Shearn, M. J., Shvarts, V., Strain, D., Su, Y., Szalay, M., Vidal, G., Villalonga, B., Vollgraff-Heidweiller, C., White, T., Yao, Z., Yeh, P., Yoo, J., Zalcman, A., Zhang, Y., Zhu, N., Neven, H., Bacon, D., Hilton, J., Lucero, E., Babbush, R., Boixo, S., Megrant, A., Chen, Y., Kelly, J., Smelyanskiy, V., Abanin, D. A., & Roushan, P. (2022b). Noise-resilient edge modes on a chain of superconducting qubits. Science, 378(6621), 785–790.

[843] Michailidis, A. A., Turner, C. J., Papić, Z., Abanin, D. A., & Serbyn, M. (2020a). Slow quantum thermalization and many-body revivals from mixed phase space. Phys. Rev. X, 10, 011055.

[844] Michailidis, A. A., Turner, C. J., Papić, Z., Abanin, D. A., & Serbyn, M. (2020b). Stabilizing two-dimensional quantum scars by deformation and synchronization. Phys. Rev. Research, 2, 022065.

[845] Micheli, A., Brennen, G. K., & Zoller, P. (2006). A toolbox for lattice-spin models with polar molecules. Nat. Phys., 2(5), 341–347.

[846] Mil, A., Zache, T. V., Hegde, A., Xia, A., Bhatt, R. P., Oberthaler, M. K., Hauke, P., Berges, J., & Jendrzejewski, F. (2020). A scalable realization of local U(1) gauge invariance in cold atomic mixtures. Science, 367(6482), 1128–1130.

[847] Mildenberger, J., Mruczkiewicz, W., Halimeh, J. C., Jiang, Z., & Hauke, P. (2022). Probing confinement in a $\mathbb{Z}_2$ lattice gauge theory on a quantum computer.

[848] Minami, K. (2019). Honeycomb lattice Kitaev model with Wen–Toric-code interactions, and anyon excitations. Nuclear Physics B, 939, 465–484.

[849] Misguich, G., Serban, D., & Pasquier, V. (2002a). Quantum Dimer Model on the Kagome Lattice: Solvable Dimer-Liquid and Ising Gauge Theory. Phys. Rev. Lett., 89, 137202.

[850] Misguich, G., Serban, D., & Pasquier, V. (2002b). Quantum Dimer Model on the Kagome Lattice: Solvable Dimer-Liquid and Ising Gauge Theory. Phys. Rev. Lett., 89(13), 137202. Publisher: American Physical Society.

[851] Miyake, H., Siviloglou, G. A., Kennedy, C. J., Burton, W. C., & Ketterle, W. (2013). Realizing the Harper Hamiltonian with Laser-Assisted Tunneling in Optical Lattices. Phys. Rev. Lett., 111, 185302.

[852] Mizuta, K., Takasan, K., & Kawakami, N. (2020). Exact Floquet quantum many-body scars under Rydberg blockade. Phys. Rev. Research, 2, 033284.

[853] Moessner, R., Sondhi, S. L., & Chandra, P. (2001a). Phase diagram of the hexagonal lattice quantum dimer model. Phys. Rev. B, 64, 144416.

[854] Moessner, R., Sondhi, S. L., & Fradkin, E. (2001b). Short-ranged resonating valence bond physics, quantum dimer models, and Ising gauge theories. Phys. Rev. B, 65, 024504.

[855] Monroe, C., Campbell, W., Duan, L.-M., Gong, Z.-X., Gorshkov, A., Hess, P., Islam, R., Kim, K., Linke, N., Pagano, G., Richerme, P., Senko, C., & Yao, N. (2021). Programmable quantum simulations of spin systems with trapped ions. Rev. Mod. Phys., 93(2), 025001.

[856] Monz, T., Schindler, P., Barreiro, J. T., Chwalla, M., Nigg, D., Coish, W. A., Harlander, M., Hänsel, W., Hennrich, M., & Blatt, R. (2011). 14-Qubit Entanglement: Creation and Coherence. Phys. Rev. Lett., 106, 130506.

[857] Morgado, M. & Whitlock, S. (2021). Quantum simulation and computing with Rydberg-interacting qubits. AVS Quantum Science, 3(2), 023501.

[858] Mori, T., Kuwahara, T., & Saito, K. (2016). Rigorous Bound on Energy Absorption and Generic Relaxation in Periodically Driven Quantum Systems. Phys. Rev. Lett., 116, 120401.

[859] Moses, S. A., Baldwin, C. H., Allman, M. S., Ancona, R., Ascarrunz, L., Barnes, C., Bartolotta, J., Bjork, B., Blanchard, P., Bohn, M., Bohnet, J. G., Brown, N. C., Burdick, N. Q., Burton, W. C., Campbell, S. L., au2, J. P. C. I., Carron, C., Chambers, J., Chan, J. W., Chen, Y. H., Chernoguzov, A., Chertkov, E., Colina, J., Curtis, J. P., Daniel, R., DeCross, M., Deen, D., Delaney, C., Dreiling, J. M., Ertsgaard, C. T., Esposito, J., Estey, B., Fabrikant, M., Figgatt, C., Foltz, C., Foss-Feig, M., Francois, D., Gaebler, J. P., Gatterman, T. M., Gilbreth, C. N., Giles, J., Glynn, E., Hall, A., Hankin, A. M., Hansen, A., Hayes, D., Higashi, B., Hoffman, I. M., Horning, B., Hout, J. J., Jacobs, R., Johansen, J., Jones, L., Karcz, J., Klein, T., Lauria, P., Lee, P., Liefer, D., Lytle, C., Lu, S. T., Lucchetti, D., Malm, A., Matheny, M., Mathewson, B., Mayer, K., Miller, D. B., Mills, M., Neyenhuis, B., Nugent, L., Olson, S., Parks, J., Price, G. N., Price, Z., Pugh, M., Ransford, A., Reed, A. P., Roman, C., Rowe, M., Ryan-Anderson, C., Sanders, S., Sedlacek, J., Shevchuk, P., Siegfried, P., Skripka, T., Spaun, B., Sprenkle, R. T., Stutz, R. P., Swallows, M., Tobey, R. I., Tran, A., Tran, T., Vogt, E., Volin, C., Walker, J., Zolot, A. M., & Pino, J. M. (2023). A race track trapped-ion quantum processor.

[860] Motta, M. & Rice, J. E. (2022). Emerging quantum computing algorithms for quantum chemistry. Wiley Interdiscip. Rev. Comput. Mol. Sci., 12(3), e1580.

[861] Moudgalya, S., Bernevig, B. A., & Regnault, N. (2020). Quantum many-body scars in a landau level on a thin torus. Physical Review B, 102(19).

[862] Moudgalya, S., Rachel, S., Bernevig, B. A., & Regnault, N. (2018). Exact excited states of nonintegrable models. Physical Review B, 98(23).

[863] Mukherjee, B., Nandy, S., Sen, A., Sen, D., & Sengupta, K. (2020). Collapse and revival of quantum many-body scars via Floquet engineering. Phys. Rev. B, 101, 245107.

[864] Nandkishore, R. & Huse, D. A. (2015). Many-body localization and thermalization in quantum statistical mechanics. Annu. Rev. Condens. Matter Phys., 6(1), 15–38.

[865] Napp, J. C., La Placa, R. L., Dalzell, A. M., Brandão, F. G. S. L., & Harrow, A. W. (2022). Efficient classical simulation of random shallow 2d quantum circuits. Phys. Rev. X, 12, 021021.

[866] Nayak, C., Simon, S. H., Stern, A., Freedman, M., & Das Sarma, S. (2008a). Non-abelian anyons and topological quantum computation. Rev. Mod. Phys., 80, 1083–1159.

[867] Nayak, C., Simon, S. H., Stern, A., Freedman, M., & Das Sarma, S. (2008b). Non-Abelian anyons and topological quantum computation. Rev. Mod. Phys., 80(3), 1083–1159.

[868] Nguyen, M.-T., Liu, J.-G., Wurtz, J., Lukin, M. D., Wang, S.-T., & Pichler, H. (2023). Quantum Optimization with Arbitrary Connectivity Using Rydberg Atom Arrays. PRX Quantum, 4, 010316.

[869] Nigmatullin, R., Hemery, K., Ghanem, K., Moses, S., Gresh, D., Siegfried, P., Mills, M., Gatterman, T., Hewitt, N., Granet, E., & Dreyer, H. (2024). Experimental Demonstration of Break-Even for the Compact Fermionic Encoding.

[870] Nishad, N., Keselman, A., Lahaye, T., Browaeys, A., & Tsesses, S. (2023). Quantum simulation of generic spin-exchange models in Floquet-engineered Rydberg-atom arrays. Phys. Rev. A, 108, 053318.

[871] Omran, A., Levine, H., Keesling, A., Semeghini, G., Wang, T. T., Ebadi, S., Bernien, H., Zibrov, A. S., Pichler, H., Choi, S., Cui, J., Rossignolo, M., Rembold, P., Montangero, S., Calarco, T., Endres, M., Greiner, M., Vuletić, V., & Lukin, M. D. (2019a). Generation and manipulation of Schrödinger cat states in Rydberg atom arrays. Science, 365(6453), 570–574.

[872] Omran, A., Levine, H., Keesling, A., Semeghini, G., Wang, T. T., Ebadi, S., Bernien, H., Zibrov, A. S., Pichler, H., Choi, S., Cui, J., Rossignolo, M., Rembold, P., Montangero, S., Calarco, T., Endres, M., Greiner, M., Vuletić, V., & Lukin, M. D. (2019b). Generation and manipulation of Schrödinger cat states in Rydberg atom arrays. Science, 365(6453), 570–574.

[873] Orland, P. & Rohrlich, D. (1990). Lattice gauge magnets: Local isospin from spin. Nuclear Physics B, 338(3), 647–672.

[874] Orús, R. (2014). A practical introduction to tensor networks: Matrix product states and projected entangled pair states. Annals of Physics, 349, 117–158.

[875] Ott, R., González-Cuadra, D., Zache, T. V., Zoller, P., Kaufman, A. M., & Pichler, H. (2024). Error-corrected fermionic quantum processors with neutral atoms.

[876] O'Brien, T. E., Tarasinski, B., & Terhal, B. M. (2019). Quantum phase estimation of multiple eigenvalues for small-scale (noisy) experiments. New J. Phys., 21(2), 023022.

[877] Pagano, A., Weber, S., Jaschke, D., Pfau, T., Meinert, F., Montangero, S., & Büchler, H. P. (2022a). Error budgeting for a controlled-phase gate with strontium-88 rydberg atoms. Phys. Rev. Res., 4, 033019.

[878] Pagano, A., Weber, S., Jaschke, D., Pfau, T., Meinert, F., Montangero, S., & Büchler, H. P. (2022b). Error budgeting for a controlled-phase gate with strontium-88 rydberg atoms. Phys. Rev. Res., 4, 033019.

[879] Pantazis, D. A., Orio, M., Petrenko, T., Zein, S., Lubitz, W., Messinger, J., & Neese, F. (2009). Structure of the oxygen-evolving complex of photosystem II: information on the S2 state through quantum chemical calculation of its magnetic properties. Phys. Chem. Chem. Phys., 11(31), 6788.

[880] Pastori, L., Olsacher, T., Kokail, C., & Zoller, P. (2022). Characterization and Verification of Trotterized Digital Quantum Simulation Via Hamiltonian and Liouvillian Learning. PRX Quantum, 3(3), 030324.

[881] Paul, S., Neese, F., & Pantazis, D. A. (2017). Structural models of the biological oxygen-evolving complex: achievements, insights, and challenges for biomimicry. Green Chem., 19(10), 2309–2325.

[882] Pedrozo-Peñafiel, E., Colombo, S., Shu, C., Adiyatullin, A. F., Li, Z., Mendez, E., Braverman, B., Kawasaki, A., Akamatsu, D., Xiao, Y., & Vuletić, V. (2020). Entanglement on an optical atomic-clock transition. Nature, 588(7838), 414–418.

[883] Peng, P., Huang, X., Yin, C., Joseph, L., Ramanathan, C., & Cappellaro, P. (2022). Deep Reinforcement Learning for Quantum Hamiltonian Engineering. Phys. Rev. Appl., 18, 024033.

[884] Peres, A. (1996). Separability Criterion for Density Matrices. Physical Review Letters, 77(8), 1413–1415.

[885] Peruzzo, A., McClean, J., Shadbolt, P., Yung, M.-H., Zhou, X.-Q., Love, P. J., Aspuru-Guzik, A., & O'Brien, J. L. (2014). A variational eigenvalue solver on a photonic quantum processor. Nat. Commun., 5(1), 4213.

[886] Pesah, A., Cerezo, M., Wang, S., Volkoff, T., Sornborger, A. T., & Coles, P. J. (2021). Absence of barren plateaus in quantum convolutional neural networks. Phys. Rev. X, 11, 041011.

[887] Pezzè, L., Smerzi, A., Oberthaler, M. K., Schmied, R., & Treutlein, P. (2018). Quantum metrology with nonclassical states of atomic ensembles. Rev. Mod. Phys., 90, 035005.

[888] Pichler, H., Wang, S.-T., Zhou, L., Choi, S., & Lukin, M. D. (2018a). Quantum Optimization for Maximum Independent Set Using Rydberg Atom Arrays.

[889] Pichler, H., Wang, S.-T., Zhou, L., Choi, S., & Lukin, M. D. (2018b). Quantum optimization for maximum independent set using Rydberg atom arrays.

[890] Pino, J. M., Dreiling, J. M., Figgatt, C., Gaebler, J. P., Moses, S. A., Allman, M., Baldwin, C., Foss-Feig, M., Hayes, D., Mayer, K., et al. (2021). Demonstration of the trapped-ion quantum ccd computer architecture. Nature, 592(7853), 209–213.

[891] Pizzi, A., Knolle, J., & Nunnenkamp, A. (2021). Higher-order and fractional discrete time crystals in clean long-range interacting systems. Nature Communications, 12(1).

[892] Pizzi, A., Malz, D., De Tomasi, G., Knolle, J., & Nunnenkamp, A. (2020). Time crystallinity and finite-size effects in clean floquet systems. Phys. Rev. B, 102, 214207.

[893] Po, H. C., Fidkowski, L., Vishwanath, A., & Potter, A. C. (2017). Radical chiral Floquet phases in a periodically driven Kitaev model and beyond. Phys. Rev. B, 96(24), 245116.

[894] Poilblanc, D., Schuch, N., Pérez-García, D., & Cirac, J. I. (2012). Topological and entanglement properties of resonating valence bond wave functions. Phys. Rev. B, 86(1), 014404. Publisher: American Physical Society.

[895] Pokhilko, P., Bezrukov, D. S., & Krylov, A. I. (2021). Is Solid Copper Oxalate a Spin Chain or a Mixture of Entangled Spin Pairs? J. Phys. Chem. C, 125(13), 7502–7510.

[896] Pokhilko, P. & Krylov, A. I. (2020). Effective Hamiltonians derived from equation-of-motion coupled-cluster wave functions: Theory and application to the Hubbard and Heisenberg Hamiltonians. J. Chem. Phys., 152(9), 094108.

[897] Pollman, F. (2025). Private communication.

[898] Potirniche, I.-D., Potter, A. C., Schleier-Smith, M., Vishwanath, A., & Yao, N. Y. (2017). Floquet Symmetry-Protected Topological Phases in Cold-Atom Systems. Phys. Rev. Lett., 119(12), 123601.

[899] Qiskit contributors (2023). Qiskit: An open-source framework for quantum computing.

[900] Rakovszky, T. & Khemani, V. (2023). The physics of (good) ldpc codes i. gauging and dualities.

[901] Raussendorf, R., Browne, D. E., & Briegel, H. J. (2003). Measurement-based quantum computation on cluster states. Physical Review A, 68(2), 022312.

[902] Russomanno, A., Iemini, F., Dalmonte, M., & Fazio, R. (2017). Floquet time crystal in the lipkin-meshkov-glick model. Physical Review B, 95(21).

[903] Sachdev, S. (1992). Kagome- and triangular-lattice Heisenberg antiferromagnets: Ordering from quantum fluctuations and quantum-disordered ground states with unconfined bosonic spinons. Phys. Rev. B, 45(21), 12377–12396. Publisher: American Physical Society.

[904] Sachdev, S. (2018). Topological order, emergent gauge fields, and Fermi surface reconstruction. Rep. Prog. Phys., 82(1), 014001.

[905] Sachdev, S. & Ye, J. (1993). Gapless spin-fluid ground state in a random quantum Heisenberg magnet. Phys. Rev. Lett., 70(21), 3339–3342. Publisher: American Physical Society.

[906] Saffman, M., Walker, T. G., & Mølmer, K. (2010). Quantum information with rydberg atoms. Rev. Mod. Phys., 82, 2313–2363.

[907] Sahay, R., Lukin, M. D., & Cotler, J. (2024). Emergent Holographic Forces from Tensor Networks and Criticality.

[908] Saleh, A. M. E., Arashi, M., & Kibria, B. G. (2019). Theory of ridge regression estimation with applications. John Wiley & Sons.

[909] Samajdar, R., Ho, W. W., Pichler, H., Lukin, M. D., & Sachdev, S. (2021). Quantum phases of Rydberg atoms on a kagome lattice. Proceedings of the National Academy of Sciences, 118(4), e2015785118.

[910] Samajdar, R., Joshi, D. G., Teng, Y., & Sachdev, S. (2022). Emergent $\mathbb{Z}_2$ gauge theories and topological excitations in Rydberg atom arrays.

[911] Samajdar, R., Joshi, D. G., Teng, Y., & Sachdev, S. (2023). Emergent $\mathbb{Z}_2$ Gauge Theories and Topological Excitations in Rydberg Atom Arrays. Phys. Rev. Lett., 130, 043601.

[912] Satzinger, K., Liu, Y.-J., Smith, A., Knapp, C., Newman, M., Jones, C., Chen, Z., Quintana, C., Mi, X., Dunsworth, A., et al. (2021a). Realizing topologically ordered states on a quantum processor. Science, 374(6572), 1237–1241.

[913] Satzinger, K. J., Liu, Y.-J., Smith, A., Knapp, C., Newman, M., Jones, C., Chen, Z., Quintana, C., Mi, X., Dunsworth, A., Gidney, C., Aleiner, I., Arute, F., Arya, K., Atalaya, J., Babbush, R., Bardin, J. C., Barends, R., Basso, J., Bengtsson, A., Bilmes, A., Broughton, M., Buckley, B. B., Buell, D. A., Burkett, B., Bushnell, N., Chiaro, B., Collins, R., Courtney, W., Demura, S., Derk, A. R., Eppens, D., Erickson, C., Faoro, L., Farhi, E., Fowler, A. G., Foxen, B., Giustina, M., Greene, A., Gross, J. A., Harrigan, M. P., Harrington, S. D.,

Hilton, J., Hong, S., Huang, T., Huggins, W. J., Ioffe, L. B., Isakov, S. V., Jeffrey, E., Jiang, Z., Kafri, D., Kechedzhi, K., Khattar, T., Kim, S., Klimov, P. V., Korotkov, A. N., Kostritsa, F., Landhuis, D., Laptev, P., Locharla, A., Lucero, E., Martin, O., McClean, J. R., McEwen, M., Miao, K. C., Mohseni, M., Montazeri, S., Mruczkiewicz, W., Mutus, J., Naaman, O., Neeley, M., Neill, C., Niu, M. Y., O'Brien, T. E., Opremcak, A., Pató, B., Petukhov, A., Rubin, N. C., Sank, D., Shvarts, V., Strain, D., Szalay, M., Villalonga, B., White, T. C., Yao, Z., Yeh, P., Yoo, J., Zalcman, A., Neven, H., Boixo, S., Megrant, A., Chen, Y., Kelly, J., Smelyanskiy, V., Kitaev, A., Knap, M., Pollmann, F., & Roushan, P. (2021b). Realizing topologically ordered states on a quantum processor. Science, 374(6572), 1237–1241.

[914] Schindler, P. M. & Bukov, M. (2024). Counterdiabatic Driving for Periodically Driven Systems.

[915] Schleier-Smith, M. H., Leroux, I. D., & Vuletić, V. (2010). States of an Ensemble of Two-Level Atoms with Reduced Quantum Uncertainty. Phys. Rev. Lett., 104, 073604.

[916] Scholl, P., Schuler, M., Williams, H. J., Eberharter, A. A., Barredo, D., Schymik, K.-N., Lienhard, V., Henry, L.-P., Lang, T. C., Lahaye, T., Läuchli, A. M., & Browaeys, A. (2021a). Quantum simulation of 2D antiferromagnets with hundreds of Rydberg atoms. Nature, 595(7866), 233–238.

[917] Scholl, P., Schuler, M., Williams, H. J., Eberharter, A. A., Barredo, D., Schymik, K.-N., Lienhard, V., Henry, L.-P., Lang, T. C., Lahaye, T., Läuchli, A. M., & Browaeys, A. (2021b). Quantum simulation of 2D antiferromagnets with hundreds of Rydberg atoms. Nature, 595(7866), 233–238.

[918] Scholl, P., Shaw, A. L., Tsai, R. B.-S., Finkelstein, R., Choi, J., & Endres, M. (2023a). Erasure conversion in a high-fidelity Rydberg quantum simulator. Nature, 622(7982), 273–278.

[919] Scholl, P., Shaw, A. L., Tsai, R. B.-S., Finkelstein, R., Choi, J., & Endres, M. (2023b). Erasure conversion in a high-fidelity Rydberg quantum simulator. Nature, 622(7982), 273–278.

[920] Scholl, P., Williams, H. J., Bornet, G., Wallner, F., Barredo, D., Henriet, L., Signoles, A., Hainaut, C., Franz, T., Geier, S., Tebben, A., Salzinger, A., Zürn, G., Lahaye, T., Weidemüller, M., & Browaeys, A. (2022a). Microwave Engineering of Programmable *XXZ* Hamiltonians in Arrays of Rydberg Atoms. PRX Quantum, 3, 020303.

[921] Scholl, P., Williams, H. J., Bornet, G., Wallner, F., Barredo, D., Henriet, L., Signoles, A., Hainaut, C., Franz, T., Geier, S., Tebben, A., Salzinger, A., Zürn, G., Lahaye, T., Weidemüller, M., & Browaeys, A. (2022b). Microwave Engineering of Programmable XXZ Hamiltonians in Arrays of Rydberg Atoms. PRX Quantum, 3(2), 020303.

[922] Schollwöck, U. (2011). The density-matrix renormalization group in the age of matrix product states. Annals of Physics, 326(1), 96–192.

[923] Schreiber, M., Hodgman, S. S., Bordia, P., Lüschen, H. P., Fischer, M. H., Vosk, R., Altman, E., Schneider, U., & Bloch, I. (2015). Observation of many-body localization of interacting fermions in a quasirandom optical lattice. Science, 349(6250), 842–845.

[924] Schuch, N., Pérez-García, D., & Cirac, I. (2011). Classifying quantum phases using matrix product states and projected entangled pair states. Phys. Rev. B, 84, 165139.

[925] Schuch, N., Poilblanc, D., Cirac, J. I., & Pérez-García, D. (2012). Resonating valence bond states in the PEPS formalism. Phys. Rev. B, 86(11), 115108. Publisher: American Physical Society.

[926] Schuch, N., Wolf, M. M., Verstraete, F., & Cirac, J. I. (2007). Computational complexity of projected entangled pair states. Phys. Rev. Lett., 98, 140506.

[927] Schuckert, A., Bohrdt, A., Crane, E., & Knap, M. (2022). Probing finite-temperature observables in quantum simulators with short-time dynamics. arXiv:2206.01756 [cond-mat, physics:quant-ph].

[928] Schuckert, A., Crane, E., Gorshkov, A. V., Hafezi, M., & Gullans, M. J. (2024). Fermion-qubit fault-tolerant quantum computing. _eprint: 2411.08955.

[929] Schweizer, C., Grusdt, F., Berngruber, M., Barbiero, L., Demler, E., Goldman, N., Bloch, I., & Aidelsburger, M. (2019a). Floquet approach to $\mathbb{Z}_2$ lattice gauge theories with ultracold atoms in optical lattices. Nature Physics, 15(11), 1168–1173.

[930] Schweizer, C., Grusdt, F., Berngruber, M., Barbiero, L., Demler, E., Goldman, N., Bloch, I., & Aidelsburger, M. (2019b). Floquet approach to $\mathbb{Z}_2$ lattice gauge theories with ultracold atoms in optical lattices. Nat. Phys., 15(11), 1168–1173.

[931] Sels, D. & Polkovnikov, A. (2017a). Minimizing irreversible losses in quantum systems by local counterdiabatic driving. Proceedings of the National Academy of Sciences, 114(20), E3909–E3916.

[932] Sels, D. & Polkovnikov, A. (2017b). Minimizing irreversible losses in quantum systems by local counterdiabatic driving. Proceedings of the National Academy of Sciences, 114(20), E3909–E3916.

[933] Semeghini, G., Levine, H., Keesling, A., Ebadi, S., Wang, T. T., Bluvstein, D., Verresen, R., Pichler, H., Kalinowski, M., Samajdar, R., et al. (2021a). Probing topological spin liquids on a programmable quantum simulator. Science, 374(6572), 1242–1247.

[934] Semeghini, G., Levine, H., Keesling, A., Ebadi, S., Wang, T. T., Bluvstein, D., Verresen, R., Pichler, H., Kalinowski, M., Samajdar, R., Omran, A., Sachdev, S., Vishwanath, A., Greiner, M., Vuletić, V., & Lukin, M. D. (2021b). Probing topological spin liquids on a programmable quantum simulator. Science, 374(6572), 1242–1247.

[935] Semeghini, G., Levine, H., Keesling, A., Ebadi, S., Wang, T. T., Bluvstein, D., Verresen, R., Pichler, H., Kalinowski, M., Samajdar, R., Omran, A., Sachdev, S., Vishwanath, A., Greiner, M., Vuletić, V., & Lukin, M. D. (2021c). Probing topological spin liquids on a programmable quantum simulator. Science, 374(6572), 1242–1247.

[936] Semeghini, G., Levine, H., Keesling, A., Ebadi, S., Wang, T. T., Bluvstein, D., Verresen, R., Pichler, H., Kalinowski, M., Samajdar, R., Omran, A., Sachdev,

S., Vishwanath, A., Greiner, M., Vuletić, V., & Lukin, M. D. (2021d). Probing topological spin liquids on a programmable quantum simulator. Science, 374(6572), 1242–1247.

[937] Serbyn, M., Abanin, D. A., & Papić, Z. (2020). Quantum Many-Body Scars and Weak Breaking of Ergodicity. arXiv e-prints, (pp. arXiv:2011.09486).

[938] Shaik, S., Hirao, H., & Kumar, D. (2007). Reactivity of high-valent iron–oxo species in enzymes and synthetic reagents: a tale of many states. Acc. Chem. Res., 40(7), 532–542.

[939] Shao, H. J., Wang, Y. X., Zhu, D. Z., Zhu, Y. S., Sun, H. N., Chen, S. Y., Zhang, C., Fan, Z. J., Deng, Y., Yao, X. C., Chen, Y. A., & Pan, J. W. (2024). Antiferromagnetic phase transition in a 3d fermionic hubbard model. Nature, 632, 267–272.

[940] Sharma, S., Sivalingam, K., Neese, F., & Chan, G. K.-L. (2014). Low-energy spectrum of iron–sulfur clusters directly from many-particle quantum mechanics. Nat. Chem., 6(10), 927–933.

[941] Shee, J., Loipersberger, M., Hait, D., Lee, J., & Head-Gordon, M. (2021). Revealing the nature of electron correlation in transition metal complexes with symmetry breaking and chemical intuition. J. Chem. Phys., 154(19), 194109.

[942] Sheng, C., He, X., Xu, P., Guo, R., Wang, K., Xiong, Z., Liu, M., Wang, J., & Zhan, M. (2018a). High-Fidelity Single-Qubit Gates on Neutral Atoms in a Two-Dimensional Magic-Intensity Optical Dipole Trap Array. Phys. Rev. Lett., 121(24), 240501.

[943] Sheng, C., He, X., Xu, P., Guo, R., Wang, K., Xiong, Z., Liu, M., Wang, J., & Zhan, M. (2018b). High-fidelity single-qubit gates on neutral atoms in a two-dimensional magic-intensity optical dipole trap array. Phys. Rev. Lett., 121, 240501.

[944] Shi, T., Demler, E., & Cirac, J. I. (2018). Variational study of fermionic and bosonic systems with non-Gaussian states: Theory and applications. Ann. Phys., 390, 245–302.

[945] Shinjo, K., Sota, S., & Tohyama, T. (2015). Density-matrix renormalization group study of the extended Kitaev-Heisenberg model. Phys. Rev. B, 91(5), 054401.

[946] Shiraishi, N. & Mori, T. (2017). Systematic construction of counterexamples to the eigenstate thermalization hypothesis. Phys. Rev. Lett., 119, 030601.

[947] Singh, K., Anand, S., Pocklington, A., Kemp, J. T., & Bernien, H. (2022). Dual-Element, Two-Dimensional Atom Array with Continuous-Mode Operation. Phys. Rev. X, 12(1), 011040.

[948] Somma, R. D. (2019). Quantum eigenvalue estimation via time series analysis. New J. Phys., 21(12), 123025.

[949] Sørensen, A. & Mølmer, K. (1999). Quantum computation with ions in thermal motion. Phys. Rev. Lett., 82, 1971–1974.

[950] Spar, B. M., Guardado-Sanchez, E., Chi, S., Yan, Z. Z., & Bakr, W. S. (2022). Realization of a Fermi-Hubbard Optical Tweezer Array. Phys. Rev. Lett., 128(22), 223202.

[951] Stricker, R., Vodola, D., Erhard, A., Postler, L., Meth, M., Ringbauer, M., Schindler, P., Monz, T., Müller, M., & Blatt, R. (2020). Experimental deterministic correction of qubit loss. Nature, 585(7824), 207–210.

[952] Sun, B.-Y., Goldman, N., Aidelsburger, M., & Bukov, M. (2022). Engineering and probing non-Abelian chiral spin liquids using periodically driven ultracold atoms.

[953] Surace, F. M., Mazza, P. P., Giudici, G., Lerose, A., Gambassi, A., & Dalmonte, M. (2020). Lattice Gauge Theories and String Dynamics in Rydberg Atom Quantum Simulators. Phys. Rev. X, 10, 021041.

[954] Szabo, A. & Ostlund, N. S. (2012). Modern quantum chemistry: introduction to advanced electronic structure theory. Courier Corporation.

[955] Tabares, C., Kokail, C., Zoller, P., González-Cuadra, D., & González-Tudela, A. (2025). Programming optical-lattice Fermi-Hubbard quantum simulators. _eprint: 2502.05067.

[956] Tagliacozzo, L., Celi, A., Zamora, A., & Lewenstein, M. (2013). Optical Abelian lattice gauge theories. Annals of Physics, 330, 160–191.

[957] Takagi, H., Takayama, T., Jackeli, G., Khaliullin, G., & Nagler, S. E. (2019a). Concept and realization of Kitaev quantum spin liquids. Nat. Rev. Phys., 1(4), 264–280.

[958] Takagi, H., Takayama, T., Jackeli, G., Khaliullin, G., & Nagler, S. E. (2019b). Concept and realization of Kitaev quantum spin liquids. Nat. Rev. Phys., 1(4), 264–280.

[959] Tarabunga, P. S., Surace, F. M., Andreoni, R., Angelone, A., & Dalmonte, M. (2022a). Gauge-Theoretic Origin of Rydberg Quantum Spin Liquids. Phys. Rev. Lett., 129, 195301.

[960] Tarabunga, P. S., Surace, F. M., Andreoni, R., Angelone, A., & Dalmonte, M. (2022b). Gauge-theoretic origin of rydberg quantum spin liquids.

[961] Tazhigulov, R. N., Sun, S.-N., Haghshenas, R., Zhai, H., Tan, A. T., Rubin, N. C., Babbush, R., Minnich, A. J., & Chan, G. K.-L. (2022). Simulating Models of Challenging Correlated Molecules and Materials on the Sycamore Quantum Processor. PRX Quantum, 3(4), 040318.

[962] Tepaske, M. S. J., Luitz, D. J., & Hahn, D. (2023). Optimal compression of constrained quantum time evolution. arXiv:2311.06347 [cond-mat, physics:quant-ph].

[963] Terhal, B. M. (2015). Quantum error correction for quantum memories. Rev. Mod. Phys., 87, 307–346.

[964] Tóth, G. (2012). Multipartite entanglement and high-precision metrology. Phys. Rev. A, 85, 022322.

[965] Turner, C. J., Desaules, J.-Y., Bull, K., & Papić, Z. (2020). Correspondence principle for many-body scars in ultracold Rydberg atoms.

[966] Turner, C. J., Michailidis, A. A., Abanin, D. A., Serbyn, M., & Papić, Z. (2018a). Weak ergodicity breaking from quantum many-body scars. Nat. Phys., 14, 745.

[967] Turner, C. J., Michailidis, A. A., Abanin, D. A., Serbyn, M., & Papić, Z. (2018b). Weak ergodicity breaking from quantum many-body scars. Nature Physics, 14(7), 745–749.

[968] Turner, C. J., Michailidis, A. A., Abanin, D. A., Serbyn, M., & Papić, Z. (2018c). Quantum scarred eigenstates in a Rydberg atom chain: Entanglement, breakdown of thermalization, and stability to perturbations. Phys. Rev. B, 98, 155134.

[969] Urban, E., Johnson, T. A., Henage, T., Isenhower, L., Yavuz, D. D., Walker, T. G., & Saffman, M. (2009). Observation of Rydberg blockade between two atoms. Nat. Phys., 5(2), 110–114.

[970] Van Den Nest, M., Dehaene, J., & De Moor, B. (2004). Graphical description of the action of local Clifford transformations on graph states. Physical Review A, 69(2), 022316.

[971] Verresen, R., Lukin, M. D., & Vishwanath, A. (2021a). Prediction of Toric Code Topological Order from Rydberg Blockade. Phys. Rev. X, 11, 031005.

[972] Verresen, R., Lukin, M. D., & Vishwanath, A. (2021b). Prediction of Toric Code Topological Order from Rydberg Blockade. Phys. Rev. X, 11, 031005.

[973] Verresen, R., Lukin, M. D., & Vishwanath, A. (2021c). Prediction of toric code topological order from Rydberg blockade. Phys. Rev. X, 11, 031005.

[974] Verresen, R., Tantivasadakarn, N., & Vishwanath, A. (2021d). Efficiently preparing Schrödinger's cat, fractons and non-abelian topological order in quantum devices.

[975] Verresen, R. & Vishwanath, A. (2022a). Unifying Kitaev Magnets, Kagomé Dimer Models, and Ruby Rydberg Spin Liquids. Phys. Rev. X, 12, 041029.

[976] Verresen, R. & Vishwanath, A. (2022b). Unifying Kitaev magnets, kagome dimer models and ruby Rydberg spin liquids.

[977] Verresen, R., Vishwanath, A., & Pollmann, F. (2019). Stable Luttinger liquids and emergent $U(1)$ symmetry in constrained quantum chains.

[978] Verstraete, F. & Cirac, J. I. (2005). Mapping local Hamiltonians of fermions to local Hamiltonians of spins. J. Stat. Mech.: Theory Exp., 2005(09), P09012.

[979] Verstraete, F., Cirac, J. I., & Latorre, J. I. (2009). Quantum circuits for strongly correlated quantum systems. Phys. Rev. A, 79(3), 032316. Publisher: American Physical Society.

[980] Verstraete, F., Murg, V., & Cirac, J. I. (2008). Matrix product states, projected entangled pair states, and variational renormalization group methods for quantum spin systems. Advances in Physics, 57(2), 143–224.

[981] Vidal, G. (2008). Class of quantum many-body states that can be efficiently simulated. Phys. Rev. Lett., 101, 110501.

[982] Villa, L., Despres, J., & Sanchez-Palencia, L. (2019). Unraveling the excitation spectrum of many-body systems from quantum quenches. Phys. Rev. A, 100(6), 063632.

[983] von Keyserlingk, C. W., Khemani, V., & Sondhi, S. L. (2016). Absolute stability and spatiotemporal long-range order in floquet systems. Physical Review B, 94(8).

[984] Vorwerk, C., Sheng, N., Govoni, M., Huang, B., & Galli, G. (2022). Quantum embedding theories to simulate condensed systems on quantum computers. Nature Computational Science, 2(7), 424–432.

[985] Wan, K., Berta, M., & Campbell, E. T. (2022). Randomized Quantum Algorithm for Statistical Phase Estimation. Physical Review Letters, 129(3), 030503.

[986] Wan, K., Huggins, W. J., Lee, J., & Babbush, R. (2023). Matchgate Shadows for Fermionic Quantum Simulation. Communications in Mathematical Physics, 404(2), 629–700. ISBN: 1432-0916.

[987] Wang, C., Harrington, J., & Preskill, J. (2003). Confinement-higgs transition in a disordered gauge theory and the accuracy threshold for quantum memory. Annals of Physics, 303(1), 31–58.

[988] Wang, Z. (2010). Topological quantum computation. Number 112. American Mathematical Soc.

[989] Wang, Z., Ge, Z.-Y., Xiang, Z., Song, X., Huang, R.-Z., Song, P., Guo, X.-Y., Su, L., Xu, K., Zheng, D., & Fan, H. (2022). Observation of emergent $\mathbb{Z}_2$ gauge invariance in a superconducting circuit. Phys. Rev. Res., 4, L022060.

[990] Waugh, J. S., Huber, L. M., & Haeberlen, U. (1968). Approach to High-Resolution nmr in Solids. Phys. Rev. Lett., 20, 180–182.

[991] Wecker, D., Hastings, M. B., Wiebe, N., Clark, B. K., Nayak, C., & Troyer, M. (2015). Solving strongly correlated electron models on a quantum computer. Physical Review A, 92(6), 062318.

[992] Wei, K. X., Ramanathan, C., & Cappellaro, P. (2018). Exploring Localization in Nuclear Spin Chains. Phys. Rev. Lett., 120, 070501.

[993] Weidinger, S. A. (2018). Non-equilibrium Field Theory of Condensed Matter Systems – Periodic Driving and Quantum Quenches. Phd thesis, Technischen Universität München.

[994] Wen, X.-G. (2007). Quantum Field Theory of Many-Body Systems: From the Origin of Sound to an Origin of Light and Electrons. Oxford University Press.

[995] Wen, X.-G. (2017). Colloquium: Zoo of quantum-topological phases of matter. Rev. Mod. Phys., 89(4), 041004. Publisher: American Physical Society.

[996] Wiese, U.-J. (2013). Ultracold quantum gases and lattice systems: quantum simulation of lattice gauge theories. Annalen der Physik, 525(10-11), 777–796.

[997] Wilczek (1992). Disassembling anyons. Phys. Rev. Lett., 69(1), 132–135.

[998] Wilson, K. G. (1974). Confinement of quarks. Physical Review D, 10(8), 2445–2459.

[999] Woodruff, D. N., Winpenny, R. E. P., & Lay, R. A. (2013). Lanthanide Single-Molecule Magnets. Chem. Rev., 113, 5110.

[1000] Wu, T.-Y., Kumar, A., Mejia, F. G., & Weiss, D. S. (2019). Stern-Gerlach detection of neutral atom qubits in a state dependent optical lattice. Nat. Phys., 15(6), 538–542.

[1001] Xu, C., Feng, J., Kawamura, M., Yamaji, Y., Nahas, Y., Prokhorenko, S., Qi, Y., Xiang, H., & Bellaiche, L. (2020a). Possible Kitaev Quantum Spin Liquid State in 2D Materials with S = 3 / 2. Phys. Rev. Lett., 124(8), 087205.

[1002] Xu, H. & Taylor, J. M. (2011). Developing a robust approach to implementing non-Abelian anyons and topological quantum computing in a modified Kitaev honeycomb lattice model.

[1003] Xu, M., Kendrick, L. H., Kale, A., Gang, Y., Ji, G., Scalettar, R. T., Lebrat, M., & Greiner, M. (2023). Frustration- and doping-induced magnetism in a fermi–hubbard simulator. Nature, 620, 971–976.

[1004] Xu, Q., Zhou, H., Zheng, G., Bluvstein, D., Ataides, J. P. B., Lukin, M. D., & Jiang, L. (2024). Fast and Parallelizable Logical Computation with Homological Product Codes.

[1005] Xu, S., Susskind, L., Su, Y., & Swingle, B. (2020b). A Sparse Model of Quantum Holography. _eprint: 2008.02303.

[1006] Yang, B., Sun, H., Ott, R., Wang, H.-Y., Zache, T. V., Halimeh, J. C., Yuan, Z.-S., Hauke, P., & Pan, J.-W. (2020). Observation of gauge invariance in a 71-site Bose–Hubbard quantum simulator. Nature, 587(7834), 392–396.

[1007] Yao, N., Potter, A., Potirniche, I.-D., & Vishwanath, A. (2017a). Discrete time crystals: Rigidity, criticality, and realizations. Physical Review Letters, 118(3).

[1008] Yao, N. Y., Potter, A. C., Potirniche, I.-D., & Vishwanath, A. (2017b). Discrete Time Crystals: Rigidity, Criticality, and Realizations. Phys. Rev. Lett., 118, 030401.

[1009] Yao, N. Y., Potter, A. C., Potirniche, I.-D., & Vishwanath, A. (2017c). Discrete Time Crystals: Rigidity, Criticality, and Realizations. Phys. Rev. Lett., 118(3), 030401.

[1010] Yarloo, H., Emami Kopaei, A., & Langari, A. (2020). Homogeneous floquet time crystal from weak ergodicity breaking. Phys. Rev. B, 102, 224309.

[1011] Young, A. W., Eckner, W. J., Schine, N., Childs, A. M., & Kaufman, A. M. (2022). Tweezer-programmable 2D quantum walks in a Hubbard-regime lattice. Science, 377(6608), 885–889.

[1012] Zache, T. V., González-Cuadra, D., & Zoller, P. (2023a). Fermion-qudit quantum processors for simulating lattice gauge theories with matter. Quantum, 7, 1140.

[1013] Zache, T. V., González-Cuadra, D., & Zoller, P. (2023b). Fermion-qudit quantum processors for simulating lattice gauge theories with matter. Quantum, 7, 1140. Publisher: Verein zur Förderung des Open Access Publizierens in den Quantenwissenschaften.

[1014] Zeng, Z., Giudici, G., & Pichler, H. (2024). Quantum dimer models with Rydberg gadgets.

[1015] Zhang, J., Hess, P. W., Kyprianidis, A., Becker, P., Lee, A., Smith, J., Pagano, G., Potirniche, I. D., Potter, A. C., Vishwanath, A., Yao, N. Y., & Monroe, C. (2017). Observation of a discrete time crystal. Nature, 543(7644), 217–220.

[1016] Zhang, S.-S., Halász, G. B., & Batista, C. D. (2022). Theory of the Kitaev model in a [111] magnetic field. Nat. Commun., 13(1), 399.

[1017] Zhou, H., Choi, J., Choi, S., Landig, R., Douglas, A. M., Isoya, J., Jelezko, F., Onoda, S., Sumiya, H., Cappellaro, P., Knowles, H. S., Park, H., & Lukin, M. D. (2020). Quantum Metrology with Strongly Interacting Spin Systems. Phys. Rev. X, 10, 031003.

[1018] Zhou, H., Martin, L. S., Tyler, M., Makarova, O., Leitao, N., Park, H., & Lukin, M. D. (2023). Robust Higher-Order Hamiltonian Engineering for Quantum Sensing with Strongly Interacting Systems. Phys. Rev. Lett., 131, 220803.

[1019] Zhou, H., Zhao, C., Cain, M., Bluvstein, D., Duckering, C., Hu, H.-Y., Wang, S.-T., Kubica, A., & Lukin, M. D. (2024). Algorithmic Fault Tolerance for Fast Quantum Computing.

[1020] Zhu, G., Lavasani, A., & Barkeshli, M. (2020). Universal logical gates on topologically encoded qubits via constant-depth unitary circuits. Phys. Rev. Lett., 125, 050502.

[1021] Zhu, G.-Y. & Zhang, G.-M. (2019). Gapless coulomb state emerging from a self-dual topological tensor-network state. Phys. Rev. Lett., 122, 176401.

[1022] Zintchenko, I. & Wiebe, N. (2016). Randomized gap and amplitude estimation. Physical Review A, 93(6), 062306. arXiv:1603.03672 [quant-ph].

[1023] Znidaric, M. (2020). Weak Integrability Breaking: Chaos with Integrability Signature in Coherent Diffusion. Phys. Rev. Lett., 125, 180605.

[1024] Zohar, E., Cirac, J. I., & Reznik, B. (2013). Simulating (2+1)-Dimensional Lattice QED with Dynamical Matter Using Ultracold Atoms. Phys. Rev. Lett., 110, 055302.

[1025] Zohar, E., Cirac, J. I., & Reznik, B. (2015). Quantum simulations of lattice gauge theories using ultracold atoms in optical lattices. Reports on Progress in Physics, 79(1), 014401.

[1026] Zohar, E., Farace, A., Reznik, B., & Cirac, J. I. (2017). Digital Quantum Simulation of Z2 Lattice Gauge Theories with Dynamical Fermionic Matter. Phys. Rev. Lett., 118(7), 070501.